

UNIVERSITY OF CALIFORNIA

Los Angeles

Novel economical approaches for the fluorine-18  
radiopharmaceuticals production via droplet  
radiochemistry

A dissertation submitted in partial satisfaction of the  
requirements for the degree Doctor of Philosophy in  
Physics and Biology in Medicine

by

Ksenia Lisova

2021

© Copyright by

Ksenia Lisova

2021

## ABSTRACT OF THE DISSERTATION

Novel economical approaches for the fluorine-18 radiopharmaceuticals production via droplet  
radiochemistry

by

Ksenia Lisova

Physics and Biology in Medicine

University of California Los Angeles, 2021

Professor Robert Michael van Dam, Chair

Positron emission tomography (PET) is a powerful medical diagnostics and research tool that uses radiolabeled molecules (tracers) to image biological processes *in vivo*. By administering only nanomolar quantities of the tracers, PET scans enable non-invasive assessment of normal biological processes in cells and their failure in disease to aid in medical diagnostics, staging of disease severity and monitoring treatment response. Short-lived radioisotopes used in the synthesis of diagnostic PET tracers necessitate that the tracer production is carried out shortly before imaging. Each production is a multistep process involving acquisition of the radioisotope, radiochemical synthesis and quality control. Radiochemical synthesis is further broken down into radiochemical reaction to link the radioisotope with a ligand, purification and formulation to obtain pure injection-ready product.

Despite impressive sensitivity and accuracy of PET in medical diagnostics, access to the wide variety of short-lived radioactive tracers is hindered due to a high cost of their preparation. The overall preparation cost covers: (i) radiosynthesis units and various consumables, (ii) large shielded fume hoods (hot-cells), (iii) reagents and radioisotope, (iv) labor and safety. A typical centralized production of PET tracers in large radiochemistry facilities alleviates the high cost per

production by splitting of the large batches and shipping those to multiple users, which is only possible for tracers in high demand such as [ $^{18}\text{F}$ ]fluorodeoxyglucose ([ $^{18}\text{F}$ ]FDG). Newly introduced dose-on-demand concept proposes convenient production of any tracer of interest directly at the imaging location, leading to a decentralized approach. While setting up dedicated conventional radiosynthesis modules for this purpose is unrealistic due to the high cost and large footprint, microfluidic approaches provide a path for a miniaturized, economical tracer production.

Our lab among others has been extensively working on the radiosynthesis miniaturization using droplet microfluidic methods. Microfluidics offers potential of cost reduction in almost all aspects of radiosynthesis. (i) The synthesizer cost can be reduced as a result of reduced system size, complexity and consumables cost, (ii) the compact units can be self-shielded not requiring use of hot-cells, (iii) the reagent and radioisotope consumption per synthesis is orders of magnitude less, (iv) the faster synthesis times and small-scale production levels reduce labor burden and improve safety. Additionally, in fluorine-18 radiochemistry, the conventional synthesizers must use high starting radioactivity to ensure good molar activity (radioactivity per moles of the substance) of the final product. Previously, our group has developed automated droplet reactors based on electrowetting on dielectric (EWOD) technology. However, those devices had limitations due to high cost and complexity of fabrication. More recently, we introduced low-cost disposable silicon chips which serve as a reactor within an ultra-compact automated radiosynthesizer unit, comparable in size to a 12 oz. coffee cup. The major part of this dissertation was adapting various conventional fluorine-18-labeling synthesis methods to a droplet format to demonstrate the versatility of this radiosynthesis approach.

For a number of tracers, we describe synthesis miniaturization process and demonstrate that the droplet syntheses exhibit higher yields and improved synthesis times in comparison to the conventional methods. All syntheses feature orders-of-magnitude reduction in reagent consumption and are able to achieve high molar activity even when lower starting amounts of the radioisotope are used. As a result, low cost per production can be achieved and such methods

are readily useable for research in particular that involves small animal PET imaging. Importantly, we further demonstrate that these syntheses are scalable, and that production of a few human doses is feasible. For validation, we also perform full clinical quality control on these tracer batches. These results suggest that in the future it would be possible to introduce this technology in a clinical setting as well for an easy access to a wide variety of PET tracers.

From the radiochemistry standpoint, microfluidic fluorine-18 radiolabeling has been shown to work for different type of ligands. Apart from small molecule radiolabeling, peptide labeling routes via droplet radiochemistry are also shown. In this work we feature isotopic exchange (IEX) fluorination that has a benefit of simplified purification but is challenging on conventional scale due to inherently lower molar activity in this type of reactions. We demonstrate that the droplet approach with its small volumes allows one to perform IEX synthesis of trifluoroborate-based peptides and prosthetic groups with high yields and molar activities.

This dissertation presents reliable methods for fluorine-18-labeled radiopharmaceutical production on demand, in a time- and cost-efficient manner for diverse PET tracers. While with the current progress, these methods can be readily applied for research purposes including pre-clinical PET imaging, and future work will focus on improvements and optimization of the droplet microfluidic technologies to advance these methods to the clinical PET.

The dissertation of Ksenia Lisova is approved.

Arion-Xenofon Hadjioannou

Magnus Dahlbom

Peter Clark

Robert Michael van Dam, Committee Chair

University of California, Los Angeles

2021

*Dedicated to my loving and supporting parents*

## TABLE OF CONTENTS

LIST OF FIGURES .....	xi
LIST OF TABLES .....	xiii
ACKNOWLEDGEMENTS .....	xiv
VITA .....	xviii
Chapter 1 : Introduction .....	1
1.1 Nuclear medicine imaging: Positron emission tomography.....	1
1.2 Radioisotope production routes.....	2
1.3 Diagnostic radioisotope fluorine-18 .....	3
1.4 Applications of selected fluorine-18-labeled PET tracers.....	4
1.5 Production of fluorine-18 .....	7
1.6 Chemistry of fluorine-18 tracer synthesis .....	9
1.7 Molar activity of fluorine-18 radiopharmaceuticals .....	13
1.8 Conventional synthesis of the radiopharmaceuticals .....	16
1.9 Quality control of PET radiopharmaceuticals .....	19
1.10 Challenges of conventional radiopharmaceutical production and alternative solutions	21
1.11 Microfluidic radiosynthesizers .....	23
1.12 Miniaturization of PET tracer purification, reformulation and quality control .....	30
1.13 Summary of the benefits of microfluidics in PET tracer production.....	34
1.14 Focus of this dissertation (summary) .....	35
Chapter 2 : Fluorine-18 radiolabeling of 4-N-acyl and 4-N-alkyl gemcitabine analogues .....	40
2.1 Introduction.....	40
2.2 Precursor preparation methods.....	42
2.2.1 Synthesis of silane precursors .....	42
2.2.2 Fluorination .....	44
2.2.3 Stability of Si-H substrate and Si-F products .....	45
2.2.4 Cytostatic Activity and Imaging .....	46
2.3 Radiosynthesis of [ <sup>18</sup> F]fluoro-silane probes.....	48
2.3.1 Macroscale radiosyntheses of 4-N-alkanoyl [ <sup>18</sup> F]6 and 4-N-alkyl [ <sup>18</sup> F]10 .....	48
2.3.2 Microscale radiosyntheses of 4-N-alkanoyl [ <sup>18</sup> F]6 and 4-N-alkyl [ <sup>18</sup> F]10.....	50
2.3.3 <i>In vivo</i> imaging of [ <sup>18</sup> F]4-N-Alkyl Gemcitabine radioligand 10.....	51
2.4 Experimental section .....	53
2.4.1 General procedure for click reactions .....	55
2.4.2 General Procedure for Fluorination Reactions.....	57
2.4.3 Cytostatic activity assays .....	59
2.4.4 Fluorescence studies with HEK293 cells .....	59
2.4.5 Radiosynthesis of [ <sup>18</sup> F]fluoro-silane probes .....	60



2.4.6 Preclinical Imaging.....	61
2.5 Conclusion.....	62
Chapter 3 : Droplet synthesis of O-(2-[ <sup>18</sup> F]fluoroethyl)-L-tyrosine ([ <sup>18</sup> F]FET).....	64
3.1 Introduction.....	64
3.2 Materials and methods.....	66
3.2.1 Reagents and supplies.....	66
3.2.2 Analytical methods.....	67
3.2.3 Microfluidic systems.....	68
3.2.4 Microscale radiosynthesis and purification of [ <sup>18</sup> F]FET.....	69
3.2.5 Preparation of samples with different molar activities.....	70
3.2.6 Analytical methods.....	71
3.2.7 <i>In vitro</i> probe uptake.....	74
3.2.8 <i>In vivo</i> preclinical imaging.....	75
3.3 Results.....	76
3.3.1 Microscale [ <sup>18</sup> F]FET synthesis optimization and automation.....	76
3.3.2 <i>In vivo</i> imaging at varying molar activities of [ <sup>18</sup> F]FET.....	80
3.4 Discussion.....	85
3.4.1 Microscale synthesis.....	85
3.4.2 [ <sup>18</sup> F]FET imaging.....	89
3.5 Conclusion.....	89
Chapter 4 : Droplet synthesis of [ <sup>18</sup> F]florbetaben ([ <sup>18</sup> F]FBB).....	91
4.1 Introduction.....	91
4.2 Materials and methods.....	93
4.2.1 Reagents.....	93
4.2.2 Formulation system components and operation.....	94
4.2.3 Analytical methods.....	95
4.2.4 Droplet synthesis production setup.....	96
4.2.5 Microvolume radiosynthesis optimization.....	97
4.2.6 Automated microvolume synthesis.....	99
4.2.7 Purification and formulation.....	99
4.2.8 Evaluation of synthesis performance.....	101
4.3 Results.....	102
4.3.1 Microvolume radiosynthesis optimization.....	102
4.3.2 Purification.....	105
4.3.3 Formulation.....	106
4.4 Discussion.....	108

4.4.1 High-throughput optimization .....	108
4.4.2 Purification and formulation .....	108
4.4.3 Probe stability and radiolysis .....	111
4.4.4 Benefits of microscale synthesis .....	115
4.5 Conclusion.....	117
Chapter 5 : High activity droplet syntheses of [ <sup>18</sup> F]FET and [ <sup>18</sup> F]FBB .....	118
5.1 Introduction.....	118
5.2 Materials and Methods .....	124
5.2.1 Reagents.....	124
5.2.2 Automated droplet synthesizer .....	126
5.2.3 [ <sup>18</sup> F]FET synthesis .....	127
5.2.4 [ <sup>18</sup> F]FBB synthesis .....	129
5.2.5 Analytical methods.....	130
5.2.6 Conventional quality control testing .....	131
5.2.7 Tracer-QC automated quality control testing .....	134
5.2.8 Tracer-QC .....	136
5.3 Results .....	139
5.3.1 [ <sup>18</sup> F]FET production and testing .....	139
5.3.2 [ <sup>18</sup> F]FBB production and testing.....	143
5.3.3 [ <sup>18</sup> F]FBB Quality Control with Tracer-QC .....	144
5.4 Discussion .....	147
5.4.1 Comparison to conventional synthesis .....	147
5.4.2 Activity scaling in droplet micro-radiosynthesizer .....	147
5.4.3 Impact of starting activity on synthesis performance .....	149
5.4.4 Quality control testing .....	150
5.4.5 Prospects for clinical use .....	152
5.5 Conclusion.....	154
Chapter 6 : Isotopic exchange labeling of [ <sup>18</sup> F]AMBF <sub>3</sub> -TATE in microliter volumes .....	155
6.1 Introduction.....	155
6.2 Materials and methods .....	160
6.2.1 Reagents and materials .....	160
6.2.2 Chip fabrication .....	161
6.2.3 Chip temperature control system .....	162
6.2.4 Microdroplet radiosynthesis of [ <sup>18</sup> F]AMBF <sub>3</sub> -TATE.....	162
6.2.5 Analytical methods for evaluation of synthesis performance .....	164
6.2.6 Murine tumor models .....	166

6.2.7 PET/CT imaging and biodistribution .....	167
6.2.8 [ <sup>18</sup> F]AMBF <sub>3</sub> -TATE dosimetry .....	168
6.2.9 Calculation of time-integrated activity coefficients (TIACs).....	169
6.2.10 Statistical analysis.....	171
6.3 Results .....	171
6.3.1 Microdroplet radiosynthesis of [ <sup>18</sup> F]AMBF <sub>3</sub> -TATE.....	171
6.3.2 Preclinical imaging .....	174
6.3.3 Dosimetry analysis.....	176
6.4 Discussion .....	177
6.4.1 Microdroplet radiosynthesis of [ <sup>18</sup> F]AMBF <sub>3</sub> -TATE.....	177
6.4.2 Preclinical imaging and dosimetry .....	181
6.5 Conclusion.....	181
Chapter 7 : Improved method for droplet labeling of trifluoroborates via isotopic exchange ....	183
7.1 Introduction.....	183
7.2 Materials and methods .....	186
7.2.1 Reagents.....	186
7.2.2 Droplet synthesis platform .....	187
7.2.3 Radiolabeling procedure on Teflon-glass chips .....	189
7.2.4 Optimization of radiolabeling.....	189
7.2.5 Synthesis automation.....	190
7.2.6 Analytical methods.....	190
7.3 Results .....	191
7.3.1 Generalization of IEX labeling.....	191
7.3.2 Translation to silicon chips.....	191
7.3.3 Investigation of [ <sup>18</sup> F]fluoride drying step.....	192
7.3.4 Investigation of IEX radiolabeling step.....	193
7.3.5 Automated synthesis.....	196
7.4 Discussion .....	196
7.4.1 Comparison of R-PPh <sub>3</sub> BF <sub>3</sub> to R-BF <sub>3</sub> syntheses .....	196
7.4.2 Effect of reactor format .....	197
7.4.3 Volatile activity losses .....	198
7.4.4 Automation.....	199
7.5 Conclusion.....	199
Chapter 8 : Future outlook .....	201
References .....	204

## LIST OF FIGURES

Figure 1.1 Mechanism of PET imaging.....	2
Figure 1.2 Production flow for fluorine-18-labeled tracers.....	7
Figure 1.3 (A) 2-step radiolabeling of [ <sup>18</sup> F]FET, (B) 1-step synthesis of [ <sup>18</sup> F]AMBF <sub>3</sub> -TATE via isotopic exchange.....	9
Figure 1.4 Illustration of molar activity effect on tracer receptor binding.....	13
Figure 1.5 Droplet platforms.....	27
Figure 1.6 Generalized droplet radiosynthesis procedure.....	28
Figure 2.1 Synthesis of 4-N-alkanoyl gemcitabine analogues with silicon-fluoride acceptors....	43
Figure 2.2 Synthesis of 4-N-alkyl gemcitabine analogues with silicon-fluoride acceptors.....	44
Figure 2.3 Stability of 4-N-alkanoyl 5.....	46
Figure 2.4 Incorporation of 8 in HEK293 cells.....	48
Figure 2.5 Radiosynthesis of [ <sup>18</sup> F] 4-N-alkanoyl and alkyl gemcitabine analogues with silicon-fluoride acceptors.....	49
Figure 2.6 Analytical HPLC chromatogram of purified 4-N-alkyl [ <sup>18</sup> F]10.....	50
Figure 2.7 Dynamic PET study results for [ <sup>18</sup> F]10.....	52
Figure 2.8 10 min static PET study results for [ <sup>18</sup> F]10.....	52
Figure 3.1 Droplet synthesis platform.....	68
Figure 3.2 Synthesis scheme for microvolume production of [ <sup>18</sup> F]FET using manual synthesis platform.....	70
Figure 3.3 UV absorbance spectrum of FET reference standard.....	73
Figure 3.4 Calibration curve for FET molar activity determination.....	74
Figure 3.5 a Effect of base to precursor ratio on fluorination efficiency and fluorination yield....	77
Figure 3.6 Results of initial optimization of fluorination conditions.....	78
Figure 3.7 Accumulation of [ <sup>18</sup> F]FET in different cell lines.....	81
Figure 3.8 PET/CT images of each mouse in the first imaging study.....	82
Figure 3.9 PET/CT images of each mouse in the second imaging study.....	83
Figure 3.10 Uptake curves for [ <sup>18</sup> F]FET dynamic study.....	84
Figure 3.11 Average tumor to muscle and tumor to blood ratios for different molar activities of [ <sup>18</sup> F]FET.....	85
Figure 4.1 Overview of microvolume synthesis procedure for [ <sup>18</sup> F]FBB, with detailed schematic of the formulation system (bottom). ....	96
Figure 4.2 Schematic of the microscale synthesis of crude [ <sup>18</sup> F]FBB.....	98
Figure 4.3 Schematic (above) and photograph (below) of the microscale C18 cartridge used for [ <sup>18</sup> F]florbetaben formulation.....	100
Figure 4.4 Photograph of the automated formulation system.....	101
Figure 4.5 Optimization summary of fluorination step.....	103
Figure 4.6 Example HPLC chromatogram of a crude [ <sup>18</sup> F]FBB sample.....	105
Figure 4.7 Example HPLC chromatogram from a formulated sample of [ <sup>18</sup> F]FBB (98% radiochemical purity).....	106
Figure 4.8 Example chromatograms showing sample degradation due to radiolysis.....	113
Figure 4.9 Example HPLC chromatograms showing evidence of photodegradation.....	115
Figure 5.1 Schematic of automated droplet synthesis.....	125
Figure 5.2 Tracer preparation scheme.....	127
Figure 5.3 Synthesis routes for (A) [ <sup>18</sup> F]FET and (B) [ <sup>18</sup> F]FBB.....	128
Figure 5.4 Tracer-QC setup.....	136
Figure 5.5 Performance of crude [ <sup>18</sup> F]FET droplet-based radiosynthesis as a function of starting activity.....	140
Figure 5.6 Example HPLC chromatograms for [ <sup>18</sup> F]FET.....	140
Figure 5.7 Performance of crude [ <sup>18</sup> F]FBB droplet-based radiosynthesis as a function of starting activity.....	143

Figure 5.8 Example HPLC chromatograms for [ <sup>18</sup> F]FBB .....	147
Figure 6.1 Radiosynthesis of [ <sup>18</sup> F]AMBF <sub>3</sub> -TATE via isotopic exchange on a microfluidic chip. ....	159
Figure 6.2 Droplet synthesizer.....	162
Figure 6.3 Schematic of the sequence of operations to perform the microdroplet radiosynthesis of [ <sup>18</sup> F]AMBF <sub>3</sub> -TATE on the chip.....	163
Figure 6.4 Calibration curve for HPLC determination of molar amount of AMBF <sub>3</sub> -TATE. ....	166
Figure 6.5 Molar activity of [ <sup>18</sup> F] AMBF <sub>3</sub> -TATE as a function of starting activity determined from crude samples. ....	172
Figure 6.6 Representative radio-HPLC chromatogram of crude [ <sup>18</sup> F]AMBF <sub>3</sub> -TATE .....	172
Figure 6.7 Representative radio-HPLC chromatogram of purified [ <sup>18</sup> F]AMBF <sub>3</sub> -TATE .....	173
Figure 6.8 MicroPET/CT imaging .....	173
Figure 6.9 Comparison of [ <sup>18</sup> F]AMBF <sub>3</sub> -TATE and [ <sup>68</sup> Ga]Ga-DOTATATE imaging.....	174
Figure 6.10 Non-decay-corrected [ <sup>18</sup> F]AMBF <sub>3</sub> -TATE time activity curves determined from microPET images, averaged over n=3 mice.....	175
Figure 7.1: Method illustration for IEX in droplet reactors.....	188
Figure 7.2: Radioactivity loss during [ <sup>18</sup> F]fluoride drying under different drying conditions on a non-patterned silicon chip.....	193
Figure 7.3: Reaction performance summary .....	195
Figure 7.4: HPLC chromatograms of non-radiolabeled and radiolabeled compound 1 .....	196

## LIST OF TABLES

Table 2.1 In vitro cytostatic activity of 4-N-modified gemcitabine analogues in L1210 lymphocytic leukemia cell line .....	47
Table 2.2 <sup>18</sup> F radiosynthetic yields of 4-N-modified gemcitabine analogues 6 and 10 .....	50
Table 3.1 Preparation of [ <sup>18</sup> F]FET with different molar activities (Experiment 1).....	70
Table 3.2 Preparation of [ <sup>18</sup> F]FET with different molar activities (Experiment 2).....	71
Table 3.3 Summary of performance of microdroplet synthesis of [ <sup>18</sup> F]FET .....	80
Table 3.4 Comparison of performance of the microvolume droplet synthesis of [ <sup>18</sup> F]FET and published results using conventional methods. ....	87
Table 4.1 Summary of synthesis performance .....	104
Table 4.2 Summary of performance of the formulation step.....	107
Table 4.3 Comparison of the performance of the microscale synthesis reported in this work to literature methods .....	110
Table 5.1 Literature reports of microfluidic production of <sup>18</sup> F-labeled radiopharmaceuticals with sufficient quantities for human PET .....	120
Table 5.2 Reagent setup in automated droplet synthesizer for syntheses of [ <sup>18</sup> F]FET and [ <sup>18</sup> F]FBB. ....	130
Table 5.3 Automation of [ <sup>18</sup> F]FBB Quality Control Testing .....	137
Table 5.4 Performance of droplet-based [ <sup>18</sup> F]FET low activity synthesis on several platforms. ....	139
Table 5.5 Conventional (manual) quality control testing results for 3 consecutive batches of [ <sup>18</sup> F]FET .....	142
Table 5.6 A comparison of low activity droplet-based [ <sup>18</sup> F]FBB synthesis performance .....	143
Table 5.7 Conventional (manual) quality control testing results for 3 consecutive batches of [ <sup>18</sup> F]FBB. ....	145
Table 5.8 Tracer-QC quality control results for additional batches of [ <sup>18</sup> F]FBB. ....	146
Table 6.1 Mean time-integrated activity coefficient (TIAC) values for the several organs scaled to humans. ....	175
Table 6.2 Mean absorbed dose coefficient values of the organs and the respective standard deviations for both methods using a one-compartment voiding bladder model.....	177
Table 6.3 Performance of synthesis of [ <sup>18</sup> F]AMBF <sub>3</sub> -TATE as determined from the collected crude product.....	179
Table 6.4 Performance of full production runs (including purification) for [ <sup>18</sup> F]AMBF <sub>3</sub> -TATE ...	180
Table 7.1 Summary of radiochemical yields for various R-PPh <sub>3</sub> BF <sub>3</sub> precursors.....	191
Table 7.2: Summary of performance of droplet-based IEX reactions using various reactor format .....	194

## ACKNOWLEDGEMENTS

I would like to start by thanking the funding sources that supported all of my doctorate work. The National Institutes of Health (R21EB015540, R21AG049918, P30CA016042, T32EB002101), the Caltech/UCLA Nanosystems Biology Cancer Center (NCIU54 CA151819), the Department of Energy Office of Science (DE-SC0012353), National Cancer Institute (R21CA212718, P30CA016042, R33CA240201, R21CA212718), the National Institute on Aging (R21AG049918), the National Institute of Mental Health (R44MH097271) and the National Institute of Biomedical Imaging and Bioengineering (T32EB002101) and the UCLA Foundation from a donation made by Ralph and Marjorie Crump for the Crump Institute for Molecular Imaging.

During my years in the PhD program, I was incredibly lucky to work alongside and learn from many great people. I would like to start by thanking all of my fellow colleagues from van Dam lab. I thank Dr. Maxim Sergeev for giving me a warm welcome to the radiochemistry lab and teaching me about the fundamentals of droplet radiochemistry. Max's explanations on any chemistry question were crystal clear and I am grateful to have had the opportunity to learn from him. I want to thank Dr. Jia Wang who has not only been an inspirational microfluidics engineer, but also a great friend. I thank Jia for taking the time to train me to fabricate microfluidic chips, for sharing her engineering expertise, and for keeping me motivated during difficult times. I would also like to thank Dr. Philip Chao for teaching me to solder and assemble electronics and help me built a formulation device for my project. I thank Dr. Noel Ha for his assistance with some of my experiments and his input on radiochemistry questions. I thank Jason Jones for teaching me how to use machine shop tools, and for his help with LabView software. I thank Alejandra Rios for her input related to the high-throughput system and for helping me with chip fabrication. I thank Travis Holloway for his help with chemistry questions, and for his efforts to troubleshoot existing tools and bring in new ones for the lab. I also thank Yingqing Lu for assisting me with the experiments. I thank the undergraduate students Kelly Fong and Christian

de Caro who were a pleasure to work with and who helped with some of the projects. I thank Jeff Collins for maintaining the radiochemistry lab, ensuring we have radioisotope and tools to work with, and for his help during the experiments. I am also thankful to Dr. Jennifer Murphy and members of her lab Dr. Gaoyuan Ma, Dr. Maruthi Kumar and James McDaniel for assisting me when I had chemistry or radiochemistry questions, and for kindly sharing the space and resources in the radiochemistry lab. I thank Bao Ying Chen who helped me to setup in vitro studies and to acquire animals for PET imaging; she has been very supportive and kind both as a friend and colleague.

I thank all the staff of the Crump preclinical imaging center and Dr. Jason Lee and Dishan Abeydeera for accommodating my in vivo PET studies. I also thank the staff of the Biomedical Cyclotron facility for generously providing a radioisotope for our lab. I thank Dr. Roger Slavik and Dr. Giuseppe Carlucci for helping us to perform quality control studies. I am also grateful to CNSI cleanroom staff Lorna Tokunaga, Krissy Do and Tony Wright for their help and advice related to fabrication questions. I thank Emily Fitch for her help with the documents and providing detailed answers to any related questions and Karen Lum, Cecilia Canadas and Erika Corrin for their help with purchasing/reimbursements and administrative matters.

I would like to thank the mentors and the administration of the Physics and Biology in Medicine program who made me feel welcome at the start of my PhD career. I thank Dr. Michael McNitt-Gray for his mentorship and support while navigating throughout my PhD, and for always being there for his students. I thank Reth Im and Alondra Correa Bautista for organizing PBM social events and handling all the administrative paperwork. I am grateful to all my fellow students from my year for being great company, and in particular Kamal Singhrao and Geraldine Chee who encouraged me to attend various social events.

I would like to thank my dearest friends who constantly inspired me with their resilience, intelligence, and kindness: Vanessa Hurtado Molina, Jeannie Nguyen, Erin Clayton, Jackie Lee and Sandy Joung. I am eternally grateful to my family, my parents Stella Lisova and Andrey



Lisov for their endless love and support, and my younger sister Yulia Lisova for her friendship, encouragement, and motivational pep talks.

I am extremely grateful to the members of my doctorate committee for providing their expert input related to my research and study. Thank you to Dr. Peter Clark for sharing your knowledge and helping me understand the biochemical aspects of the PET tracer uptake, for assisting with PET image analysis and animal studies for my projects. Thank you to Dr. Arion Chatziioannou for sharing your expertise related to PET imaging, and for helping us to acquire high-quality images with the novel HiPET animal scanner. Thank you to Dr. Magnus Dahlbom for the engaging and inspiring lectures on the fundamentals of nuclear medicine, and for the insightful discussions that helped me to understand the basic principles and also see the bigger picture in this field.

I am endlessly grateful to Dr. R. Michael van Dam for his guidance and mentorship throughout the years of my PhD. I thank Dr. van Dam for making my research experience vibrant by giving me numerous opportunities to design and perform experiments, present and publish my work, establish collaborations, attend scientific conferences and communicate with other researchers. I am thankful that as a mentor he gave me space to explore and learn from my mistakes, while always being helpful and willing to resolve the issues or questions that arised. Dr. van Dam is an incredible professor who is not only dedicated to his work but also spends a lot of time with his students. He sets a great example of work integrity, patience, organization, problem-solving, and critical thinking. Though I am yet to master these skills, I am confident that what I have learned during my PhD will be useful for many years ahead no matter the path I choose. I thank Dr. van Dam for his patience and encouragement during this last year of my PhD which has been particularly challenging, due to the stress much amplified by the global pandemic. Thank you to Dr. van Dam for giving me this opportunity to conduct cutting-edge research, for all the advice and help, for cultivating optimism and scientific curiosity, and for helping me grow as a scientist and an individual. Thank you very much!

Chapter 2: Fluorine-18 radiolabeling of 4-N-acyl and 4-N-alkyl gemcitabine analogues is a modified version of:

Gonzalez C, Sanchez A, Collins J, et al. The 4-N-acyl and 4-N-alkyl gemcitabine analogues with silicon-fluoride-acceptor: Application to 18F-Radiolabeling. *European Journal of Medicinal Chemistry*. 2018;148:314-324.

Chapter 3: Droplet synthesis of O-(2-[<sup>18</sup>F]fluoroethyl)-L-tyrosine ([<sup>18</sup>F]FET) is a modified version of:

Lisova K, Chen BY, Wang J, Fong KM-M, Clark PM, van Dam RM. Rapid, efficient, and economical synthesis of PET tracers in a droplet microreactor: application to O-(2-[<sup>18</sup>F]fluoroethyl)-L-tyrosine ([<sup>18</sup>F]FET). *EJNMMI radiopharm chem*. 2019;5:1.

Chapter 4: Droplet synthesis of [<sup>18</sup>F]florbetaben ([<sup>18</sup>F]FBB) is a modified version of

Lisova K, Wang J, Chao PH, van Dam RM. A simple and efficient automated microvolume radiosynthesis of [<sup>18</sup>F]Florbetaben. *EJNMMI Radiopharmacy and Chemistry*. 2020;5:30.

Chapter 5: High activity droplet syntheses of [<sup>18</sup>F]FET and [<sup>18</sup>F]FBB is a modified version of a manuscript in preparation

Chapter 6: Isotopic exchange labeling of [<sup>18</sup>F]AMBF<sub>3</sub>-TATE in microliter volumes is a modified version of

Lisova K, Sergeev M, Evans-Axelsson S, et al. Microscale radiosynthesis, preclinical imaging and dosimetry study of [<sup>18</sup>F]AMBF<sub>3</sub>-TATE: A potential PET tracer for clinical imaging of somatostatin receptors. *Nuclear Medicine and Biology*. 2018;61:36-44.

Chapter 7: Improved method for droplet labeling of trifluoroborates via isotopic exchange is a modified version of a manuscript in preparation

## VITA EDUCATION

- 09/2015 - present: PhD candidate (advanced in 03/2019) in Physics and Biology in Medicine, David Geffen School of Medicine, University of California Los Angeles (UCLA)
- 09/2015 - 08/2017: Master of Science in Physics and Biology in Medicine, UCLA
- 08/2011 - 05/2015: Bachelor of Science in Physics, Arizona State University (ASU)

## RESEARCH EXPERIENCE

- 03/2016 - present: Graduate student researcher  
Crump Institute for Molecular Imaging, University of California Los Angeles  
Department of Molecular and Medical Pharmacology
- 06/2014 - 05/2015: Undergraduate student researcher  
Department of Biophysics, Arizona State University

## SELECTED PUBLICATIONS

- Ksenia Lisova**, Jia Wang, Philip H. Chao, R. Michael van Dam. A simple and efficient automated microvolume radiosynthesis of [<sup>18</sup>F]Florbetaben. *EJNMMI radiopharm. chem.* 5, 30 (2020). <https://doi.org/10.1186/s41181-020-00113-w>
- Jia Wang, Travis Holloway, **Ksenia Lisova**, R. Michael van Dam. Green and efficient synthesis of the radiopharmaceutical [<sup>18</sup>F]FDOPA using a microdroplet reactor. *Reaction Chemistry & Engineering.* 2020. DOI: 10.1039/C9RE00354A
- Jia Wang, Alejandra Rios, **Ksenia Lisova**, Roger Slavik, Arion F. Chatziioannou, R. Michael van Dam. High-throughput radio-TLC analysis. *Nuclear Medicine and Biology* 82-83: 41-48, 2020
- Ksenia Lisova**, Bao Ying Chen, Jia Wang, Kelly Mun-Ming Fong, Peter M. Clark, R. Michael van Dam. Rapid, efficient, and economical synthesis of PET tracers in a droplet microreactor: application to O-(2-([<sup>18</sup>F]fluoroethyl)-L-tyrosine ([<sup>18</sup>F]FET). *EJNMMI radiopharm. chem.* 5, 1 (2020). <https://doi.org/10.1186/s41181-019-0082-3>
- Ksenia Lisova**, Maxim Sergeev, Susan Evans-Axelsson, Andreea D. Stuparu, Seval Beykan, Jeffrey Collins, Jason Jones, Michael Lassmann, Ken Herrmann, David Perrin, Jason T. Lee, Roger Slavik, R. Michael van Dam. "Microscale radiosynthesis, preclinical imaging and dosimetry study of [<sup>18</sup>F]AMBF<sub>3</sub>-TATE: a potential PET tracer for clinical imaging of somatostatin receptors". *Nuclear Medicine and Biology* 61: 36-44, 2018
- Cesar Gonzalez, Andersson Sanchez, Jeffrey Collins, **Ksenia Lisova**, Jason T. Lee, R. Michael van Dam, M. Alejandro Barbieri, Cheppail Ramachandran and Stanislaw F. Wnuk. "The 4-N-Acyl and 4-N-Alkyl Gemcitabine Analogues with Silicon-Fluoride-Acceptor: Application to <sup>18</sup>F-Radiolabeling". *European Journal of Medicinal Chemistry* 148: 314-324, 2018.

## CONFERENCES AND MEETINGS

- 05/2019: Poster presentation. 23<sup>rd</sup> International Symposium of Radiopharmaceutical Sciences (ISRS), Beijing, China
- 09/2018: Poster presentation. 2018 World Molecular Imaging Congress (WMIC), Seattle, USA
- 07/2018: Poster presentation. 2018 Training Grantees Meeting National Institute of Biomedical Imaging and Bioengineering (NIBIB), Washington DC, USA
- 05/2017: Oral presentation at 22<sup>nd</sup> International Symposium of Radiopharmaceutical Sciences (ISRS), Dresden, Germany  
Poster presentation. 22<sup>nd</sup> International Symposium of Radiopharmaceutical Sciences (ISRS), Dresden, Germany

# Chapter 1: Introduction

## 1.1 Nuclear medicine imaging: Positron emission tomography

Positron emission tomography (PET) is a highly sensitive non-invasive molecular imaging technique used to visualize molecular interactions and processes in living tissues by tracking the distribution of an administered radiolabeled imaging agent. The first concept of PET imaging was introduced in 1950s by David E. Khul, Luke Chapman and Roy Edwards, followed by development of the first transaxial tomograph in the 1975 by Michel Ter-Pogossian, Michael E. Phelps and Edward J. Hoffmann (1,2). Since then, PET has been extensively used in diagnostics of cancer, neurodegenerative diseases, cardiology and many other fields of medicine and in research. A PET radiopharmaceutical (tracer) consist of a biologically active molecule chemically linked with a radioactive positron-emitting isotope. Upon administration of a radiopharmaceutical, it circulates throughout the body, and its concentration in different organs and regions of tissues can be quantitatively imaged during a PET scan. The positrons emitted upon decay rapidly travel through matter losing their energy and annihilate at rest with an electron in the surroundings producing 2 gamma-rays (511 keV) at a nearly 180° angle. PET scanners rely on coincidence detection of these gamma-rays using a circular ring of scintillation detectors placed around the subject. These coincidence events are then processed and corrected, to map the distribution of the radiopharmaceutical inside the subject, ultimately creating a 3D image (Figure 1.1). To provide an anatomical reference for the highly sensitive PET signal, PET is commonly used in conjunction with computed tomography (i.e., PET/CT) or magnetic resonance imaging (i.e., PET/MRI). The high sensitivity of PET allows one to obtain detailed images with only picomole to nanomole amounts of the radiopharmaceutical administered, thus minimizing the possibility of any biological effects caused by the tracer (3).

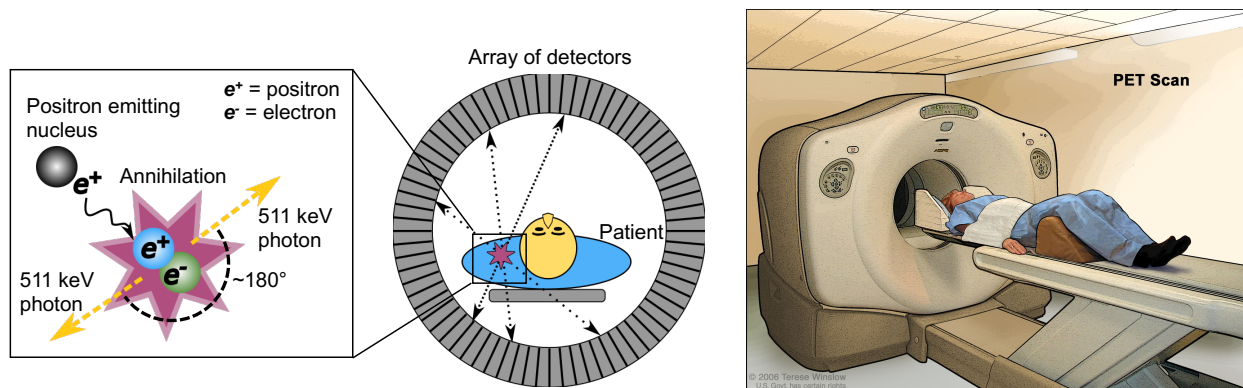


**Figure 1.1 Mechanism of PET imaging**

PET image is formed based on detection of sets of coincident 511 keV photons emitted upon annihilation event after positron decays. PET scan image courtesy of National Cancer Institute.

## 1.2 Radioisotope production routes

Diagnostic PET radiopharmaceuticals are labeled with short-lived, isotopes that emit low-energy positrons, such as nonmetal elements from Period 2 of the periodic table: carbon-11 ( $t_{1/2} = 20.4$  min), nitrogen-13 ( $t_{1/2} = 10.0$  min), oxygen-15 ( $t_{1/2} = 2.0$  min), fluorine-18 ( $t_{1/2} = 109.8$  min); or radiometals such as : gallium-68 ( $t_{1/2} = 67.7$  min), zirconium-89 ( $t_{1/2} = 78.4$  h), or rubidium-82 ( $t_{1/2} = 1.3$  min). Production of positron-emitting radionuclides typically requires either a cyclotron or a generator. Cyclotrons are powerful particle accelerators directing a beam of particles along a circular trajectory many times until the particle energies reach the MeV range. The accelerated particles are then directed into an appropriate target to initiate nuclear reactions and create unstable radioactive isotopes. Control over bombardment energies allows one to create varying quantities of radioactive isotopes, and in the case of nuclear medicine applications, compact medical cyclotrons produce generous quantities of the radioisotopes suitable for radiopharmaceutical synthesis (4,5). Another route of positron-emitting isotopes production is by using radionuclide generators. These devices contain a parent-daughter radionuclide pair, where the parent isotope decays to another isotope which can be periodically

extracted. Generator devices are typically smaller, and multiple units may be required to support radiopharmaceutical production needs (5,6).

### **1.3 Diagnostic radioisotope fluorine-18**

The labeling approach and applications depend on the properties of the individual radioisotope – such as the half-life, positron energy and atom chemical properties. The most used radioisotope in PET is fluorine-18 due to its convenient half-life (109.8 min), high positron decay yield (97%) and low positron energy (maximum 0.634 MeV). The nearly 2-hour half-life provides a sufficient time for tracer synthesis and transportation to the PET imaging location, while allowing for a reasonably short decay to minimize radiation exposure to the tissues of the patient. Due to the abundant positron emission decay route (only 3% of decays occur by electron capture) amount of the emissions not contributing to PET image is limited, minimizing unnecessary radiation exposure. Low positron energy permits a high resolution of the PET scan as the positrons annihilate close to their emission location (mean positron range for F-18 in soft tissue is 0.3 mm). Very high spatial resolution of 3-5 mm can be achieved with modern human PET scanners, and down to 1-2 mm with small animal scanners (7–10). Over the years of PET practice, fluorine-18 radiopharmaceuticals have found applications in many fields of medical diagnostics and research. To date, these radiopharmaceuticals are available to image tumors and detect metastases for diagnostics in oncology (11,12), non-invasively classify and grade neurodegenerative diseases (12–14), determine metabolic and functional status of the heart (15–17), assess immune checkpoints and response to therapy (18,19), identify and characterize new drugs (20,21), evaluate treatment response (22–25) and enable personalized dosimetry in theranostics (26).

## 1.4 Applications of selected fluorine-18-labeled PET tracers

The vast majority of PET scans are performed using a versatile fluorine-18-labeled glucose analogue, 2-[<sup>18</sup>F]fluoro-2-deoxy-D-glucose ([<sup>18</sup>F]FDG) (27,28). [<sup>18</sup>F]FDG-PET visualizes glucose metabolism, which is significantly upregulated in metabolically active tumors, making it applicable for imaging and grading of malignant lesions, and detecting metastases. In addition, the assessment of abnormalities in glucose metabolism in various organs can be used to aid in the diagnosis of Alzheimer's disease and Parkinson's disease, epilepsy localization, heart disease, detecting inflammatory response related to infectious disease, and studying skeletal muscle (12,29–33). Apart from [<sup>18</sup>F]FDG, a few other tracers are routinely used in clinical diagnostics and research, and many are being evaluated and validated. By far the largest diagnostic categories where clinical PET is applied are neuroimaging and oncology. Discussed below are several commonly used tracers that will be revisited later in this work.

A variety of neurotracers have been developed since the discovery of PET to image abnormalities in the brain due to disease or other factors. Significant progress has been made in Alzheimer's disease diagnostics with PET. A hallmark of Alzheimer's disease (AD) is the prevalence of extracellular  $\beta$ -amyloid ( $A\beta$ ) plaques and neurofibrillary tangles (NFTs). While the standard non-biomarker assessment of AD patients is challenging due to AD dementia symptoms being similar to other types of dementia, multiple tracers were discovered to non-invasively image  $A\beta$  or tau proteins (that aggregate into NFTs) (34) and provide more specific and conclusive diagnosis (35). Based on the current studies, it is believed that  $A\beta$  precedes and accelerates tau pathologies (36). A carbon-11-labeled thioflavin T analogue named Pittsburgh compound B ([<sup>11</sup>C]PiB) was developed with high affinity for the aggregated  $A\beta$ . While [<sup>11</sup>C]PiB is considered a gold standard PET tracer for the imaging of Alzheimer's the half-life of carbon-11 is only 20 minutes, making its clinical availability limited. On the basis of [<sup>11</sup>C]PiB, several fluorine-18-labeled analogues were developed such as [<sup>18</sup>F]flumetamol, [<sup>18</sup>F]florbetapir,

[<sup>18</sup>F]florbetaben ([<sup>18</sup>F]FBB). Fluorine-18-labeled analogues show similar performance and success in detecting Alzheimer's disease, however, the longer half-life of fluorine-18 (110 min) compared to carbon-11 (20 min) provides more practical flexibility for synthesis and distribution of the tracers. Amyloid PET used in patients with cognitive impairment improves the diagnostic confidence in the detection of Alzheimer's and its severity, and helps to apply a proper therapeutic plan (35,37). Other subcategories of neurotracers target dopaminergic pathways (e.g. [<sup>18</sup>F]fallypride, [<sup>18</sup>F]fluorodopa), neuroinflammation (e.g. [<sup>18</sup>F]flutriciclamide), glutamate receptors (e.g. 3-[<sup>18</sup>F]fluoro-5-[(pyridin-3-yl)ethynyl]benzotrile ([<sup>18</sup>F]FPEB)), cholinergic system (e.g. [<sup>18</sup>F]fluoroethoxybenzovesamicol ([<sup>18</sup>F]FEOBV)), serotonin receptors (e.g. trans-4-[<sup>18</sup>F]fluoro-N-2-[4-(2-methoxyphenyl) piperazin-1-yl]ethyl-N-(2-pyridyl)cyclohexane carboxamide ([<sup>18</sup>F]FCWAY)) and can be used to assess a wide variety of neuropsychiatric or neurological disorders (38).

In oncology, imaging tumors using PET comprises several different tracer categories and biomarker identification approaches. The diverse PET tracers are capable of non-invasively assessing tumor metabolism, angiogenesis, cell proliferation and tumor hypoxia to improve diagnostic accuracy and monitor treatment efficiency. An important hallmark of cancer is glucose overconsumption in the tumor cells, and the glucose analogue [<sup>18</sup>F]FDG has been widely used as a cancer diagnostic tool for many decades (39). [<sup>18</sup>F]FDG, however has some limitations. In particular when imaging brain tumors (e.g. gliomas) the high glucose utilization (and consequently high [<sup>18</sup>F]FDG uptake) in a normal brain makes it challenging to distinguish glioma tissue from healthy brain tissue. Amino acid tracers, such as [<sup>18</sup>F]FET, thus offer an advantage, since, outside of the tumor, the brain uptake of amino acids is low (40,41). Amino acid PET has been of great interest in clinic, due to its effectiveness in glioma differentiation and grading. A typical brain tumor diagnostic technique based on magnetic resonance imaging (MRI), while providing excellent structural information, makes it challenging to differentiate tumor tissue from non-neoplastic changes especially in the post-treatment stage. The amino



acid PET correlates with an increased rate of protein synthesis, and consequently increased carrier-mediated transport of the amino acids into the cells, indicative of actively growing tumor tissue. A most notable fluorine-18 amino acid tracer, the tyrosine analogue, O-(2-[<sup>18</sup>F]fluoroethyl)-L-tyrosine ([<sup>18</sup>F]FET) (designed based on the success of the carbon-11-labeled [<sup>11</sup>C]MET) demonstrated diagnostic potential in delineation of brain tumors, definition of biopsy sites for therapy planning and treatment response assessment. Other less common tracers are designed to target angiogenesis, i.e. formation of new blood vessels (e.g. [<sup>18</sup>F]-Galacto-RGD, [<sup>18</sup>F]fluciclatide), cell proliferation (e.g. [<sup>18</sup>F]fluorothymidine ([<sup>18</sup>F]FLT), 2'-deoxy-2'-[<sup>18</sup>F]fluoro-5-methyl-1-beta-D-arabinofuranosyluracil ([<sup>18</sup>F]FMAU)) or hypoxia (e.g. [<sup>18</sup>F]fluoromisonidazole ([<sup>18</sup>F]FMISO)). These tracers are capable of providing valuable information about tumor aggressiveness and treatment resistance, allowing personalized treatment to improve the oncology patients recovery (42,43).

Another important category of oncology PET tracers are peptide-based ligands. A lot of effort has been spent to improve diagnostic accuracy of neuroendocrine tumors (NETs). Somatostatin receptor subtype 2 (SSTR2) is overexpressed in most NETs, causing increased binding of a hormone somatostatin. Somatostatin analogues, such as octreotide, radiolabeled with positron emitters help to visualize the SSTR2 density and distribution and to evaluate the severity of the disease. Usually, octreotide analogues are conjugated with chelating agents (e.g. tetraxetan (DOTA)) to enable stable radiometal labeling – specifically, for gallium-68-labeled peptides [<sup>68</sup>Ga]Ga-DOTA-Tyr(3)-octreotate ([<sup>68</sup>Ga]Ga-DOTA-TATE), [<sup>68</sup>Ga]Ga-DOTA-Nai(3)-octreotide ([<sup>68</sup>Ga]Ga-DOTA-NOC), [<sup>68</sup>Ga]Ga-DOTA(0)-Phe(1)-Tyr(3)-octreotide ([<sup>68</sup>Ga]Ga-DOTA-TOC). Chelation agents conjugated onto a peptide enable efficient radiometal incorporation, either for diagnostic purposes (with gallium-68) or radiometal therapy (with lutetium-177). Such combination of therapeutics with diagnostics is referred to as theranostics, where the same targeting molecule can be first used for PET imaging and patient-specific diagnosis (e.g. when labeled with short-lived gallium-68), then for personalized treatment via

localized tumor irradiation (e.g. when labeled with long-lived  $\beta^-$ -emitter Lutetium-177) (26). While gallium-68-labeled octreotide tracers are used in clinical practice, the generator-based production route of this radioisotope limits the amount of tracer and thus the number of patient doses that can be produced per batch. To address these challenges fluorine-18 octreotide analogues that can take advantage of the established fluorine-18 tracer network are being developed (43–45).

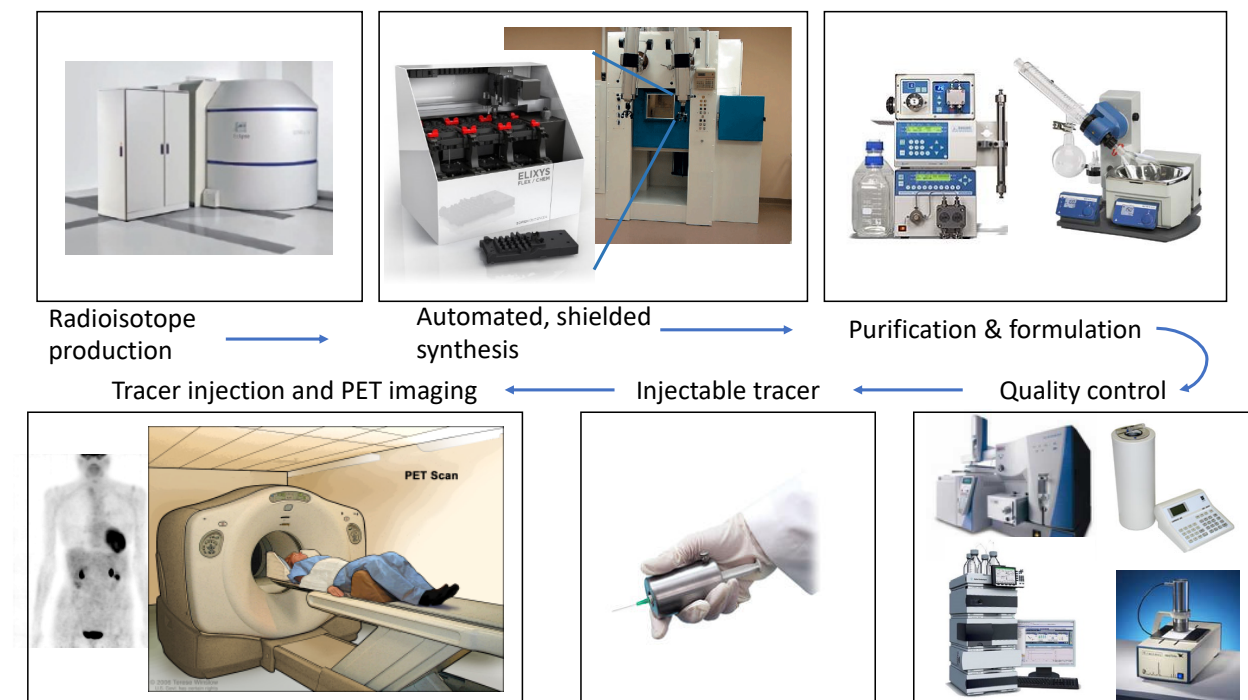


**Figure 1.2 Production flow for fluorine-18-labeled tracers.**

## 1.5 Production of fluorine-18

Fluorine-18 has become the most attractive radionuclide for PET tracer development owing to its favorable nuclear and chemical properties. Production of fluorine-18 is achieved in a cyclotron. Due to the 110 min half-life, either the batches of this radioisotope must be ordered from a cyclotron facility and shipped to a radiochemistry facility, or on-site access to a cyclotron is required. There are two main nuclear reactions that produce fluorine-18, that can result in either nucleophilic  $[^{18}\text{F}]\text{F}^-$  or electrophilic  $[^{18}\text{F}]\text{F}_2$  form. The first method  $[^{18}\text{O}(\text{p},\text{n})^{18}\text{F}]$  produces

aqueous [ $^{18}\text{F}$ ]F<sup>-</sup> by bombardment of the oxygen-18 enriched water with 2-15 MeV protons ( $^1\text{H}$ ). Similarly, the bombardment of an oxygen-18 enriched oxygen gas target is also feasible. The second reaction [ $^{20}\text{Ne}(\text{d},\alpha)^{18}\text{F}$ ] involves the bombardment of the high pressure neon gas target with deuterons (46–48). However, the latter two methods require the use of F<sub>2</sub> carrier gas to efficiently recover the produced [ $^{18}\text{F}$ ]F<sub>2</sub> after the bombardment. This leads to an important difference between nucleophilic or electrophilic form of fluorine-18 in terms of the resulting molar activity. Molar activity is defined as a ratio of radioactivity per total number (mols) of the substance, and is typically expressed in curie per micromole (Ci/μmol) or gigabecquerel per micromole (GBq/μmol). The electrophilic form of fluorine-18 will have lower molar activity (< 0.3 Ci/μmol [ $< 1$  GBq/μmol]) than its nucleophilic analogue (typically 20-300 Ci/μmol [1-10 TBq/μmol]) due to the addition of the carrier in the former (47,48). The importance of molar activity in the context of PET imaging will be discussed later. A vast majority of fluorine-18 syntheses use nucleophilic [ $^{18}\text{F}$ ]fluorine due to its simpler handling, higher molar activity and widespread availability from commercial nuclear pharmacies and academic medical research centers (49).

## 1.6 Chemistry of fluorine-18 tracer synthesis

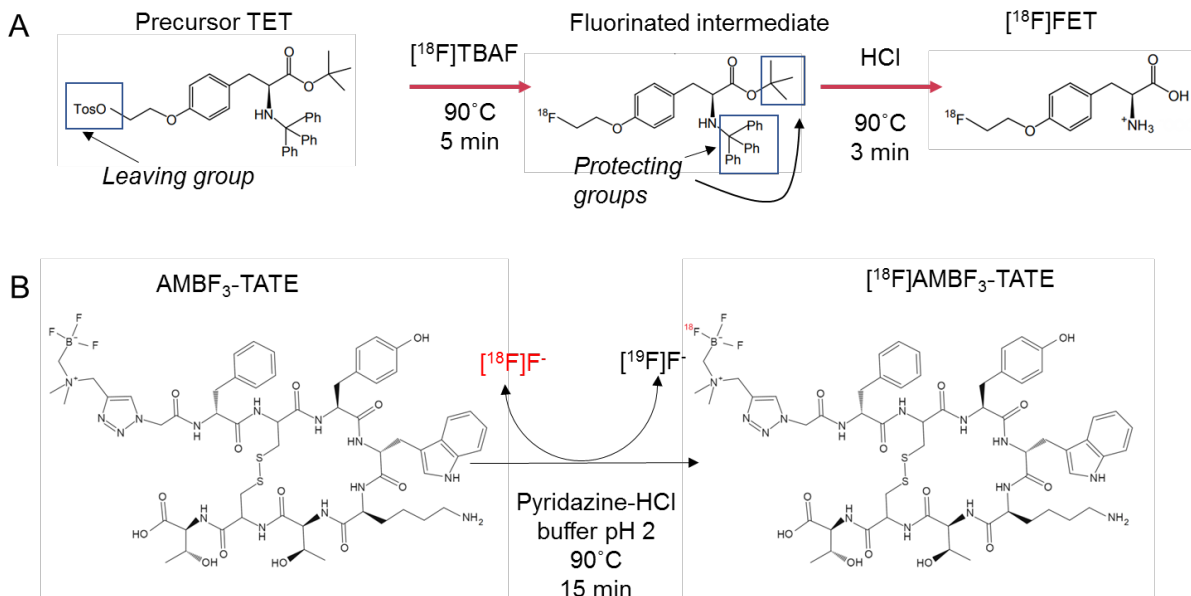


**Figure 1.3 (A) 2-step radiolabeling of  $[^{18}\text{F}]\text{FET}$ , (B) 1-step synthesis of  $[^{18}\text{F}]\text{AMBF}_3\text{-TATE}$  via isotopic exchange.**

Nucleophilic  $[^{18}\text{F}]\text{fluorine}$  is initially received in  $[^{18}\text{O}]\text{H}_2\text{O}$  from a cyclotron. Because fluorine ion is a strong nucleophile it forms hydrogen bonds with surrounding water, which makes it unreactive. To remove  $[^{18}\text{O}]\text{H}_2\text{O}$  water,  $[^{18}\text{F}]\text{fluoride}$  is usually trapped in a strong anion-exchange (SAX) cartridge, from which it is eluted in a mostly aqueous solution containing an anion to displace the  $[^{18}\text{F}]\text{fluoride}$  from the cartridge, and also containing a base and/or phase-transfer catalyst (PTC) such as  $\text{TBAHCO}_3$  or a combination of  $\text{K}_2\text{CO}_3$  and Kryptofix 222 ( $\text{K}_{2.2.2}$ ), into the reaction vessel. This eluate is then evaporated, followed by additional azeotropic drying steps (i.e. evaporation in the presence of additional acetonitrile) to ensure complete removal of the water. The use of PTC such as cryptand-counteranion complex  $\text{K}_{2.2.2}/\text{K}_2\text{CO}_3$  or tetrabutylammonium cation enhances the fluorine ion solubility and reactivity in organic solvents during the subsequent radiofluorination step. After azeotropic drying, nucleophilic  $[^{18}\text{F}]\text{fluorine}$  is generally incorporated into the precursor molecule either via aliphatic nucleophilic fluorination ( $\text{S}_{\text{N}}2$ ) into aliphatic positions or aromatic nucleophilic substitution ( $\text{S}_{\text{N}}\text{Ar}$ ) into aromatic

molecules.  $S_N2$  reactions are characterized by fluorine ion binding to the carbon atom of the precursor molecule containing a suitable leaving group (such as a weak base), under basic or neutral conditions in presence of an aprotic solvent (such as acetonitrile, DMF, DMSO). Reactivity of the leaving group (e.g. leaving group reactivity of  $Cl < Br < I < \text{tosylate} \sim \text{mesylate} < \text{nosylate} < \text{triflate}$ ) and its position (e.g. substitution efficiency in primary benzylic  $>$  primary aliphatic  $\gg$  secondary aliphatic positions) will have direct effect on the efficiency of the nucleophilic substitution. Apart from choosing the optimal leaving group, the  $S_N2$  substitution reactions are typically optimized for the ratio of PTC to precursor and reaction temperatures to minimize an undesired byproduct formation often caused by the decomposition of base-sensitive precursors while maximizing radiofluorination efficiency. Additionally, the precursor molecule may contain protecting groups that ensure site-specific radiolabeling of the precursor molecule. The protecting groups remain stable under the radiofluorination reaction conditions, and are removed following radiofluorination using high temperatures with the addition of acids or bases (deprotection step). A typical optimized nucleophilic aliphatic radiofluorination requires  $<$  15 min reaction time at moderate temperatures ( $\sim 100$  °C) to achieve an efficient radiochemical yield (RCY), and, if necessary, is followed by a deprotection (hydrolysis) step. Many radiopharmaceuticals are synthesized using  $S_N2$  displacement of an aliphatic leaving group (e.g.  $[^{18}\text{F}]\text{FDG}$ ,  $[^{18}\text{F}]\text{FET}$ ,  $[^{18}\text{F}]\text{FLT}$ ). As an example, the synthesis of a PET tracer  $[^{18}\text{F}]\text{FET}$  (Figure 1.3 A) used for brain tumor imaging, discussed in detail in **Chapter 4**, requires a 2 step synthesis:  $S_N2$  substitution of the precursor containing a tosylate leaving group with tetrabutylammonium-activated  $[^{18}\text{F}]\text{fluoride}$ , and the deprotection of the N-protecting group using hydrochloric acid (47,50,51).

Direct incorporation of fluorine into aromatic rings via  $S_NAr$  substitution reactions requires the electron deficient aromatic ring to ensure efficient labeling, which limits the applications of this method in PET tracer synthesis. Activation of the phenyl ring is typically achieved by electron withdrawing groups (e.g.  $-\text{NO}_2$ ,  $-\text{CN}$ ,  $-\text{CF}_3$ ) placed in ortho or para position

of the leaving group of the precursor. Typically, trimethyl-ammonium salt or nitro groups are used as the leaving groups for direct  $S_NAr$  radiofluorination. High ( $>100$  °C) temperatures and aprotic solvents (DMF, DMSO, MeCN) are typically necessary in these reactions. (47,51). Because of the demanding  $S_NAr$  radiofluorination route, alternative methods to achieve aromatic substitution are being explored, such as the use of heteroarenes, diaryliodonium salts or metal-mediated approaches (47,52).

The commonly-employed fluorine-18 tracer syntheses methods described above usually require harsh reaction conditions (organic solvents; temperature  $> 100$  °C) but large complex biomolecules such as antibodies and peptides may degrade or hydrolyze during such labeling process. Since labeling of peptides and antibodies is of great value to PET imaging due to their specificity and biological importance, alternative indirect radiolabeling methods are employed using prosthetic groups, or secondary labeling agents. Prosthetic groups are small and simple molecules that are able to survive harsh radiolabeling conditions and, once radiolabeled with fluorine-18, can be conjugated to sensitive biomolecules under milder reaction conditions (53). Some well-known prosthetic groups such as [ $^{18}F$ ]fluorobenzoate ([ $^{18}F$ ]SFB), 6-[ $^{18}F$ ]fluoronicotinic acid tetrafluorophenyl ester ([ $^{18}F$ ]F-Py-TFP) or N-maleoylethyl-4-[ $^{18}F$ ]fluorobenzamide ([ $^{18}F$ ]FBEM). However, because of the need to perform synthesis and purification of the prosthetic group, and then conjugation to the biomolecule followed by purification, such syntheses can be very time-consuming.

Notably, a radiofluorination approach that can alleviate this problem and that can be more generally applied to both direct and indirect labeling methods, is isotopic exchange (IEX) fluorination. Precursors for IEX reactions are chemically identical to the radiofluorinated product, and radiolabeling with fluorine-18 occurs through the substitution of a [ $^{19}F$ ]F $^-$  fluorine atom on a precursor molecule with [ $^{18}F$ ]F $^-$ . In other reactions, it can be difficult to separate the chemically-similar product and precursor (or derivatives of the reactive precursor), requiring lengthy procedures such as high-performance liquid chromatography (HPLC). In contrast, for IEX

reactions, only removal of the unreacted radioisotope and the reaction buffer components is needed, which can be achieved by simpler methods (e.g. with a disposable cartridge). Most success in precursor design for IEX was achieved using boron trifluoride ( $\text{BF}_3$ ) and silicon fluoride acceptor (SiFA) based IEX chemistry. The SiFA and R- $\text{BF}_3$  radiolabeling strategies were successfully implemented under aqueous conditions, obviating the typical azeotropic  $^{18}\text{F}$ fluoride drying step, and have been mostly applied in the context of peptide radiolabeling (54,55). IEX synthesis will be further covered in **Chapter 6**, for 1-step direct radiolabeling of an octreotide analogue ammoniomethyl- $^{18}\text{F}$ trifluoroborate-octreotate ( $^{18}\text{F}$ AMBF<sub>3</sub>-TATE) (Figure 1.3 B), used as a neuroendocrine tumor PET tracer, and in **Chapter 7** for labeling of several o-trifluoroborato-phenylphosphonium based prosthetic groups designed for indirect peptide labeling (56).

## 1.7 Molar activity of fluorine-18 radiopharmaceuticals

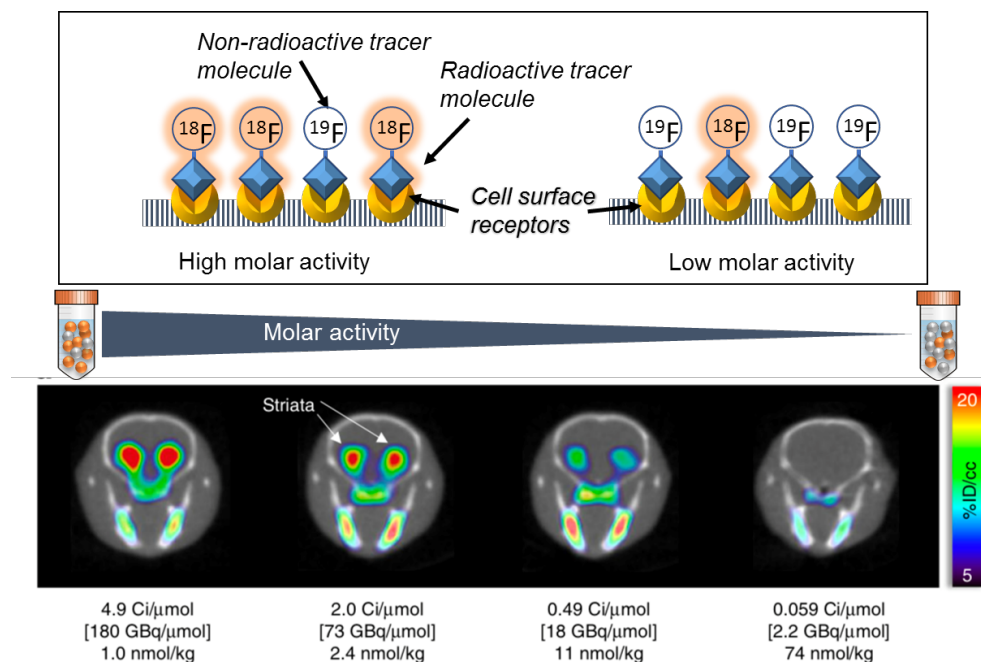


**Figure 1.4 Illustration of molar activity effect on tracer receptor binding**

Comparing effect of different molar activities on target visualization with example of [ $^{18}\text{F}$ ]fallypride PET/CT imaging in mice. Lower images show 10 min static scans after 60 min [ $^{18}\text{F}$ ]fallypride conscious uptake in transverse projections of the mouse brain acquired from administering the same amount of activity but different molar activities as indicated (Adapted from Sergeev et al. (57) with permission from Springer Nature, Copyright © 2018).

Due to the abundance of a stable isotope of fluorine ( $\text{F-19}$ ) in nature and its presence as a contaminant in the reagents and materials used in radiotracer preparation, it will always compete with radioactive [ $^{18}\text{F}$ ]fluorine during radiolabeling reactions. As a result, tracers comprise a mixture of both  $^{18}\text{F}$ - (radioactive) and  $^{19}\text{F}$ -labeled (non-radioactive) molecules. In fact, the theoretical maximum for molar activity, in a case where all the molecules are  $^{18}\text{F}$ -labeled, is 1710 Ci/ $\mu$ mol [63.3 TBq/ $\mu$ mol] while produced tracers typically have molar activities <15 Ci/ $\mu$ mol [550 GBq/ $\mu$ mol]. For PET imaging modest  $\sim 1$  Ci/ $\mu$ mol [ $\sim 40$  GBq/ $\mu$ mol] is already considered a good value, and values  $>5$  Ci/ $\mu$ mol [ $> 180$  GBq/ $\mu$ mol] are considered high.



Fluorine-19 contamination is already present in the initial fluorine-18 isotope production (e.g. from [ $^{18}\text{O}$ ]H $_2$ O target, delivery tubing), resulting in molar activity values in a 20-300 Ci/ $\mu\text{mol}$  range [1-10 TBq/ $\mu\text{mol}$ ] (49,57). The radiosynthesis process further lowers the molar activity due to a significant  $^{19}\text{F}$  contamination from the reagents, disposable cartridges, or Teflon tubing used in the production process (57).

The radioactive vs non-radioactive tracer molecules are chemically identical, they cannot be separated through chemical purification methods and are going to have the same target binding affinity *in vivo*, but only the radioactive ones will produce a detectable signal during a PET scan. The injectable radioactivity amount is typically fixed to ensure a sufficient number of coincidence events and high-quality PET images, while minimizing radiation exposure to the subject. However, variations in molar activity will cause a discrepancy in the injected mass of the radiopharmaceutical: for example, a typical clinical 10 mCi [400 MBq] injection with high (e.g. 5 Ci/ $\mu\text{mol}$  [180 GBq/ $\mu\text{mol}$ ]) molar activity will contain 2 nmol of compound, while similar 10 mCi with low molar activity (e.g. 0.03 Ci/ $\mu\text{mol}$  [1 GBq/ $\mu\text{mol}$ ]) tracer will have 400 nmol of the injected compound. Thus, low molar activity leads to increased mass of the radiopharmaceutical (per injected activity) which may adversely affect imaging due to target saturation with non-radioactive (fluorine-19 labeled) tracer molecules. This is especially critical for preclinical research where generally higher molar activities are desired for imaging with small animals compared to humans, since a higher tracer dose per subject mass needs to be administered to achieve a sufficient PET image resolution. For example, the reported human/mouse mass scale factors are ranging 2500-3750 while administered tracer quantity in mice is only 100x less than that in humans. As a result, a 30x higher quantity of the radiopharmaceutical per mass is used in mouse vs. human PET scan, increasing potential risk of pharmacological effects (58,59). In conventional radiosyntheses, to compensate for fluorine-19 contamination in larger reagent volumes and quantities and achieve high molar activity, the macroscale radiopharmaceutical production must use high starting activity (>37 GBq), which subsequently increases possible

radiation exposure and can lead to radiolytic decomposition of the product. Importantly, for a few patient scans (~0.4 GBq each) or small animal scans (<0.004 GBq per animal) only a small fraction of a macroscale batch (~10s of GBq) will be needed for imaging, thus also leading to a lot of waste generated from large-scale syntheses (unless the whole batch can be efficiently split among multiple imaging procedures). Another approach to maximize the molar activity is to reduce contamination of fluorine-19 by reducing the quantity of the reagents. The conventional methods can only afford a limited reagent reduction due to a fixed ~1 mL optimal volume scale, while using very small amounts and volumes of the reagents is feasible using microfluidics. Microfluidic technology allows to reduce reagent volumes (and quantities) by 2-3 orders of magnitude, making reagent fluorine-19 contamination negligible compared to the contamination introduced from the fluorine-18 source itself. It was shown that even with small amount of starting radioactivity high molar activities are achievable. Thus, microfluidics provides a valuable tool for the radiochemists allowing to achieve very high molar activities while using minimal quantities of the reagents and the radioisotope (57).

The exact impact of molar activity for different tracers and targets is not studied very thoroughly, possibly in part due to a lack of efficient strategies to produce tracers with high molar activity that would be needed to perform such studies. Generally, radiochemists aim to achieve a molar activity in a moderate range (e.g. 1-5 Ci/ $\mu$ mol [37-185 GBq/ $\mu$ mol]). Maximizing molar activity would be desired in many cases to reduce the total radiopharmaceutical mass injected and limit the possible pharmacological effects and target saturation, which may be especially crucial for new tracer validation studies in small animals. To give an example, it has been shown that molar activity visibly affects target visualization *in vivo* during PET imaging of dopamine receptors in mice (Figure 1.4) (57) using [ $^{18}$ F]fallypride. Neuroreceptors such as these are low-tissue density targets and are easily saturable. On the other hand, imaging of subcutaneous tumors with amino acid transport tracer [ $^{18}$ F]FET did not show any visible impact of molar activity on the ability to resolve the tumors. The mechanism of [ $^{18}$ F]FET uptake is

different from the receptor-binding [ $^{18}\text{F}$ ]fallypride, since [ $^{18}\text{F}$ ]FET participates in amino acid transport pathways and may recirculate and enter/leave cells multiple times, thus making “target” saturation unlikely (unless a very large quantity of the non-radioactive tracer is injected) (50). A precise effect of molar activity on imaging quality needs to be assessed experimentally as it will depend on the target abundance, tracer uptake properties and other physiological factors.

## **1.8 Conventional synthesis of the radiopharmaceuticals**

Millions of clinical PET scans are conducted in the US every year and even more numerous pre-clinical PET studies are performed routinely, each requiring a radiopharmaceutical synthesized shortly before the scan. Fluorine-18 half-life of 110 min provides a moderate timeframe for synthesis and tracer transport, while being sufficiently short that decontamination of apparatus is possible by waiting (10 half-lives; ~18 h). In the production of fluorine-18 labeled tracers, a shorter reaction time is preferred (<30 min), with a minimal number of reaction steps involving the radionuclide (ideally only 1 or 2) – to minimize activity decay, losses within the apparatus, and radiation exposure. A typical production of a  $^{18}\text{F}$ -labeled PET tracer involves: (i) radiochemical linking of the radioisotope to the desired ligand to form a crude radiopharmaceutical compound; (ii) purification to isolate the desired product from the byproducts and excess radioisotope; (iii) formulation and sterile filtration to deliver a final product suspended in stabilizing, injectable sterile matrix; and (iv) quality control testing to ensure identity, purity, and safety of the final product (Figure 1.2). To enable a safe and reliable routine PET tracer production, syntheses are carried out using automated modules which are placed inside the shielded fume hoods, known as hot-cells, and are operated remotely often with preprogrammed synthesis sequences. Generally, these modules are designed to control the reagent delivery into a reactor, apply heating and gas flow if necessary, recover crude synthesis product and transfer it to perform subsequent purification and formulation with minimal

user intervention. Cassette-based automated modules, such as GE FASTlab (60), Siemens Explora (61), IBA Synthera (62), use single-use cassettes, eliminating the need for cleaning and enabling quick reset between syntheses and straightforward setup and operation. Additionally, some of these systems feature compact design allowing one to fit at least two units per hot-cell and are somewhat adaptable for preparation of various radiopharmaceuticals through module customization or custom cassette use. The versatility of cassette-based modules is limited due to the use of inexpensive materials (plastics) and is not generally suitable for new tracer development due to moderate temperatures and pressure tolerance. Another type of automated radiosynthesizers comprises fixed-tubing modules such as GE TRACERlab FX series (63), GmbH Synthra (64) or Eckert & Ziegler Modular-Labs (65), which employ highly inert materials and reactor(s) and contain numerous reconfigurable interconnected parts for customizable reactants manipulation. Since parts of these systems are generally non-disposable, validated cleaning procedures are required between each synthesis. Despite affording flexibility in setting up various syntheses, frequent reconfigurations add possibilities for errors, making such devices hard to maintain. Often such systems are left alone after configuring for a particular synthesis, and additional synthesis modules (and hot cells) are needed to produce other tracers. Hybrid modules, such as ELIXYS FLEX/CHEM (Sofie, Inc.) (66,67), combine the simplicity of disposable-cassette-based modules and the versatility to withstand harsher conditions and support complex reactions of fixed-tubing modules. ELIXYS hybrid module contains multiple reactors (3) with disposable cassettes for the reagents. This system is easy to reset between syntheses, only requiring cassette replacement with a small number of connections and has great flexibility for novel tracer syntheses. It can withstand significantly higher reaction temperatures (and pressures) than most disposable-cassette systems (66). To automate the purification and formulation process, the ELIXYS hybrid system can be combined with an optional PURE/FORM (68) module or other means to incorporate those steps (69).

Purification in automated systems is typically performed using integrated semi-preparative high-performance liquid chromatography (HPLC) units. Most used reversed-phase HPLC purification strategy provides a flexible route to remove non-reacted precursor molecules and by-products or impurities based on different polarity of the analytes. The sample is delivered into a stationary phase (column) where the analytes are retained and a mobile phase (typically a combination of organic and aqueous solvent) flows through the column, moving the analytes at different speeds depending on their polarity and the mobile phase properties. If a proper method is selected, the various analytes elute off the column with different retention times, which can be observed through a generated signal vs time chromatogram from UV absorbance (for non-radioactive species) and radiation detectors. Conventional scale radiosynthesizers use milliliter volume scales and milligram scale quantities of the precursor, requiring semi-preparative HPLC columns, that are capable of handling 10s of mg of the analytes. For this range of compound quantities, HPLC columns usually are ~ 10 x 250 mm in size and require high flow rates (> 5 mL/min), resulting in large isolated product output volumes, typically in 5-30 mL (given 1-3 min peak width) (70).

In some cases, solid-phase extraction (SPE) using disposable cartridges can be employed for purification, providing vastly simpler and quicker purification route. Frequently used reverse-phase C18 SPE procedure involves flowing of the tracer in aqueous solution (<5-10% of organic solvent v/v; by aqueous dilution of the crude reaction mixture if needed) through a pre-conditioned C18 cartridge. The solvent is diverted to waste while the product stays trapped on the cartridge resin. An additional cartridge rinse step is performed to wash out the residual solvents and some impurities, after which the tracer is released using 1-2 mL of ethanol (EtOH). SPE methods generally work well if impurities are sufficiently chemically different from the desired product, such as for [<sup>18</sup>F]fluorine removal. For example, IEX reactions (e.g. [<sup>18</sup>F]AMBF<sub>3</sub>-TATE synthesis in **Chapter 6**) where the chemical identity of the product and precursor are the same and need not (and cannot) be separated, only require removal of

unreacted fluoride ion, solvents, and buffer additives, which can be easily done with the SPE approach. In a routine synthesis of [ $^{18}\text{F}$ ]FDG a series of specialized cartridges is employed for convenient purification. Generally, the specific conditions used in the cartridge purification method, such as the one for [ $^{18}\text{F}$ ]FDG, are unique and cannot be applied to other tracers. Development and optimization of tracer-specific cartridge purification methods is, in most cases, a much more complicated and time-consuming process than HPLC-based method development (71).

A reformulation step is often necessary after purification in order to modify the matrix in which the radiopharmaceutical is suspended (e.g. HPLC mobile phase) to a safe, biocompatible formulation matrix that also ensures tracer stability and solubility. This is typically done through the evaporation of the solvent (e.g. using a rotary evaporator) and the resuspension in the injectable matrix (e.g. saline), SPE and/or dilution (e.g. to reduce EtOH concentration <10% v/v), depending on the starting solution composition. Both rotary evaporator and SPE processes may take a significant amount of time due to 10s of mL volumes that need to be handled. Commonly employed formulation via SPE requires elution of the product using 1-2 mL of ethanol, followed by a subsequent dilution to lower ethanol concentration <10%, resulting in 10-20 mL and higher final product volumes. Alternatively, excess ethanol can be evaporated and the dried product can be resuspended in desired solution (e.g. saline) (72,73).

## **1.9 Quality control of PET radiopharmaceuticals**

Strict regulatory requirements exist for the quality control (QC) testing of PET radiopharmaceuticals released for clinical use to ensure the safety of the administered tracer, and are described in regulatory documents, such as the U.S. Pharmacopeia (USP) (74) and the U.S. Food and Drug Administration (FDA) (75) or the European Pharmacopoeia (EP) (76). QC consists of several tests performed on each batch of the radiopharmaceutical prior to its application to patients to ensure tracer does not contain impurities or toxic components that

could cause unwanted pharmacological effects or interfere with tracer biodistribution. These tests include pharmaceutical tests for pH, color, clarity, chemical identity/purity, residual solvents, pyrogenicity and sterility, as well as radioactive tests for radiochemical identity/purity, radioisotope identity/purity and radioactivity concentration. Since a lot of effort has been spent on automation and optimization of the tracer synthesis itself, it is fair to say that the QC currently remains the most challenging procedure in the whole PET tracer production due to the need for diverse equipment, high degree of manual intervention, and its dependence on operator's experience and judgement (77,78). Although QC requires handling of relatively small quantities of radioactivity, direct handling of the radioactive compound, such as for measurement of pH or clarity assessment, is known to result in high radiation exposure to the personnel (79). Usually, QC is setup by installing multiple pieces of equipment (such as gas chromatography (GC), thin layer chromatography (TLC), dose calibrators, radio-HPLC, endotoxin measurement devices), allocating space for various testing stations, developing standard protocols, and performing ongoing maintenance, calibrations, and documentation. Some vendors (e.g. Elysia-Raytest) simplify the installation process by taking care of the equipment delivery, setup, and staff training; and the moderate reduction of QC equipment footprint is achieved by stacking necessary devices within compact shielded cabinets. To further reduce the labor burden of the QC process and improve the radiation safety of these procedures, few companies have prototyped automated cabinets (Cardinal Health, Siemens, Sumimoto), and miniaturized units such as QC-1 (80(p1)). Furthermore, instead of relying on conventional multi-instrument methods of acquiring QC data, systems such as Tracer-QC by Trace-Ability Inc. (81) and the Biomarker Generator system by ABT Molecular Imaging Inc (82), have redesigned QC tests to minimize equipment needed. The unique features of Biomarker Generator and the Tracer QC is that they both use novel QC approaches to perform as many QC tests as possible using a single analytical instrument. For example, Biomarker Generator QC relies on innovative HPLC methodologies to perform the majority of the QC tests (residual solvents, radiochemical

purity/identity, residual Kryptofix 222) and more importantly this system is fully integrated with a radiosynthesis module and a compact cyclotron. Even though the system does not include radionuclide purity/identity, endotoxin or sterility tests, it greatly simplifies QC and PET tracer production as a whole. In the Tracer QC system, on the other hand, novel QC methods were developed to enable sample analysis from a single optical plate reader. This system relies on non-contact optical measurements from the sample, with the addition of specific indicators to detect trace amount of chemicals, and scintillating materials to detect radioactivity. For the QC of [<sup>18</sup>F]FDG the plate reader alone is sufficient to perform USP compliant quality assessment, but to enable diversity of the supported PET tracers, the second-generation system Tracer-QC rHPLC is integrated with HPLC for tracer-specific chromatographic tests. The application of this system will be highlighted in **Chapter 5** for the QC of the [<sup>18</sup>F]FBB tracer. Though automated approaches for QC exist, their usage is currently not widespread due to the equipment cost, lack of diverse tracer-specific QC methods and challenging validation and approval procedures to comply with traditional QC standards (77).

## **1.10 Challenges of conventional radiopharmaceutical production and alternative solutions**

As discussed above, production of radiopharmaceuticals is a complicated multistep process that requires sophisticated techniques and infrastructure, as well as extensive knowledge and understanding of this field to create efficient strategies. The biggest challenge is that for a single radiopharmaceutical produced, typically a number of bulky complex instruments is needed. Additionally, the necessity for shielding of the radioactive materials, good manufacturing practice (GMP) requirements and time constraints defined by isotope decay further complicate radiopharmaceutical synthesis and delivery.

The highly specialized labs, typically built around a cyclotron, cost millions of dollars to set up and few hundreds of thousands of dollars to maintain yearly (83). The automated



synthesis modules are designed to work with large quantities of the radioisotope (e.g. an entire fluorine-18 batch from cyclotron) and, because the apparatus becomes contaminated after use, are often limited to producing one tracer per day. The production of several tracers or tracer batches per day requires immediate access to the cyclotron (or multiple shipments of the radioisotope) and multiple automated synthesis modules. Production of a single PET tracer batch can cost a few thousand dollars and many radiopharmaceutical facilities produce large batches of a single tracer, which are divided up into many individual doses and distributed to off-site imaging centers. With such a “centralized” tracer production model the high cost per production can be split up between the users when producing highly demanded [ $^{18}\text{F}$ ]FDG thus delivering this tracer to the researchers and clinicians at a reasonable price. However, the individual specialized tracers are in relatively low demand, and without the ability to efficiently divide up and distribute a large tracer batch a single radiopharmaceutical dose will cost as much as the whole batch (27,69). These high costs are even more difficult to justify for non-clinical research uses (and development) of diverse radiopharmaceuticals.

Recent technological advancements in PET radiopharmaceutical production have the potential to revolutionize the field and make PET more accessible, versatile and cost-efficient for both clinical use and research. The miniaturization of PET production makes it possible to create efficient systems compatible with different levels of the radioactivity for synthesis of a variety of radiopharmaceuticals on demand. A significant effort has been made in the microfluidics field to create efficient, small-footprint devices to replace conventional large-scale equipment and reduce tracer production costs through reduced space requirements, reduced shielding, and more efficient operation. Unlike conventional equipment, compact micro-radiosynthesizers could be moved out of centralized radiopharmacies and instead be located directly in clinics. By decentralizing production, access to a wide variety of tracers becomes possible, as each site could prepare the particular compounds needed by the local environment. With this approach, the radiopharmaceuticals can be produced on-demand and in sufficient

quantities without generating any extra waste. Such technology would be immensely beneficial in a pre-clinical setting, where very small quantities of the tracers are required to image small animals or perform in vitro studies. Microfluidics can revolutionize the PET tracer production by replacing a “centralized” bulk production with the new “decentralized” approach. With this model, the radiopharmacies with a large installation base of cyclotrons would only need to distribute the aliquots of radioisotope to the imaging centers, where miniaturized self-shielded radiochemical modules would produce single dose or multidose tracer batches as needed. Notably, only nanograms of radiopharmaceuticals are administered during each PET scan, making microfluidics a perfect fit for the radiopharmaceutical niche due to its inherent advantage when handling smaller quantities of reagents (83–86)

### **1.11 Microfluidic radiosynthesizers**

Microliter-scale radiofluorination reactions enabled by microfluidics offer many advantages over conventional radiochemistry and lead to potential cost-reduction of PET tracer synthesis. The consumption of the reagents is reduced 1-2 orders of magnitude, which can significantly cut the cost per synthesis with scarce or expensive precursors. Especially the cost reduction will be noticeable during the optimization stages for novel tracers. Microliter-scale reactions are also much faster than the macroscale ones, which reduces the cost of labor, and allows to perform more productions per day. Additionally, as mentioned earlier, in microscale syntheses large starting activities are not necessary to achieve high molar activity of the final tracer. This means that smaller batches of usable PET tracer can be produced to support few imaging studies without wasting the starting radioisotope. Thus, efficient dose-on-demand tracer production can be easily achieved with microfluidic radiosynthesizers and would also result in reduced shielding requirements and improved safety of operation. Potentially reduced shielding and overall small system size creates an opportunity to build self-shielded compact radiosynthesis units that can be placed on a benchtop. Without the need for large hot-cells and

laboratory space, the cost of radiosynthesizer installation can be significantly reduced. A significant progress has been made to develop automated microscale radiosynthesizers, and several miniaturization approaches has been shown (84–86).

In general, there are two major types of microfluidic radiosynthesizers based on the mode of production: ones based on continuous flow microfluidics, and others based on batch micro-reactors. The flow-based microfluidic radiosynthesizers allows one to perform radiolabeling reactions continuously as the mixed reagents flow inside a heated channel or capillary. The benefits of this technique are uniformity of the reaction conditions due to efficient mixing and a very high surface-to-volume ratio, permitting efficient heat transfer throughout the reaction volume and rapid synthesis (87–89). Flow-based radiosynthesizers, such as commercially available Advion NanoTek, has been used to synthesize fluorine-18 labeled tracers as well as the tracers labeled with carbon-11, nitrogen-13 and various radiometals (90–94). Some of these devices are capable of using 10s of microliters of the reagents to perform low-starting activity optimization syntheses. To perform synthesis with larger quantities of radioisotope either requires a corresponding increase of the precursor volume or instead requires the preconcentration of radioactivity prior to the synthesis (69,95,96).

Microfluidic batch synthesizers perform radiolabeling in 10s of microliters or less of reaction mixture volume enclosed in a small reactor. A variety of approaches have been reported. In the simplest batch reactors, parts of the conventional apparatus are miniaturized to a small scale, using on-chip valves, micro pumps and tiny reaction chambers or miniature conical vials. A few groups have demonstrated successful implementations of small-scale batch production by using micro-vials with 5-20  $\mu\text{L}$  volumes for synthesis of [ $^{18}\text{F}$ ]FET (97), custom PEEK/pDCPD 50  $\mu\text{L}$  reactor with integrated microvalves for clinically-used batches of [ $^{18}\text{F}$ ]fallypride (98), and integrated PDMS chip with 0.1 mL reaction chamber with externally-controlled valves for [ $^{18}\text{F}$ ]fallypride synthesis (99). The application of microliter droplet manipulation in radiopharmaceutical synthesis have gained a lot of interest in the past several

years, and a few droplet-based approaches have been developed (86). Initial droplet-based synthesizers were based on electrowetting-on-dielectric (EWOD). EWOD reactors apply electric potentials to liquid droplets changing the surface tension properties to initiate reagent movement and mixing. EWOD reactors are comprised of two substrates between which the droplets are sandwiched, enclosing reagent pathways as well as heated reaction site (100–102). To enable hands-free droplet manipulation, the bottom layer contains the set of electrodes covered by a dielectric layer and hydrophobic coating (Teflon AF), and the top layer contains a ground electrode with hydrophobic coating. Such reactors were able to carry out a variety of PET tracer syntheses, however the fabrication of these complex multi-layer chips remained a challenge. Even though EWOD demonstrated potential in efficiently scaling down reaction volumes and ability to achieve extremely good tracer production results, the costs and complexities have hindered development and more widespread use of this technology for radiochemistry. Since each chip is supposed to be disposable, it significantly elevates the cost per synthesis, undesired for the purpose of microfluidics in radiopharmaceutical production (86,103). Magnetic droplet reactors (MDM) rely on magnetic particles introduced in the reaction volume to manipulate the reagents with a moving magnet mounted below the substrate. In one reported work with such reactor, the substrate consisted of a Teflon sheet placed atop a plastic stage, but contained no heater and the labeling was carried out at room temperature. Notably, the magnetic particles modified with anion exchange resin allowed one to perform the trapping of reagents and solvent removal (typical for QMA cartridge procedures). Automated tracer production was achieved using magnetic robot arms, however due to the lack of heating such platform could not be easily applied to a majority of PET tracer syntheses. EWOD and MDM devices alike suffer from high degree of complexity, limited flexibility and expensive cost (71,84,86,91,103).

To overcome the challenges of EWOD and MDM, other types of droplet platforms are being explored. Notably, square-shaped (25.0 x 25 mm) Teflon-coated glass chips have been

used as a cheaper alternative to EWOD to enable droplet reaction studies and optimizations. They have identical materials in contact with the reaction mixture and similar thermal properties as EWOD substrates, however such chips have no simple path to automation on their own (104). The reagents were dispensed manually using micro pipettes onto a designated reaction site region, and the chip was mounted on a temperature control platform with a heater and a heat sink (Figure 1.5A). Such simple setup demonstrated practical use for synthesis of tracers (e.g. [ $^{18}\text{F}$ ]fallypride, 1- $^{18}\text{F}$ fluoro-4-nitrobenzene ( $^{18}\text{F}$ FNB), [ $^{18}\text{F}$ ]AMBF<sub>3</sub>-TATE) for pre-clinical imaging (57,105). In **Chapters 6 and 7** of this work, Teflon-coated glass substrates were used to perform the IEX synthesis of [ $^{18}\text{F}$ ]AMBF<sub>3</sub>-TATE and trifluoroborate-based prosthetic groups. Similar to the EWOD “sandwich” configuration, the droplet placed on the bottom substrate was covered with a second substrate placed atop (Figure 1.5A). Glass chips however were prone to Teflon layer damage caused by physical contact, harsh chemicals, and potential radiation; and required a lot of manual intervention (such as placement and removal of the cover plate) which would be hard to automate. In 2017 our lab introduced an automated platform with a passive transport (PT) silicon chip (25.0 x 27.5 mm) to develop an automated alternative to electrode activated droplet movement on EWOD (106). By creating a hydrophilic tapered pattern on a hydrophobic surface, droplet of liquid can be spontaneously moved along the diverging direction of this taper without external force, causing the taper to act as a unidirectional ‘channel’. Such spontaneous movement occurs due to a larger contact line on the wider side of the channel creating a net force on the droplet directed towards the wider end. In the PT reactor, droplets of reagents are dispensed as needed at the ends of a set of radially-oriented tapered channels (one for each reagent), which then passively move to the central reaction site, enabling facile reagent addition. The radiosynthesizer system comprised a heating and cooling system, with a Teflon-patterned silicon PT chip placed atop the ceramic heater, and dispensers/collection tubing in the positions above the chip. The reagent delivery was fully automated using pressure-driven piezoelectric dispensers aligned above the ends of the channels, reactions were carried

out on an open surface of the chip and the final reaction product was automatically recovered using retractable collection tubing directly from the reaction site into a designated vial via vacuum (Figure 1.5B, Figure 1.6) (50,106,107). An automated tracer synthesis using the PT chip was performed for the production of [ $^{18}\text{F}$ ]fallypride, [ $^{18}\text{F}$ ]FET and [ $^{18}\text{F}$ ]FDG. However, it was found that the PT mechanism was sensitive to this type of solvent, temperature and volumes, causing volume spreading outside of the reaction site along the channels. Because such issues could cause a decrease in the reaction yields and inconsistencies in synthesis performance, the tracer production on the PT chip would require cumbersome optimization, complicating the adoption of such a platform for versatile everyday use (86,108).

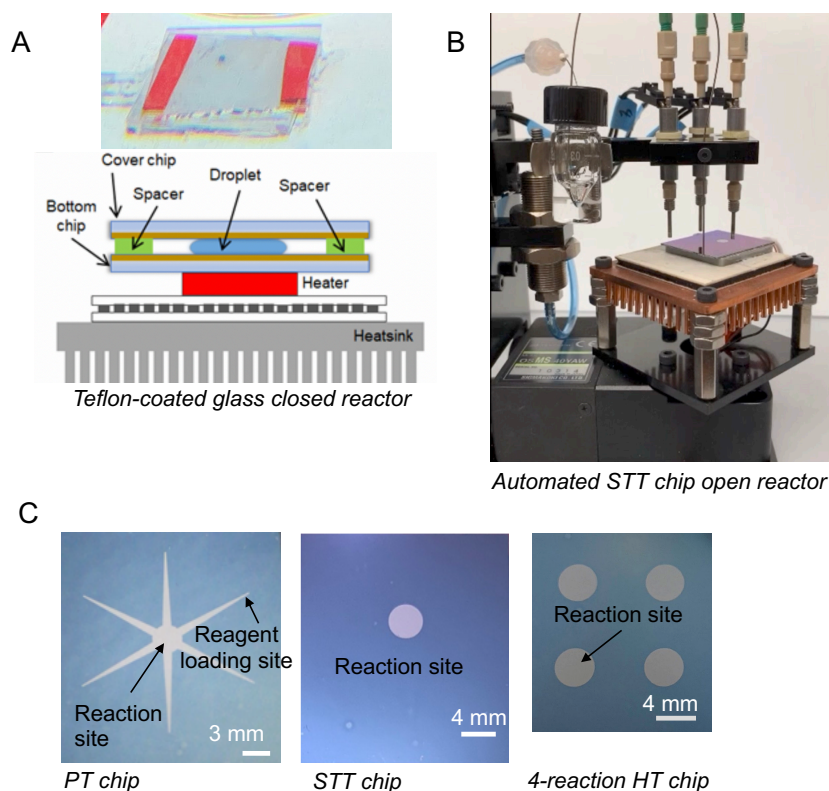


**Figure 1.5 Droplet platforms**

(A) Closed reactor consisting of 2 Teflon-coated glass substrates with separating stripes on the sides to make space for a sandwiched droplet. (B) Automated compact radiosynthesizer with a surface tension trap (STT) chip; (C) Various patterned chips for droplet radiochemistry.

Direct dispensing of the reagents into the reaction site would alleviate the challenges of the PT mechanism. Recently, direct dispensing was implemented and automated using patterned Teflon-coated silicon chips, similar size and material as the passive transport chips described previously. Instead of a star-shaped hydrophilic pattern, only a circular reaction site (4 mm diameter) was etched on the Teflon coating to create a surface tension trap (STT) for the reagents. With Teflon-coated glass and EWOD substrates that have a uniform hydrophobic coating, it was a challenge to keep the reaction volume confined in place, though for EWOD it was achieved with the help of the electrodes. In contrast, the STT chip would trap the reaction volume within the pattern boundaries, preventing reagent or product from spreading. To automate the reagent delivery in a compact manner and afford the use of multiple reagent dispensers, the chip and heater were mounted on a rotating platform, to enable the alignment of the reaction site below each of the circularly arranged dispensers (Figure 1.5B). This simple platform afforded the efficient radiosynthesis of several tracers such as [ $^{18}\text{F}$ ]FET, [ $^{18}\text{F}$ ]FBB, [ $^{18}\text{F}$ ]fallypride and [ $^{18}\text{F}$ ]FDOPA (86,108,108–110). To expedite the optimization process on droplet-based STT chips, our lab developed a high-throughput (HT) platform with 4 heaters and designed multi-reactor chips with either 4 or 16 reaction sites (Figure 1.5C, HT chip). As a proof of concept, these chips were operated manually (111) and a robotic system is currently in development to automate the reagent manipulation and product recovery as well as TLC sampling (112).

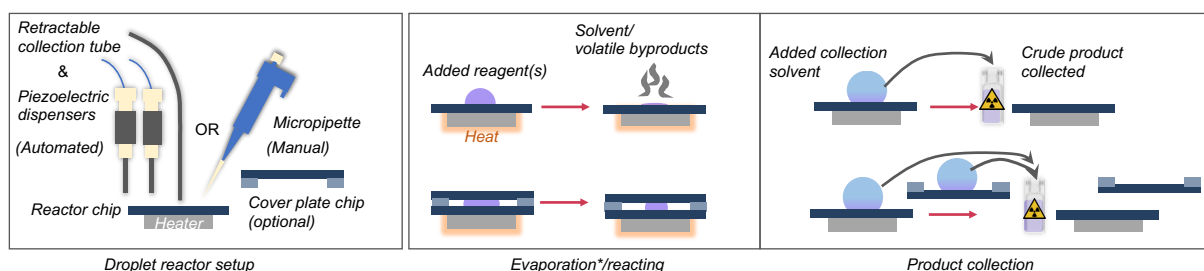


**Figure 1.6 Generalized droplet radiosynthesis procedure**

A diagram showing a simplified procedure and setup of droplet synthesis of PET tracers using either Teflon-glass chips (closed reactor with cover plate), PT or STT silicon chips (open chip reactors). Note that the evaporation of [ $^{18}\text{F}$ ]fluoride is always performed without a cover plate.

All of the droplet reactors carry out reactions in 10  $\mu\text{L}$  or less, allowing one to achieve > 100x reduction in the amount of precursor compared to conventional syntheses (50,109). Synthesis time is typically also shorter, most reaction steps need <5 min to achieve a high yield, while overall crude synthesis (1 or 2 reaction steps) from dispensing and drying of [ $^{18}\text{F}$ ]fluoride until crude product recovery may take less than 30 min. Due to the small volume of these microfluidic reactors, the amount of cyclotron produced fluorine-18 (e.g. > 40 GBq in 1-5 mL) that can be directly loaded to the reactor is limited (e.g. 0.4 GBq in 0.01 mL). Nevertheless, droplet reactors can readily produce sufficient quantities (10s of MBq) for pre-clinical *in vivo* and *in vitro* applications. To overcome the limitation of macro-to-micro interface and enable a high range of starting activities in microfluidic syntheses for clinical applications or lower-yielding syntheses, several strategies are employed. In EWOD chips it was possible to dry a large volume (200  $\mu\text{L}$ ) in a special uncovered region of an extended bottom chip, from where the evaporated droplet (shrunk to  $\sim 5 \mu\text{L}$ ) was transferred to the reaction site. On the PT platform, a larger [ $^{18}\text{F}$ ]fluoride volume was loaded in small (2  $\mu\text{L}$ ) increments and dried sequentially within the reaction site. A similar strategy was employed on the STT chips but by drying 30  $\mu\text{L}$  at a time. This technique is described in **Chapter 5**, enabling the production of clinically relevant quantities of [ $^{18}\text{F}$ ]FET and [ $^{18}\text{F}$ ]FBB. The downside of the sequential drying method is that each iteration takes time (e.g. 1.5 min for 30  $\mu\text{L}$ , or 10 sec for 2  $\mu\text{L}$ ), which causes activity loss due to radioactive decay, thus scaling is limited (e.g. 1 mL of [ $^{18}\text{F}$ ]fluoride/[ $^{18}\text{O}$ ]H $_2$ O would require at least 50 min of sequential loading and evaporation steps). To enable efficient scaling of a few mL volume into a  $\mu\text{L}$ -scale, a stand-alone automated device was developed in our lab. The isotope concentration device would trap a large solution of the radioisotope on a miniature strong anion exchange (SAX) cartridge followed by the subsequent elution of the fluorine-18 in a small volume. The automated concentration system could concentrate 1 mL of



[<sup>18</sup>F]fluoride/[<sup>18</sup>O]H<sub>2</sub>O into ~12 μL of volume in just 10 minutes (113). This system was used in conjunction with a PT-base droplet radiosynthesizer to produce [<sup>18</sup>F]fallypride with different starting activities between 0.0003 – 1.1 Ci [0.011 – 41 GBq]. Despite the observation that synthesis yield diminished with radioactivity, up to 0.19 Ci [7.2 GBq] of [<sup>18</sup>F]fallypride was produced using this method, which is equivalent to multiple doses for human injections (10 mCi [0.4 GBq] each) for PET scans (86,107).

### **1.12 Miniaturization of PET tracer purification, reformulation and quality control**

Unlike the impressive progress achieved with miniaturization of radiosynthesizers, limited success was shown for development of miniature purification, formulation and QC units. Large footprint and high cost of the related instrumentation strongly undermines the potential of microfluidic radiosynthesis, though there are miniaturization options being explored. As with the conventional syntheses, highly versatile HPLC remains the main purification tool in microfluidic syntheses as well. Due to a lower reagent quantity used in microscale syntheses, required HPLC purification column size can be reduced from semi-prep (10 x 250 mm) to analytical (4.6 x 250 mm). Microscale production deals with 10s to 100s of micrograms of analytes in microliter volumes, compared to 10s of milligrams in a typical conventional procedure. The main benefit of the analytical columns is that they operate at lower flow rates (1-2mL/min vs >5 mL/min) and exhibit narrower analyte peak widths, thus allowing one to recover purified product in 1-3 mL volume, 10-fold less than with the semi-preparative columns. Though analytical columns also are more economic in solvent consumption and can achieve faster purification times, the macroscale pumps and valves of these HPLC systems still lead to large footprint of the overall unit. Nevertheless, analytical HPLC purification has been used for a number of microscale tracer productions (84,86), including the [<sup>18</sup>F]FET and [<sup>18</sup>F]FBB syntheses in **Chapters 3, 4 and**

5 of this work (50,109). On the other hand, more potential in miniaturization has been shown using SPE. For some syntheses, purification can be achieved with disposable SPE cartridges, and a few examples of miniaturized SPE purification for microfluidic-base syntheses were reported in literature. Such as, for production of [ $^{18}\text{F}$ ]FDG purification was achieved using miniature SPE modules with a combination of 4 different resins (up to 80 mg total resin mass). In one example a miniature cartridge was simply built by packing a thin piece of perfluoroalkoxy alkane tubing with the resins from a commercial purification cartridge, using which the purified product was eluted in 0.3 mL of aqueous volume (106). In another report, a glass microfluidic chip was built enclosing small chambers packed with the SPE resins. A train of multiple chips each with a single type of resin, or a single multi-resin chip were used for purification affording eluted product in ~1 mL of water. Unfortunately only 90% purity was achieved (>95% is acceptable) with either method and further optimization was needed (114). Another example of a miniaturized cartridge was shown for purification of [ $^{18}\text{F}$ ]FLT following droplet radiosynthesis on EWOD. The cartridge, however, had a relatively high resin mass (180 mg) and the purified product was eluted with 0.5 mL ethanol which was evaporated in a subsequent step to achieve high final product concentration (115). On-chip removal of [ $^{18}\text{F}$ ]fluoride from crude product mixture of [ $^{18}\text{F}$ ]fallypride was demonstrated using alumina surface integrated into a cover plate for an EWOD chip. Adsorption of the [ $^{18}\text{F}$ ]fluoride ions onto alumina was facilitated by heating and mixing of the 10  $\mu\text{L}$  product mixture as it was squeezed between the EWOD plates (116). While removal of [ $^{18}\text{F}$ ]fluoride can be easily adapted for purification of many fluorine-18-labeled tracers, SPE removal of other tracer specific impurities would require significant optimization efforts and may not be readily achievable for every radiopharmaceutical.

Reformulation of the purified fluorine-18-labeled radiopharmaceuticals for microvolume syntheses, can be achieved using miniature reverse-phase SPE or evaporation techniques (84). In particular, in **Chapter 4** of this work, SPE formulation was performed using a custom automated device and disposable miniature C18 cartridges (10 mg resin) during synthesis of

[<sup>18</sup>F]FBB (109). The main difference between conventional and microscale SPE methods is elution volume, which with many conventional cartridges has to be at least 1-2 mL, while in the selected work an efficient recovery on a micro cartridge was achieved with only 0.15 mL of ethanol. For a safe formulation, ethanol concentration typically needs to remain <10% (<15% in case of [<sup>18</sup>F]FBB), thus requiring an addition of aqueous media to the product eluted off the cartridge. Maintaining a small formulation volume is crucial for microfluidic syntheses, especially if using less amount of starting activity, to avoid the product becoming too dilute to be used for PET imaging. Miniaturized cartridges help to reduce elution volume and subsequently final formulation volume, but other volume reduction strategies may include evaporation or usage of specialized concentration devices. For example, in our lab, a PET tracer concentration device was developed based on gas membrane distillation, allowing to concentrate large (10s of mL) volumes of the tracer into 1-1.5 mL. The device also features rapid (<14 min) complete evaporation of 10 mL volume followed by efficient product recovery in a small volume of saline (72).

Quality control of radiopharmaceuticals is an essential part of tracer production to ensure safety and reliability of the PET scans for both pre-clinical and clinical applications. As discussed earlier, these tests can be categorized as pharmaceutical tests focused on molecular identity, physiological compatibility, and tests ensuring lack of toxic microbiological, pyrogenic, chemical or particulate contaminants; and radioactive tests that validate radiochemical and radionuclide purity/identity, proper tracer concentration and molar activity. Conventional procedures suffer from need of various complex analytical equipment and significant lab space, manual sample handling and, importantly, may consume few milliliters of the tracer which makes these procedures incompatible with microfluidic PET tracer production. Some of the currently use-ready products such as Tracer-QC already offer a compact, miniaturized alternative to the conventional QC, as had been discussed previously, but still may require ~1 mL of sample. Apart from reduced sample consumption, microfluidic devices have higher

sensitivity which may allow to reduce testing time. Further miniaturization of individual tests to reduce sample size had been discussed in literature, however no complete set of miniature QC methods currently exist (78). The most crucial analytical device in radiochemical production necessary for clinical applications as well as pre-clinical research, method optimization and tracer development is the HPLC. HPLC allows to determine molar activity, radiochemical purity/identity of the final product and assess presence of various impurities. Even though micro-HPLC columns and even commercialized HPLC-chip do exist, those devices still rely on bulky high-pressure pumps, injection valves and detection modules (78). Alternative to HPLC approach had been demonstrated using capillary electrophoresis (CE). CE relies on separation of analytes by application of an electric field that pulls the analytes apart based on their electrophoretic properties and interactions with the sample capillary and the separation buffer. A microchip CE device had been developed in our lab, and its use was demonstrated using [<sup>18</sup>F]FLT tracer as an example. The CE chip features orders of magnitude reduction of consumed sample and possible analysis time reduction down to seconds. The device consists of a very thin capillary, and only requires nanoliters of sample while providing exceptional separation quality and detection efficiency. Microchip CE device is much simpler than the HPLC, however due to small sample volumes achieving high sensitivity is currently a challenge. Additionally, fluoride ion was not pulled through the capillary using existing method and was not detected, unlike all the rest of the impurities. Thus, further development is needed for the CE-chip to fully replace HPLC in versatility and functionality (78,117,118).

### **1.13 Summary of the benefits of microfluidics in PET tracer production**

The use of microfluidic systems for radiopharmaceutical production has demonstrated potential to revolutionize the PET tracer production, syntheses optimization and new tracer discovery. Microfluidic systems feature small footprint, reduced reaction volumes and improved synthesis efficiency. The reduction of reagent consumption plays an important role in cost reduction for syntheses using scarce or expensive precursors. In particular, for new tracer development, where the availability of the novel precursor is challenging, microfluidics can perform 100x more syntheses than a conventional system with the same reagent quantity. This grants an economic approach in radiolabeling method validation, optimization of the reaction conditions and in supporting pre-clinical studies. Despite the small volume and reagent scale, it has been shown that microfluidic radiosynthesizers are capable of producing clinically-relevant quantities of the radiotracers as well. The application of compact, self-shielded radiosynthesizers for clinical production, as discussed earlier, would support the dose-on-demand production and a transition from centralized radiopharmaceutical distribution to decentralized. To achieve high molar activity, good product yields and sufficient tracer concentration, conventional radiopharmaceutical synthesizers are often used with ~1 Ci-level [ $\sim 37$  GBq] of starting activity, producing multiple doses of tracers ( $>100$  mCi [ $>4$  GBq]). However, for a single patient scan ( $\sim 10$  mCi [ $\sim 0.4$  GBq]) or small animal scans ( $\sim 0.1$  mCi [ $\sim 0.004$  GBq]) such large quantities are not needed. In contrast, microfluidic radiosynthesis units can use low ( $<100$  mCi [ $<4$  GBq]) starting activities to produce smaller batches (few clinical doses), with high molar activity and in sufficient radioactivity concentration. These economic microfluidic radiosynthesizers can potentially enable clinical dose-on-demand

production of a wide variety of radiopharmaceuticals using minimal starting materials, limiting radiation exposure and reducing waste in comparison to conventional methods (84,91,103,119). Additionally, as miniaturization efforts continue and the production of radiopharmaceuticals on a microscale become more optimized and reliable, a reduced effort in quality control may be possible. Microscale syntheses inherently use very small reagent and solvent quantities, and thus trace amounts of those toxic components in the final product formulation are expected to be far below acceptable limits. For example, the total amount of a toxic solvent (e.g. DMSO or MeCN) per reaction may be so low, that even with the failure of the purification step to remove any of the solvent, its amount in the final formulation is guaranteed to not exceed acceptable values. Thus, potential simplification of purification and quality control process in microfluidics-based productions creates an opportunity to further streamline the PET tracer production process (120).

#### **1.14 Focus of this dissertation (summary)**

When considering the current state of the world, where obtaining research space and research funding is extremely and increasingly competitive - novel, cutting edge methods need to be developed and applied to make research more accessible and affordable. As discussed above, the benefits of low-cost microfluidic radiopharmaceutical production can be used for efficient dose-on-demand tracer production in both a clinical and pre-clinical setting, as well as in radiochemistry-related research. In this work we aim to show that microfluidic syntheses are indeed practical, efficient, economic and applicable in research. We synthesize fluorine-18-labeled radiopharmaceuticals using simple and inexpensive microfluidic devices, while producing high quality tracers usable for PET imaging. In the various chapters of this manuscript we demonstrate application of microfluidic to new tracer development and validation, small-scale on-demand tracer production for pre-clinical studies and production of clinically-suitable

batches of the radiopharmaceuticals. The selected works feature drastic reduction in precursor consumption in comparison to conventional methods, very high molar activities achieved using small quantities of the radioisotope, and versatility of microfluidic techniques applied to different tracer syntheses. The ability of microscale radiochemistry to greatly improve molar activities without the need of large radioisotope quantities is particularly valuable for isotopic exchange (IEX) radiolabeling. In IEX syntheses precursor and product are inseparable, which simplifies purification but lowers molar activity when a lot of precursor is used. While conventional approaches must use extremely high starting activities to achieve good molar activity, we show that on microscale precursor consumption can be reduced to a few nmol and high molar activity can be achieved even with low starting radioisotope amounts. This is a valuable breakthrough that can potentially open up this class of reactions to many researchers, who can take advantage of this rapid one-step labeling approach with simple purification. In the scope of this dissertation, we also expand the application of microfluidic synthesizers beyond our own lab in collaborative work with other chemistry and biology labs and the industry. While the translation of the microfluidic technology for routine use in clinical PET diagnostics will take significant effort to optimize and validate the microfluidic systems, this work demonstrates that the technology can be readily applied for preclinical use and supply researchers with diverse PET tracers.

First, the work described in Chapter 2 was a collaborative project with Dr. S. Wnuk's group at the Florida International University, who developed radiolabeled analogues of a known drug Gemcitabine. I performed a microscale droplet labeling of the novel tracers side by side with conventional ELIXYS FLEX/CHEM synthesis, using the same batches of reagents, though in smaller quantities. The microscale synthesis was carried out manually using a Teflon-coated glass closed reactor in 30  $\mu$ L volume. The droplet synthesis readily demonstrated much higher yields than the conventional procedure using 10x less precursor, which can be likely reduced even further. Such reduction in precursor consumption would be beneficial for any novel tracers where the precursor cannot be efficiently supplied in large quantities, increasing opportunities

for optimization and testing per single precursor batch. Collaborative effort in this work demonstrates the practical potential for droplet chemistry aiding in testing of the novel tracers for research purposes.

Our lab has developed open-chip droplet radiosynthesizer platforms which were used for synthesis of tracers such as [ $^{18}\text{F}$ ]fallypride, [ $^{18}\text{F}$ ]FDOPA and [ $^{18}\text{F}$ ]FDG (106,108,110). To further demonstrate the versatility of the droplet synthesizer, in Chapter 3, I adapted a 2-step one pot synthesis of amino acid tracer [ $^{18}\text{F}$ ]FET used in glioma imaging to be synthesized manually on a STT chip and automatically on a PT chip. A synthesis on a microscale was adapted from a conventional scale synthesis with brief optimization of the base and precursor amounts. The study highlights that [ $^{18}\text{F}$ ]FET can be produced in a shorter time than reported conventional syntheses, and exhibits high yields. The study was taken further by performing PET imaging on tumor bearing mice to look into the effect of molar activity on image quality. As discussed previously, the molar activity effect on imaging in various applications is rarely reported and tracer-specific studies are needed. Notably, the economic droplet approach synthesizes enough tracer for long dynamic scans in 8 animals per day, facilitated by use of the novel HiPET (121) scanner with high sensitivity and up to 4 animals imaged at a time.

Chapter 4, shows further expansion of the STT droplet platform to the synthesis of [ $^{18}\text{F}$ ]FBB, a neurotracer used in Alzheimer's diagnostics. I adapted the tracer synthesis from a known conventional procedure and optimized using a high-throughput 4-heater platform (111). Additionally, this tracer required a lot of attention during the purification and formulation phases due to its sensitivity to radiolysis and room light. In particular, I found that the formulation by evaporation did not yield a pure product, necessitating the use of alternative approaches such as SPE. To afford this tracer in high purity I developed a new microscale formulation protocol. I adapted the SPE formulation technique using C18 resin onto a microvolume scale by making small SPE cartridges, and eventually built an automated system for a safe and rapid formulation. The simplicity of the formulation setup built for this tracer allows it to be used for



any tracer in the future. The formulation system was capable of trapping the product in 30 mL of volume on 10 mg of SPE resin, followed by a rinsing protocol and elution in only 0.15 mL of ethanol in just 17 min.

While Chapters 3 and 4 focused on small quantities of produced [ $^{18}\text{F}$ ]FET and [ $^{18}\text{F}$ ]FBB, suitable for pre-clinical applications only, in Chapter 5 we take a step forward and perform automated high activity syntheses, suitable for 1-2 human doses of the tracer, and demonstrating that consecutively produced batches pass all the necessary quality controls. Radioactivity scaling is typically a problem for microscale synthesis due to the macro-to-micro interface challenge, specifically due to mL-scale volumes of cyclotron-produced fluorine-18. While the concentration of full radionuclide batches to droplet format is feasible using off-chip methods, the whole volume may not be necessary to produce just a few human doses. In this study I scaled the starting radioactivity to up to ~100 mCi [~4 GBq] by employing sequential drying steps directly on chip. This greatly simplifies the typical strategies to overcome macro-to-micro interface, as no external devices are required; reducing room for error and overcoming potential system complexity. The ability to use very simple and cheap disposable chips and a compact low-cost device to synthesize tracers is particularly attractive for the field of radiochemistry, as the major issue with the introduction of microfluidics devices in radiopharmaceutical production is the high cost of the complex systems. In this work, I arranged the quality control testing to ensure the suitability of the product for human injections. While for both syntheses, conventional QC approaches were used, for [ $^{18}\text{F}$ ]FBB we also collaborated with Trace-Ability Inc. to perform a more convenient and faster QC testing using a compact Tracer-QC apparatus.

Chapter 6 describes the adaptation of IEX chemistry to a Teflon-coated closed glass reactor. A novel [ $^{18}\text{F}$ ]AMBF<sub>3</sub>-TATE tracer for imaging of SSTR2 neuroendocrine tumors, obtained from collaborating with Dr. D. Perrin, exhibited good yields and high molar activity when synthesized even at low starting activities. I carried out the synthesis of this tracer for in

vivo studies with tumor bearing mice to demonstrated its efficiency in detecting neuroendocrine tumors similar to the current gold standard [<sup>68</sup>Ga]DOTA-TATE. The use of fluorine-18-based diagnostic tracer offers advantages due to the limited production quantities of a generator-produced gallium-68. More importantly, this work highlights the unique advantage of miniaturized droplet chemistry in its capability to reduce precursor quantities down to a few nmol while still giving high fluorination yields.

Chapter 7 also describes IEX chemistry in droplet format, but with a different trifluoroborate (R-BF<sub>3</sub>) precursor obtained in collaboration with Dr. E. Gras lab. Previously I showed that using the same reaction conditions as synthesis of [<sup>18</sup>F]AMBF<sub>3</sub>-TATE on glass substrates, labeling via IEX was immediately efficient with other R-BF<sub>3</sub> precursors designed as potential prosthetic groups for biomolecule radiolabeling (56). Teflon-coated glass chips, however, are not very robust and our lab has since switched to silicon chips for all other chemistry types. In this ongoing work I investigate and compare performance of IEX micro radiosynthesis on glass and silicon substrates. I addressed the challenge of the fluorine-18 radioactivity loss during drying on the fully Teflon-coated as well as the patterned silicon which was not seen before with Teflon-coated glass substrates. After the modification of drying procedures by adding a high boiling point DMSO and optimizing drying times, I was able to achieve similar high yields on silicon and glass reactors. Importantly, this work allows to transfer the synthesis from a closed reactor to an open reactor. The adaptation to the open reactor is particularly valuable, as it provides a direct route for the automation of the IEX chemistry on an existing automated droplet platform. The labelling of R-BF<sub>3</sub> based prosthetic groups on a droplet reactor has a potential to greatly expand the diversity of tracers produced with such technology and further promote its versatility. This is an ongoing work, and as more optimization data is collected, the method will be expanded to radiolabeling of other R-BF<sub>3</sub> compounds.

## Chapter 2: Fluorine-18 radiolabeling of 4-N-acyl and 4-N-alkyl gemcitabine analogues

### 2.1 Introduction

Gemcitabine (2',2'-difluoro-2'-deoxycytidine, dFdC), is a chemotherapeutic nucleoside analogue used as first line therapy in pancreatic and lung cancers (122). Gemcitabine, like many other nucleosides, enters cells via the human equilibrative nucleoside transport protein 1 (hENT1) and is subsequently activated via phosphorylation by deoxycytidine kinase (dCK) and other kinases to its triphosphate form (123,124). The triphosphate is a substrate for DNA synthesis inhibiting DNA polymerase by chain termination during replication and repair processes, triggering apoptosis (125).

Gemcitabine, even if beneficial for the treatment of a variety of tumors, can have its efficacy diminished by increased toxicity to normal cells and rapid intracellular deamination into inactive 2',2'-difluorouridine (dFdU) by cytidine deaminase (CDA).(126–128). In order to tackle these issues, various prodrug strategies have been developed through hydrolysable lipophilic acyl modifications on the exocyclic 4-N-amine or 5'-hydroxyl group of the nucleoside (129–135), and such approaches were recently reviewed (136). These modifications facilitate the uptake by cells slowing also the release of gemcitabine through hydrolysis, which increases its bioavailability while also providing resistance to enzymatic deamination by CDA. Gemcitabine analogues have been also designed and synthesized as theranostic delivery systems with cellular specificity and imaging capabilities (137–140). Increased bioavailability of gemcitabine 4-N-alkyl analogues have been scarcely explored and thus their synthesis and mode of activity need further investigation. Recently, Pulido et al. showed that 4-N-alkyl analogues had modest cytostatic activity with neither measurable deamination nor conversion to gemcitabine observed (141,142). This increased stability of the 4-N-alkyl analogues within the cell, compared to 4-N-

alkanoyl counterparts, provides an opportunity for their development as novel derivatives of gemcitabine and to study their distribution via PET.

Although  $^{18}\text{F}$ -radiolabeling has progressed tremendously in recent years, the incorporation of the fluorine-18 label into biomolecules normally involves a large number of steps and burdensome labeling procedures (47,143–147). This is definitely the case in the synthesis of  $^{18}\text{F}$ -labeled nucleoside analogues, which usually involves multiple protection and deprotection steps, and therefore can lead to an overall increased reaction time and decreased radiochemical yield. Since practical syntheses of gemcitabine are based on incorporation of a geminal difluoro unit in their early synthetic stages (148,149), preparation of 2'-[ $^{18}\text{F}$ ]dFdC is not feasible due to short half-life of the  $^{18}\text{F}$  isotope (150). Recently, the gemcitabine analogue 1-(2-deoxy-2-[ $^{18}\text{F}$ ]fluoro- $\beta$ -D-arabinofuranosyl)cytosine ([ $^{18}\text{F}$ ]FAC) was developed enabling noninvasive prediction of tumor responses to gemcitabine and is utilized as a probe for PET imaging of dCK activity (151–153). Although FAC generally follows the known *ex vivo* biodistribution of gemcitabine, it is missing a geminal difluoromethylene unit at C2' which is reported to be critical for anticancer properties of dFdC and its inhibitory activity of ribonucleotide reductases (154). Therefore, we have undertaken efforts to investigate other dFdC derivatives with the geminal difluoro unit already incorporated and bearing a silane moiety, which would allow convenient  $^{18}\text{F}$  labelling.

The use of compounds bearing Si-F bond in radiochemistry has been explored since 1958 (155), with *in vivo* studies reported as early as the 1970s (156). The Si-F bond was considered as an alternative to C-F bonds due to its increased bond strength (565 kJ/mol for Si-F versus 485 kJ/mol for C-F) (157). However, early on, it was discovered that even with this increased stability, the Si-F bond is highly susceptible to hydrolysis in physiological conditions (157). This tendency can be prevented by the use of bulky substituents on Si-atom since they have been shown to shield the Si-F bond from hydrolysis while also increasing lipophilicity. This makes these silicon-fluoride acceptors potential  $^{18}\text{F}$ -labeled tracers for PET imaging (158–161).

Herein, we report synthesis of clickable 4-N-alkanoyl and 4-N-alkyl gemcitabine analogues with silicon-fluoride acceptors, high-yield  $^{18}\text{F}$ -radiolabeling via a macro and micro-droplet approach, in vitro anti-cancer and cell localization evaluation, and preliminary in vivo biodistribution studies with PET imaging.

## 2.2 Precursor preparation methods

### 2.2.1 Synthesis of silane precursors

The strategy for the synthesis of gemcitabine analogues bearing silicon fluoride acceptors attached to an exo-amino group of cytosine ring involve: (a) synthesis of gemcitabine analogues having terminal azido or alkyne group at an alkyl chain attached to 4-amino group, and (b) copper(I) catalyzed click reaction with the corresponding silane reagent having terminal alkyne or azido group. Thus, condensation of gemcitabine **1** with 11-azidoundecanoic acid under peptide coupling conditions [(N-dimethylaminopropyl)-N'-ethyl-carbodiimide (EDC)/1-hydroxybenzotriazole (HOBt)/ N,N-Diisopropylethylamine (DIPEA)] in DMF at 65°C afforded 4-N-(11-azidoundecanoyl)gemcitabine **2** (70%; Figure 2.1). The 11-azidoundecanoic acid **S4** was prepared by esterification of the commercially available 11-bromoundecanoic acid and subsequent azidation ( $\text{NaN}_3/\text{DMF}$ ) followed by saponification with the overall 81% yield. Condensation of **1** with 5-hexynoic acid under similar conditions gave 4-N-(hexynoyl)gemcitabine **3** but with lower yield contaminated with mono and/or di sugar 5-hexynoate esters. However, transient protection of **1** with trimethylsilyl group followed by condensation with 5-hexynoic acid in the presence of EDC provided **3** (63%).

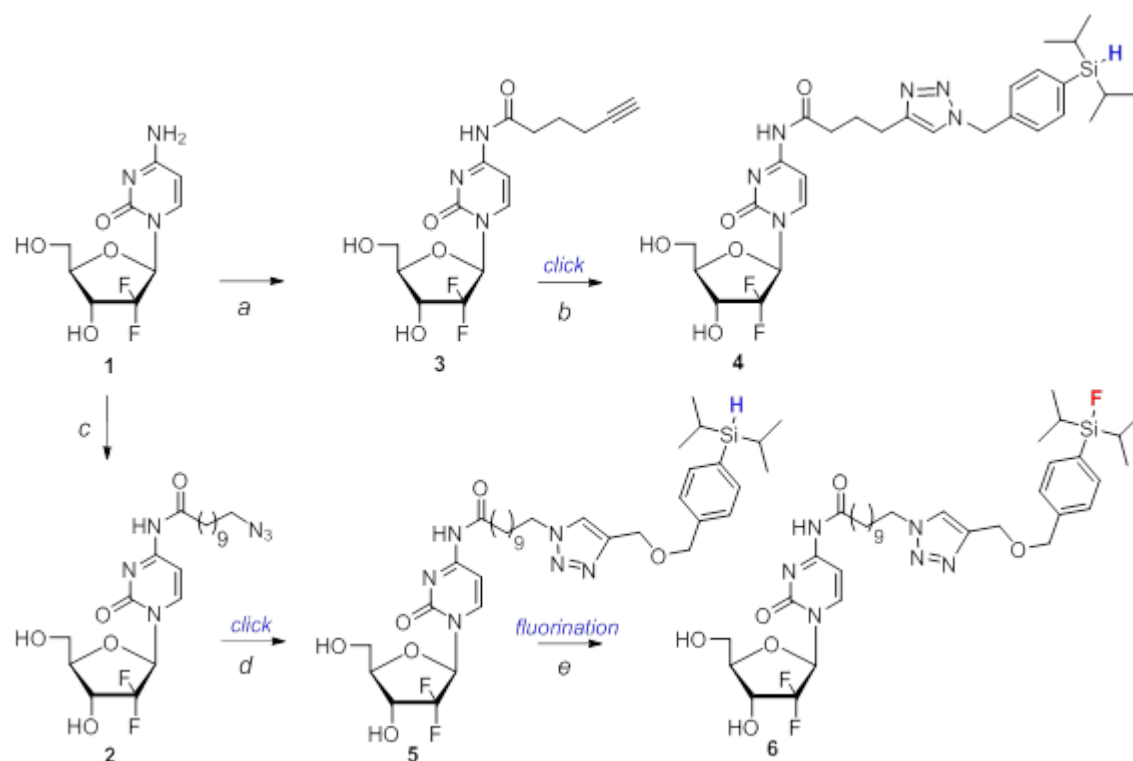


**Figure 2.1 Synthesis of 4-N-alkanoyl gemcitabine analogues with silicon-fluoride acceptors**

(a) (i) TMSCl/Pyr/CH<sub>3</sub>CN, 3 h, (ii) CH<sub>3</sub>≡C(CH<sub>2</sub>)<sub>3</sub>COOH/EDC/CH<sub>3</sub>CN/65°C; (iii) EtOH, 45°C, 5 h; (b) S4/HOBt/DIPEA/EDC/DMF/60°C/overnight; (c) S9 or S10/Sodium ascorbate/Cu<sub>2</sub>SO<sub>4</sub>/t-butanol/water (3:1), 6 h; (d) KF/18-crown-6/AcOH/CH<sub>3</sub>CN/80°C/25 min.

Copper-catalyzed click reaction of alkyne **3** with azido building block **S9** (4-(azidomethyl)phenyldiisopropylsilane) in the presence of sodium ascorbate and copper(I) sulfate gave silicon-fluoride acceptor **4** (92%). Alternatively azide **2** coupled with alkyne building block **S10** (diisopropyl(4-((prop-2-yn-1-yloxy)methyl)phenyl)silane) gave **5** (87%). The two bifunctional silicon building blocks **S9** and **S10** were prepared from 4-(diisopropylsilyl)benzylalcohol **S8**.

The synthesis of the 4-N-alkyl gemcitabine analogues with silicon-fluoride acceptor started from displacement of a 4-N-tosylamine group from **7** with freshly prepared 7-azidoheptylamine **S7**. Thus, reaction of transient protected with trimethylsilyl group **1** with TsCl in the presence of pyridine followed by deprotection with methanolic ammonia afforded protected 4-N-

tosylgemcitabine (142) **7** (90%, Figure 2.2). Treatment of **7** with 7-azidoheptylamine **S7** effected displacement of the *p*-toluenesulfonamido group from the C4 position of the cytosine ring to give 4-*N*-(7-azidoheptyl) gemcitabine **8** (82%). The 7-azidoheptylamine **S7** was prepared from 1,7-dibromoheptane by treatment with 2 eq. of NaN<sub>3</sub>, followed by selective Staudinger reduction of one of the azido group in intermediary 1,7-diazidoheptane **S6** with triphenylphosphine in 83% overall yield. Click reaction of azido **8** with alkyne building block **S10** gave silane **9** (90%).

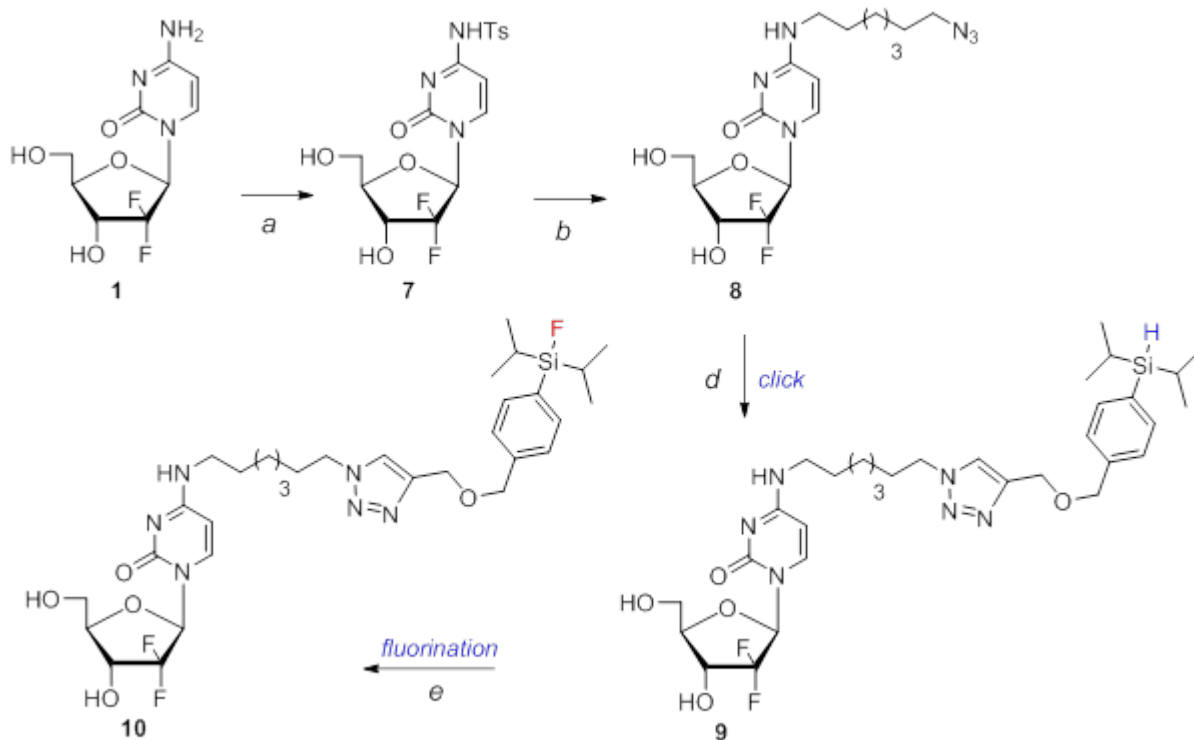


**Figure 2.2 Synthesis of 4-*N*-alkyl gemcitabine analogues with silicon-fluoride acceptors**

(a) (i) TMSCl/Pyr, (ii) TsCl, (iii) MeOH/NH<sub>3</sub>; (b) **S7**/TEA/1,4-dioxane; (c) **S10**/Sodium ascorbate/Cu<sub>2</sub>SO<sub>4</sub>/t-butanol/water (3:1)/6 h; (d) KF/18-crown-6/AcOH/CH<sub>3</sub>CN/80°C/25 min.

### 2.2.2 Fluorination

Treatment of silane precursors **5** or **9** with KF in the presence of 18-crown-6 in CH<sub>3</sub>CN at 80 °C for 20 min followed by quick cooling and filtration, followed by silica column chromatography (**5** → 10% MeOH/CHCl<sub>3</sub>) gave the respective fluorinated products **6** (63%, Scheme1), and **10** (62%, Figure 2.2). Also, fluorination of **4** afforded (fluoro)diisopropylsilyl)

product **11** (65%, see Experimental Part). Besides desired silyl fluorides **6**, **10** and **11** the corresponding silanols resulting from the hydrolysis from Si-OH were also isolated during purification on column (~20-25%). The structure of the silanols were confirmed by the absence of hydrogen from of Si-H bond (e.g., in **5** at 3.92 ppm) and lack of fluorine signal (e.g., in **6** at -188.86 ppm) by  $^1\text{H}$  or  $^{19}\text{F}$  NMR and additionally defined by HRMS.

### 2.2.3 Stability of Si-H substrate and Si-F products

Stability of 4-*N*-alkanoyl **5** and 4-*N*-alkyl **9** substrates as well as their fluorinated products **6** and **10** were examined employing RP-HPLC with isocratic mobile phase of CH<sub>3</sub>CN/water containing 0.1% of TFA which is compatible with the purification protocols for the [ $^{18}\text{F}$ ]-labeled products (*vide infra*). The 4-*N*-alkanoyl **5** were found to be prone to hydrolysis of the amide bond. For example gemcitabine (10-15%, 30 min) was detected after **5** was dissolved in 35% CH<sub>3</sub>CN/0.1% TFA (Figure 2.3). The RP-HPLC of the fluoro product **6** showed hydrolysis of the acyl chain to gemcitabine (15%, 30 min) and Si-F bond to the corresponding silanol (20%, 30 min). HPLC after 2 h showed larger amounts of silanol (30%) and gemcitabine (20%).



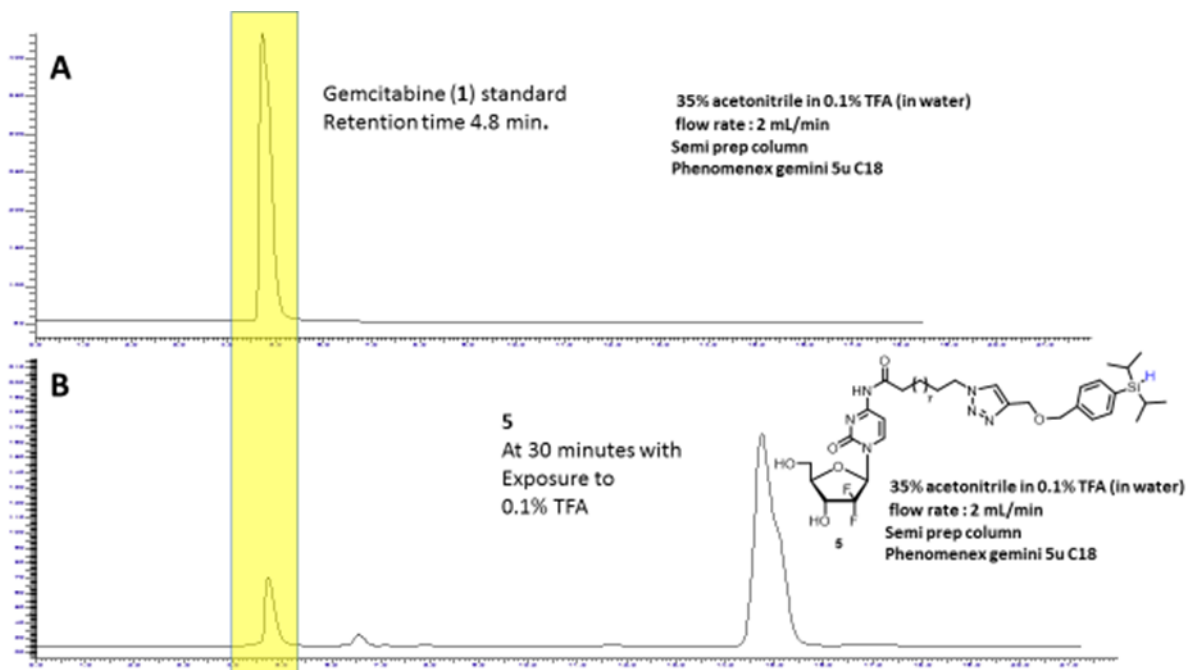


**Figure 2.3 Stability of 4-N-alkanoyl 5**

(chromatogram A: 1, chromatogram B: 5 after 30 min) in 35 %CH<sub>3</sub>CN / 0.1% TFA

On the other hand, the 4-*N*-alkyl substrate **9** was found to be stable with only very minor formation of byproduct peak(s) (e.g., gemcitabine) observed after long exposure (8 h) to 35% CH<sub>3</sub>CN/0.1% TFA. The fluorinated product **10** in the 25% CH<sub>3</sub>CN/0.1% TFA in water hydrolyzes to silanol (25%, 1 h, 55%, 3 h). However, hydrolysis of **10** in TFA-free system (25% CH<sub>3</sub>CN/water) occurred to a lesser extent (25%, 1 h, 30%, 3 h). These studies show that 4-*N*-alkyl analogues are more stable under acidic conditions than 4-*N*-acyl counterparts, indicating their advantage in developing them as PET imaging agents for gemcitabine prodrugs.

#### 2.2.4 Cytostatic Activity and Imaging

The anti-proliferation capabilities of the 4-*N*-alkanoyl (**2**, **3**, **5** and **6**) and 4-*N*-alkyl (**8** and **9**) gemcitabine analogues were assessed (72 h) in L1210 mouse lymphocytic leukemia cells (Table 2.1). All 4-*N*-alkanoyl analogues demonstrated potent antiproliferative activities with IC<sub>50</sub> = 8.0 μM, IC<sub>50</sub> = 7.5 μM, IC<sub>50</sub> = 65.3 μM and IC<sub>50</sub> = 40.0 μM, respectively. These IC<sub>50</sub> values are comparable to the reported IC<sub>50</sub> of gemcitabine (23.7 μM) for an identical incubation time (72

h)(162). However, 4-*N*-alkylgemcitabine derivatives **8** and **9** showed less antiproliferative activities having IC<sub>50</sub> >200 μM.

Compounds	IC <sub>50</sub> (μM)	IC <sub>75</sub> (μM)
<b>2</b>	8.0 ±0.4	14.9± 2.4
<b>3</b>	65.3±0.6	88.3±1.1
<b>5</b>	7.5±0.4	13.3±1.1
<b>6</b>	40.0±1.9	78.3±5.6
<b>8</b>	>200	>200
<b>9</b>	>200	>200

**Table 2.1 In vitro cytostatic activity of 4-*N*-modified gemcitabine analogues in L1210 lymphocytic leukemia cell line**

Additionally, we tested proliferation of human embryonic kidney HEK293 cells (48h) with 4-*N*-alkanoyl **2** and **5** and 4-*N*-alkyl analogues **8** and **9**. These analogues were found to have different levels of inhibition in a dose dependent manner and blocked cell proliferation [**2** (79±10%), **5** (42±5%), **8** (45±9%), **9** (50±9%) versus 38±4% for gemcitabine at 50 μM concentration; and **2** (89±15%), **5** (63±6%), **8** (61±11%), **9** (78±15%) versus 45±6% for gemcitabine at 100 μM concentration]. These results show *comparable* antiproliferative activities for 4-*N*-alkanoyl and 4-*N*-alkyl analogues. This might be due to the fact HEK293 cells have higher CDA activity than that reported for many other cells and organs (163,164); and that CDA expression/activity is known to affect anticancer therapy (165,166). Also, the low cytotoxicity of or high resistance to cytidine analogues such as gemcitabine have been associated with high levels of CDA expression in cancer cells (167,168). However, the fact that 4-*N*-alkyl cytidine analogues (including 4-*N*-alkyl analogues of gemcitabine) are not substrates of CDA (142,169) can contribute to their cytotoxicity in HEK293 cells since their metabolism to inactive uracil metabolites is either very slow or prohibited.

Even though 4-*N*-alkyl analogues **8** and **9** showed lower cytotoxic activities in the cells tested, we decided to further study cellular uptake of **8** with HEK293 cells since the lipophilic 4-

*N*-alkyl derivatives of gemcitabine show a stability toward fluorination protocols compatible with  $^{18}\text{F}$  fluorination. We were interested to study whether nucleoside **8** would be internalized and/or localized in the nucleus of cells and incorporated into DNA, or they are trapped in an extranuclear compartment.

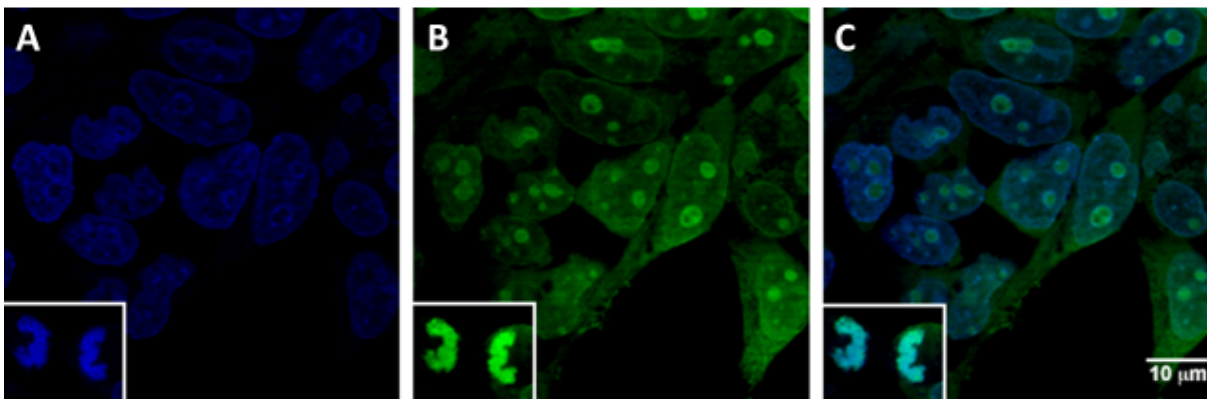


**Figure 2.4 Incorporation of **8** in HEK293 cells**

Incorporation assessed after 24 h, followed by fixation and addition of Fluor 488-Alkyne and copper (I): A) Nuclear staining with DAPI, B) Cell staining with Fluor 488-Alkyne. C) Merged A & B microscopy images. Inset: Staining of DNA during cell division. Scale bars: 10  $\mu\text{m}$ .

To determine whether 4-*N*-alkyl analogue **8** was localized inside cells, we carried out *in vitro* fluorescence studies with HEK293 cells. The cells were incubated with 100  $\mu\text{M}$  of **8** for 24 h, fixed and labeled with Fluor 488-alkyne in presence of copper (I). Fluor 488-labeled cells (Figure 2, B; seen in green) was evidence that 4-*N*-alkyl **8** was uptaken by the cells. Also, strong nuclear staining was evident by its co-localization with DAPI (Figure 2.4, A; seen in blue), as well as on the DNA during cell division. As expected, the omission of analogue **8** did not show any fluorescent green signal (data not shown).

## 2.3 Radiosynthesis of [ $^{18}\text{F}$ ]fluoro-silane probes

### 2.3.1 Macroscale radiosyntheses of 4-*N*-alkanoyl [ $^{18}\text{F}$ ]**6** and 4-*N*-alkyl [ $^{18}\text{F}$ ]**10**

The one-pot syntheses of 4-*N*-alkanoyl [ $^{18}\text{F}$ ]**6** and 4-*N*-alkyl [ $^{18}\text{F}$ ]**10** were performed on the ELIXYS FLEX/CHEM radiosynthesizer employing silane-labeling protocols.<sup>41</sup> Thus, by

adding silane precursor **9** in DMSO with 1% v/v AcOH to the previously dried [ $^{18}\text{F}$ ]KF/K<sub>222</sub> complex and reacting at 100°C for 25 min, followed by HPLC purification, 4-*N*-alkyl [ $^{18}\text{F}$ ]**10** was produced with  $6.6 \pm 3.2$  % ( $n = 5$ ) decay-corrected isolated radiochemical yield and >99% radiochemical purity (Figure 2.5, Table 2.2, **Error! Reference source not found.**). Analogously, the  $^{18}\text{F}$ -fluorination of precursor **5** gave 4-*N*-alkanoyl [ $^{18}\text{F}$ ]**6** in ~0.5% ( $n = 1$ ) decay-corrected crude radiochemical yield. Optimization of the protocol for the synthesis of [ $^{18}\text{F}$ ]**6** was not performed.

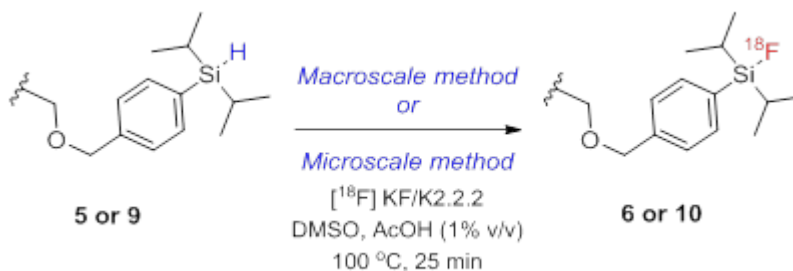


**Figure 2.5 Radiosynthesis of [ $^{18}\text{F}$ ] 4-*N*-alkanoyl and alkyl gemcitabine analogues with silicon-fluoride acceptors**

Entry	Analogue	Macroscale radiosynthesis <sup>a</sup>	Microscale radiosynthesis <sup>b</sup>
		Average decay-corrected isolated RCY (%)	Decay-corrected crude RCY (%)
<b>1</b>	<b>6</b>	0.5	10
<b>2</b>	<b>10</b>	6.6 ± 3.2 (n=5)	24.4 ± 4.1 (n=5)

**Table 2.2** <sup>18</sup>F radiosynthetic yields of 4-N-modified gemcitabine analogues **6** and **10**

<sup>a</sup> 2-3 mg scale reactions; <sup>b</sup> 0.2 mg scale reactions.

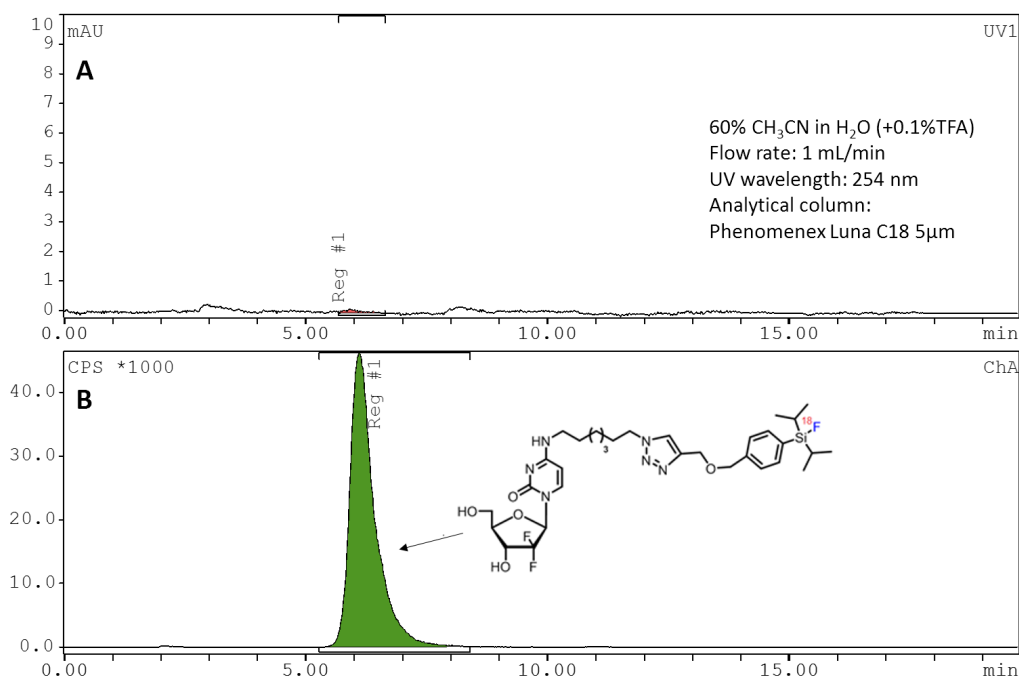


**Figure 2.6** Analytical HPLC chromatogram of purified 4-N-alkyl [<sup>18</sup>F]**10**

The chromatogram is shown for the product produced at macroscale. A: UV detector, chromatogram B: gamma detector.

### 2.3.2 Microscale radiosyntheses of 4-N-alkanoyl [<sup>18</sup>F]**6** and 4-N-alkyl [<sup>18</sup>F]**10**

The [<sup>18</sup>F] labeled **6** and **10** were synthesized more efficiently using microscale approach on simple microfluidic chips (104,120). By adding silane precursor **5** or **9** in DMSO with 1% v/v AcOH to the previously dried [<sup>18</sup>F]KF/K<sub>222</sub> residue on one chip, covering with a second chip, and

heating at 100°C for 20 min, a decay-corrected crude radiochemical yield (i.e. without purification) for 4-*N*-alkanoyl [<sup>18</sup>F]**6** was 10% (n = 1) and for 4-*N*-alkyl [<sup>18</sup>F]**10** was 24.4 ± 4.1 (n = 5). Additionally, 4-*N*-alkyl [<sup>18</sup>F]**10** is radiochemically stable at ambient temperature for over 4 hours after formulation in saline with 10% v/v EtOH, with no significant radiolysis or other degradation observed.

### 2.3.3 *In vivo* imaging of [<sup>18</sup>F]4-*N*-Alkyl Gemcitabine radioligand **10**

To determine the distribution and uptake of [<sup>18</sup>F]**10**, preliminary *in vivo*, static and dynamic PET imaging studies were performed in wild-type mice. For static PET imaging, a WT C57BL/6 mouse was injected with [<sup>18</sup>F]**10** via tail vein and imaged for 10 min after 1 h uptake. For dynamic PET imaging, a 1 h PET acquisition was started concurrently at the beginning of a 10 sec infusion via a tail vein catheter of [<sup>18</sup>F]**10** and histogrammed into a series of images. Both static and dynamic PET imaging show the tracer first in the liver, kidneys, and GI tract (also the gallbladder in the static scan), but significant bone signal is evident after 15-20 min post-injection (Figure 2.7 Dynamic PET study results for [<sup>18</sup>F]**10**

(Left) Dynamic biodistribution of [<sup>18</sup>F]**10** in WT C57BL/6 mouse. (Right) Maximum intensity projection at 1 h post-injection (left: coronal; right: sagittal). and Figure 2.8). One cause of bone signal is *in vivo* defluorination of the PET tracer, releasing [<sup>18</sup>F]fluoride, which is strongly incorporated into hydroxyapatite crystals of bone. More detailed analysis of tracer metabolites *in vivo* is needed to determine whether defluorination is occurring or whether bone signal is actually uptake in bone marrow.

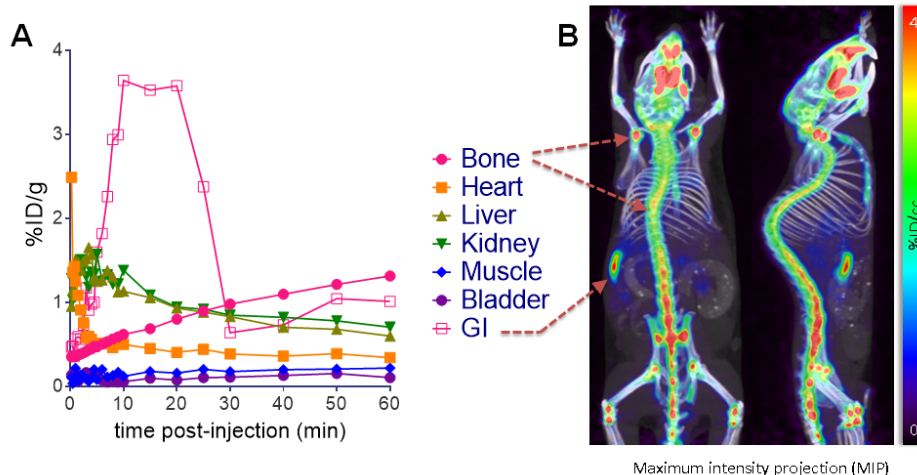


**Figure 2.7 Dynamic PET study results for  $[^{18}\text{F}]10$**

(Left) Dynamic biodistribution of  $[^{18}\text{F}]10$  in WT C57BL/6 mouse. (Right) Maximum intensity projection at 1 h post-injection (left: coronal; right: sagittal).

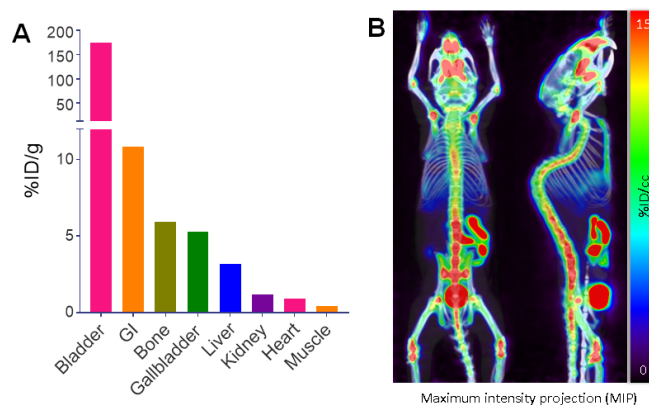


**Figure 2.8 10 min static PET study results for  $[^{18}\text{F}]10$**

(Left) Biodistribution of  $[^{18}\text{F}]10$  from 10 min static scan in WT C57BL/6 mouse at 1 h post-injection. (Right) Maximum intensity projection of 10 min static scan at 1 h post-injection (left: coronal; right: sagittal).

It appears that  $[^{18}\text{F}]4\text{-N-alkyl}$  gemcitabine radioligand **10** undergoes renal (high kidney, bladder) and possibly hepatobiliary (high gut and liver) clearances, with possible defluorination. It is noteworthy that biodistribution of the 4-N-alkyl radioligand does not reflect biodistribution of  $[^{14}\text{C}]$ gemcitabine (127).

## 2.4 Experimental section

The  $^1\text{H}$  (400 MHz),  $^{13}\text{C}$  (100 MHz), or  $^{19}\text{F}$  (376 MHz) NMR spectra were recorded at ambient temperature in solutions of  $\text{CDCl}_3$  or  $\text{MeOH-}d_4$  as noted. The reactions were followed by TLC with Merck Kieselgel 60-F<sub>254</sub> sheets and products were detected with a 254 nm light or with Hanessian's stain. Column chromatography was performed using Merck Kieselgel 60 (230-400 mesh). Reagent grade chemicals were used and solvents were dried by reflux distillation over  $\text{CaH}_2$  under nitrogen gas, unless otherwise specified, and reactions carried out under  $\text{N}_2$  atmosphere. The carboxylic acid and amine derivatives used for the coupling with gemcitabine were commercially available or synthesized such as 11-azidoundecanoic acid (**S4**) and 7-Azido-1-aminoheptane (**S7**). The purity of some of the synthesized compounds was determined by HPLC on Phenomenex Gemini RP-C18 with isocratic at various mobile phases ( $\text{CH}_3\text{CN}/\text{H}_2\text{O}$ ) and flow rates.

*4-N-(11-Azidoundecanoyl)-2'-deoxy-2',2'-difluorocytidine (2)*. *N,N*-Diisopropylethylamine (35  $\mu\text{L}$ , 26 mg, 0.2 mmol), 1-hydroxybenzotriazole (27 mg, 0.2 mmol), **S3** (46 mg, 0.2 mmol), and 1-ethyl-3-(3-dimethylaminopropyl)carbodiimide (45  $\mu\text{L}$ , 31 mg, 0.2 mmol) were sequentially added to a stirred solution of gemcitabine hydrochloride (**1**; 50 mg, 0.17 mmol) in DMF (4 mL) at ambient temperature under  $\text{N}_2$  atmosphere. The reaction mixture was then gradually heated to 65 °C (oil-bath) and was kept stirring overnight. The crude mixture was evaporated and the residue column chromatographed (0  $\rightarrow$  10%  $\text{MeOH}/\text{CHCl}_3$ ) to give **2** (56 mg, 70%): UV ( $\text{CH}_3\text{OH}$ )  $\lambda$  max 299 nm ( $\epsilon$  6500),  $\lambda$  min 250 nm ( $\epsilon$  12 900);  $^1\text{H}$  NMR ( $\text{CD}_3\text{OD}$ )  $\delta$  1.24–1.47 (m, 12H, 6  $\times$   $\text{CH}_2$ ), 1.51–1.75 (m, 4H, 2  $\times$   $\text{CH}_2$ ), 2.45 (t,  $J$  = 7.4 Hz, 2H,  $\text{CH}_2$ ), 3.27 (t,  $J$  = 6.9 Hz, 2H,  $\text{CH}_2$ ), 3.81 (dd,  $J$  = 2.8, 12.4 Hz, 1H,  $\text{H5}'$ ), 3.89–4.05 (m, 2H,  $\text{H5}''$ ,  $\text{H4}'$ ), 4.30 (td,  $J$  = 8.5, 12.2 Hz, 1H,  $\text{H3}'$ ), 6.17–6.35 (m, 1H,  $\text{H1}'$ ), 7.50 (d,  $J$  = 7.6 Hz, 1H,  $\text{H5}$ ), 8.34 (d,  $J$  = 7.6 Hz, 1H,  $\text{H6}$ );  $^{13}\text{C}$  NMR  $\delta$  25.92, 27.80, 29.90, 30.11, 30.20, 30.33, 30.41, 30.50, 38.17, 52.47, 60.30 ( $\text{C5}'$ ), 70.27 (dd,  $J$  = 22.2, 23.6 Hz,  $\text{C3}'$ ), 82.92 (d,  $J$  = 8.6 Hz,  $\text{C4}'$ ), 86.42 (dd,  $J$  = 26.6, 37.6 Hz,  $\text{C1}$ ),



98.25 (C5), 120.87 (t,  $J = 259.9$  Hz, C2'), 145.96 (C6), 157.68 (C2), 164.83 (C4), 176.00 (CO);  $^{19}\text{F}$  NMR  $\delta$  -120.05 (d of m,  $J = 239.7$  Hz, 1F), -119.10 (d of m,  $J = 240.1$  Hz, 1F). HRMS (ESI+)  $m/z$  calcd for  $\text{C}_{20}\text{H}_{30}\text{F}_2\text{N}_6\text{NaO}_5$   $[\text{M}+\text{Na}]^+$  495.2146; found 495.2141.

*4-N-(5-Hexynoyl)-2'-deoxy-2',2'-difluorocytidine (3)*. Trimethylsilyl chloride (250  $\mu\text{L}$ , 2 mmol) was added to a solution of **1** (200 mg, 0.7 mmol) in ACN (2 mL) and pyridine (3 mL) at 0  $^\circ\text{C}$ . The mixture was stirred for 4 h from 0  $^\circ\text{C}$  to room temperature. A solution of commercially available 5-hexynoic acid (230  $\mu\text{L}$ , 2.1 mmol) in ACN (2 mL), previously activated by EDC (50  $\mu\text{L}$ , 1 mmol), was added to the reaction mixture, which was heated at 60 $^\circ\text{C}$  for 18 hours. After the solution was cooled down to room temperature, ethanol (5 mL) was added and the mixture was heated at 45  $^\circ\text{C}$  for 4 h. After evaporation under vacuum, the resulting residue was column chromatographed (80  $\rightarrow$  100% EtOAc/hexane) to give **3** (**170**) (157.6 mg, 63%):  $^1\text{H}$  NMR ( $\text{CD}_3\text{OD}$ )  $\delta$  1.84–1.86 (m, 2H,  $\text{CH}_2$ ), 2.26–2.28 (m, 3H,  $\text{CH}_2$ , CH), 2.60 (t,  $J = 7.3$  Hz, 2H,  $\text{CH}_2$ ), 3.82–3.84 (m, 1H,  $\text{H}5'$ ), 3.89–4.07 (m, 2H,  $\text{H}5''$ ,  $\text{H}4'$ ), 4.31 (dd,  $J = 12.1, 20.6$  Hz, 1H,  $\text{H}3'$ ), 6.24–6.26 (m, 1H,  $\text{H}1'$ ), 7.49 (d,  $J = 7.6$  Hz, 1H,  $\text{H}5$ ), 8.34 (d,  $J = 7.6$  Hz, 1H,  $\text{H}6$ );  $^{13}\text{C}$  NMR  $\delta$  18.42, 24.96, 33.47, 60.50 (C5'), 68.14 (CH), 70.20 (C) 70.34 (t,  $J = 23.1$  Hz, C3'), 82.35 (d,  $J = 8.6$  Hz, C4'), 86.1 (dd,  $J = 26.6, 38.3$  Hz, C1'), 96.30 (C5'), 123.91 (t,  $J = 259.3$  Hz, C2'), 142.51 (C6), 157.78 (C2), 167.74 (C4), 175.97 (CO);  $^{19}\text{F}$  NMR  $\delta$  -120.14 (d of m,  $J = 244.4$  Hz, 1F), -119.23 (d of m,  $J = 243.6$  Hz, 1F).

*4-N-(7-Azidoheptanyl)-2'-deoxy-2',2'-difluorocytidine (8)*. Freshly prepared 7-Azido-1-aminoheptane (**S7**; 112.5 mg, 0.72 mmol) was added to a suspension of **7** (100 mg, 0.24 mmol) in 1,4-dioxane (5 mL) and TEA (0.100 mL, 63 mg, 0.72 mmol) and the mixture was left stirring at 65 $^\circ\text{C}$ . After 24 h, volatiles were evaporated and the resulting residue was column chromatographed (5% MeOH/ $\text{CHCl}_3$ ) to give **8** (**238**) (238 mg, 82%): UV ( $\text{CH}_3\text{OH}$ )  $\lambda$  max 267 nm ( $\epsilon$  8200),  $\lambda$  min 227 nm ( $\epsilon$  7400);  $^1\text{H}$  NMR ( $\text{CD}_3\text{OD}$ )  $\delta$  1.31–1.41 (m, 12H,  $6 \times \text{CH}_2$ ), 1.51–1.70 (m, 4H,  $2 \times \text{CH}_2$ ), 3.25 (t,  $J = 6.9$  Hz, 2H,  $\text{CH}_2$ ), 3.45 (t,  $J = 7.0$  Hz, 2H,  $\text{CH}_2$ ) 3.77–3.83 (m, 1H,  $\text{H}5'$ ), 3.91–3.99 (m, 2H,  $\text{H}5''$ ,  $\text{H}4'$ ), 4.25 (dt,  $J = 10.5, 20.8$  Hz, 1H,  $\text{H}3'$ ), 5.85 (d,  $J = 7.6$  Hz, 1H,  $\text{H}5$ ),

6.23–6.25 (m, 1H, H1'), 7.71 (d,  $J = 7.6$  Hz, 1H, H6);  $^{13}\text{C}$  NMR  $\delta$  27.75, 27.86, 29.84, 29.88, 29.92, 41.65, 52.45, 60.56 (C5'), 70.66 (t,  $J = 23.1$  Hz, C3'), 82.22 (d,  $J = 8.6$  Hz, C4'), 86.26 (dd,  $J = 26.6, 38.3$  Hz, C1'), 97.32 (C5), 124.02 (t,  $J = 259.2$  Hz, C2'), 140.80 (C6), 158.29 (C2), 165.38 (C4);  $^{19}\text{F}$  NMR  $\delta$  -119.86 (d of m,  $J = 246.2$  Hz, 1F), -119.89 (d of m,  $J = 240.2$  Hz, 1F). HRMS (ESI+)  $m/z$  calcd for  $\text{C}_{16}\text{H}_{25}\text{F}_2\text{N}_6\text{O}_4$  [M+H] $^+$  403.1902; found 403.1913.

#### 2.4.1 General procedure for click reactions

Sodium ascorbate (0.02 mmol), copper sulfate (0.02 mmol), nucleoside (0.1 mmol) and silicon-fluoride acceptor (0.1 mmol) were suspended in a mixture of *tert*-butanol/water (3:1 (v/v), 3 mL). The reaction mixture was left at room temperature for 1-6 hours. The reaction mixture was extracted with  $\text{CHCl}_3$  (10 mL). The organic layer was washed with sat  $\text{NH}_4\text{Cl}$  (10 mL), brine (10 mL), dried over  $\text{Na}_2\text{SO}_4$ , filtered and evaporated under reduced pressure. The crude product was purified by chromatography ( $\text{CHCl}_3/\text{MeOH}$  95:5) to afford the desired triazole adducts:

*4-N-[4-(1-(4-(diisopropylsilyl)benzyl)-1H-1,2,3-triazol-4-yl)butanoyl]-2'-deoxy-2',2'difluorocytidine (4)* Treatment of **3** (35 mg, 0.1 mmol) with **S9** (24.7 mg, 0.1 mmol) using procedure reported in general procedure gave **4** (52.6 mg, 87%). UV ( $\text{CH}_3\text{OH}$ )  $\lambda$  max 299 nm ( $\epsilon$  6700), 248 nm ( $\epsilon$  13000);  $^1\text{H}$  NMR ( $\text{CD}_3\text{OD}$ )  $\delta$  0.96 (d,  $J = 7.3$  Hz, 6H, *i*Pr), 1.03 (d,  $J = 7.3$  Hz, 6H, *i*Pr), 1.18–1.20 (m, 4H, 2  $\times$   $\text{CH}_2$ ), 2.46 (t,  $J = 7.3$  Hz, 2H,  $\text{CH}_2$ ), 2.71 (t,  $J = 7.4$  Hz, 2H,  $\text{CH}_2$ ), 3.74–3.76 (m, 1H, H5'), 3.89–3.95 (m, 3H, H5'', H4', Si-H), 4.24–4.26 (m, 1H, H3'), 5.50 (s, 2H,  $\text{CH}_2$ ), 6.19 (t,  $J = 7.5$  Hz, 1H, H1'), 7.28 (d,  $J = 8.0$  Hz, 2H, Ar), 7.35 (d,  $J = 7.6$  Hz, 1H, H5), 7.51 (d,  $J = 8.0$  Hz, 2H, Ar), 7.56 (s, 1H), 8.10 (d,  $J = 7.6$  Hz, 1H, H6);  $^{13}\text{C}$  NMR  $\delta$  11.18, 18.65, 18.83, 24.96, 25.17, 37.04, 54.09, 59.93 (C5'), 69.68 (CH), 70.34 (t,  $J = 23.1$  Hz, C3'), 81.82 (d,  $J = 8.6$  Hz, C4'), 85.70 (dd,  $J = 26.6, 38.3$  Hz, C1'), 97.03 (C5'), 122.39 (t,  $J = 259.3$  Hz, C2'), 128.07, 134.96, 136.86, 138.11, 145.43 (C6), 148.04, 155.77 (C2), 163.85 (C4), 174.28 (CO);  $^{19}\text{F}$  NMR  $\delta$  -120.10 (d of m,  $J = 233.4$  Hz, 1F), -119.20 (d of m,  $J = 240.9$  Hz, 1F). HRMS (ESI+)  $m/z$  calcd for  $\text{C}_{28}\text{H}_{38}\text{F}_2\text{N}_6\text{NaO}_5\text{Si}$  [M+Na] $^+$  627.2538; found 627.2522.

*4-N-[11-(4-((4-(diisopropylsilyl)benzyloxy)methyl)-1H-1,2,3-triazol-1-yl)undecanoyl]-2'-deoxy-2',2'-difluorocytidine (5)*. Treatment of **2** (30 mg, 0.06 mmol) with **S10** (15.6 mg, 0.06 mmol) using procedure reported in general procedure gave **5** (40.5 mg, 92%). UV (CH<sub>3</sub>OH)  $\lambda$  max 299 nm ( $\epsilon$  6500), 250 nm ( $\epsilon$  12900),  $\lambda$  min 278 nm ( $\epsilon$  3800); <sup>1</sup>H NMR (CD<sub>3</sub>OD)  $\delta$  0.96 (d,  $J$  = 7.3 Hz, 6H, *i*Pr), 1.05 (d,  $J$  = 7.3 Hz, 6H, *i*Pr), 1.24–1.47 (m, 12H, 6  $\times$  CH<sub>2</sub>), 1.51–1.75 (m, 4H, 2  $\times$  CH<sub>2</sub>), 2.38 (t,  $J$  = 7.3 Hz, 2H, CH<sub>2</sub>), 3.81 (dd,  $J$  = 2.8, 12.4 Hz, 1H, H5'), 3.89–3.96 (m, 3H, H5'', H4', Si-H), 4.30 (td,  $J$  = 8.5, 12.2 Hz, 1H, H3'), 4.33 (t,  $J$  = 7.1 Hz, 2H), 4.55 (s, 2H, CH<sub>2</sub>), 4.61 (s, 2H, CH<sub>2</sub>), 6.19 (t,  $J$  = 7.5 Hz, 1H, H1'), 7.33–7.35 (m, 3H, H5, Ar), 7.51 (d,  $J$  = 8.0 Hz, 2H, Ar), 7.74 (s, 1H), 8.10 (d,  $J$  = 7.6 Hz, 1H, H6); <sup>13</sup>C NMR  $\delta$  25.92, 27.80, 29.90, 30.11, 30.20, 30.33, 30.41, 30.50, 38.17, 52.47, 60.30 (C5'), 70.27 (dd,  $J$  = 22.2, 23.6 Hz, C3'), 82.92 (d,  $J$  = 8.6 Hz, C4'), 86.42 (dd,  $J$  = 26.6, 37.6 Hz, C1), 98.25 (C5), 120.87 (t,  $J$  = 259.9 Hz, C2'), 145.96 (C6), 157.68 (C2), 164.83 (C4), 176.00 (CO); <sup>19</sup>F NMR  $\delta$  -120.09 (d of m,  $J$  = 239.2 Hz, 1F), -119.13 (d of m,  $J$  = 240.2 Hz, 1F). HRMS (ESI+)  $m/z$  calcd for C<sub>36</sub>H<sub>54</sub>F<sub>2</sub>N<sub>6</sub>NaO<sub>6</sub>Si [M+Na]<sup>+</sup> 755.3738; found 755.3731.

*4-N-[7-(4-((4-(diisopropylsilyl)benzyloxy)methyl)-1H-1,2,3-triazol-1-yl)heptanyl]-2'-deoxy-2',2'-difluorocytidine (9)* Treatment of **8** (40 mg, 0.1 mmol) with **S10** (26.0 mg, 0.1mmol) using procedure reported in general procedure gave **9** (59.6 mg, 90%). UV (CH<sub>3</sub>OH)  $\lambda$  max 267 nm ( $\epsilon$  8200),  $\lambda$  min 228 nm ( $\epsilon$  7500); <sup>1</sup>H NMR (CD<sub>3</sub>OD)  $\delta$  0.99 (d,  $J$  = 7.3 Hz, 6H, *i*Pr), 1.05 (d,  $J$  = 7.3 Hz, 6H, *i*Pr), 1.31–1.41 (m, 12H, 6  $\times$  CH<sub>2</sub>), 1.50–1.52 (m, 2H, CH<sub>2</sub>), 1.90–1.93 (m, 2H, CH<sub>2</sub>), 3.41–3.43 (m, 2H, CH<sub>2</sub>), 3.80–3.82 (m, 1H, H5'), 3.91–4.02 (m, 3H, H5'', H4', Si-H), 4.42–4.44 (m, 3H, H3', CH<sub>2</sub>), 4.60 (s, 2H, CH<sub>2</sub>), 4.65 (s, 2H, CH<sub>2</sub>), 5.82 (d,  $J$  = 7.6 Hz, 1H, H5), 6.23–6.25 (m, 1H, H1') , 7.38 (d,  $J$  = 8.0 Hz, 2H, Ar), 7.48 (d,  $J$  = 8.0 Hz, 2H, Ar), 7.71 (d,  $J$  = 7.6 Hz, 1H, H6), 7.99 (s, 1H, CH); <sup>13</sup>C NMR  $\delta$  11.26, 18.76, 18.96, 27.01, 27.34, 30.93, 40.97, 50.50, 60.31 (C5'), 64.42, 70.26 (t,  $J$  = 23.1 Hz, C3'), 72.37, 81.75 (d,  $J$  = 8.6 Hz, C4'), 84.92 (dd,  $J$  = 26.6, 38.3 Hz, C1'), 95.97 (C5'), 124.04 (t,  $J$  = 259.3 Hz, C2'), 127.88, 133.36, 140.78, 135.56, 136.34, 138.84, 140.78 (C6), 141.02, 155.92 (C2), 164.77 (C4); <sup>19</sup>F NMR  $\delta$  -119.86 (d of m,  $J$  =

246.2 Hz, 1F), -119.89 (d of m,  $J = 240.2$  Hz, 1F). HRMS (ESI+)  $m/z$  calcd for  $C_{32}H_{48}F_2N_6NaO_5Si$   $[M+Na]^+$  685.3322; found 685.3324.

#### 2.4.2 General Procedure for Fluorination Reactions

Solid KF (4.7 mg, 0.08 mmol, 4 eq.) was added to a stirred solution of **5** (15 mg, 0.02 mmol,) and 18-Crown-6 ether (21 mg, 0.08 mmol, 4 eq.) in  $CH_3CN$  (3 mL) in a round bottom flask under  $N_2$  atmosphere. To this mixture acetic acid (2  $\mu$ L, 0.02 mmol, 1 eq.) was then added and the resulting reaction mixture was stirred at 80 °C for 25 min. The reaction mixture was then left to cool (~5 min.) and filtered to remove the left over 18-crown ether and KF. The filtrate was washed with  $CH_3CN$  (2 mL) and the combined mother liquors were then concentrated under reduced pressure to give crude **6**. The resulting residue was chromatographed (MeOH/ $CHCl_3$  10:90) to give pure **9** (9.5 mg, 63%).

*4-N-[11-(4-((4-(Fluorodiisopropylsilyl)benzyloxy)methyl)-1H-1,2,3-triazol-1-yl)undecanoyl]-2'-deoxy-2',2'-difluorocytidine (6)*. Treatment of **5** (15 mg, 0.02 mmol) using procedure reported in in general procedure gave **6** (9.5 mg, 63%). UV ( $CH_3OH$ )  $\lambda$  max 299 nm ( $\epsilon$  6500), 250 nm ( $\epsilon$  12900),  $\lambda$  min 278 nm ( $\epsilon$  3800);  $^1H$  NMR ( $CD_3OD$ )  $\delta$  0.99 (d,  $J = 7.3$  Hz, 6H, *i*Pr), 1.07 (d,  $J = 7.3$  Hz, 6H, *i*Pr), 1.24–1.47 (m, 12H, 6  $\times$   $CH_2$ ), 1.78–1.80 (m, 2H,  $CH_2$ ), 1.90–1.92 (m, 2H,  $CH_2$ ), 2.44 (t,  $J = 7.4$  Hz, 2H,  $CH_2$ ), 3.81 (dd,  $J = 2.8, 12.4$  Hz, 1H, H5'), 3.89–3.99 (m, 2H, H5'', H4'), 4.29 (t,  $J = 10.4$  Hz, 1H, H3'), 4.40 (t,  $J = 7.0$  Hz, 2H), 4.60 (s, 2H,  $CH_2$ ), 4.66 (s, 2H,  $CH_2$ ), 6.26 (t,  $J = 7.5$  Hz, 1H, H1'), 7.41 (d,  $J = 7.8$  Hz, 2H, Ar), 7.49 (d,  $J = 7.6$  Hz, H5), 7.54 (d,  $J = 8.1$  Hz, 2H, Ar), 7.99 (s, 1H), 8.34 (d,  $J = 7.6$  Hz, 1H, H6);  $^{13}C$  NMR  $\delta$  13.22, 25.92, 27.80, 29.90, 30.11, 30.20, 30.33, 30.41, 30.50, 38.17, 52.47, 60.30 (C5'), 70.27 (dd,  $J = 22.2, 23.6$  Hz, C3'), 82.92 (d,  $J = 8.6$  Hz, C4'), 86.42 (dd,  $J = 26.6, 37.6$  Hz, C1), 98.25 (C5), 120.87 (t,  $J = 259.9$  Hz, C2'), 128.07, 135.53, 135.56, 136.34, 138.84, 145.93 (C6), 148.76, 145.93 (C6), 157.66 (C2), 164.78 (C4), 175.25 (CO);  $^{19}F$  NMR  $\delta$  - 188.86 (s, 1F), -120.09 (d of m,  $J =$

239.2 Hz, 1F), -119.13 (d of m,  $J = 240.2$  Hz, 1F). HRMS (ESI+)  $m/z$  calcd for  $C_{36}H_{54}F_3N_6O_6Si$   $[M+H]^+$  751.3753; found 751.3770.

*4-N-[7-(4-((4-(fluorodiisopropylsilyl)benzyloxy)methyl)-1H-1,2,3-triazol-1-yl)heptanyl]-2'-deoxy-2',2'-difluorocytidine (10)*. Treatment of **9** (15 mg, 0.023 mmol) using procedure reported in general procedure gave **10** (9 mg, 62 %). UV (CH<sub>3</sub>OH)  $\lambda$  max 267 nm ( $\epsilon$  8200),  $\lambda$  min 228 nm ( $\epsilon$  7500); <sup>1</sup>H NMR (CD<sub>3</sub>OD)  $\delta$  0.99 (d,  $J = 7.3$  Hz, 6H, *i*Pr), 1.05 (d,  $J = 7.3$  Hz, 6H, *i*Pr), 1.31–1.41 (m, 12H, 6  $\times$  CH<sub>2</sub>), 1.50–1.52 (m, 2H, CH<sub>2</sub>), 1.90–1.92 (m, 2H, CH<sub>2</sub>), 3.38–3.40 (m, 2H, CH<sub>2</sub>), 3.80–3.82 (m, 1H, H5'), 3.91–4.02 (m, 3H, H5'', H4', Si-H), 4.24–4.26 (m, 1H, H3'), 4.41 (t,  $J = 6.9$  Hz, 2H, CH<sub>2</sub>), 4.60 (s, 2H, CH<sub>2</sub>), 4.65 (s, 2H, CH<sub>2</sub>), 5.82 (d,  $J = 7.6$  Hz, 1H, H5), 6.21–6.23 (m, 1H, H1'), 7.41 (d,  $J = 8.0$  Hz, 2H, Ar), 7.52 (d,  $J = 8.0$  Hz, 2H, Ar), 7.71 (d,  $J = 7.6$  Hz, 1H, H6), 8.01 (s, 1H, CH); <sup>13</sup>C NMR  $\delta$  11.26, 18.76, 18.96, 27.01, 27.34, 30.93, 40.97, 50.50, 60.31 (C5'), 64.42, 70.26 (t,  $J = 23.1$  Hz, C3'), 72.37, 81.75 (d,  $J = 8.6$  Hz, C4'), 84.92 (dd,  $J = 26.6, 38.3$  Hz, C1'), 95.97 (C5'), 124.04 (t,  $J = 259.3$  Hz, C2'), 127.88, 133.36, 140.78, 135.56, 136.34, 138.84, 140.78 (C6), 141.02, 155.92 (C2), 164.77 (C4). <sup>19</sup>F NMR  $\delta$  - 188.82 (s, 1F), -119.75 (d of m,  $J = 244.1$  Hz, 1F), -119.98 (d of m,  $J = 239.1$  Hz, 1F). HRMS (ESI+)  $m/z$  calcd for  $C_{32}H_{47}F_3N_6NaO_5Si$   $[M+Na]^+$  703.3227; found 703.3234.

*4-N-[4-(1-(4-(fluorodiisopropylsilyl)benzyl)-1H-1,2,3-triazol-4-yl)butanoyl]-2'-deoxy-2',2'-difluorocytidine (11)*. Treatment of **4** (15 mg, 0.025 mmol) using procedure reported in general procedure gave **11** (10 mg, 65%). UV (CH<sub>3</sub>OH)  $\lambda$  max 299 nm ( $\epsilon$  6700), 248 nm ( $\epsilon$  13000); <sup>1</sup>H NMR (CD<sub>3</sub>OD)  $\delta$  0.99 (d,  $J = 7.3$  Hz, 6H, *i*Pr), 1.06 (d,  $J = 7.3$  Hz, 6H, *i*Pr), 1.18–1.20 (m, 2H, CH<sub>2</sub>), 1.91–1.93 (m, 2H, CH<sub>2</sub>), 2.50 (t,  $J = 7.3$  Hz, 2H, CH<sub>2</sub>), 2.78 (t,  $J = 7.4$  Hz, 2H, CH<sub>2</sub>), 3.82–3.84 (m, 1H, H5'), 3.93–4.05 (m, 2H, H5'', H4'), 4.29–4.31 (m, 1H, H3'), 5.59 (s, 2H, CH<sub>2</sub>), 6.21 (t,  $J = 7.5$  Hz, 1H, H1'), 7.35 (d,  $J = 7.9$  Hz, 2H, Ar), 7.47 (d,  $J = 7.6$  Hz, 1H, H5), 7.57 (d,  $J = 8.1$  Hz, 2H, Ar), 7.81 (s, 1H), 8.33 (d,  $J = 7.6$  Hz, 1H, H6); <sup>13</sup>C NMR  $\delta$  13.22, 13.35, 16.82, 17.01, 25.46, 25.53, 37.18, 54.70, 60.30 (C5'), 70.01 (CH), 70.34 (t,  $J = 23.1$  Hz, C3'), 81.72 (d,  $J = 8.6$  Hz, C4'), 82.92 (dd,  $J = 26.6, 38.3$  Hz, C1'), 98.27 (C5'), 123.93 (t,  $J = 259.3$

Hz, C2'), 128.39, 134.45, 135.53, 135.56, 136.34, 138.84, 145.93 (C6), 148.76, 157.66 (C2), 164.78 (C4), 175.25 (CO);  $^{19}\text{F}$  NMR  $\delta$  - 188.89 (s, 1F), -120.10 (d of m,  $J$  = 233.4 Hz, 1F), -119.20 (d of m,  $J$  = 240.9 Hz, 1F). HRMS (ESI+)  $m/z$  calcd for  $\text{C}_{28}\text{H}_{37}\text{F}_3\text{N}_6\text{NaO}_5\text{Si}$   $[\text{M}+\text{Na}]^+$  645.2445; found 645.2392.

### 2.4.3 Cytostatic activity assays

Murine leukemia L1210 cells were obtained from American Type Culture Collection (ATCC, Manassas, VA). The gemcitabine analogues tested (Table 1) were added to murine leukemia L1210 cell cultures in 96-well microtiter plates. After 72 h of incubation at 37 °C, the percentage surviving cells were assayed according to method described in the Cell Proliferation kit I (MTT) (Roche Biochemicals, Indianapolis, IN). The 50% inhibitory concentration ( $\text{IC}_{50}$ ) was defined as the compound concentration required to inhibit cell proliferation by 50%.

Human HEK293 cells were obtained from ATCC (Manassas, VA). The gemcitabine analogues tested (**2**, **5**, **8** and **9**) were added (50  $\mu\text{M}$  and 100  $\mu\text{M}$ ) to human HEK293 cell cultures in 12-well plates. After 48 h of incubation at 37 °C, the number of living cells was determined by a Coulter counter.

### 2.4.4 Fluorescence studies with HEK293 cells

HEK293 cells were seeded in plates containing glass coverslips and incubated overnight. After incubation, fresh media solutions containing **8** (100  $\mu\text{M}$ ) was added and then incubated for various durations (6, 12 and 24 hr). Cells were fixed in paraformaldehyde (3.7%) for 15 min at room temperature, quenched, and washed with PBS as essentially described by Neef et al.<sup>56</sup>

Cells on coverslips were incubated upside-down with 50  $\mu\text{L}$  of freshly prepared staining mix (10  $\mu\text{M}$  Fluor alkyne, 1 mM  $\text{CuSO}_4$ , and 10 mM sodium ascorbate in PBS) for 1 h at room temperature in the dark. Cells were then washed with 0.1% Triton X-100 and PBS, respectively. Cells were then stained with DAPI for 15 min at room temperature in the dark. After incubation,

cells were washing with PBS and coverslips were mounted and viewed on an Olympus FV1200 Laser confocal microscope.

#### 2.4.5 Radiosynthesis of [ $^{18}\text{F}$ ]fluoro-silane probes

Unless otherwise stated, reagents and solvents were commercially available and used without further purification. Purification of [ $^{18}\text{F}$ ]**10** was performed by semi-preparative HPLC using a WellChrom K-501 HPLC pump and reversed-phase Gemini-NX (5  $\mu\text{m}$ , 10 x 250 nm, Phenomenex) column. Analytical HPLC was performed to confirm identity and radiochemical purity of the compound in a Knauer Smartline HPLC system with C18 reversed-phase Luna column (5  $\mu\text{m}$ , 10 x 250 nm, Phenomenex). Radio-TLC was performed on precut silica plates (Baker-flex®, J.T.Baker). The radiochemical purity (RCP) was determined by using both radio-TLC and radio-HPLC radiation-detector chromatograms. For more detailed information, see supporting information.

*[ $^{18}\text{F}$ ]4-N-alkyl (10). Microscale radiochemical synthesis.* The microdroplet synthesis was performed using two Teflon-coated glass chips as shown in Figure S6 (see supporting information). The first was placed (Teflon-coated side up) on the heater. [ $^{18}\text{F}$ ]fluoride in [ $^{18}\text{O}$ ]H<sub>2</sub>O (10  $\mu\text{L}$ ; ~150 MBq [4 mCi]) was mixed with 12  $\mu\text{L}$  of a 70:30 v/v CH<sub>3</sub>CN/H<sub>2</sub>O solution containing K<sub>222</sub> (0.23  $\mu\text{g}$ ) and K<sub>2</sub>CO<sub>3</sub> (0.07  $\mu\text{g}$ ) and deposited in the center of the chip. Additional CH<sub>3</sub>CN (10  $\mu\text{L}$ ) was added to aid in azeotropic drying, and the chip was heated at 105°C until the droplet on chip shrank to a small volume (~1  $\mu\text{L}$ ). Next, 0.2 mg precursor **9** in 30  $\mu\text{L}$  of DMSO with 1% v/v AcOH was added to the dried [ $^{18}\text{F}$ ]KF/K<sub>222</sub> residue, and the reaction droplet was covered with the second glass chip (Teflon-coated side down). Tape affixed to the edges of the top chip resulted in a gap of ~150  $\mu\text{m}$  between the substrates. The chip was heated at 100°C for 20 min. Crude product was extracted from chip by adding 20  $\mu\text{L}$  of 1:1 v/v MeOH:H<sub>2</sub>O solution and then collecting the diluted mixture with a pipette. This process was repeated 2x for each substrate (~80  $\mu\text{L}$  total volume). Without purification, the microscale synthesis took ~45 min.

Decay-corrected crude radiochemical yield for 4-*N*-alkyl [<sup>18</sup>F]**10** was 24.4 ± 4.1% (n=5). *Note:* See supporting information for more detailed protocol and macroscale synthesis.

#### 2.4.6 Preclinical Imaging

Animal studies were approved by the UCLA Animal Research Committee and were carried out according to the guidelines of the Division of Laboratory Animal Medicine at UCLA. PET/CT was performed on the Genisys 8 PET/CT (Sofie Biosciences, USA). The Genisys 8 PET/CT is an integrated scanner with a PET subsection that consists of 8 detectors with BGO scintillator array arranged in a box geometry and a back section consisting of a rotating CT gantry. For static PET scans, a WT C57BL/6 mouse was injected with approximately 75 µCi [<sup>18</sup>F]**10** via tail vein. After 60 min of conscious uptake, mice were anesthetized with 1.5% isoflurane and placed in a dedicated imaging chamber. MicroPET images were acquired for 600 sec with an energy window of 150-650 keV, reconstructed using maximum-likelihood expectation maximization as recommended by the vendor. All images were corrected for CT-based photon attenuation, detector normalization and radioisotope decay (scatter correction was not applied) and converted to units of percent injected dose per gram (%ID/g). For dynamic PET scans, a WT C57BL/6 mouse was anesthetized with 2% isoflurane, placed in a dedicated imaging chamber with heating, and catheterized. Dynamic microPET imaging was started concurrently at the beginning of a 10 sec infusion via the catheter with approximately 75 µCi of [<sup>18</sup>F]**10**. Data was acquired in listmode for 3600 sec with an energy window of 150-650 keV and histogrammed into a frame sequence of 4 x 15 sec, 8 x 30 sec, 5 x 60 sec, 4 x 300 sec, 3 x 600 sec. Images were reconstructed using maximum-likelihood expectation maximization as recommended by the vendor. All images were corrected for photon attenuation, detector normalization and radioisotope decay (scatter correction was not applied) and converted to units of percent injected dose per gram (%ID/g). All PET acquisitions were immediately followed by CT acquisition. The CT section consists of a gantry and flywheel that uses a 50 kVp, 200 uA x-



ray source and flat-panel detector. The CT acquires images in a continuous-rotation mode and with standard CT acquisition time of 50 s. Standard scans are acquired with 720 projections at 55 ms per projection, and reconstructed using a Feldkamp algorithm.

## 2.5 Conclusion

We have demonstrated that copper(I) catalyzed click reaction of the 4-*N*-alkanoyl or alkyl gemcitabine analogues having terminal azide or alkyne group on the alkyl chain with the silane reagents having terminal alkyne or azido group provided 4-*N*-alkanoyl and alkyl gemcitabine analogues with silicon-fluoride acceptors. RP-HPLC analysis showed that the 4-*N*-alkyl analogues were more stable in aqueous acidic conditions, indicating their advantage in developing them as PET imaging tracers. The silane 4-*N*-alkyl precursor **9** was successfully fluorinated to [<sup>18</sup>F]**10** using conventional and microscale radiosynthetic methods in high radiochemical purity and stability of up to 4 h. Preliminary static and dynamic PET studies in wild-type mice have shown the initial biodistribution of [<sup>18</sup>F]4-*N*-alkyl tracer **10** in the liver, kidneys and GI tract followed by increasing signal in the bone. The 4-*N*-alkanoylgemcitabine analogues showed more potent antiproliferative activity in L1210 cells compared to the 4-*N*-alkylgemcitabine derivatives. However, 4-*N*-alkanoyl and 4-*N*-alkyl analogues had comparable antiproliferative activities in the HEK293 cells, which have high levels of CDA expression. The 4-*N*-alkyl gemcitabine derivatives were shown to be localized inside HEK293 cells by fluorescence microscopy after click labelling with Fluor 488-alkyne. The chemical and enzymatic stabilities of 4-*N*-alkylcytidine analogues described here as well as their compatibility with <sup>18</sup>F-labeling provide a potential avenue for developing new PET imaging tracers for gemcitabine derivatives. Future work would involve optimizing the structure to improve the in vivo stability and the biodistribution of these analogs.



# Chapter 3: Droplet synthesis of O-(2-[<sup>18</sup>F]fluoroethyl)-L-tyrosine ([<sup>18</sup>F]FET)

## 3.1 Introduction

Positron emission tomography (PET) is a non-invasive molecular imaging tool based on the use of positron-emitting isotopes to track the position and dynamics of biologically relevant molecules in the body. PET provides high-sensitivity quantitative visualization of physiological parameters *in vivo*, such as metabolic rate, receptor density, gene expression, or blood flow, which makes it a versatile and potent tool for clinical diagnosis, treatment planning, treatment monitoring, as well as research (171–175).

Safe preparation of various target-specific PET tracers is a complex and expensive process, requiring skilled personnel operating expensive automated radiosynthesis equipment within radiation-shielded “hot cells”. With conventional apparatus, in which the chemistry is carried out in mL volume scales, relatively high reagent amounts (1s to 10s of mg) are needed to achieve a sufficient concentration for good reaction yield in a short time, and for [<sup>18</sup>F]fluoride chemistry high amounts of radioactivity (10s of GBq) are needed to achieve high molar activity (176). These factors contribute to inefficient use of resources in the preparation of small batches of tracers, such as needed for preclinical imaging, or for a single clinical PET scan, where much of the prepared batch would be wasted.

On the other hand, emerging microfluidic radiosynthesis methods require much lower amounts of reagents and radionuclide, and through substantially reduced instrument size and cost, have the potential to significantly reduce costs and resources needed for radiopharmaceutical production. Microscale reactions also tend to be faster and, due to the low precursor mass used, the crude products can be purified with simpler methods (e.g. analytical-scale high-performance liquid chromatography (HPLC) or cartridge instead of semi-preparative

HPLC). These advantages are especially relevant for smaller batch production of PET tracers, but can also benefit the production of larger batches (177).

Of the several different microfluidic approaches reported in the last decade (71,120,178–180), microvolume reaction approaches offer the greatest potential for reagent and instrument reductions (98,106,181–184). A particular configuration we are exploring is performing reactions in microliter-sized droplets on simple Teflon-coated silicon microfluidic chips, which has advantages of simple operation, low-cost disposable chips, and a compact system size, which reduces the necessary shielding. Previous work has shown application of this method for the rapid and efficient synthesis of [<sup>18</sup>F]FDG and [<sup>18</sup>F]fallypride (106). In this paper, we demonstrate further versatility of this approach by adapting the macroscale synthesis of O-(2-[<sup>18</sup>F]fluoroethyl)-L-tyrosine ([<sup>18</sup>F]FET) to this platform, and then use the produced [<sup>18</sup>F]FET for pre-clinical imaging.

[<sup>18</sup>F]FET is an amino acid PET probe (185), finding use in glioma imaging (40) as well as providing a route for protein labeling with fluorine-18 (186). The radiosynthesis of [<sup>18</sup>F]FET from the commercially available precursor (2S)-O-(2'-tosyloxyethyl)-N-trityl-tyrosine-tert-butyl ester (TET) consists of a radiofluorination step followed by a hydrolysis step. The conventional synthesis typically results in good radiochemical yields (RCYs), ranging from 19 – 64% (184,187–190). Some efforts have been made to carry out the synthesis in microfluidic format. Bouvet *et al.* performed the reaction in a commercial flow radiochemistry system using either microwave or heat activation of the reaction. An RCY of 50% was obtained with only 59 nmol of precursor in a 30 µL reaction in < 45 min (188), but to scale to larger production amounts (e.g., > 200 MBq) would require longer synthesis times and higher precursor amounts. Iwata *et al.* performed batch synthesis in 10 – 20 µL volumes (180 – 350 nmol of precursor) within a small glass vial by first loading a larger volume of methanolic solution containing [<sup>18</sup>F]fluoride and phase transfer catalyst, evaporating the solvent, then adding the small volume of precursor solution and performing the reaction (184). Yields of up to 64 ± 11% (*n* = 3 ~ 6) were reported at scales of < 400 MBq. An

automated procedure for this method was not described and may be challenging in practice due to the difficulty of manipulating small volumes in what is essentially a conventional apparatus.

We report a simple and rapid method for [ $^{18}\text{F}$ ]FET synthesis based on microvolume droplet approach. The probe production with this method results in high RCY and high molar activity using a very small amount of precursor and low starting activity. The low precursor amount enables purification via analytical, rather than semi-preparative, scale HPLC. This low-cost approach allowed us to carry out a large dynamic imaging study of up to 8 mice within a single day, thus demonstrating that the method will be a favorable option for pre-clinical studies of [ $^{18}\text{F}$ ]FET.

## 3.2 Materials and methods

### 3.2.1 Reagents and supplies

For the radiochemistry portion of this work, no-carrier-added [ $^{18}\text{F}$ ]fluoride was produced by the  $^{18}\text{O}(p, n)^{18}\text{F}$  reaction from [ $^{18}\text{O}$ ]H<sub>2</sub>O (84% isotopic purity, Zevacor Pharma, Noblesville, IN, USA) in an RDS-112 cyclotron (Siemens; Knoxville, TN, USA) at 11 MeV using a 1 mL tantalum target with havar foil. Acetonitrile (MeCN; anhydrous, 99.8%), methanol (MeOH; anhydrous, 99.8%), ethanol (EtOH; 200 proof, > 99.5%), hydrochloric acid (HCl; 1M), hexyl alcohol (2,3-dimethyl-2-butanol, 98%), trifluoroacetic acid (TFA, 99%), deionized (DI) water, phosphate buffered saline (PBS; pH 7.4) were purchased from Millipore Sigma (St. Louis, MO, USA). Saline (0.9% sodium chloride injection, USP) was obtained from Hospira Inc. (Lake Forest, IL, USA). All reagents were used as received without further purification. 18M $\Omega$  water was obtained from a purification system (RODI-C-12BL, Aqua solutions, Inc., Georgia, USA). Tetrabutylammonium bicarbonate 0.075M (TBAHCO<sub>3</sub>, > 99%), (2S)-O-(2'-tosyloxyethyl)-N-trityl-tyrosine-tert-butyl ester (TET, >95%) precursor, O-2-fluoroethyl-L-tyrosine standard (FET-HCl, > 95%) were purchased from ABX GmbH (Radeberg, Germany).

To perform uptake assays, GS025 and GBM39 cells were kindly provided by Dr. David Nathanson (UCLA), the ParcB3 cells were provided by Dr. Peter Clark (UCLA), and the HCT-15

and HCC827 cells were purchased from ATCC (Manassas, VA, USA). Poly-L-lysine, protease inhibitor (cOmplete™), Hank's balanced salt solution (HBSS; 10×), and fetal bovine serum (FBS), were purchased from Millipore Sigma (St. Louis, MO, USA). 96 well plates, 96 well filter plates, 0.25% trypsin, 100× penicillin-streptomycin (10,000 U/mL, Gibco™), RPMI-1640 medium (1×, Gibco™), GlutaMAX™ – I (100×, Life Technologies), Dulbecco's Modified Eagle Medium (DMEM/F12), (100×), epidermal growth factor recombinant human protein (EGF), fibroblast growth factor recombinant human protein (FGF-Basic), heparin, and B27 supplement (50×) were purchased from Thermo Fisher (Waltham, MA, USA).

### 3.2.2 Analytical methods

A calibrated ion chamber (CRC 25-PET, Capintec, Florham Park, NJ, USA) was used to perform radioactivity measurements. For radio-thin-layer chromatography (TLC) analysis, TLC plates (Baker-flex silica gel IB-F sheets 2.5×7.5 cm, J.T. Baker, Phillipsburg, NJ) were spotted with 1 µL samples of the crude intermediate, crude final product, or purified final product, and were developed in 80% v/v MeCN in H<sub>2</sub>O, and then scanned with a radio-TLC scanner (miniGita star, Raytest, Inc., Wilmington, NC, USA), or with a Cerenkov luminescence imaging system (181). Retention factors of the observed radioactive species were: 0.0 ([<sup>18</sup>F]fluoride), 0.3 ([<sup>18</sup>F]FET), and 0.8 (fluorinated intermediate).

Radio-HPLC analysis and purification was performed on an analytical-scale Smartline HPLC system (Knauer, Berlin, Germany) with 200 µL injection loop, a pump (Model 1000), degasser (Model 5050), a UV detector (Model 2500) and a radiometric detector (Bioscan B-FC-4000, Bioscan Inc., Washington DC, USA). Samples were separated using a C18 column (Luna, 4.6 x 250 mm, 5 µm, Phenomenex, Torrance, CA, USA) with guard column (SecurityGuard C18, Phenomenex) at a flow rate of 1 mL/min. UV absorbance was measured at 269 nm. Using 10% v/v EtOH in 18MΩ H<sub>2</sub>O mobile phase, the expected retention time of [<sup>18</sup>F]fluoride was between 2-

3 min, and around 5 min for [ $^{18}\text{F}$ ]FET. The fluorinated intermediate was eluted off the column using 100% MeCN.

### 3.2.3 Microfluidic systems

Radiochemistry was performed in droplet format on the surface of microfluidic chips comprising a silicon wafer with a patterned Teflon AF coating. The detailed fabrication was previously reported (106). A combination of hydrophobic (Teflon) and hydrophilic (exposed silicon wafer) regions allows liquid droplets to be manipulated or maintained in a desired location to perform reactions.

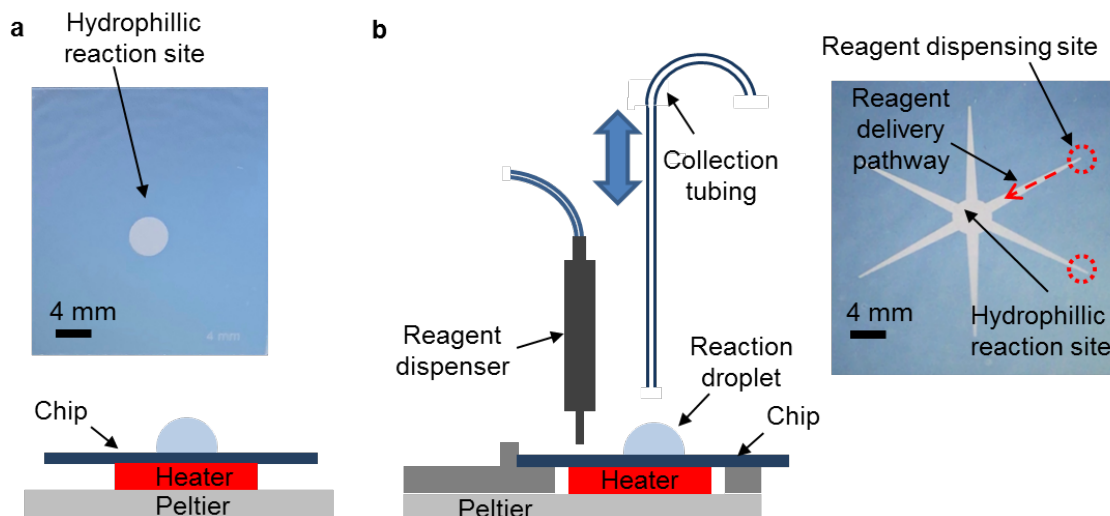


**Figure 3.1 Droplet synthesis platform**

Side view schematic of manual (a) and automated (b) microvolume synthesis platform, and top view photographs of corresponding chips used.

One type of chip, used for the synthesis optimization studies, had a 4 mm circular hydrophilic region (i.e. Teflon coating etched away) serving as a reaction site (Figure 3.1a). During use, the chips were mounted to a temperature control platform comprising a ceramic heater affixed to a Peltier device, which was in turn mounted on a heat sink with a fan. A thin layer of thermal paste was present between all device components to ensure good thermal contact. Reagents were loaded and product was collected manually via pipette with 10 or 200  $\mu\text{L}$  tips.

Another type of chip, used for automated synthesis, had six radial tapered hydrophilic pathways leading toward a central hydrophilic reaction site (Figure 3.1b). The chip was similarly mounted to a temperature-control platform, but reagents were added via electronically controlled piezoelectric actuators around the periphery of the chip and crude product was collected by a retractable needle. The tapered pathways spontaneously transport reagent droplets from the periphery to the center of the chip. Complete details of this setup were reported previously (106).

### 3.2.4 Microscale radiosynthesis and purification of [<sup>18</sup>F]FET

The microscale synthesis was adapted from previously described macroscale protocols (187,190) by scaling down reagent volumes (Figure 3.2). Cyclotron produced [<sup>18</sup>F]fluoride (37 – 740 MBq in ~10 – 20  $\mu$ L) was mixed with 110 nmol of TBAHCO<sub>3</sub> (i.e., 1.5  $\mu$ L of 75mM solution), deposited on the chip and then evaporated to dryness at 100°C. After cooling to 30°C, 10  $\mu$ L of 6mM TET (60 nmol) in 1:1 v/v MeCN:hexyl alcohol was added to the chip. The reaction mixture was heated at 90°C for 5 min, and then cooled to 30°C. Next, 20  $\mu$ L of 1M HCl was added and the deprotection reaction was performed by heating to 90°C for 3 min. The crude product was recovered by adding 20  $\mu$ L of 1:1 v/v MeOH:H<sub>2</sub>O and collecting from the chip. The collection process was repeated a total of 4 times to ensure high recovery of the crude product. After synthesis, the product was diluted to 150 – 175  $\mu$ L using HPLC mobile phase (10% v/v EtOH in 18M $\Omega$  water) and purified via analytical-scale radio-HPLC. The product peak was collected (typically 1.0 – 1.5 min duration) into a sterile glass vial. Solvent was evaporated by heating the vial to 120 °C with an oil bath and applying a nitrogen stream above the surface of the solvent. When dry (typically after 10 – 15 min), the [<sup>18</sup>F]FET was then resuspended either in sterile saline for *in vivo* imaging, or pH 7.4 phosphate-buffered saline (PBS) for cell uptake experiments. Numerous intermediate measurements were taken during synthesis to carefully analyze its performance.



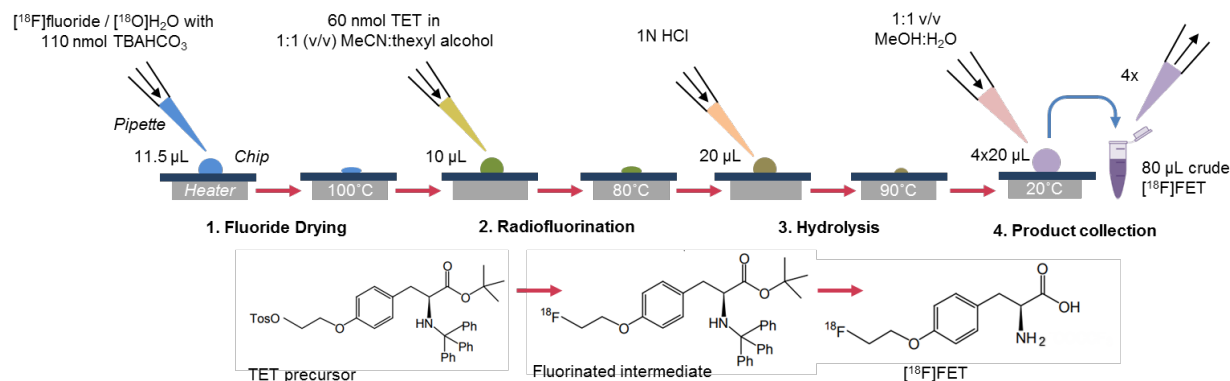


**Figure 3.2 Synthesis scheme for microvolume production of  $[^{18}\text{F}]\text{FET}$  using manual synthesis platform.**

### 3.2.5 Preparation of samples with different molar activities

Samples of  $[^{18}\text{F}]\text{FET}$  with different molar activities were prepared from a single batch by dividing the batch and then spiking in different amounts of the reference standard. The molar activity of the batch was measured, then the batch was formulated in 100  $\mu\text{L}$  of sterile saline and divided into 4 portions. The needed amounts of FET reference standard (prepared in stock solutions of 50  $\mu\text{M}$ , 100  $\mu\text{M}$  or 5 mM) to achieve the desired molar activities were then calculated, added, and then the volumes were topped off with additional sterile saline to achieve a final concentration of 3 MBq/100  $\mu\text{L}$ . In parallel with imaging, portions of each sample were re-analyzed via radio-HPLC to measure the final molar activity. Summaries of preparations for two experiments, starting with batches of  $[^{18}\text{F}]\text{FET}$  having molar activities of 35.5 GBq/ $\mu\text{mol}$  and 48.1 GBq/ $\mu\text{mol}$ , are shown in Table 3.1 and Table 3.2, respectively.

$[^{18}\text{F}]\text{FET}$ activity, MBq	$[^{18}\text{F}]\text{FET}$ volume, $\mu\text{L}$	FET standard concentration, $\mu\text{M}$	FET standard added volume, $\mu\text{L}$	Saline volume, $\mu\text{L}$	Final molar activity, GBq/ $\mu\text{mol}$
8.9	25	—	0	231	35.5
8.9	25	50	5.8	225	10.0
8.9	25	50	26	205	4.81
8.9	25	50	85	146	1.48

**Table 3.1 Preparation of  $[^{18}\text{F}]\text{FET}$  with different molar activities (Experiment 1).**

Sample activity, MBq	Activity added volume, $\mu\text{L}$	Standard concentration, $\mu\text{M}$	Standard added volume, $\mu\text{L}$	Saline added volume, $\mu\text{L}$	Final molar activity, $\text{GBq}/\mu\text{mol}$
8.7	20	0	0	215	48.1
8.7	20	100	3	212	4.81
7.8	66	100	26	141	1.85
7.8	66	5000	3	164	0.37

**Table 3.2 Preparation of [ $^{18}\text{F}$ ]FET with different molar activities (Experiment 2).**

### 3.2.6 Analytical methods

During the development and optimization of the microscale synthesis, numerous intermediate measurements were taken to thoroughly analyze the performance. All radioactivity values were decay-corrected to a common reference time. The starting activity loaded on the chip was determined by calculating the difference in activity of a source vial and pipette tip before and after addition to the chip. The activity of the crude reaction product recovered from the chip, and the residual activity on the chip after the collection step were measured as well (The residual activity on the pipette tip used for collection was found to be negligible). Collection efficiency was calculated as the activity of the recovered crude product divided by the starting activity. Unaccounted activity loss was defined by subtracting the collected activity and the residual activity on chip from the starting activity and expressing as a fraction of starting activity.

To assess reaction efficiency, a small portion of the collected crude product was analyzed via radio-TLC or/and radio-HPLC.

During initial optimization, only the fluorination step was performed resulting in formation of the fluorinated intermediate (with intact protecting groups). After collection of the crude mixture from the chip, a small (1  $\mu\text{L}$ ) sample was analyzed via radio-TLC, which exhibited two peaks ([ $^{18}\text{F}$ ]fluoride and the intermediate). Fluorination efficiency was found from radio-TLC chromatogram by dividing the peak area corresponding to the intermediate by the sum of areas of all peaks. Fluorination yield was computed by multiplying the fluorination efficiency by collection efficiency.

When analyzing samples after performing both fluorination and hydrolysis, a small (1  $\mu\text{L}$ ) sample of the crude reaction mixture was taken for TLC analysis, which exhibited three peaks ( $[^{18}\text{F}]$ fluoride,  $[^{18}\text{F}]$ FET, and the intermediate). The radiochemical conversions (RCCs) for the intermediate and  $[^{18}\text{F}]$ FET were computed as the area under the corresponding peak divided by the area under all peaks. The fluorination yield was computed as the sum of the intermediate and  $[^{18}\text{F}]$ FET RCCs, multiplied by the collection efficiency. The hydrolysis efficiency was determined by dividing the peak area corresponding to  $[^{18}\text{F}]$ FET by the sum of the intermediate and  $[^{18}\text{F}]$ FET peak areas. Finally, the crude RCY was calculated by multiplying the  $[^{18}\text{F}]$ FET RCC by the collection efficiency.

Purification efficiency was calculated as the activity of the collected product after HPLC purification divided by the expected amount of pure product (i.e., the total activity of the crude product multiplied by the radiochemical purity (RCP)). To determine RCP, the crude product was analyzed via both radio-TLC and radio-HPLC. The radio-TLC chromatogram was used to compute the fraction of  $[^{18}\text{F}]$ fluoride incorporated into other species, computed as the total area of all non-fluoride peaks divided by the total area of all peaks. The radio-HPLC chromatogram was used to determine the fraction of non-fluoride peaks attributable to  $[^{18}\text{F}]$ FET. This fraction was computed as the peak area of  $[^{18}\text{F}]$ FET divided by the total area of all non-fluoride peaks. The RCP was computed as the radio-TLC fraction multiplied by the radio-HPLC fraction. In general, the radio-HPLC chromatogram obtained during the purification process could be used for this analysis (unless peaks were saturated).

The formulation efficiency was calculated as a ratio of the activity of final formulated product to the initial activity of the purified  $[^{18}\text{F}]$ FET.

The molar activity was determined using analytical radio-HPLC directly from the purification chromatogram. It was calculated by dividing the activity of  $[^{18}\text{F}]$ FET injected into HPLC by molar quantity of FET injected. The molar quantity of FET was determined using the area under the FET peak in the UV chromatogram and a calibration curve. Since several different

wavelengths for UV detection of FET in HPLC have been reported in literature (i.e., 200 nm (189), 220 nm (187), 280 nm (184), we first measured the FET absorbance spectrum to determine a suitable wavelength. The absorbance of FET reference standard (500  $\mu\text{M}$ ) was scanned across a range of wavelengths 200-350 nm using a microfluidic UV absorbance detection device (191) and the absorbance spectrum of the solvent was subtracted. The resulting spectrum is shown in **Figure S1**. We did not select the maximum at 222 nm due to the high noise level, but instead chose the maximum at 269 nm.

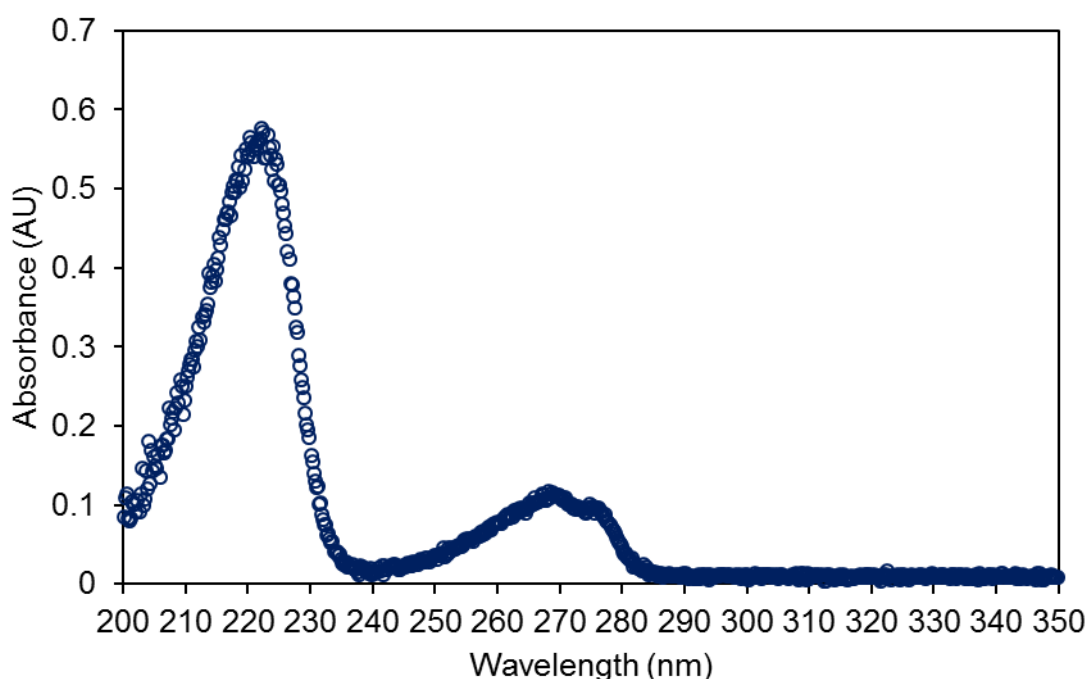


**Figure 3.3 UV absorbance spectrum of FET reference standard.**

A calibration curve was then created for use in molar activity determinations. Different volumes of 50  $\mu\text{M}$  FET reference standard (in HPLC mobile phase, i.e. 10% v/v EtOH:H<sub>2</sub>O) were injected into the analytical HPLC, i.e. 10  $\mu\text{L}$  (0.5 nmol), 20  $\mu\text{L}$  (1 nmol), 30  $\mu\text{L}$  (1.5 nmol), 40  $\mu\text{L}$  (2 nmol), 50  $\mu\text{L}$  (2.5 nmol) and 100  $\mu\text{L}$  (5 nmol). The areas of the result peaks in the HPLC chromatogram were plotted as a function of molar amount of FET, and a linear least-squares fit was calculated.

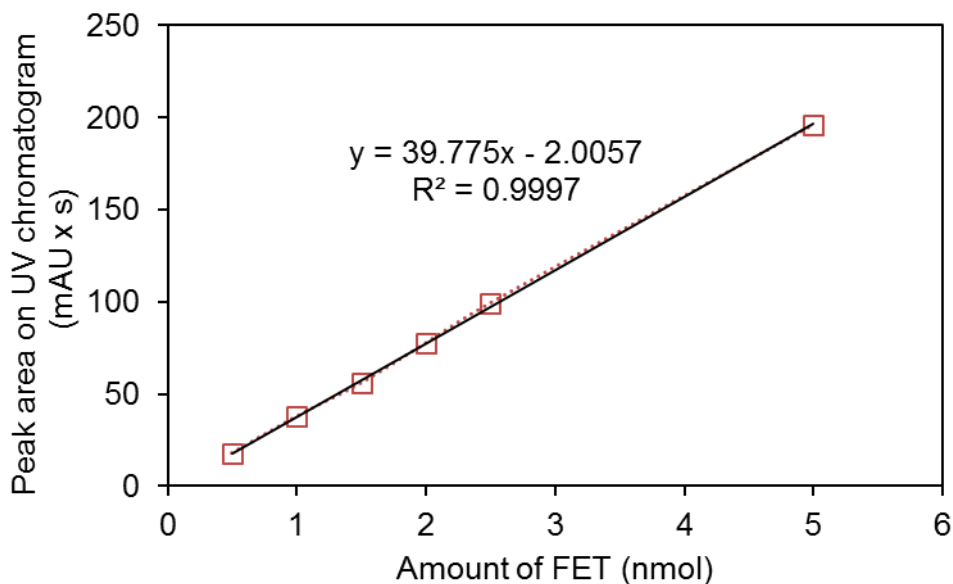


**Figure 3.4 Calibration curve for FET molar activity determination.**

### 3.2.7 *In vitro* probe uptake

*In vitro* uptake of [ $^{18}\text{F}$ ]FET was compared across two glioblastoma cell lines (GS025, GBM39), a prostate cancer cell line (ParcB3), a lung cancer cell line (HCC827), and a colon cancer cell line (HCT-15). The GS025, GBM39, and ParcB3 suspension cells were grown in stem cell media, and the HCC827 and HCT-15 adherent cells were grown in supplemented RPMI. The suspension cells were plated into 96-well plates and adherent cells into 96-well filter plates at 150,000 cells/mL concentration in 1x HBSS. [ $^{18}\text{F}$ ]FET was diluted to a concentration of 370 Bq/ $\mu\text{L}$  with either PBS (for uptake experiments) or PBS containing 5 mM FET (for blocking experiments). Cell uptake experiments were performed by adding 100  $\mu\text{L}$  [ $^{18}\text{F}$ ]FET (37 kBq) to each of a set of cell wells ( $n=4$ ), and blocking experiments (to confirm specificity) were performed by adding 100  $\mu\text{L}$  [ $^{18}\text{F}$ ]FET (37 kBq) with FET (500 nmol) to each of a set of cell wells ( $n=4$ ). The cells were incubated at 37°C for 10 min, then transferred into individual gamma counter tubes and sample radioactivity was measured on a gamma counter (WIZARD 3" 1480, Perkin Elmer, Waltham, MA,

USA). The uptake values were normalized to total protein amounts for each sample. The statistical significance of the values was validated by a two-tailed T test ( $p < 0.05$ ).

### **3.2.8 *In vivo* preclinical imaging**

Male NOD *scid* gamma (NSG) mice ~ 7 week-old were obtained from the UCLA Department of Radiation Oncology. These mice ( $n = 10$ ) were engrafted with  $0.5 \times 10^6$  HCC827 cells suspended in a 1:1 (v/v) mixture of supplemented RPMI media and Corning® Matrigel® Basement Membrane Matrix (Corning Life Sciences) in the left and right shoulders.

To perform dynamic PET imaging, mice were kept under 2% isoflurane anesthesia during the tracer uptake for 60 min. Mice were injected with 1.5 – 3.1 MBq of the tracer, and were scanned 4 at a time using the recently developed HiPET scanner (121). The first study was performed with 4 mice injected with probe of different molar activities in a range of 1.5 –36 GBq/ $\mu$ mol ( $n = 1$  each). The second study with 8 mice covered molar activities ranging from 0.4 – 48 GBq/ $\mu$ mol ( $n = 2$  each) (see ESM, Section 4 for details). The concentration of FET in blood was estimated to range between 0.02 and 3.5  $\mu$ M assuming 2 mL average mouse blood volume. All mice received 10 min CT scans (CrumpCAT (192)) following the PET imaging experiment. After PET/CT image registration, regions of interest (ROI) were drawn with AMIDE version 1.0.5 software, and the results were analyzed by comparing mean intensity values of the tumors and other regions across different time points (12 frames of 5 min each). The reference ROIs were selected as follows: a spherical ROI (3 mm diameter) inside the lower left ventricle of the heart (blood uptake reference), and a similar shaped ROI within the leg muscle region beside the femur (muscle reference). The tumor ROIs were selected as an ellipsoid to cover the majority of the tumor volume to minimize the effect of inhomogeneous uptake within a single tumor. The whole-body 3D isocontour ROI was selected based on a minimum signal threshold value set to include all PET signal within the mouse body. The injected dose per volume (% ID/cc) was determined

by dividing the integrated intensity in the ROI of interest by the integrated intensity in the whole-body ROI and then dividing by the volume of the ROI.

### 3.3 Results

#### 3.3.1 Microscale [<sup>18</sup>F]FET synthesis optimization and automation

To adapt the 2-step synthesis of [<sup>18</sup>F]FET from the macroscale to the microscale, the precursor and base quantities were initially scaled down nearly 300 – 490-fold from values reported in conventional synthesis (187,190), i.e. to 75 nmol of TBAHCO<sub>3</sub> (1 μL, 0.075M) and 30 nmol of the TET precursor in 20 μL. We used TBAHCO<sub>3</sub> rather than K<sub>222</sub>/K<sub>2</sub>CO<sub>3</sub> (184,187) based on the suggestion by Hamacher and Coenen (190), who observed higher yields due to the lower basicity and reduced competing elimination reaction. One significant change we made was altering the fluorination reaction solvent. The syntheses reported by Hamacher and Coenen (190), Bourdier *et al.* (187) and Lakshminarayanan *et al.* (189) all used MeCN as the fluorination solvent, but in the droplet format, we found that the MeCN evaporated very quickly, resulting in poor yields. After exploring several solvent combinations that have been previously reported in droplet reactions (120), a 1:1 v/v mixture of MeCN and hexyl alcohol was selected. During early syntheses the fluorination temperature was set at 80°C, slightly lower than what has been reported in conventional syntheses (i.e., 85 °C (190) or 100 °C (187)) to further mitigate evaporation, and the reaction time was set for 5 min. Under these conditions, fluorination yield was 36±7% (*n* = 4).

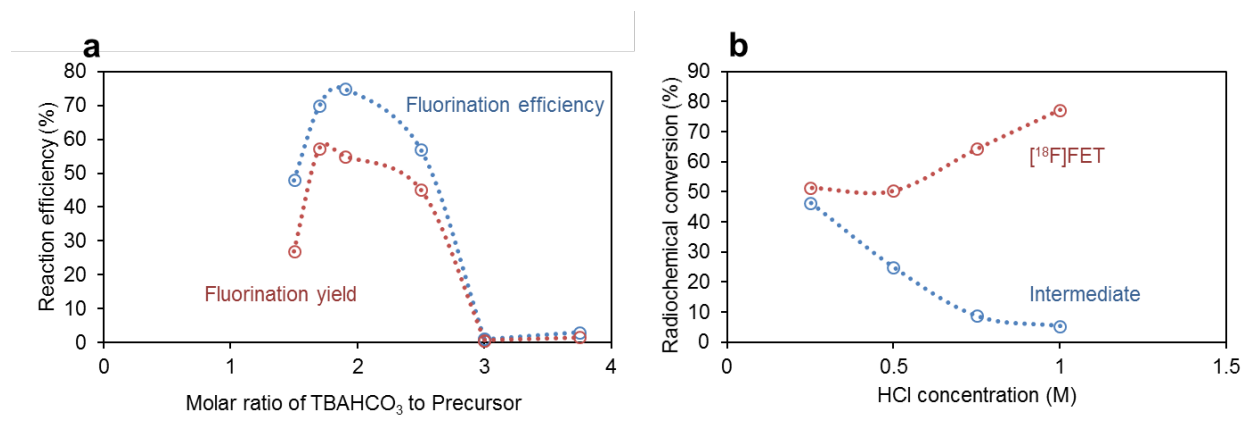


**Figure 3.5 a Effect of base to precursor ratio on fluorination efficiency and fluorination yield**

( $n = 1$  for each data point). Syntheses carried out at 80°C for 5 min with 30 nmol or 60 nmol of precursor. b Effect of deprotectant (10  $\mu$ L HCl) concentration on deprotection reaction at 90°C for 3 min ( $n = 1$  for each condition). Synthesis performed with 60 nmol precursor and 110 nmol TBAHCO<sub>3</sub> at 90°C for 5 min.

Investigation of the ratio of base to precursor (Figure 3.5a) indicated that the originally chosen ratio ( $\sim 2.5$ ) was close to optimal: a steep drop in fluorination efficiency was observed for base to precursor ratios below 1.7 and higher than 2.5. When fluorinating with 110 nmol of TBAHCO<sub>3</sub> per 60 nmol of precursor (1.9 ratio) at 80°C the fluorination yield reached  $50 \pm 1\%$  ( $n = 4$ ). Increasing the temperature to 90°C further improved the fluorination yield to  $63 \pm 3\%$  ( $n = 4$ ) (Figure 3.6). Lower reaction temperature (75°C) resulted in similar yield as the 80°C reaction, though solvent evaporation was slightly reduced (Figure 3.6). Later, the reaction volume was reduced to 10  $\mu$ L keeping the same amount (60 nmol) of precursor per reaction to make it more compatible with chip chemistry, however no significant change in reaction yield was observed.



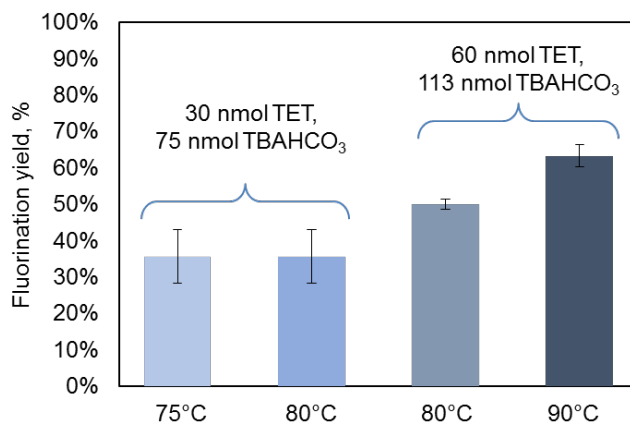


**Figure 3.6 Results of initial optimization of fluorination conditions**

Error bars represent standard deviations ( $n = 4$ )

For the deprotection step, we initially attempted to use TFA as reported by Hamacher and Coenen (190) and Bouvet *et al.* (188); however, we observed rapid evaporation of TFA and low deprotection efficiency. We then explored the use of HCl, as reported by Bourdier *et al.* (187) and Lakshminarayanan *et al.* (189). Using a deprotection reagent volume of 10  $\mu\text{L}$  heated for 3 min at 90 °C, we explored the effect of different HCl concentrations (Figure 3.5b). Higher concentrations resulted in more complete deprotection of the intermediate. The use of 10  $\mu\text{L}$  of 1.0 M HCl was sufficient to deprotect most of the intermediate (~ 94%). Increasing the volume from 10 to 20  $\mu\text{L}$  led to improved hydrolysis and was used in all subsequent experiments. Conveniently, the acid nearly fully evaporates during the hydrolysis step leaving only trace amounts of liquid, obviating the need for neutralization.

The manual synthesis of the crude product, under optimized conditions, required  $24 \pm 2$  min ( $n = 4$ ). The collection efficiency was  $64 \pm 5\%$  ( $n = 4$ ) and radiochemical conversion of [<sup>18</sup>F]FET was  $92 \pm 4\%$  ( $n = 4$ ) resulting in crude RCY of  $59 \pm 7\%$  ( $n = 4$ ). Fluorination yield was estimated to be  $62 \pm 8\%$  ( $n = 4$ ), and hydrolysis efficiency was  $96 \pm 2\%$  ( $n = 4$ ). Only  $1.3 \pm 0.5\%$  ( $n = 4$ ) of the starting activity was attributed to residual activity on the chip after collection of the

crude product, though an additional loss of  $35 \pm 6\%$  ( $n=4$ ) was observed, potentially corresponding to loss of unreacted [ $^{18}\text{F}$ ]fluoride in the form of [ $^{18}\text{F}$ ]HF during the acidic deprotection step.

Production of [ $^{18}\text{F}$ ]FET for imaging was performed using this manual protocol, followed by purification by analytical HPLC ( $\sim 5$  min) and formulation (10 – 15 min), resulting in an overall synthesis time of 40 min. The loss during purification and formulation was  $7 \pm 3\%$  ( $n = 4$ ) and overall decay corrected RCY was  $55 \pm 7\%$  ( $n = 4$ ). The identity of the purified product was confirmed via analytical radio-HPLC by co-injection with the reference standard. Radiochemical purity of the final product as determined via radio-HPLC was  $> 98\%$ . Molar activity was 48 – 119 GBq/ $\mu\text{mol}$  at the end of synthesis.

We also performed the synthesis using the automated droplet radiosynthesizer (i.e. with the passive transport microfluidic chips) and observed a crude decay-corrected RCY of  $54 \pm 6\%$  ( $n = 5$ ) (a detailed comparison of the performance of the manual and automated droplet synthesis processes is summarized in Table 3.3). In general, the performance was very similar, the main difference being slightly lower collection efficiency with the automated procedure. An advantage of the automated synthesis is that the synthesis of the crude product was completed in a shorter time (5 min less).

	Manual (n = 4)	Automated (n = 5)
Collection efficiency (%)	64±5	59±10
Residual chip activity (%)	1.3±0.5	3±1
Volatile activity loss (%)	35±6	38±11
Fluorination yield (%)	62±8	59±10
Radiochemical conversion to FET (%)	92±4	93±6
Deprotection efficiency (%)	96±2	93±6
Crude RCY (%)	59±7	54±6
Crude synthesis time (min)	24±2	19±2
Crude RCY, non-decay-corrected (%)	51±6	48±5

**Table 3.3 Summary of performance of microdroplet synthesis of [<sup>18</sup>F]FET**

Optimized manual operation or automated operation conditions were used. All values are decay-corrected unless otherwise specified.

### 3.3.2 *In vivo* imaging at varying molar activities of [<sup>18</sup>F]FET

As a demonstration of the ability to perform a preclinical imaging study with [<sup>18</sup>F]FET produced using the microscale method, we prepared [<sup>18</sup>F]FET of different molar activities to investigate the impact on *in vivo* imaging. It has been previously seen with imaging of [<sup>18</sup>F]fallypride that molar activity can significantly affect the PET imaging contrast in the striata of the brain (57), whereas variations in molar activity of [<sup>18</sup>F]FDOPA were reported not to impact the imaging of neuroendocrine tumors (31). [<sup>18</sup>F]FET is one of the major fluorine-18 labeled amino acids used in glioma imaging, grading and therapy planning. [<sup>18</sup>F]FET is an L-tyrosine analogue, and it helps to visualize amino acid transport activity that is upregulated in many growing tumors (40,194).

To perform experiments, samples with different molar activities were prepared from a single batch of [<sup>18</sup>F]FET. The batch was divided into four aliquots, then each aliquot was spiked

with different amounts of the reference standard and saline to achieve different molar activity values with the same radioactivity concentration.

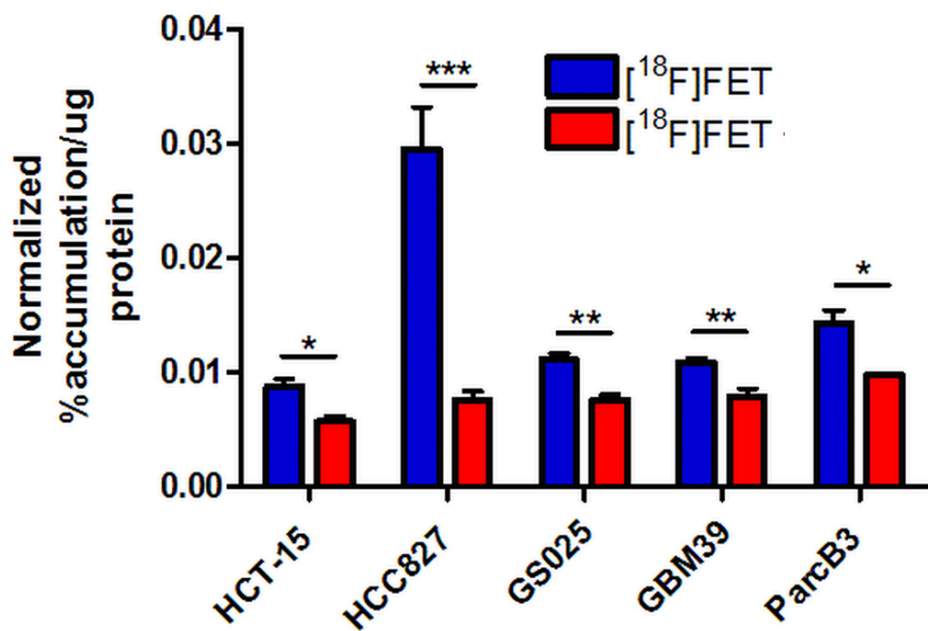


**Figure 3.7 Accumulation of [<sup>18</sup>F]FET in different cell lines**

Error bars represent standard deviation (n = 4). (\*) p < 0.05, (\*\*) p < 0.01, (\*\*\*) p < 0.001. The red bars indicate incubation with both [<sup>18</sup>F]FET and 2.5 mM FET reference standard to establish specificity.

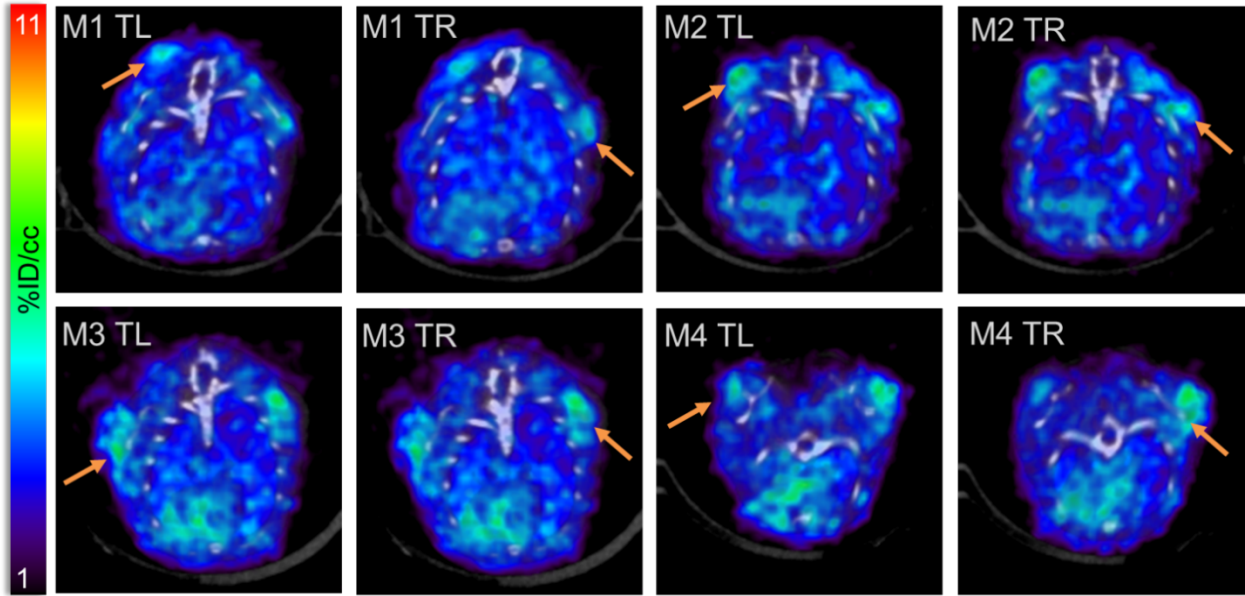


**Figure 3.8 PET/CT images of each mouse in the first imaging study**

Acquired 36 d post tumor implantation. Each image is a transverse slice through the middle of the indicated tumor, representing a 10 min frame of data 50-60 min post-injection. Each tumor is highlighted by an arrow. M# indicates the mouse number, TL indicates left shoulder tumor, TR indicates right shoulder tumor.

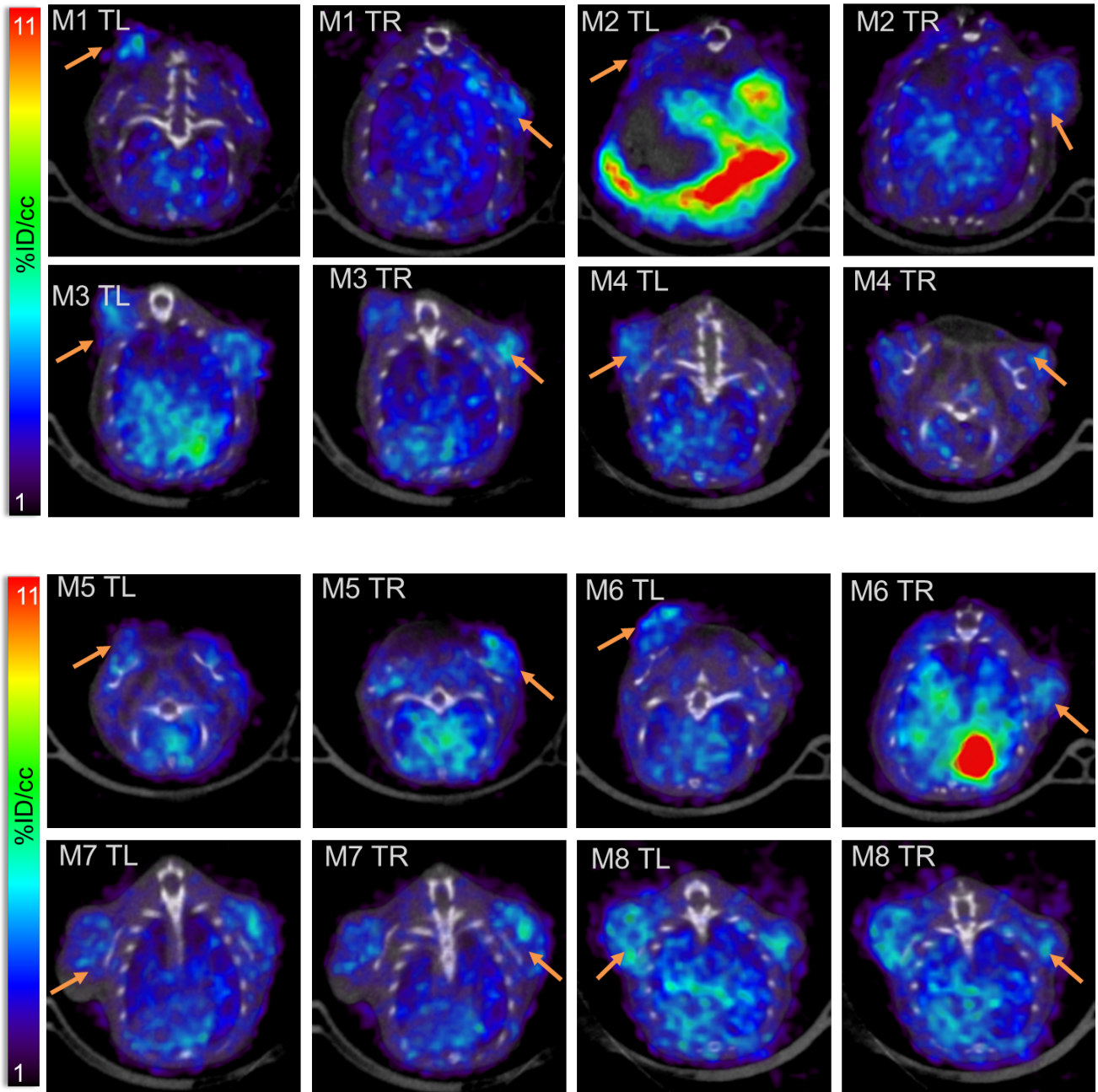


**Figure 3.9 PET/CT images of each mouse in the second imaging study**

Acquired 50 d post tumor implantation. Each image is a transverse slice through the middle of the indicated tumor, representing a 10 min frame of data 50-60 min post-injection. Each tumor is highlighted by an arrow. M# indicates the mouse number, TL indicates left shoulder tumor, TR indicates right shoulder tumor.

The cell uptake comparison among few different cell lines had shown that the lung cancer cell line HCC827 had a significantly higher probe uptake than any of the other cell lines tested

(GS025, GBM39, ParcB3, HCT-15) (Figure 3.7) and was used for *in vivo* study. Subcutaneous tumor HCC827 xenograft models had reached sufficient tumor size for imaging (~ 4 mm diameter) after 36 days when an initial imaging experiment was performed (Figure 3.8), followed by another study at 50 days post-implantation (Figure 3.9). Dynamic PET/CT scans were performed with injections of different molar activities. In all cases, the signal in the blood was high after injection and decreased over time. Muscle and tumor uptake rose gradually and plateaued at ~ 30 min, remaining nearly constant until the end of the scan. No bone uptake was observed in scans, confirming the lack of *in vivo* defluorination. Combined dynamic imaging data is summarized in Figure 3.10.

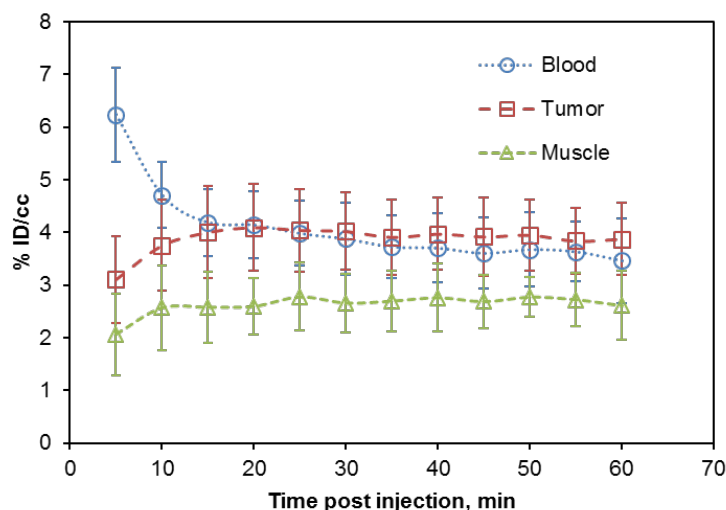


**Figure 3.10 Uptake curves for [<sup>18</sup>F]FET dynamic study**

Plotted are average values in ROI for tumor, blood (left ventricle of heart) and muscle (region near femur) is averaged over both imaging studies (i.e. averaged over n = 12 animals for heart and muscle, and averaged over n = 24 for tumors) to show general trends in dynamic biodistribution. Error bars represent standard deviation. %ID/cc is percent of injected dose per cubic centimeter.

The tumor to blood ratio increased during the first 15 – 20 min and then remained nearly constant for the rest of the scan, while the tumor to muscle ratio remained nearly constant throughout the scan. Qualitatively, it is apparent there is no strong correlation between the tumor uptake ratios and the molar activity values. Tumors imaged at low molar activity were as easily

visible as tumors imaged at high molar activity of the injected probe. The uptake ratios averaged during the final 30 – 60 min of the scans summarized for different molar activity values did not exhibit any correlation either (Figure 3.11). The statistically insignificant correlation between uptake ratios and molar activity was confirmed using a Spearman correlation test ( $r_s = -0.3$  for tumor to muscle ratio,  $r_s = 0.1$  for tumor to blood ratio).

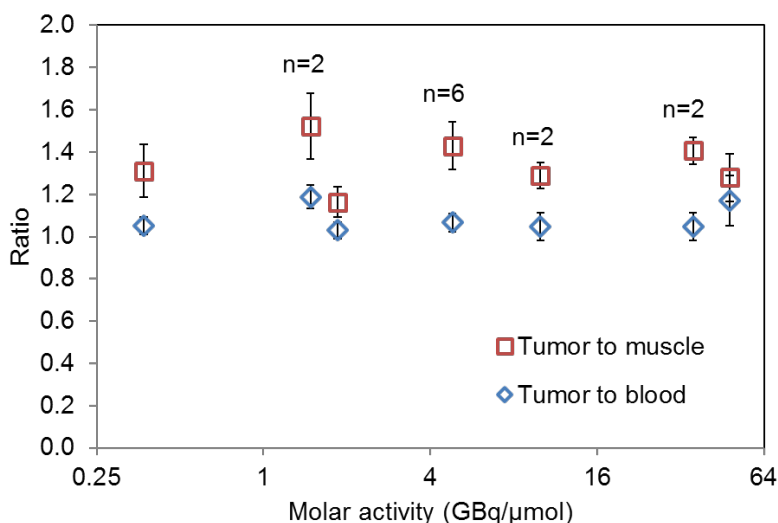


**Figure 3.11 Average tumor to muscle and tumor to blood ratios for different molar activities of [<sup>18</sup>F]FET**

Tumor to muscle and tumor to blood ratios averaged for all tumors within the same molar activity value group ( $n = 4$  except as otherwise indicated) and averaged over the dynamic imaging data from 30 – 60 min. Error bars represent standard deviation.

## 3.4 Discussion

### 3.4.1 Microscale synthesis

The microscale synthesis described here was performed quickly, reliably and in high yield, allowing production of the tracer for pre-clinical studies. A comparison of the performance of the microvolume synthesis compared to conventional synthesis is included in Table 2. The consumption of reagents was reduced drastically ( $> 150 \times$  less precursor) compared to conventional methods, while still achieving comparable RCY. Though optimization runs (requiring



numerous intermediate measurements), and batches for imaging (where molar activity adjustments were needed at the end) took longer to prepare, the fully-automated microvolume synthesis can be completed in 35 min (19 min synthesis + 6 min purification via analytical-HPLC + 10 min formulation). This is significantly faster than macroscale synthesis methods, and is a significant advantage when considering non-decay-corrected RCY. The short synthesis time originates from the smaller reaction volume, which enables faster temperature change and shorter solvent removal times, as well as from the low precursor mass, which enables the use of analytical scale HPLC purification rather than semi-preparative. Interestingly, the droplet method also resulted in shorter synthesis time and higher yield compared to recent reports of [ $^{18}\text{F}$ ]FET synthesis in smaller volumes (10s of microliters) using manual liquid manipulation or flow-through reactors (Table 3.4).

(190)	Conventional	Custom FDG module	14800	N/R	500	33-36 (n=?)	80	>18
(187)	Conventional	TracerLab FX <sub>FN</sub>	9000	18-41 (n=22)	2000	35±5 (n=22)	63	>90
(189)	Conventional	Modified GE TracerLab FX-C	13280	N.R.	1000	19±1 (n=?)	N.R.	N.R. <sup>b</sup>
(184)	Small volume in vial	300µL Reacti-vial	180-350	<0.4	10-20	N. R. <sup>c</sup> (n=3-6)	N.R.	N.R.
(186)	Small volume in vial	300µL Reacti-vial	350	0.95-2.6 (n=9)	20-30	38±6 (n=9)	60	570±240 (n=9)
(188)	Flow-through / capillary	Advion NanoTek® capillary reactor	59 <sup>d</sup>	0.005-0.2 <sup>d</sup> (n=?)	20	38 (n=?)	<45	N.R.

**Table 3.4 Comparison of performance of the microvolume droplet synthesis of [<sup>18</sup>F]FET and published results using conventional methods.**

N.R. = not reported. <sup>a</sup> Synthesis time includes purification and formulation, except Bouvet et al. which does not include formulation. <sup>b</sup> The paper assumes the molar activity value of the tracer is the same as the [<sup>18</sup>F]fluoride in the irradiated target, which is not valid. <sup>c</sup> The decay-corrected RCY was reported as 34 – 64%, but no synthesis time was given, so an estimate of the non-decay corrected RCY could not be made. <sup>d</sup> Unlike the other reaction formats, increasing the scale in a flow-through reactor requires increased reagent volumes and increased precursor consumption.

Under optimized conditions, a batch of [ $^{18}\text{F}$ ]FET suitable for preclinical imaging throughout the day (e.g. 37 – 110 MBq; assuming 0.93 – 7.4 MBq per injection for 5 – 10 mice) could be produced on the microscale platform starting with only 110 – 330 MBq of [ $^{18}\text{F}$ ]fluoride. Limiting the activity to relatively low levels in this manner could have significant advantages for shielding the apparatus (i.e., thinner shielding would be adequate) and possibly operating the synthesis outside of a hot cell.

The droplet synthesis (even with starting activities lower than 0.74 GBq) resulted in high molar activities, comparable to the values achieved on macroscale synthesizers starting with > 30 GBq of fluorine-18. It should be appreciated that, when the starting activity is scaled down in macroscale radiosynthesizers, one observes a linear decrease in the resulting molar activity (176). Thus, high amounts of starting activity must often be used in macroscale synthesizers, even if only a relatively small amount of the final tracer is needed. Compared to microscale synthesis, this can result in higher cost of the radioisotope, and the need for considerably more shielding to work with the higher activity levels.

Overall, the microvolume synthesis of radiopharmaceuticals has a number of advantages over conventional scale radiosynthesizers such as more compact apparatus, reduced shielding, rapid synthesis, high yield, and efficient use of radioisotope. These advantages have the potential to drive down the costs of materials and infrastructure, which can be a significant benefit for limited resource settings or preclinical tracer production. Another advantage – low precursor consumption – not only helps to simplify the purification step, but can also represent a significant cost reduction, especially for tracers with expensive precursors, or in situations where precursor is scarce, such as the development of novel tracers or optimization of synthesis protocols. While the strengths of this technology are in reducing costs of small batches of tracers, e.g. to support *in vitro* or preclinical studies, various microfluidic technologies are constantly improving and expanding their applications in the radiopharmacy field, and could also lead to improvements in

the efficiency of clinical PET tracer production in the future (91), such as enabling the production of additional tracers with minimal need for extra space or capital.

### 3.4.2 [<sup>18</sup>F]FET imaging

Over the range tested (0.37 – 48 GBq/μmol), the molar activity had no statistically significant effect on imaging of subcutaneous HCC827 tumors. [<sup>18</sup>F]FET accumulates in cells following transport by Na<sup>+</sup>-dependent and -independent amino acid transporters and is not incorporated into proteins over the time course of the imaging experiments (195,196). The results suggest that the [<sup>18</sup>F]FET transporters on the lung cancer cell line HCC827 do not become saturated within the range of molar activity values tested. Though the *in vitro* experiments suggest that the transporters can be “saturated” with sufficient concentration of FET in the media (i.e., 2.5 mM in the case “spiked” with FET; 0.15 μM in the non-spiked condition), the estimated concentration of FET in blood during the *in vivo* experiments was much lower (i.e. 3.5 μM for the lowest molar activity of 0.37 GBq/μmol, assuming 2 mL blood volume).

## 3.5 Conclusion

In this work the synthesis of [<sup>18</sup>F]FET was adapted to an automated microdroplet synthesis platform (106). The product was obtained in high RCY of up to 55 ± 7% (*n* = 4, decay-corrected) after purification, in sufficient quantities to perform a demonstration of a multi-animal dynamic PET imaging study, and could readily be scaled to higher amounts using radionuclide concentration methods (113). Synthesis time was shorter than conventional approaches, precursor consumption was reduced by two orders of magnitude, and the synthesis could be performed with a very small apparatus. The low precursor consumption enabled faster and simpler purification (i.e., analytical HPLC instead of semi-preparative HPLC), and, for tracers with expensive precursors, could help to reduce the synthesis cost. The molar activity was high (48 – 119 GBq/μmol at the end of synthesis), even when starting with activities as low as 0.3 GBq. Though low molar activity of [<sup>18</sup>F]FET, (down to 0.37 GBq/μmol) did not appear to adversely affect

imaging of subcutaneous tumors in this study, the ability to produce small batches with high molar activity may be important in other applications of this or other tracers.

## Chapter 4: Droplet synthesis of [<sup>18</sup>F]florbetaben ([<sup>18</sup>F]FBB)

### 4.1 Introduction

Positron emission tomography (PET) is a powerful molecular imaging tool with extensive applications in disease diagnostics and drug development, among other areas. Many tracers (labeled with positron-emitting isotopes) have been developed that can bind to specific molecular targets *in vivo* and allow tracking of their dynamics and location throughout the whole body. For example, a number of tracers were developed to target amyloid-beta (A $\beta$ ) plaques which are correlated with the progression of Alzheimer's disease (197), and it is believed that the high sensitivity and specificity of PET can aid in early diagnosis of dementia and its grading (198).

N-methyl-[<sup>11</sup>C]2-(4'-methylaminophenyl)-6-hydroxybenzothiazole ([<sup>11</sup>C]PIB), a radiofluorinated thioflavin T analogue, was the first selective radiotracer for Alzheimer's disease research and diagnostics (199). However, the short half-life of carbon-11 (20 min) restricts the access to this probe, especially at locations not having their own cyclotron and expertise in <sup>11</sup>C-radiochemistry, thus alternative tracers labeled with longer-lived isotopes (e.g. fluorine-18,  $t_{1/2}$  = 110 min) were developed. In fact, several <sup>18</sup>F-labeled amyloid imaging agents have been reported, including [<sup>18</sup>F]Florbetapir, [<sup>18</sup>F]Florbetaben and [<sup>18</sup>F]Flutemetamol, and were approved for use in clinical practice in the United States (200). In this work we focus on [<sup>18</sup>F]Florbetaben (also known by several other names: [<sup>18</sup>F]FBB, [<sup>18</sup>F]BAY94-9172, NeuraCeq, [<sup>18</sup>F]AV1, [<sup>18</sup>F]AV1/ZK), a stilbene derivative that was designed to selectively bind to A $\beta$  plaques (201). [<sup>18</sup>F]Florbetaben ([<sup>18</sup>F]FBB) and other similar tracers are extremely useful for studying cases of Alzheimer's disease both in the clinic and in research. Clinically, the tracers are used for accurate dementia grading and early detection in at-risk populations. In research, these tracers

are useful for testing of new treatments and understanding their influence on disease progression (202–207). Though the influence of molar activity in amyloid imaging has not been widely reported, in general preclinical imaging in small animal models (e.g. mice) requires tracers with high molar activity (57,59,208). There seem to be mixed reports about the importance of molar activity in small animal amyloid imaging (209), but it has been reported that detection of relatively immature (small and diffuse) amyloid lesions in mouse brain (with [<sup>11</sup>C]PIB) is especially sensitive to molar activity (210).

Further development and use of these tracers in a preclinical context is hindered by limited access and/or high cost of tracers such as [<sup>18</sup>F]Florbetaben. Current methods and reagent kits are optimized for large-scale production, making economical production of small batches not possible with current radiosynthesizer technologies. To address these concerns, we sought to optimize production of [<sup>18</sup>F]Florbetaben at the microliter scale while providing high-quality product suitable for *in vivo* preclinical applications. Due to the small physical size of microfluidic radiosynthesizers, very low amounts of reagents and radionuclide are needed, reducing the cost of materials and equipment, and required radiation shielding (98,106,181–183). The synthesis of multiple tracers and prosthetic groups have been successfully implemented in microliter droplet-reactor format, including [<sup>18</sup>F]FDG (104,106), [<sup>18</sup>F]fallypride (106,108,211), [<sup>18</sup>F]FET (50), [<sup>18</sup>F]FDOPA (212), [<sup>18</sup>F]AMBF<sub>3</sub>-TATE (105), [<sup>18</sup>F]SFB (213) and sulfonyl [<sup>18</sup>F]fluoride (214), providing a strong suggestion that [<sup>18</sup>F]Florbetaben could also be implemented.

To date there are no reported methods (droplet or other formats) for microfluidic synthesis of [<sup>18</sup>F]florbetaben. Synthesis of [<sup>18</sup>F]florbetaben via conventional methods typically follows a 2-step synthesis using an N-Boc-protected precursor (201,206,215,216), followed by semi-preparative HPLC purification and reformulation via C18 solid-phase extraction (SPE) (206,215,217). Here we develop an automated microliter droplet-based synthesis of this probe and demonstrate the benefits of using small scale production. The synthesis is performed in a

microdroplet reactor, with purification via analytical-scale HPLC, and formulation carried out on a system built in-house for small-volume SPE. The low-cost approach presented here uses tiny amounts of reagents and achieves high molar activity without the need for high starting activity (as required in traditional radiosynthesizers), producing high-quality [ $^{18}\text{F}$ ]Florbetaben readily applicable for small animal imaging and with potential of scaling up to clinical doses.

## 4.2 Materials and methods

### 4.2.1 Reagents

No-carrier-added [ $^{18}\text{F}$ ]fluoride was produced by the  $^{18}\text{O}(p, n)^{18}\text{F}$  reaction from [ $^{18}\text{O}$ ]H $_2\text{O}$  (84% isotopic purity, Zevacor Pharma, Noblesville, IN, USA) in an RDS-112 cyclotron (Siemens; Knoxville, TN, USA) at 11 MeV using a 1 mL tantalum target with havar foil. Acetonitrile (MeCN; anhydrous, 99.8%), methanol (MeOH; anhydrous, 99.8%), ethanol (EtOH; 200 proof, >99.5%), hydrochloric acid (HCl; 1M), dimethylsulfoxide (DMSO, 98%), deionized (DI) water, and polyethylene glycol 400 (PEG 400) were purchased from Millipore Sigma (St. Louis, MO, USA). All reagents were used as received without further purification. N-Boc protected mesylate FBB precursor ([methanesulfonic acid 2-{2-[2-(4-{2-[4-(tert-butoxycarbonyl-methyl-amino)-phenyl]-vinyl]-phenoxy]-ethoxy]-ethoxy}-ethyl ester) and FBB reference standard (4-[(E)-2-(4-{2-[2-(2-[ $^{18}\text{F}$ ]fluoroethoxy) ethoxy] ethoxy} phenyl) vinyl]-N-methylaniline) were generously provided by Life Molecular Imaging GmbH as a part of [ $^{18}\text{F}$ ]Florbetaben synthesis kits. Kryptofix 222 (K $_{222}$ ) and potassium carbonate (K $_2\text{CO}_3$ ) were purchased from ABX GmbH (Radeberg, Germany). Sodium phosphate dibasic (Na $_2\text{HPO}_4\cdot 7\text{H}_2\text{O}$ ) and sodium phosphate monobasic (NaH $_2\text{PO}_4\cdot \text{H}_2\text{O}$ ) were purchased from Fisher Scientific (Thermo Fisher Scientific, Waltham, MA). Ultrapure 18 M $\Omega$  water was acquired through a Milli-Q Integral 3 purification system (Millipore Sigma, St. Louis, MO, USA).

Dry scavenger mix (used in multiple steps of the reaction), consisting of sodium ascorbate with L-ascorbic acid (87:13 w/w), was obtained from the [ $^{18}\text{F}$ ]Florbetaben production



kits provided by Life Molecular Imaging GmbH. HPLC mobile phase was prepared by first dissolving 1.785 g of Na<sub>2</sub>HPO<sub>4</sub>·7H<sub>2</sub>O and 0.461 g of NaH<sub>2</sub>PO<sub>4</sub>·H<sub>2</sub>O in 0.40 L of 18 MΩ H<sub>2</sub>O to make 25 mM phosphate buffer (pH 7.2), then adding in 0.60 L of MeCN. Collection mixture to recover the crude [<sup>18</sup>F]Florbetaben from the chip consisted of MeCN mixed with 33 mg/mL dry scavenger mix in DI water (1:1, v/v). Stabilization / dilution solution for formulation contained 39 mg/mL of dry scavenger mix in a 4:13 (v/v) mixture of PEG 400 and DI water.

#### **4.2.2 Formulation system components and operation**

PFA tubing (0.125" OD x 0.0625" ID), PFA tubing (0.0625" OD x 0.02" ID), and 1/4-28" fittings and unions (for 0.125" OD and 0.0625" OD tubing) were purchased from IDEX Corporation (Lake Forest, IL, USA). The larger tubing was used for the 3-way valve to waste line; smaller tubing was used for all other fluid connections. The Rheodyne model EV750-105 selector valve was purchased from IDEX, and the data acquisition module (DAQ) model E-1608 was purchased from Measurement computing (Norton, MA). The 3-way liquid valve model LVM105R-5C-2, pressure regulator model ITV0050-2UL (with 0.001-0.9 MPa output), 3-port solenoid valves model S070B-5DG (vacuum to ~0.5MPa), mounted on a manifold bar base (SS073-B01-03 C), were all purchased from SMC Pneumatics (SMC, Japan).

A schematic of the automated formulation system is shown in the Figure 4.1 and a photograph of the system is shown in Figure 4.4. Control of all electronic components was performed by controlling a DAQ with a custom interface created in LabView (National Instruments). The input of the pressure regulator was connected to a nitrogen source (set at 58 psi) and the output connected to 3 separate 3-way pneumatic valves for supplying pressure to the headspace of the purified product vial (for trapping step), DI water reservoir (for washing step), and EtOH reservoir (for elution step). The analog voltage from the DAQ to the pressure regulator was calibrated to enable precise control of pressure from the LabView program. On/off positions of the 3-way liquid valve and pneumatic valves were switched by a DAQ-controlled

custom Darlington board. The input of the micro-cartridge was connected via the selector valve to the product vial, DI water reservoir and EtOH reservoir, and the output of the cartridge was connected via the 3-way liquid valve to either waste or the formulated product vial.

#### 4.2.3 Analytical methods

A calibrated ion chamber (CRC 25-PET, Capintec, Florham Park, NJ, USA) was used to perform radioactivity measurements. For radio-thin-layer chromatography (radio-TLC) analysis, reverse phase TLC plates (RP-18 silica gel 60 F254 sheets; aluminum backing; Millipore Sigma, St. Louis, MO, USA) were cut into 15 x 60 mm pieces (with 40 mm developing distance), spotted with 1  $\mu$ L of the sample and developed in 90% (v/v) MeCN in H<sub>2</sub>O. TLC plates were analyzed with a Cerenkov luminescence imaging system as previously described (218) or a conventional radio-TLC scanner (miniGita star, Raytest, Inc., Wilmington, NC, USA). Retention factors of the observed radioactive species were: 0.0 ([<sup>18</sup>F]fluoride), 0.4 ([<sup>18</sup>F]FBB), and 0.8 (fluorinated intermediate).

Radio-HPLC analysis (and purification) were performed on an analytical-scale Smartline HPLC system (Knauer, Berlin, Germany) with 200  $\mu$ L injection loop, a pump (Model 1000), degasser (Model 5050), UV detector (Model 2500) and a radiometric detector (Bioscan B-FC-4000, Bioscan Inc., Washington DC, USA). Samples were separated using a C18 column (Luna, 5  $\mu$ m particles, 100Å pores, 250 x 4.6 mm, Phenomenex, Torrance, CA, USA) with guard column (SecurityGuard C18, Phenomenex). UV absorbance was measured at 254 nm. Using isocratic conditions with a MeCN : 25 mM phosphate buffer 60:40 (v/v) mobile phase delivered at 1.5 mL/min, the observed retention time of [<sup>18</sup>F]fluoride was between 2-3 min, 6 min for [<sup>18</sup>F]FBB, and 14 min for the fluorinated intermediate.

#### 4.2.4 Droplet synthesis production setup

Radiochemistry was performed in droplet format using Teflon-coated silicon chips that had small circular regions of Teflon etched away, leaving hydrophilic patches that act as surface-tension traps to confine reagents during the multi-step radiosynthesis. Temperature control was achieved by affixing the chip atop a ceramic heater with thermal paste. The details of the chip fabrication were previously reported (106). Initially, the conditions were optimized manually using chips containing 4 reaction sites (111) on a platform with 4 heaters. Based on optimized conditions, the synthesis was adapted onto an ultra-compact automated droplet radiosynthesizer (108) allowing for reduced radiation exposure and operation time via automation.

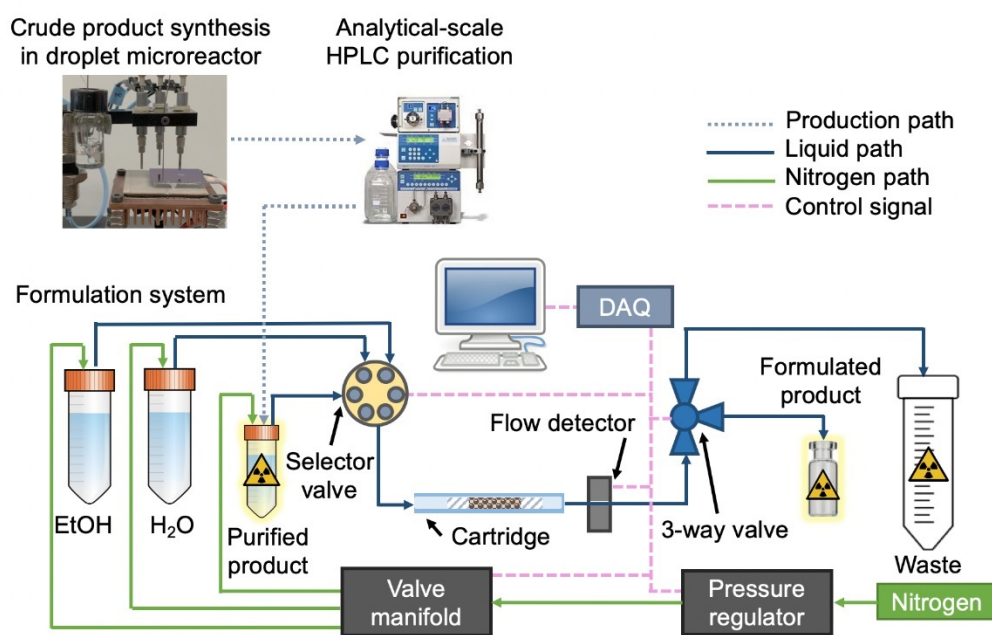


**Figure 4.1 Overview of microvolume synthesis procedure for  $[^{18}\text{F}]$ FBB, with detailed schematic of the formulation system (bottom).**

The overall setup comprises a droplet synthesizer, analytical-scale HPLC purification, and a newly-developed automated solid-phase extraction setup to perform formulation using custom micro-cartridges with C18 resin (Figure 4.1). Briefly, the inlet of the cartridge was connected to a selector valve and the outlet to a 3-way valve. Using the selector valve, different

solutions could be flowed through the cartridge such as the [ $^{18}\text{F}$ ]FBB fraction vial (trapping step), a vial with aqueous sodium ascorbate solution (washing step), and a vial with ethanol (elution step). The 3-way valve was used to direct the cartridge output to waste (trapping and washing steps) or the product vial (elution step). The liquid movement was initiated by applying nitrogen pressure to the vials containing [ $^{18}\text{F}$ ]FBB (15 psi), water (15 psi) and ethanol (3 psi). A program written in LabView (National Instruments, Austin, TX) automatically controlled the valves and pressure sources via a data acquisition module (DAQ) to complete the trapping, washing, and elution steps.

#### **4.2.5 Microvolume radiosynthesis optimization**

The microvolume synthesis was adapted from the common 2-step approach, which consists of fluorination of the Boc-protected precursor using [ $^{18}\text{F}$ ]KF/ $\text{K}_{222}$ , followed by a hydrolysis step (201). A schematic representation of the microvolume synthesis process is shown in Figure 4.2.

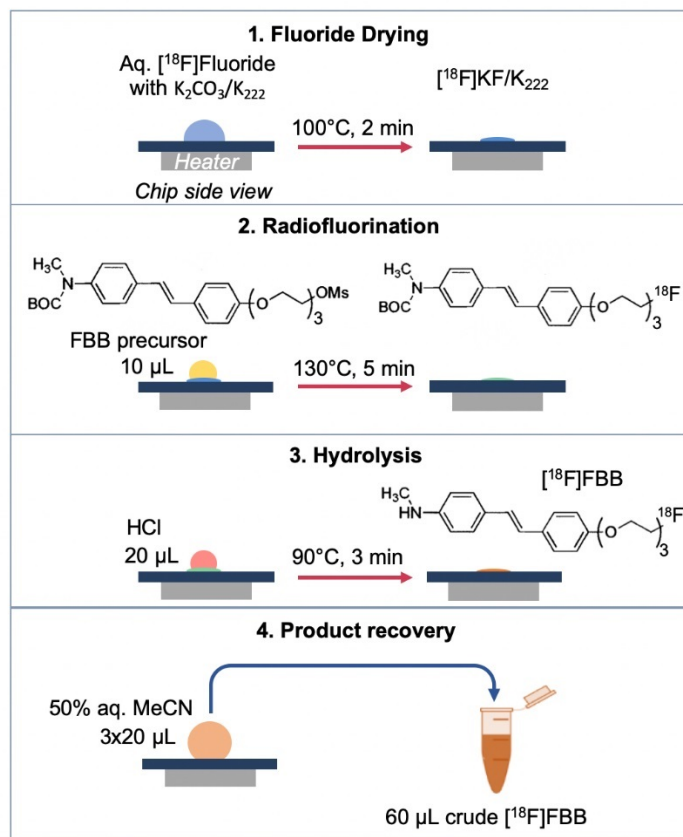


**Figure 4.2 Schematic of the microscale synthesis of crude [<sup>18</sup>F]FBB.**

Initial pre-optimization conditions for microvolume synthesis were selected by scaling down the conventional synthesis conditions reported in Collins *et al.* (219). The fluorination reaction volume was reduced 90-fold from 1.8 mL to 20 μL, but the precursor concentration was maintained at 4 mM, resulting in a precursor amount of 120 nmol. The fluorination solvent was changed from MeCN to DMSO, since MeCN evaporated too quickly in droplet format. The total amount of cryptand phase-transfer catalyst was reduced 180-fold (from 49 μmol to 275 nmol of K<sub>2</sub>CO<sub>3</sub> and from 68 μmol to 383 nmol of K<sub>222</sub>). First, the effect of temperature on the fluorination reaction was studied, followed by optimization of the amount of K<sub>2</sub>CO<sub>3</sub>/K<sub>222</sub>, and then amount of precursor. Each set of conditions was repeated n = 4 times, with reagents delivered manually via pipette.

For each experiment, aqueous [ $^{18}\text{F}$ ]fluoride (10-20  $\mu\text{L}$ ;  $\sim 7.4 - 370 \text{ MBq}$ ) was mixed with the desired amount of  $\text{K}_{222}/\text{K}_2\text{CO}_3$  in 4.5  $\mu\text{L}$   $\text{H}_2\text{O}$  and loaded to the reaction site to be evaporated to dryness at 100  $^\circ\text{C}$  for 2 min. Next the desired amount of precursor in DMSO was added to the dried fluoride residue and reacted at the desired temperature for 5 min. For initial optimization experiments the crude product of the fluorination reaction was collected and analyzed. In other cases, the hydrolysis step was performed by adding 20  $\mu\text{L}$  of 1N HCl to the reaction mixture and heating at 90  $^\circ\text{C}$  for 3 mins. To recover the crude product (or intermediate), 20  $\mu\text{L}$  of collection mixture was added to resuspend the product on chip, and then transferred into the crude product vial. To ensure thorough recovery from the chip, the collection procedure was repeated 2 more times (3 more times for the automated setup). To avoid radiolysis and photodegradation, the crude product vial was preloaded with 64  $\mu\text{L}$  of water with 33 mg/mL of dry scavenger mix and kept in the dark.

#### **4.2.6 Automated microvolume synthesis**

The automated synthesis of [ $^{18}\text{F}$ ]FBB was performed on identical chips, but using a custom-built platform (108) that supported automated reagent dispensing and product recovery. The reaction conditions were identical to the optimized manual synthesis conditions, except that the deprotection was performed using 1M HCl:MeCN 1:1 (v/v). This 20  $\mu\text{L}$  acidic mixture was dispensed at the beginning of deprotection and another 20  $\mu\text{L}$  after 1.5 min. The diluted acid was used to reduce damage to the reagent dispensers.

#### **4.2.7 Purification and formulation**

To perform purification, the crude product collected in aqueous scavenger solution was diluted with aqueous sodium phosphate buffer to a total volume of 175  $\mu\text{L}$  and delivered into an analytical radio-HPLC system with 200  $\mu\text{L}$  injection loop, and separated as described in the “Analytical methods” section. The [ $^{18}\text{F}$ ]FBB peak (retention time 6 min) was collected (for 1.0 –

1.5 min) into a 50 mL conical tube (Falcon, Corning, USA) pre-loaded with 33 mg/mL dry scavenger mix in 3 mL water and covered by aluminum foil.

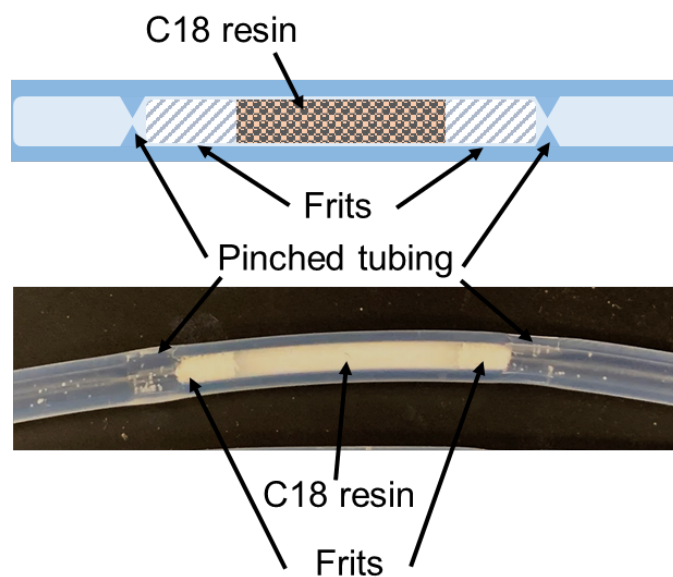


**Figure 4.3 Schematic (above) and photograph (below) of the microscale C18 cartridge used for [<sup>18</sup>F]florbetaben formulation.**

Formulation was performed by diluting the purified [<sup>18</sup>F]FBB with 30 mL of DI water, and carrying out solid phase extraction (SPE) using a miniature C18 cartridge made by packing C18 resin (5 or 10 mg) into lengths of tubing. The tubing was stretched slightly (~10 % length increase) prior to using to reduce the inner diameter allowing for a tighter fit with the frits, then cut into 10 cm long pieces. One small frit was cut from the larger frit piece using a 1/16" biopsy punch and directly pushed out from the punch into one end of the tubing (the "input" side). Using a thin rod, the frit was push until it was 2.5 cm distance into the tubing. The tubing next to the frit was gently pinched to prevent frit movement. The C18 resin was obtained by emptying a commercial C18 cartridge. The desired mass of resin (10 mg) was weighed in a PCR tube to which 200  $\mu$ L of MeOH was added and stirred. To load the slurry into the tubing, the cartridge was connect to vacuum on the input side of the tubing, and the output end was dipped into the PCR tube, drawing the resin into the tubing. The PCR tube was filled with additional MEOH and vacuum was applied to ensure all resin ended up inside the tubing-cartridge. This washing was

performed twice. After the resin was loaded, another frit was inserted from the “output” side of the tubing, pushed gently until it touched the resin, and then the tubing was pinched to fix all the components in place. A diagram and photograph are shown in Figure 4.3. Preconditioning of miniature cartridges was performed with 5 mL MeOH followed by 6 mL of DI water at approximately 1 mL/min. An automated solid-phase extraction setup was built to perform the formulation step (Figure 4.1). In the final formulation procedure, the diluted [ $^{18}\text{F}$ ]FBB was trapped on the cartridge, and then the cartridge was washed by flowing through 10 mL DI water containing 10 mg/mL of dry scavenger mix to remove residual solvents and impurities. (The amount of scavenger is the same as reported by Rominger *et al.* (206)). Finally, the trapped [ $^{18}\text{F}$ ]FBB was eluted from the cartridge using 150  $\mu\text{L}$  EtOH into an amber-colored glass product vial preloaded with 850  $\mu\text{L}$  of stabilization solution.

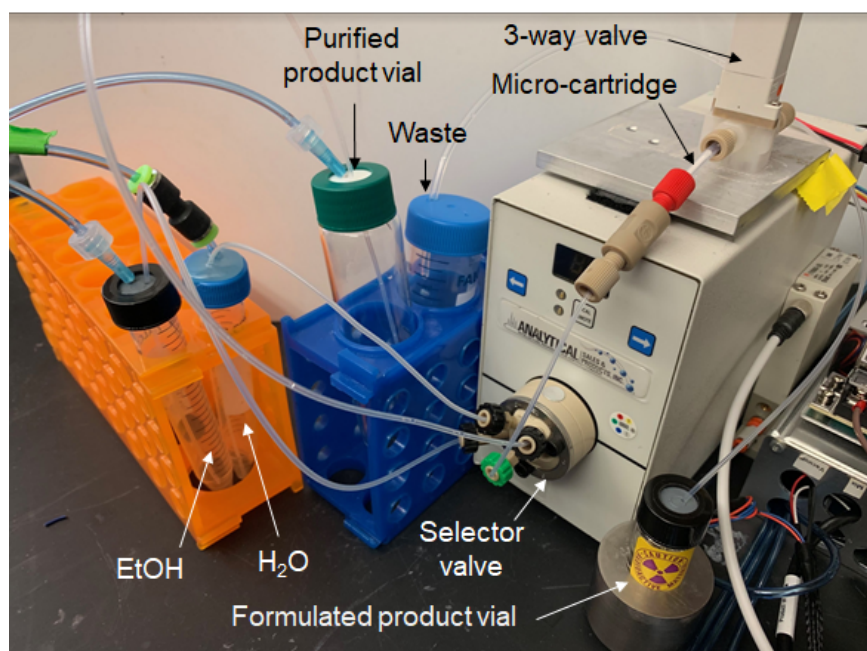


**Figure 4.4 Photograph of the automated formulation system.**

#### **4.2.8 Evaluation of synthesis performance**

Multiple measurements were collected during the synthesis to calculate several parameters related to the synthesis performance. Unless otherwise specified, all reported percentage values (yields, efficiencies) are decay-corrected (d.c.). Starting activity was



determined by calculating a difference in activity measurements of a source vial before and after addition of the radionuclide from the vial to the chip (accounting for losses in pipette tips). Collection efficiency is the ratio of activity of the crude reaction mixture recovered from the chip relative to the starting activity. Residual chip activity is the percentage of starting activity that remained on the chip after the synthesis and crude reaction mixture recovery. Radiochemical conversion is the percentage of the desired product ( $[^{18}\text{F}]\text{FBB}$ ) in the crude mixture as determined by radio-TLC. Crude  $[^{18}\text{F}]\text{FBB}$  radiochemical yield (crude RCY) is calculated by multiplying the collection efficiency by the radiochemical conversion. Isolated yield is the ratio of the activity of the purified product collected after HPLC purification to the starting activity. Formulated product yield is calculated by dividing the activity of the final formulated product by the starting activity.

To carefully evaluate the formulation performance, additional parameters were calculated relative to the activity of pure  $[^{18}\text{F}]\text{FBB}$  fraction obtained after HPLC purification. The formulation efficiency is the ratio of formulated product activity to the activity of the  $[^{18}\text{F}]\text{FBB}$  fraction. Activity in waste is the ratio of activity in the waste container relative to the  $[^{18}\text{F}]\text{FBB}$  fraction, and fraction collection vial residual activity is the percentage of activity remaining in the initial  $[^{18}\text{F}]\text{FBB}$  fraction vial after the formulation process is complete. Cartridge residual activity is the percentage of the initial  $[^{18}\text{F}]\text{FBB}$  activity that remained on the cartridge after formulation. Residual in the system is the percentage of the initial  $[^{18}\text{F}]\text{FBB}$  fraction that was not recovered (i.e. remaining in various portions of the formulation system, e.g. valves, tubing, etc.).

## **4.3 Results**

### **4.3.1 Microvolume radiosynthesis optimization**

The influence of fluorination temperature, base amount, and precursor concentration on the fluorination step (as measured by the resulting amount of fluorinated intermediate) is summarized in Figure 4.5. Fluorination efficiency increased as temperature was increased from

90 to 130 °C, and while there was a very slight reduction in collection efficiency over this temperature range, the overall RCY of the intermediate increased with increasing temperature (Figure 4.5A). We thus chose 130 °C as the optimal reaction temperature. The amount of base had a more complex influence on reaction performance (Figure 4.5B). At low base amount (< 70 nmol  $K_2CO_3$  / 100 nmol  $K_{222}$ ), the collection efficiency, fluorination efficiency and RCY of the intermediate increased strongly with base amount, while at moderate amounts (70 - 280 nmol  $K_2CO_3$  / 100 - 390 nmol  $K_{222}$ ), there was relatively little change and the RCY remained nearly constant. Higher amounts of base led to a gradual reduction in fluorination efficiency and RCY of the intermediate (though collection efficiency was constant). Based on this data, the optimal base quantity was 275 nmol  $K_2CO_3$  / 383 nmol  $K_{222}$ . For low precursor amount (< 40 nmol), there was a rapid increase in fluorination efficiency (and RCY of the intermediate) as precursor amount was increased, and at higher amounts, the slight decrease in collection efficiency canceled out the slight increase in fluorination efficiency resulting in nearly constant RCY of the intermediate (Figure 4.5C). We chose 80 nmol of precursor as the optimum value. Using the optimal conditions together, the RCY of the fluorinated intermediate (without deprotection) was  $70 \pm 6\%$  (n=4).

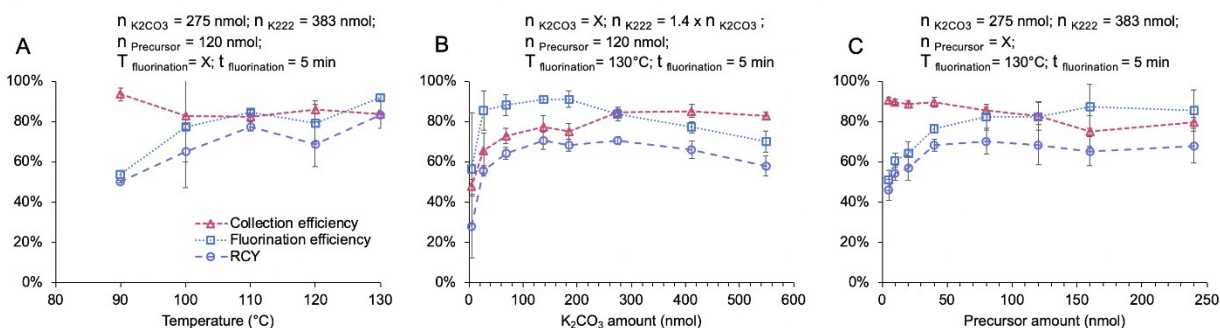


**Figure 4.5 Optimization summary of fluorination step**

For all reactions, [ $^{18}F$ ]Fluoride (aq) was evaporated to dryness with 4.5  $\mu$ L of base and phase-transfer catalyst in DI  $H_2O$ , then reacted with 20  $\mu$ L precursor in DMSO for 5 minutes. The resulting product was analyzed via radio-TLC. (A) Effect of temperature on reaction performance; (B) Effect of base amount on the reaction ( $K_{222}$  amount is 1.4x that of  $K_2CO_3$ ); (C) Effect of precursor concentration on the reaction. Data points represent the average of n = 4 repeat measurements, and error bars represent standard deviations. In each panel, the

changing variable is listed with an “X” (above the graphs), and the fixed values of all other parameters are as indicated. The legend from A applies to all panels.

It was observed that there was a residual volume of DMSO left at the end of the fluorination reaction. Concerned that this DMSO would adversely affect downstream purification on the analytical scale HPLC (as observed previously in our lab) and would dilute the deprotection solution, we opted later to reduce the reaction volume to 10  $\mu$ L. Based on our optimization data seen in Figure 4.5, we did not expect much change in performance by this effective doubling of base and precursor concentrations.

After this change, the amount of residual DMSO was reduced, and after deprotection with 20  $\mu$ L of 1 M HCl, the crude RCY of [ $^{18}$ F]FBB was  $63 \pm 6\%$  (n=4) (i.e.,  $66 \pm 6\%$  collection efficiency and  $96 \pm 1\%$  radiochemical conversion). When the synthesis was automated and performed at similar activity levels ( $\sim 7.4$  MBq starting activity), we observed a crude RCY of  $58 \pm 7\%$  (n=5) (i.e.,  $69 \pm 9\%$  collection efficiency,  $86 \pm 9\%$  radiochemical conversion).

	<b>Manual Synthesis</b>	<b>Automated Synthesis</b>
	n = 3	n = 3
<b>Starting activity (MBq)</b>	$260 \pm 100$	$330 \pm 120$
<b>Collection efficiency (%)</b>	$87 \pm 1$	$83 \pm 3$
<b>Residual chip activity (%)</b>	$0.4 \pm 0.2$	$1.2 \pm 0.3$
<b>Radiochemical conversion of the crude (%)</b>	$88 \pm 6$	$72 \pm 4$
<b>Crude [<math>^{18}</math>F]FBB yield (%)</b>	$78 \pm 6$	$60 \pm 5$
<b>Crude synthesis time (min)</b>	$30 \pm 8$	$28 \pm 1$
<b>Isolated [<math>^{18}</math>F]FBB yield (%)</b>	$61 \pm 2$	$53 \pm 8$
<b>Molar activity d.c.* (GBq/<math>\mu</math>mol)</b>	$370 \pm 60$	$260 \pm 80$

**Table 4.1 Summary of synthesis performance**

Results are shown for syntheses performed manually or on the automated setup. All % values are calculated in reference to starting activity. \*Molar activity is reported at the end of HPLC purification.

To produce quantities compatible with preclinical applications, further experiments were carried out with  $\sim 300$  MBq starting activity level and the results are summarized in Table 4.1.

Using the manual procedure for crude synthesis, the crude RCY was  $78 \pm 6$  (n = 3) (i.e.  $87 \pm 1\%$

collection efficiency and  $88 \pm 6\%$  radiochemical conversion). The automated synthesis with  $\sim 300$  MBq starting activity resulted in  $60 \pm 5\%$  ( $n = 3$ ) crude RCY ( $83 \pm 3\%$  collection efficiency,  $72 \pm 4\%$  radiochemical conversion).

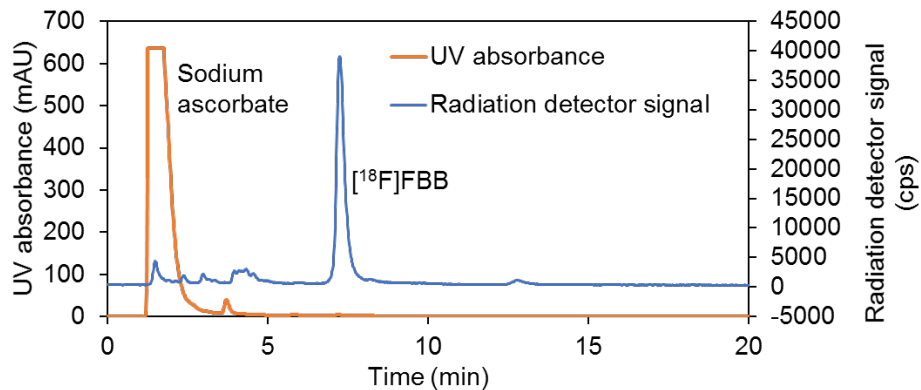


**Figure 4.6 Example HPLC chromatogram of a crude [<sup>18</sup>F]FBB sample.**

#### 4.3.2 Purification

The crude [<sup>18</sup>F]FBB was purified using isocratic analytical scale radio-HPLC (Figure 4.6). The product was collected in  $\sim 3$  mL volume, taking  $\sim 12$  min for purification. In manual runs with  $\sim 300$  MBq of starting activity, the isolated yield after purification was  $61 \pm 2\%$  ( $n=3$ ) with molar activity of  $370 \pm 60$  GBq/ $\mu$ mol decay-corrected to the end of purification (Table 4.1). Similarly, the equivalent experiments using automated procedure of the crude synthesis resulted in  $53 \pm 8\%$  ( $n = 3$ ) isolated yield and  $260 \pm 80$  GBq/ $\mu$ mol molar activity.

### 4.3.3 Formulation

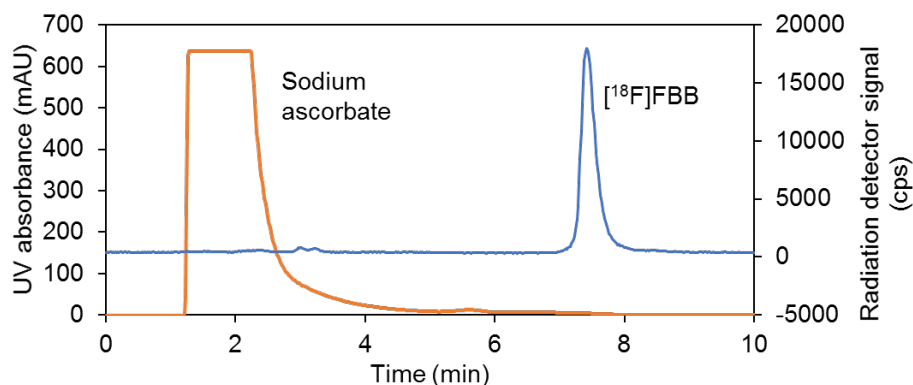


**Figure 4.7 Example HPLC chromatogram from a formulated sample of [<sup>18</sup>F]FBB (98% radiochemical purity).**

To ensure sufficient activity concentration of the formulated [<sup>18</sup>F]FBB, we developed custom-made miniature C18 cartridges with small bed volumes that could be eluted with a significantly reduced amount of EtOH compared to conventional C18 Sep-pak cartridges. To assess trapping capacity during preliminary runs of the formulation protocol, we used 5 nmol of FBB reference standard spiked with small amount of purified [<sup>18</sup>F]FBB (15 MBq) to simulate moderate activity levels. (In syntheses starting with ~370 MBq activity, we determined from the HPLC purification chromatogram that the mass of FBB was  $0.7 \pm 0.3$  nmol ( $n=3$ ), therefore addition of 5 nmol would roughly correspond to a ~2.6 GBq batch of [<sup>18</sup>F]FBB.) When performing trapping with 5 mg resin only 77% of the product activity was trapped on the cartridge and 19% of the activity was found in waste (untrapped), and 77% of the initial [<sup>18</sup>F]FBB was recovered at the end of elution. However, trapping was more efficient for the 10 mg resin cartridge with only  $1 \pm 1\%$  ( $n=3$ ) lost in waste (untrapped), and the elution recovered  $91 \pm 5\%$  ( $n=3$ ) of the initial [<sup>18</sup>F]FBB. Results are summarized in Table 4.2. Due to the nearly quantitative trapping performance, 10 mg cartridges were used for the remaining experiments.

	Manual Formulation*	Manual Formulation*	Automated Formulation
Mass of C18 resin in cartridge (mg)	5	10	10
Number of repeats	$n = 1$	$n = 3$	$n = 3$
Starting pure [ <sup>18</sup> F]FBB activity (MBq)	7.4	$15 \pm 11$	$112 \pm 51$

Formulation efficiency (%)	77	91 ± 5	81 ± 5
Formulation time (min)	18	22	17
<b>Losses:</b>			
Activity in waste (%)	19	1 ± 1	3 ± 3
Fraction collection vial residual activity (%)	3	6 ± 4	2 ± 1
Cartridge residual activity (%)	0	0 ± 1	1 ± 1
Residual in the system (%)	N/A	N/A	14 ± 4

**Table 4.2 Summary of performance of the formulation step**

All % values are calculated in reference to starting pure [<sup>18</sup>F]FBB activity. \*Initial manual formulation runs were performed using 5 nmol of FBB spiked with purified [<sup>18</sup>F]FBB product, to mimic the mass loading of a higher activity level, while working with less radioactivity.

These experiments were repeated using the automated formulation system (with 10 mg cartridge), resulting in 81 ± 5% (n=3) recovery of the initial pure [<sup>18</sup>F]FBB using 150 µL EtOH, which was collected into 850 µL of stabilization solution. After 25 min formulation of 110 ± 50 MBq (n=3) of activity, there was 1 mL of 77 ± 35 MBq (n=3) of injection ready product. Minor activity losses were measured 3 ± 3% (n=3) in waste after trapping and washing steps, and only 1 ± 1 % remained on the cartridge, however it was observed that 14 ± 4% of the initial activity remained unaccounted for within the formulation system components (Table 4.2). Residual activity in the formulation system components was difficult to accurately measure, but substantial portions were found in the fluid path used in trapping. In the future it can be possible to perform additional rinsing step to improve product recovery.

In summary, after total of 55 min synthesis time (30 for crude synthesis, 8 min for purification and 17 min for formulation) the radiochemically pure (>98%) [<sup>18</sup>F]FBB was acquired (Figure 4.7) in 49 ± 3 % (n=3) yield with measured 340 ± 60 GBq/µmol molar activity at the end of synthesis.

## 4.4 Discussion

### 4.4.1 High-throughput optimization

Initial optimization of the reaction was performed using high-throughput techniques (i.e., multiple reactions in parallel) (111), allowing the study of multiple reaction parameters with a high number of replicates. Notably, testing 21 sets of conditions (altering 3 parameters) with  $n = 4$  repeats for each condition (a total of 84 experiments) was performed in only 6 radiochemistry sessions (12 hours). Optimization of each parameter was performed sequentially in a one variable at a time (OVAT) fashion, and it is possible that additional iterations of optimization using parameters from the previous round, or more efficient and comprehensive optimization approaches such as design of experiments (DoE), could yield slight improvements, but this was not explored here.

Having extensive data about the overall impact of each parameter can be used to increase the robustness of a synthesis, i.e. by choosing parameter values where the performance is insensitive to variances in the variable (close to horizontal slope). While our optimization focused on yield, the data could also be used to optimize other outcomes, for example, minimizing the amount of precursor (to minimize cost or simplify purification) while achieving an acceptable yield.

### 4.4.2 Purification and formulation

In this work purification was performed via analytical scale HPLC, which has been previously reported for purification of tracers produced in microfluidic systems (50,98,106,108,211,212). Analytical-scale purification allows very short purification times (several min) and small volume (~1-2 mL) of pure fraction. The simplest purification and formulation route for [ $^{18}\text{F}$ ]florbetaben (and the one recommended for the Life Molecular Imaging kits) would be purification via ethanolic mobile phase (sodium ascorbate buffer:EtOH, 40:60, v/v) such that the collected fraction can be formulated simply by dilution. However, when scaling

to an analytical HPLC system, the pressure limit was exceeded for amounts of EtOH > 20% (v/v) at 1 mL/min, and the late retention time of [<sup>18</sup>F]FBB when using lower amounts of EtOH was not practical. It is possible that other column types or sizes could avoid this problem, but we instead used an MeCN-based mobile phase for separation, which required a downstream formulation step to remove the acetonitrile after purification. Under this condition, the crude product was rapidly and efficiently purified and collected within 8 min of injecting the crude reaction mixture.

Initially, we tried evaporative solvent exchange to remove MeCN, performing evaporation at 100 °C followed by resuspension of the dried product in PBS. However, evaporation of 2-3 mL of volume of collected crude product took a significant amount of time (15 min). We also observed the solution change from clear to cloudy, and after resuspension in formulation buffer, a significant amount of product (~70% of initial pure [<sup>18</sup>F]FBB) was stuck to the vial, likely due to the poor solubility of this compound.



Reference	This work	(201)	(217)	(220)	(206)	(215)	(219)	(221)
Number of replicates	n=3	NR	NR	n=4	NR	n=10	n=3	NR
Precursor amount (mg)	0.052	4	NR	5	5	NR*	7	5
Reaction solvent	DMSO	DMSO	NR	DMSO	MeCN	NR*	MeCN	MeCN
Reaction volume (mL)	0.01	0.2	NR	0.5	1	NR*	1.8	1
Formulated product yield (%; d.c.)	49 ± 3	30***	NR	23 ± 3	18	7.8 ± 2.6	60 ± 9 **	18
Formulation method	SPE (micro C18 cartridge)	NR	SPE (Sep-pak C18)	SPE (Sep-pak plus C18)	SPE (Sep-pak light C18)	SPE (Strata-X 33 µm, reversed phase)	NR	SPE (Sep-pak light C18)
Synthesis time (min)	55	90***	60	45****	75	50	44**	75
Molar activity at EOS (GBq/µmol)	340 ± 60	48 - 56	170	25 - 30	80	220 ± 170	NR	50-90

**Table 4.3 Comparison of the performance of the microscale synthesis reported in this work to literature methods**

Abbreviations: NR = not reported; EOS = End of synthesis; SPE = solid-phase extraction.

\* The conditions are not reported precisely, but the Zhang et al. method is cited as a reference for the procedure.

\*\* The reported data is up to the end of HPLC purification (excluding formulation). Yield is therefore overestimated and synthesis time underestimated.

\*\*\*The formulation procedure is not reported or discussed. Yield may be an overestimate and synthesis time an underestimate.

\*\*\*\*In this rapid method, purification was performed with SPE (no HPLC), but not all impurities were removed.

Instead, formulation via solid-phase extraction was explored using a C18 cartridge as widely reported by others (Table 4.3) (206,215,217). However, commercial C18 cartridges (Waters Sep-pak C18 Plus Light, 130 mg, Waters Corporation, Milford, MA) were not suitable for small batch syntheses: to efficiently elute the product from the cartridge, 1-2 mL EtOH was needed, which would then be diluted with stabilizing solution to a total volume of 7-14 mL to lower the EtOH concentration to 15% (acceptable limit for the formulation of this probe). For preparation of small batches of [<sup>18</sup>F]FBB (e.g. < 185 MBq), the resulting concentration (<26

MBq/mL) would be too dilute for small animal imaging. Instead, we explored the use of custom miniature cartridges made by packing C18 resin into lengths of tubing, which allowed minimization of the final formulated volume. Cartridges made inside 0.02" ID tubing exhibited extremely low flow rates, but cartridges packed inside 0.0625" ID tubing had suitable flow rates. With these miniature cartridges, the product could be efficiently recovered with only 150  $\mu$ L EtOH, enabling formulation (to dilute EtOH to an acceptable level of 15%) in a final volume of 1 mL.

Unfortunately, the formulation requires extra time (17 min), leading to some radioactive decay during the process. The formulation process was very efficient when performed manually, however the presence of extra fluidic components in the automated system resulted in slightly reduced efficiency. Additional losses in the automated formulation system resulted in a 10 point drop in formulation efficiency compared to manual method (i.e. 81% versus 91%).

In the current formulation protocol, the trapping step takes up the majority of time, requiring ~10 min in total to process nearly 30 mL of volume, while the washing and elution steps take 3 and 4 min, respectively. Possible directions for improvement would be to optimize the HPLC purification method to reduce peak width and collection volume, leading to a lower dilution volume, or optimizing the applied pressure during trapping to achieve both highest trapping efficiency and flow rate.

#### **4.4.3 Probe stability and radiolysis**

It has been reported that N-methylaniline substituents can make this, and structurally similar, beta-amyloid PET tracers, quite susceptible to radiolysis (222). In fact, significant radiolysis (8 point reduction in radiochemical purity) was already observed within 10 min for [ $^{18}$ F]AV-19 in isotonic saline with 5% EtOH at a modest activity concentration of 185 MBq/mL. Scott *et al.* found that addition of appropriate radical scavengers extended stability of the compound to multiple hours even in larger scale productions yielding 7.4 GBq of product (222).

To ensure highest radiochemical purity and stability of [ $^{18}\text{F}$ ]FBB produced with microvolume method, the scavenger had to be introduced at various steps of the production. Using literature reports as a guide (206,222), scavenger was introduced into the collection solution during collection of the crude product from the chip, pre-loaded in the collection vial prior to recovery of the pure fraction from HPLC, in the dilution solution used prior to formulation, and pre-loaded in the final product vial.

Evidence of radiolytic degradation is shown in the chromatograms of Figure 4.8. Both samples were obtained after fraction collection from HPLC and stored in amber glass vials. For the upper chromatogram, a 0.2 mL (~7 MBq) aliquot was taken and diluted with 1 mL sodium ascorbate solution (33 mg/mL in DI water), and stored for 2 h. For the lower chromatogram, 0.2 mL (~7 MBq) of the same purified sample was stored at room temperature in the HPLC mobile phase (no ascorbate) for 2 h.

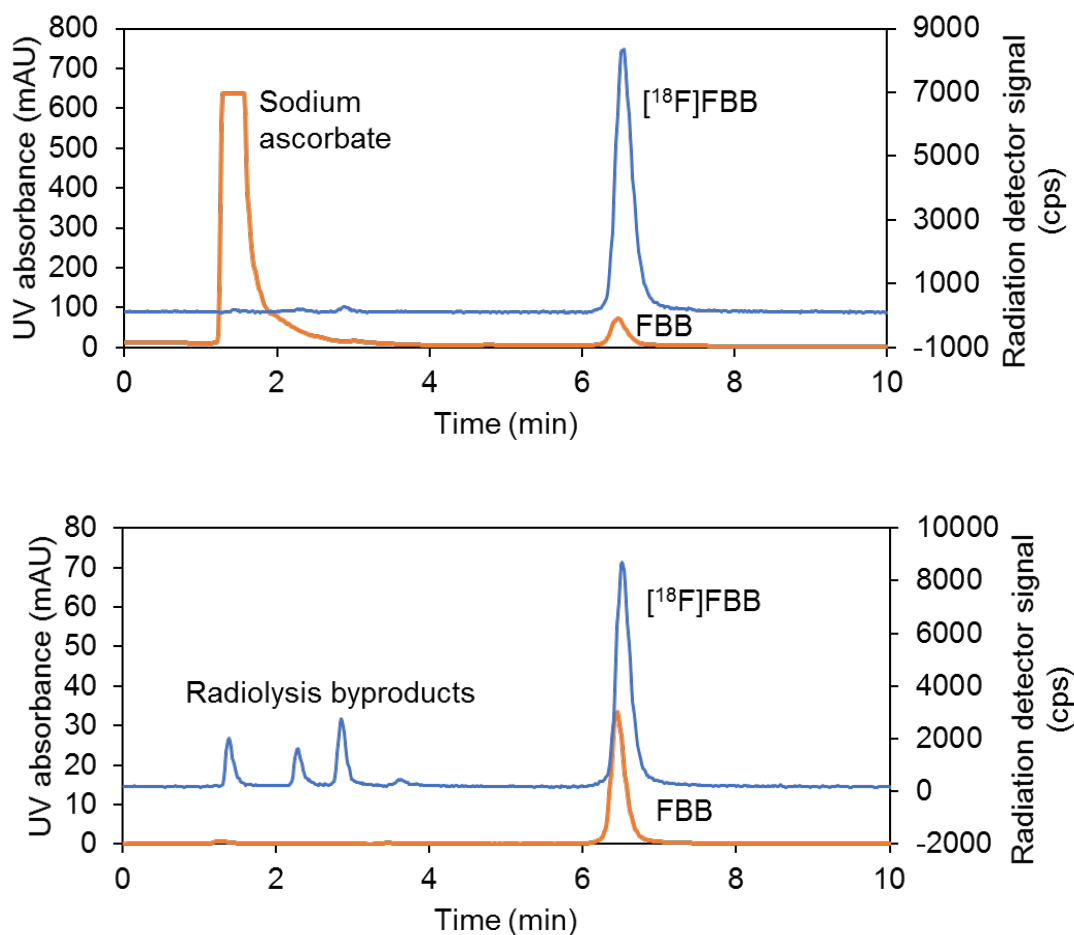


**Figure 4.8 Example chromatograms showing sample degradation due to radiolysis**

(Top) Sample after 2 h incubation in ascorbate-containing buffer (1.2 mL total volume) remained at 98% radiochemical purity. (Bottom) Sample after 2 h incubation without ascorbate in the buffer (0.2 mL volume) dropped to 72% radiochemical purity due to formation of radiolysis byproducts. Both samples were divided up from the same original batch after HPLC purification each having ~7 MBq of activity, and were mixed with FBB reference standard just prior to obtaining the HPLC chromatograms.

Additionally, we observed photodegradation of the [ $^{18}\text{F}$ ]FBB when it was stored exposed to room light resulting in an impurity peak right after observed [ $^{18}\text{F}$ ]FBB peak on the HPLC. To confirm this, we performed studies with the non-radioactive FBB standard. In Figure 4.9 are shown HPLC chromatograms of FBB standard dissolved in HPLC mobile phase before and

after being stored at room temperature for 1.5 hours. The upper chromatogram belongs to fresh sample at  $t = 0$ . For the middle chromatogram, the sample was stored in a transparent glass vial under room light, resulting in a secondary peak appearance after FBB peak. For the lower chromatogram, an aliquot of the same sample was stored under identical conditions except in an amber glass vial.

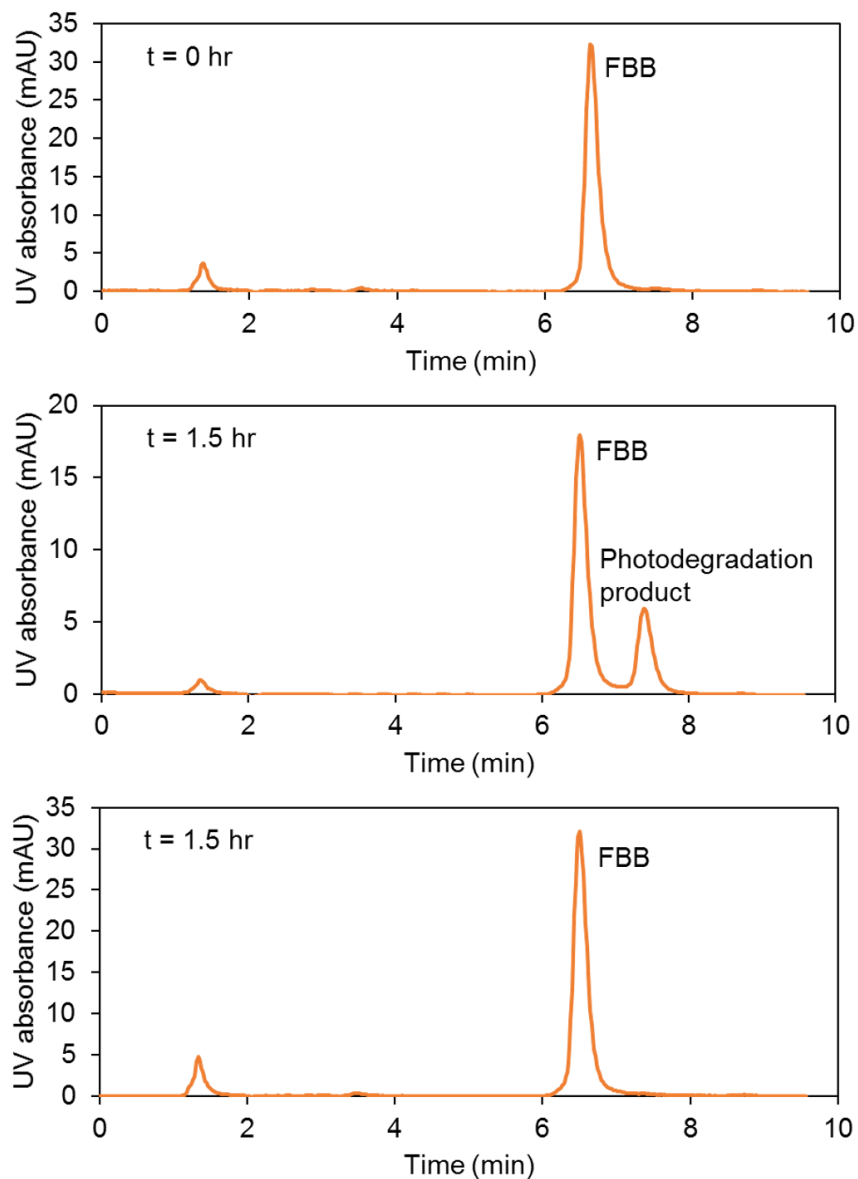


**Figure 4.9 Example HPLC chromatograms showing evidence of photodegradation**

(Top) Initial sample. (Middle) Sample stored in a transparent vial in ambient room light for 1.5 h.  
 (Bottom) Sample stored in an amber vial for 1.5 h.

#### 4.4.4 Benefits of microscale synthesis

The whole production (synthesis, purification, formulation) can be completed in 55 min with high yield (~50% decay-corrected). The 2-step reaction itself was quite fast, due largely to

the small volume reaction which requires very little time for heating/cooling or performing solvent evaporation steps (e.g. during [<sup>18</sup>F]fluoride drying). Though not explored here, there is room to improve and develop a faster analytical-scale HPLC separation process, and to shorten the formulation process as discussed in detail above. It is also feasible to increase the amount of starting activity (i.e. loading larger volume of [<sup>18</sup>F]fluoride or using a radioisotope concentrator (113)) to produce higher amounts of the probe.

Another advantage of the microscale synthesis is that high molar activity 340 GBq/μmol could be achieved at the end of synthesis, even when starting with low amounts (<350 MBq) of [<sup>18</sup>F]fluoride, something that cannot be achieved with conventional macroscale synthesis processes (57). Due to the importance of high molar activity when imaging certain tracers in small animals, the ability to achieve high molar activity in small batches can be a huge advantage, avoiding significant waste of radionuclide and probe that would otherwise be needed (i.e. to prepare a large batch to ensure high molar activity, but discard most of it since only a small quantity is needed for animal imaging). High molar activity of the amyloid tracer [<sup>11</sup>C]PIB has been reported to be particularly important for detection of relatively immature amyloid lesions in small animal models (210), suggesting it could be critical in certain cases for [<sup>18</sup>F]FBB imaging as well. Additionally, high molar activity provides a longer duration over which the molar activity can be adjusted to be within a desired range for experiments, and helps to lower the total injected mass of the tracer.

In comparison with literature methods (Table 4.3), the yield of this microvolume synthesis is among the highest, while only consuming ~1% the amount of precursor as other methods. In combination with the simple apparatus and compact size, this could lead to lower costs in production of [<sup>18</sup>F]FBB, and potentially enable new models of production and distribution for preclinical research. The microvolume synthesis approach could also provide a way for existing production facilities to add capability for production of additional tracers without significant need for additional hot cell space.

## 4.5 Conclusion

We implemented an efficient synthesis of [ $^{18}\text{F}$ ]FBB in microdroplet format on simple chips with surface-tension traps acting as reaction sites. The overall synthesis was fast (55 min), high-yielding ( $49 \pm 3\%$ ,  $n=3$ ), and had high molar activity ( $340 \pm 60 \text{ GBq}/\mu\text{mol}$ ,  $n=3$ ). The combination of a droplet radiosynthesizer with analytical-scale radio-HPLC purification system, and a miniature SPE-based formulation system, provides a platform for streamlined and economical production of [ $^{18}\text{F}$ ]FBB, and could be extended to other tracers in a straightforward manner.



## Chapter 5: High activity droplet syntheses of [<sup>18</sup>F]FET and [<sup>18</sup>F]FBB

### 5.1 Introduction

Diagnostic radiopharmaceuticals (tracers) used in positron-emission tomography (PET) imaging enable a wide range of research and clinical applications including cancer diagnostics and tumor severity grading (5,42,223), evaluation of response to cancer therapy (18,224), diagnostics of neurodegenerative disease (33,225,226), cardiac function assessment (227,228), drug development (21,229,230) and development of novel gene- and cell-based therapies (231–233). Of thousands of developed tracers to probe different biological targets and processes (234,235), only very few are routinely available. Complexity of short-lived PET tracer manufacturing has led to a centralized production model, where large batches of the tracers are produced in radiochemistry labs and are split to be distributed to a number of PET centers. Since a significant demand is needed to justify the high costs of establishing and performing the syntheses using conventional instrumentation and facilities, availability of specialized tracers is limited. Recent advancements in PET radiochemistry directed at development of batch-on-demand systems are creating new possibilities to expand availability of diverse diagnostic radiopharmaceuticals at low cost. Microfluidics offers a promising approach to enable economic production of one to a few patient doses due to advantages such as reduced (10-100x) reagent consumption, faster reaction kinetics, improved product yields, and reduced equipment footprint and shielding size (71,84,86,91,120,178). Numerous reports have established the feasibility of synthesizing various radiopharmaceuticals using microfluidic synthesizers. However, due to the disparity between the volume of radioisotope solutions (~1 mL) and reaction volumes of microscale systems (as low as 1s to 10s of  $\mu$ L), many reports have reported only relatively small

amounts of product activity, suitable only for preclinical imaging (84,86,180). Nevertheless, clinically-relevant quantities of various diagnostic radiopharmaceuticals has been produced with such microscale systems: [<sup>13</sup>N]NH<sub>3</sub> (236), [<sup>68</sup>Ga]Ga-PSMA-11 (237(p11)), [<sup>89</sup>Zr]Zr-DFO-Trastuzamab (93), [<sup>18</sup>F]FDG (238,239), [<sup>18</sup>F]FET (97), [<sup>18</sup>F]fallypride (98,107), [<sup>18</sup>F]FT807 (240), [<sup>18</sup>F]FPEB (241), [<sup>18</sup>F]FLT (242) and [<sup>18</sup>F]FMISO (242,243). A summary of reports of the <sup>18</sup>F-labeled ones is included in Table 5.1.

Reference	Microfluidic synthesis platform	Synthesis format	Tracer(s) produced	Starting activity (GBq)	Product activity (GBq)	Molar activity (GBq/ $\mu$ mol)	Synthesis time (min)	Precursor consumed (nmol)	Reaction volume ( $\mu$ L)	QC testing reported?	Used in humans?
Iwata et al. 2020 (97)	Disposable glass vials with a fused 300- $\mu$ L insert	Batch	[ <sup>18</sup> F]FET	Up to 6	N.R.	480 $\pm$ 130 (n=7) ***	50	177	60	No	No
Awasthi 2014 (239)	ABT BG75	Batch	[ <sup>18</sup> F]FDG	~1.9	0.4-0.6	N.R.	40-60	N.R.	N.R.	Yes	No
Akula et al. 2019 (242)	Advion NanoTek	Flow	[ <sup>18</sup> F]FMISO	13**	2.1	>74	53	11751	2000	No	No
			[ <sup>18</sup> F]FLT	13**	2.2	>74	77	24100	2000	No	No
Zheng et al. 2014 (243)	Advion NanoTek	Flow	[ <sup>18</sup> F]FMISO	~5.6	1.5-1.9	120 $\pm$ 30 (n=4)	106 $\pm$ 11 (n=15)	940	200	Yes	Yes
Liang et al. 2014 (241)	Advion NanoTek	Flow	[ <sup>18</sup> F]FPEB	80.9	1.7 $\pm$ 0.4 (n=3)	160 $\pm$ 10 (n=3)	75	21459	1000	Yes	No
Liang et al. 2014 (240)	Advion NanoTek	Flow	[ <sup>18</sup> F]T807	16.1 $\pm$ 4.4 (n=3)	4.4 $\pm$ 0.1 (n=3)	220 $\pm$ 50 (n=3)	<100	1562	400	Yes	Yes
Frank et al. 2018 (238)	GE ISAR	Batch	[ <sup>18</sup> F]FDG	Up to 170	>100	N.R.	<25	N.R.	650*	No	No
Lebedev et al. 2013 (98)	PEEK/pDC PD chip with syringe-	Batch	[ <sup>18</sup> F]Fallypride	Up to 111	N.R.	N.R.	45	1936	50	Yes	Yes
Wang et al. 2020 (107)	Droplet-based radiosynthesizer	Batch	[ <sup>18</sup> F]Fallypride	Up to 41	Up to 7.2	Up to 270	50	616	8	Yes	No
			[ <sup>18</sup> F]FBB	3.2 $\pm$ 0.8 (n=6)	0.5 $\pm$ 0.2 (n=6)	480 $\pm$ 160 (n=5)	60	80	10	Yes	No
This work	Droplet-based radiosynthesizer	Batch	[ <sup>18</sup> F]FET	2.3	0.7	460	60	60	10	Yes	No

**Table 5.1 Literature reports of microfluidic production of <sup>18</sup>F-labeled radiopharmaceuticals with sufficient quantities for human PET**

N.R. = not reported. \* Precise reaction volume was not reported, but the total reactor size was 650  $\mu\text{L}$ . \*\*Total activity used for [ $^{18}\text{F}$ ]FLT and [ $^{18}\text{F}$ ]FMISO sequential syntheses combined is reported, approximately half used in each synthesis. \*\*\* Molar activity reported for varying levels of starting radioactivity ranging 0.1 – 6 GBq.

Microfluidic reactors can be classified in two categories: continuous-flow synthesizers, where the reaction volume is flowed through a microchannel or capillary, and batch-mode synthesizers, that contain a fixed reaction volume confined within a miniature reaction chamber (99) or within an isolated droplet (86,120). In the continuous-flow systems, radioisotope and precursor solution streams are mixed prior to entering the heated reaction zone. Scaling of the product activity can be easily achieved by increasing radioisotope volume and also a corresponding increase of precursor solution volume, or by concentrating the isotope prior to synthesis. The first microfluidically-produced PET tracer suitable for human use was demonstrated using the commercial NanoTek radiosynthesizer (Advion, Inc., Ithaca, NY): Liang *et al.* synthesized 1.7 GBq of [ $^{18}\text{F}$ ]FPEB using a starting activity of up to 170 GBq (241). In a separate report, Liang *et al.* also reported the synthesis of 4.4 GBq batches of [ $^{18}\text{F}$ ]T807 (each with 16 GBq starting activity), for the first time administering the tracer produced by continuous-flow reactor to a human subject (240(p807)). Using the same system, Zheng *et al.* reported the synthesis of up to 1.9 GBq of [ $^{18}\text{F}$ ]FMISO (with 5.6 GBq starting activity) for use in clinical research. Another clinical-scale synthesis using this system was shown by Akula *et al.*, who reported the sequential production of 2 tracers [ $^{18}\text{F}$ ]FLT and [ $^{18}\text{F}$ ]FMISO in  $\sim 2$  GBq quantities each from 13 GBq of starting radioactivity (242). Despite impressive scalability, continuous-flow reactors use relatively large total reaction volumes (100s of  $\mu\text{L}$ ), with 100s of  $\mu\text{g}$  of precursor to prepare these clinical-scale batches, and require an extended time for the initial [ $^{18}\text{F}$ ]fluoride preparation step (86).

Batch reactors offer a drastic reduction in precursor consumption ( $<100 \mu\text{g}$ ) which is independent of the amount of loaded radioisotope. However, to produce clinically-relevant quantities of the radiopharmaceutical in these tiny reaction volumes, pre-concentration of

[<sup>18</sup>F]fluoride is necessary. By adapting conventional azeotropic drying to the ISAR platform (GE Global Research Europe), Frank *et al.* reported the synthesis of >100 GBq of [<sup>18</sup>F]FDG with starting activity up to 170 GBq (238). Using the BG75 system (ABT Molecular Imaging, Knoxville, TN) system, which integrates into a small cyclotron, Awasthi *et al.* reported synthesis of [<sup>18</sup>F]FDG from 1.9 GBq of starting activity, concentrated via azeotropic drying in the reaction vial, to produce single, injectable human doses (0.4-0.6 GBq) (239). Iwata *et al.* developed a trap-and-release process using a combination of commercially-available cation- and anion-exchange cartridges to trap 1 mL of cyclotron-produced [<sup>18</sup>F]fluoride (up to 6 GBq) and release it in a 0.2 mL methanolic solution that could be rapidly evaporated in a small vial designed for 5-20  $\mu$ L subsequent reaction to produce [<sup>18</sup>F]FET (97). For a 50  $\mu$ L batch reactor platform, Lebedev *et al.* performed an upstream trap-and-release process on a miniature QMA cartridge to concentrate a full cyclotron-target volume of [<sup>18</sup>F]fluoride (e.g.  $\sim$ 100 GBq in 2 mL) into < 45  $\mu$ L. This could be loaded into the reactor and evaporatively dried, enabling the synthesis of up to 38 GBq of [<sup>18</sup>F]fallypride (98). Chao *et al.* designed a standalone radioisotope concentrator system based on a similar mini-QMA approach, capable of concentrating milliliter-scale [<sup>18</sup>F]fluoride batches into  $\sim$ 12  $\mu$ L volume (113). The device was subsequently integrated with an automated droplet radiosynthesizer, and concentration of activities up to 41 GBq was demonstrated. Production of quantities of formulated [<sup>18</sup>F]fallypride up to 7.2 GBq were demonstrated (107).

While these methods are all effective, integration with a concentrator increases system complexity and synthesis time, and, except for the Iwata *et al.* method (97), requires optimization of base quantities using during the [<sup>18</sup>F]fluoride elution process. Instead, a simpler sequential drying approach can be used with droplet reactors, in which the initial radioisotope solution is subdivided into smaller portions each added and then rapidly evaporated (due to the high surface to volume ratio of small volumes), to build up the amount of activity in the reaction site. For example, Chen *et al.* heated a 200  $\mu$ L droplet of [<sup>18</sup>F]fluoride solution on an open

surface until it shrunk to 5  $\mu\text{L}$  and then transported this concentrated droplet into an electrowetting-on-dielectric (EWOD) radiosynthesis chip for completion of the drying step (244). We later demonstrated the possibility for rapid concentration by evaporation by sequentially loading to 2  $\mu\text{L}$  portions to a pre-heated chip (106). Since each drying iteration takes time, there is a practical limit on the volume/amount of radioactivity that can be concentrated, but evaporation is quite quick for modest batches. Drying of volumes in a range of a few hundred microliters is feasible, and can provide enough starting radioactivity for synthesis of clinically-relevant batches (86). In this work, we leverage the larger volume of the reaction site of the surface-tension trap (STT) chip (108) compared to the passive transport (PT) chip (106), and concentrate [ $^{18}\text{F}$ ]fluoride by loading it in 30  $\mu\text{L}$  increments. The goal of the present work is to demonstrate that tracers other than [ $^{18}\text{F}$ ]fallypride can be produced at clinically-relevant scales using this simple approach for [ $^{18}\text{F}$ ]fluoride concentration and thus simple overall apparatus. Previously, we reported production of O-(2-[ $^{18}\text{F}$ ]fluoroethyl)-L-tyrosine ([ $^{18}\text{F}$ ]FET) (50) and 4-[(E)-2-(4-{2-[2-(2-[ $^{18}\text{F}$ ]fluoroethoxy)ethoxy] ethoxy}phenyl)vinyl]-N-methylaniline ([ $^{18}\text{F}$ ]Florbetaben, [ $^{18}\text{F}$ ]FBB, Neuraceq<sup>TM</sup>, BAY-949172) (109,245) in small quantities in droplet reactions. Here, the methods are adapted to produce batches of [ $^{18}\text{F}$ ]FET and [ $^{18}\text{F}$ ]FBB sufficient for single to a few human doses, and to ensure the tracer batches meet the necessary specifications for clinical use via quality control (QC) testing. Some of the QC tests were performed using the TracerQC automated testing platform (Trace-Ability, Inc., Van Nuys, CA, USA), showing the successful integration of a novel compact microfluidic radiosynthesis platform and a modern QC testing platform, and demonstrating the possibility for clinically-relevant radiotracer production with an overall compact, user-friendly system.

## 5.2 Materials and Methods

### 5.2.1 Reagents

No-carrier-added [ $^{18}\text{F}$ ]fluoride was produced by the  $^{18}\text{O}(p, n)^{18}\text{F}$  reaction from [ $^{18}\text{O}$ ]H<sub>2</sub>O (84% isotopic purity, Zevacor Pharma, Noblesville, IN, USA) in an RDS-112 cyclotron (Siemens; Knoxville, TN, USA) at 11 MeV using a 1 mL tantalum target with havar foil. Acetonitrile (MeCN; anhydrous, 99.8%), methanol (MeOH; anhydrous, 99.8%), 2,3-dimethyl-2-butanol (thexyl alcohol (TA); 98%), ethanol (EtOH; 200 proof, >99.5%), hydrochloric acid (HCl; 1M), dimethylsulfoxide (DMSO; 98%), deionized (DI) water, and polyethylene glycol 400 (PEG 400), Kryptofix 222 (K<sub>222</sub>) and potassium carbonate (K<sub>2</sub>CO<sub>3</sub>) were purchased from Millipore Sigma (St. Louis, MO, USA). Sodium phosphate dibasic (Na<sub>2</sub>HPO<sub>4</sub>·7H<sub>2</sub>O) and sodium phosphate monobasic (NaH<sub>2</sub>PO<sub>4</sub>·H<sub>2</sub>O) were purchased from Fisher Scientific (Thermo Fisher Scientific, Waltham, MA). Saline (0.9% sodium chloride injection, USP) was obtained from Hospira Inc. (Lake Forest, IL, USA). Tetrabutylammonium bicarbonate 0.075M (TBAHCO<sub>3</sub>, >99%), (2S)-O-(2'-tosyloxyethyl)-N-trityl-tyrosine-tert-butyl ester (TET; >95%) (FET precursor), O-2-fluoroethyl-L-tyrosine (FET-HCl; >95%) (FET reference standard) were purchased from ABX GmbH (Radeberg, Germany). ([methanesulfonic acid 2-{2-[2-(4-{2-[4-(tert-butoxycarbonyl-methyl-amino)-phenyl]-vinyl}-phenoxy)-ethoxy]-ethoxy}-ethyl ester) (FBB precursor) and (4-[(E)-2-(4-{2-[2-(2-[ $^{18}\text{F}$ ]fluoroethoxy) ethoxy] ethoxy} phenyl) vinyl]-N-methylaniline) (FBB reference standard) were generously provided by Life Molecular Imaging GmbH as a part of [ $^{18}\text{F}$ ]Florbetaben synthesis kits (Life Molecular Imaging GmbH, Berlin, Germany). Dry scavenger (to prevent radiolysis), consisting of sodium ascorbate with L-ascorbic acid (87:13 w/w), was also obtained from the same [ $^{18}\text{F}$ ]Florbetaben kits. All reagents were used as received without further purification. Ultrapure 18 MΩ H<sub>2</sub>O was obtained from a Milli-Q Integral 3 purification system (Millipore Sigma, St. Louis, MO, USA).

Stock  $K_{222}/K_2CO_3$  solution (for  $[^{18}F]$ FBB synthesis) was prepared by first making an aqueous 61 mM  $K_2CO_3$  mixture and adding  $K_{222}$  to reach 85 mM concentration. Stock solutions were prepared for FET precursor (6 mM in MeCN:TA 1:1 (v/v)), FBB precursor (8 mM in DMSO), and for  $[^{18}F]$ FET collection solution (1:1 MeOH:H<sub>2</sub>O (v/v)) and  $[^{18}F]$ FBB collection solution (1:1 MeCN: H<sub>2</sub>O (v/v)). Acid mixture used for deprotection in both syntheses was made by mixing MeCN and HCl 1:1 (v/v). Scavenger solution for  $[^{18}F]$ FBB was prepared either at 33 mg/mL or 10 mg/mL in H<sub>2</sub>O. Formulation dilution solution for  $[^{18}F]$ FBB contained 39 mg/mL of dry scavenger in a 4:13 (v/v) mixture of PEG 400 and H<sub>2</sub>O.

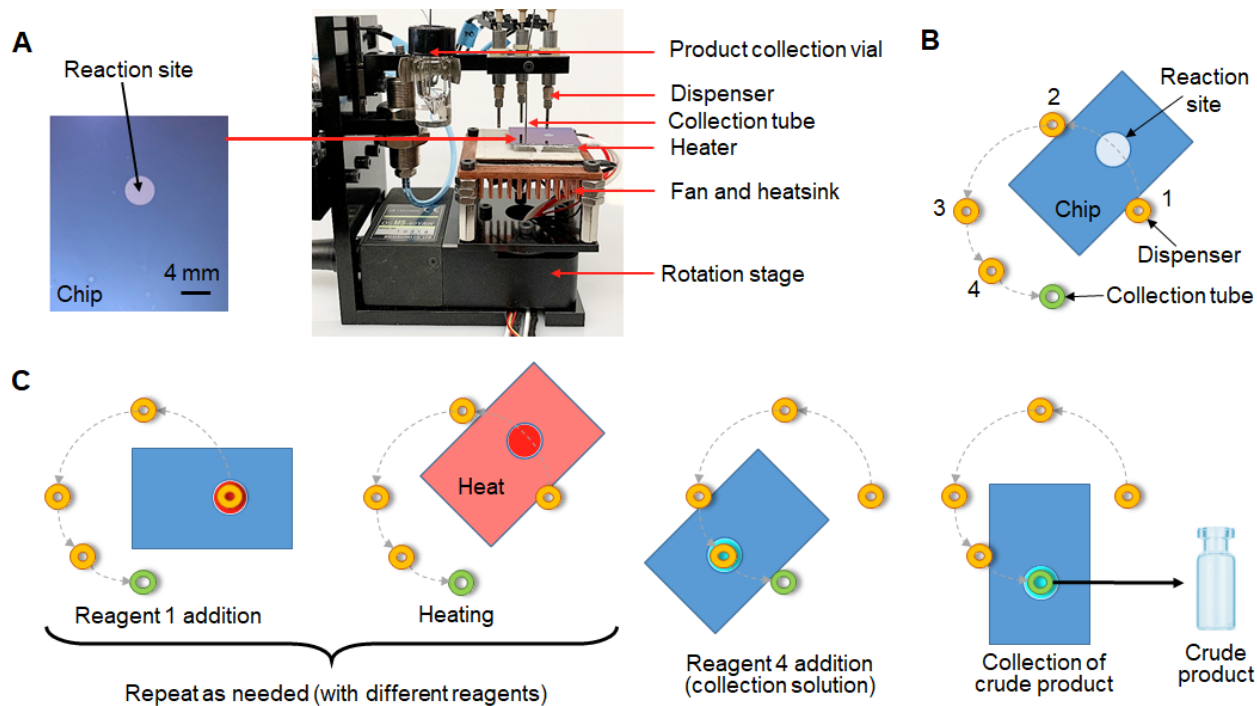


**Figure 5.1 Schematic of automated droplet synthesis**

- (A) Photographs of a disposable reaction chip (left) and automated droplet synthesizer (right).  
 (B) Top view schematic of dispenser arrangement for a multi-step droplet synthesis. (C) Simplified schematic showing position of rotating platform during various steps of a typical radiosynthesis (reagent addition, heating, and collection of crude product).



### 5.2.2 Automated droplet synthesizer

Radiosyntheses were performed in droplet format on the surface of disposable silicon-Teflon chips (surface-tension trap (STT) chips) and using an automated radiosynthesizer system to dispense reagents and recover syntheses products (Figure 5.1 Schematic of automated droplet synthesisA) (108). Each 25.0 x 27.5 mm<sup>2</sup> chip was coated with hydrophobic Teflon layer with an etched hydrophilic circular reaction site (4 mm diameter), which acted as a surface-tension trap to confine reagents during the multi-step radiosynthesis. The details of the STT chip fabrication were previously reported (108). The chip was placed atop a heater that can rotate, and reagents were delivered by piezoelectric dispensers arranged in a circular pattern above the chip. Dispensers were calibrated and primed before use as described previously (106).

The basic operation is illustrated in Figure 5.1 Schematic of automated droplet synthesisB For each reagent addition, the heater and chip were rotated to position the reaction site under the corresponding dispenser, and then the desired amount of the reagent was added to the reaction site. During the heated reaction steps the chip was positioned so that the reaction site is not directly under any of the dispensers. For crude product recovery, the chip was first rotated to position the reaction site under collection solution dispenser, and after the solution was dispensed, the reaction site was positioned under the collection tubing. When the retractable collection tubing was lowered into the droplet (with end of tubing ~0.5 mm above the chip surface) the vacuum was applied to transfer the droplet to the product collection vial. The collection process was repeated 4 times.

For synthesis with high (up to multi-GBq) starting activities, the volume of [<sup>18</sup>F]fluoride solution needed exceeds the optimal capacity of the reaction site (~30 µL for aqueous solutions). In the previous work reported by our group, the activity was scaled up by interfacing with an upstream micro-QMA cartridge system (107,113). In this work we focused on simpler and faster approach of drying in smaller increments. The desired quantity of [<sup>18</sup>F]fluoride was

pre-mixed with appropriate base in optimal amount, then dispensed and dried on chip in portions of up to 30  $\mu\text{L}$  at a time. Up to 4 droplets were used to load activities in the range 0.02 – 4 GBq.

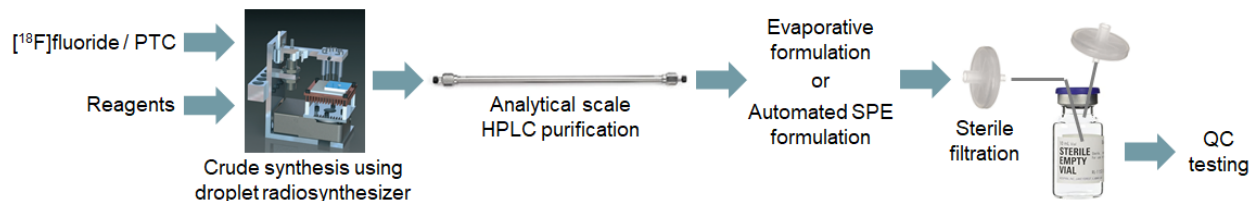


**Figure 5.2 Tracer preparation scheme**

PTC = phase transfer catalyst. SPE = Solid-phase extraction.

Following crude synthesis of the tracers, purification was achieved using analytical-scale HPLC with a tracer-specific method reported previously (50,109). Then the tracers were reformulated either by evaporation and resuspension (<sup>18</sup>F]FET)(50), or automated solid-phase extraction (SPE) (<sup>18</sup>F]FBB) (109) (Figure 5.2).

### 5.2.3 [<sup>18</sup>F]FET synthesis

The production of [<sup>18</sup>F]FET was performed using identical reaction conditions as previously reported for manual droplet-based synthesis (50) adapted from a conventional 2-step synthesis route (187,190). In this earlier work, automation was achieved using a previous generation design of microfluidic chip with tapered hydrophilic channels to transport reagents passively from fixed loading sites to the central reaction zone (106), and the synthesis here was adapted from the manual reactions performed on chips containing only a 4 mm circular hydrophilic reaction site (50).

The synthesizer was set up by loading stock solutions into reagent dispensers as indicated in Table 5.2. As the last setup step, the desired activity of [<sup>18</sup>F]fluoride was mixed with 1.5  $\mu\text{L}$  of 0.075M TBAHCO<sub>3</sub> (i.e. 113 nmol TBAHCO<sub>3</sub>) and loaded in the corresponding dispenser. The 2-step (fluorination and deprotection) crude synthesis was carried out as shown

in Figure 5.3A. The [ $^{18}\text{F}$ ]fluoride /  $\text{TBAHCO}_3$  solution was loaded 30  $\mu\text{L}$  at a time, each droplet dried at 100  $^\circ\text{C}$  for 1.5 min. To the dried residue, precursor solution (10  $\mu\text{L}$ ) was added and the radiofluorination step was performed (5 min, 90 $^\circ\text{C}$ ). Acid mixture was then added to perform deprotection (3 min, 90 $^\circ\text{C}$ ). 20  $\mu\text{L}$  was added at the beginning, and another 20  $\mu\text{L}$  was added after 1.5 min. The crude mixture was recovered with FET collection solution (4x20  $\mu\text{L}$ ). To obtain purified [ $^{18}\text{F}$ ]FET, the crude collection mixture was diluted with 100  $\mu\text{L}$  water (to lower MeCN concentration, improve separation quality and reduce losses during sample transfer) and injected into analytical radio-HPLC for purification (conditions described below). The [ $^{18}\text{F}$ ]FET peak was collected in a pyrex vial (WHEATON $^\circledR$  V vial 5 mL, Millville, NJ, USA), evaporated to dryness in an oil bath at 120  $^\circ\text{C}$  and resuspended in 5 mL of sterile saline. The formulated product was sterile filtered (13 mm diameter, 0.22 mm pore size, PVDF membrane; Fisherbrand $^\text{TM}$ , Waltham, MA, USA) into a sterile product vial (2 mL, ALK, Denmark) and samples taken under aseptic conditions for QC testing. Batches intended for QC testing used at least 1 GBq of starting [ $^{18}\text{F}$ ]fluoride activity.

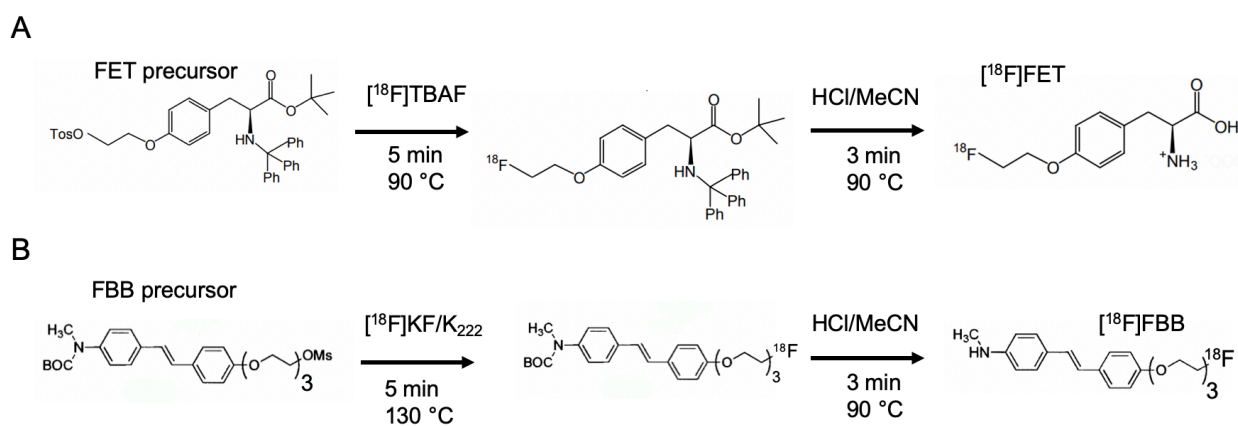


**Figure 5.3 Synthesis routes for (A) [ $^{18}\text{F}$ ]FET and (B) [ $^{18}\text{F}$ ]FBB**

## 5.2.4 [<sup>18</sup>F]FBB synthesis

Automated production of [<sup>18</sup>F]FBB in droplet format, adapted from a 2-step conventional synthesis route Figure 5.3B using a Boc-protected precursor (201), was previously reported (109). In this work the volume of precursor solution was increased from 10 to 15  $\mu$ L to reduce sensitivity of the reaction performance (109) in case of dispensing errors associated with the viscous DMSO-based precursor solution.

The configuration of dispensers is described in Table 5.2. The desired activity of [<sup>18</sup>F]fluoride was mixed with 4.5  $\mu$ L of K<sub>222</sub>/K<sub>2</sub>CO<sub>3</sub> stock solution (i.e. 383 nmol K<sub>222</sub>, 275 nmol K<sub>2</sub>CO<sub>3</sub>) and dispensed 30  $\mu$ L at a time, with each droplet dried at 100 °C for 1.5 min. To the dried residue, precursor solution (10 or 15  $\mu$ L) was added, and then the chip was heated for 5 min at 130 °C to perform radiofluorination of the precursor. Then, the acid solution was added (20  $\mu$ L at t=0, and another 20  $\mu$ L at t=1.5 min) to remove protecting groups (5 min, 90°C). The product was recovered with FBB collection solution (4x20 $\mu$ L) into a vial pre-filled with 64  $\mu$ L of 33 mg/mL scavenger solution, diluted with 50  $\mu$ L H<sub>2</sub>O, and purified via analytical HPLC (conditions described below). The purified product was formulated via SPE using an automated system (109), from where it was eluted in ethanol and diluted with formulation dilution solution to achieve 15% EtOH concentration in a final volume of 5 mL, and sterile filtered (Whatman®, Anotop® 10 mm diameter, 0.02  $\mu$ m pore size; Cytiva, Marlborough, MA, USA). Samples were taken for QC testing. Batches intended for QC testing used at least 2 GBq starting activity. In case of samples analyzed with the Tracer-QC system, the elution step during formulation was performed with 150  $\mu$ L EtOH, and the final formulated volume was 1 mL.

Tracer	[ <sup>18</sup> F]FET	[ <sup>18</sup> F]FBB
Dispenser 1	[ <sup>18</sup> F]fluoride / TBAHCO <sub>3</sub>	[ <sup>18</sup> F]fluoride / K <sub>222</sub> / K <sub>2</sub> CO <sub>3</sub>
Dispenser 2	FET precursor solution	FBB precursor solution

<b>Dispenser 3</b>	FET deprotection solution	FBB deprotection solution
<b>Dispenser 4</b>	FET collection solution	FBB collection solution

**Table 5.2 Reagent setup in automated droplet synthesizer for syntheses of [<sup>18</sup>F]FET and [<sup>18</sup>F]FBB.**

### 5.2.5 Analytical methods

A calibrated ion chamber (CRC 25-PET, Capintec, Florham Park, NJ, USA) was used to perform radioactivity measurements. Radioactivity recovery was determined by dividing radioactivity of collected crude product by the amount of starting activity (correcting for decay). Fluorination efficiency was determined from radio-TLC as a percentage of desired product in the crude product. Crude radiochemical yield (crude RCY) was calculated by multiplying radioactivity recovery and fluorination efficiency. Overall RCY is a ratio of final formulated product activity to the starting activity. Molar activity was quantified based on isolated product radioactivity collected after HPLC purification and area under the corresponding UV peak of the purification chromatogram converted to molar quantity using a calibration curve.

Fluorination efficiency was determined via radio-thin-layer chromatography (radio-TLC). For [<sup>18</sup>F]FET, silica gel 60 F254 plates (Merck KGaA, Darmstadt, Germany) were cut into 15 x 60 mm pieces (with 40 mm developing distance), spotted with 0.5 μL of the sample and developed in 80% (v/v) MeCN in H<sub>2</sub>O. TLC plates were analyzed with a Cerenkov luminescence imaging system as previously described (111). Retention factors of the observed radioactive species were: 0 ([<sup>18</sup>F]fluoride), 0.3 ([<sup>18</sup>F]FET), and 0.8 (fluorinated intermediate). For [<sup>18</sup>F]FBB, reverse phase TLC plates (RP-18 silica gel 60 F254 sheets; aluminum backing; Millipore Sigma, St. Louis, MO, USA) were prepared and used in a similar fashion, but developed in 90% (v/v) MeCN in H<sub>2</sub>O. Retention factors of the observed radioactive species were: 0.0 ([<sup>18</sup>F]fluoride), 0.4 ([<sup>18</sup>F]FBB), and 0.8 (fluorinated intermediate).

Radio-HPLC analysis and purification were performed on an analytical-scale Smartline HPLC system (Knauer, Berlin, Germany) with 200  $\mu$ L injection loop, a pump (Model 1000), degasser (Model 5050), UV detector (Model 2500) and a radiometric detector (Bioscan B-FC-4000, Bioscan Inc., Washington DC, USA). Samples were separated using a C18 column (Luna, 5  $\mu$ m particles, 100 $\text{\AA}$  pores, 250 x 4.6 mm, Phenomenex, Torrance, CA, USA) with guard column (SecurityGuard C18, Phenomenex). For [ $^{18}\text{F}$ ]FET, separation was performed isocratically using 10% (v/v) EtOH in H<sub>2</sub>O at a flow rate of 1 mL/min, and UV absorbance was measured at 269 nm. The retention time of [ $^{18}\text{F}$ ]fluoride was ~2-3 min, and ~5 min for [ $^{18}\text{F}$ ]FET. The fluorinated intermediate and other impurities were eluted off the column by switching the mobile phase to 95:5 (v/v) MeCN:H<sub>2</sub>O. For [ $^{18}\text{F}$ ]FBB, the mobile phase was 60:40 (v/v) MeCN : 25 mM phosphate buffer at a flow rate of 1.5 mL/min, and UV absorbance was measured at 254 nm. The observed retention times were ~2-3 min for [ $^{18}\text{F}$ ]fluoride, 6 min for [ $^{18}\text{F}$ ]FBB, and 14 min for the fluorinated intermediate.

### **5.2.6 Conventional quality control testing**

Quality control tests were performed on 3 consecutive batches of [ $^{18}\text{F}$ ]FET and 3 consecutive batches of [ $^{18}\text{F}$ ]FBB. The details of the conventional QC are described below. Quality control tests for appearance, pH, radionuclide purity and identity, bacterial endotoxins, sterility, radiochemical and chemical purity were determined as previously described (107).

#### Molar activity

Molar activity was estimated by quantifying amount of the tracer in purification chromatogram using ultraviolet (UV) peak and cold standard calibration curve, then dividing by radioactivity of the isolated product after purification.

#### Residual content of TBAHCO<sub>3</sub>

Residual TBAHCO<sub>3</sub>, which has acceptable limit of 2.6 mg/V, in the purified sample was determined using a thin-layer chromatography (TLC) spot test method reported by Kuntzsch et

al. (246). For 5 mL formulation volume the calculated limit would be 520 mg/L, however the expected quantity of TBAHCO<sub>3</sub> would be much less. Thus, a low concentration standard solution of TBAHCO<sub>3</sub> (45 mg/L) was created and spotted alongside the formulated [<sup>18</sup>F]FET (2 µL) onto a silica TLC plate (JT4449-2, J.T. Baker, Center Valley, PA, USA), and air dried. 10 µL of a developing solution (0.72M NH<sub>4</sub>OH in 90% MeOH) was added on top of each spot, dried, and then the TLC strip was developed in a chamber containing iodine crystals for 1 min. The color intensity of the spot of the purified sample was compared to that of the standard solution to confirm the residual amount was below the injectable limit.

#### Residual content of K<sub>222</sub>

Residual kryptofix content was determined using a TLC spot test as reported by Halvorsen and Kvernenes (247). The iodoplatinated TLC strips were prepared according to the reported procedure. The standard solutions containing 50 µg/mL (injectable limit) and 12.5 µg/mL of kryptofix in a formulation matrix identical to [<sup>18</sup>F]FBB formulation matrix were prepared. 2 µL of [<sup>18</sup>F]FBB sample was spotted alongside the standards onto a iodoplatinated TLC strip, the spots were air dried followed by addition of 1% H<sub>2</sub>O<sub>2</sub> (2.5 µL). After 1 min of drying the sample spots were analyzed for K<sub>222</sub> content.

#### Residual solvent analysis

The concentration of residual solvents (i.e. methanol, acetonitrile, hexyl alcohol, ethanol and DMSO) was determined using gas chromatography mass spectrometry (GCMS).

#### Residual solvent analysis of [<sup>18</sup>F]FET samples

Gas chromatography mass spectrometry (GC-MS) measurements were carried out on a GC system (6890N, Agilent) equipped with mass spectrometry detector (5975 MSD) and autosampler (7683B). The instrument was controlled by Enhanced Chemstation software version E.01. The inlet was operated in split mode at 250 °C. Ultra-high purity He (Airgas West, Culver City, CA) was used as the carrier gas with the flowrate set to 1.2 mL / min. Separation was carried out on a 30 m x 250 µm x 0.25 µm DB-Wax column (Agilent J&W). The GC oven

was initially held at 70 °C, heated to 140 °C at 10 °C/min, and then heated to 260 °C at 30 °C/min. The MSD was operated in the scan mode and used EI ionization.

Instrument response for known concentrations of pure analytes in butanol was measured to determine the analyte concentrations in the samples. More specifically, a 4-point calibration curve was generated for all solvents (MeOH, MeCN, TA, EtOH). The concentration of the residual analytes was then interpolated from this calibration curve.

#### Residual solvent analysis of [<sup>18</sup>F]FBB samples

The concentrations of residual solvents (i.e. acetonitrile, DMSO, ethanol) were determined using headspace gas chromatography mass spectrometry (GCMS). To 100 µL of each sample, 1 µL of <sup>2</sup>H<sub>6</sub>-DMSO was added as an internal standard. For acetonitrile and DMSO, an aliquot (10 µL) of each sample was transferred to 10 mL glass headspace vials fitted with magnetic caps. For measurement of ethanol concentrations, the samples were diluted 1 to 100 with water prior to the transfer. Samples were incubated for 20 min at 200 °C with gentle agitation every 10 seconds. After incubation, 1 mL of headspace vapor was withdrawn with a heated (110 °C) syringe and injected onto a GC inlet (1/10 split, 250 °C). Ultra-high purity He (Airgas West, Culver City, CA) was used as the carrier gas at constant flow (1 mL/min). Separations were carried out on a bonded-phase non-polar fused silica capillary column (60 m x 250 µm x 0.25 µm Zebron ZB-5plus column, Phenomenex). The GC oven was initially held at 50 °C for 2 min, then was heated to 250 °C at 10 °C/min. The end of the column (GC/EI-MS transfer line at 250 °C) was inserted into the EI source (200 °C, 70 eV) of a high resolution Orbitrap mass spectrometer (Thermo Scientific Q Exactive GCMS, calibrated with perfluorotributylamine immediately prior to the analysis of each batch of samples), scanning from m/z 30-500 at a resolution (FWHM) of 60,000. Data were collected with instrument manufacturer-supplied software (Thermo Xcalibur v4.1). Instrument response from known concentrations of pure analytes in PEG400/water mixtures containing the same amount of internal standard was measured to determine the analyte concentrations in the samples. More



specifically, a five-point calibration curve was generated for all three solvents at the following concentration levels: 0, 25.625, 51.25, 102.5, and 205 PPM for acetonitrile; 0, 312.5, 325, 1250, 2500 PPM for DMSO; and 0, 3.75, 7.5, 15, and 30% (w/v) for ethanol. Calibration curves for acetonitrile and ethanol were constructed by directly comparing absolute peak area (ordinate) and solvent concentration (abscissa). On the other hand, for the DMSO calibration curve, ratios of DMSO/<sup>2</sup>H<sub>6</sub>-DMSO peak areas were used as the ordinate to account for potential sulfoxide oxidation.

### **5.2.7 Tracer-QC automated quality control testing**

An additional 3 batches of [<sup>18</sup>F]FBB were prepared and transported to Trace-Ability, Inc. (Van Nuys, CA, USA), and tested using an automated QC testing system (Tracer-QC, Trace-Ability, Inc.).

#### Color

A spectrophotometric measurement of the sample is performed together with a positive control solution containing one or more color standards with known absorbance.

#### Clarity

A turbidimetric analysis of the sample along with positive and negative control solutions is conducted through spectrophotometric measurements.

#### pH

The solution to be analyzed is mixed with an indicator solution, which produces a pH-dependent change in the indicator's absorbance spectrum within the sample and indicator mixture.

#### Bacterial Endotoxin

Enzymatic activation of serine proteases from horseshoe crab amebocyte lysate by interaction with bacterial endotoxin is used to produce a chromogenic signal that can be analyzed spectrophotometrically.

### Radioactivity Concentration

The radioactivity of an aliquot of sample solution is determined from the intensity of its radioluminescent emission.

### Radionuclidic Identity (Half-life)

The time-dependent radioactivity of an aliquot of sample solution is determined from the intensity of its radioluminescent emission.

### Chemical Identity, Chemical Purity, and/or Chemical Content via High Performance Liquid Chromatography (HPLC)

While chemical identity, chemical purity, and chemical content are all separate properties that each have distinct meaning and corresponding product specification, in common practice they can be derived from the same experiment simultaneously in cases where a product specification calls for the determination of more than one. In addition, these tests can be carried out concomitantly with determination of radiochemical identity, radiochemical impurity, and/or specific identity. For the Tracer-QC platform, all liquid handling required for sample preparation and injection is handled by the pipetting robot, mated to a conventional HPLC system utilized to set flow rates and/or gradients and detect elution of compounds.

### Radiochemical Identity, Radiochemical Purity, and/or Specific Activity via Radio-HPLC

While radiochemical identity, radiochemical purity, and specific activity are all separate properties that each have a distinct meaning and corresponding product specification, in common practice they can be derived from the same experiment simultaneously in cases where a product specification calls for determination of more than one. In addition, these tests can be carried out concomitantly with determination of chemical identity, and/or chemical purity. Determination of specific activity is not a separate experiment per se, but requires determination of radioactivity concentration, chemical content, and radiochemical purity.

## 5.2.8 Tracer-QC

Tracer-QC enables complete automation of PET tracer QC relying on a plate reader, liquid handler and HPLC that are integrated and operating as one system enabled by software and disposable kits (Figure 5.4). This concept uses optical measurements for all non-chromatographic QC tests augmented with seamless integration of an HPLC. The most innovative concept in this solution is in the indicators contained in the kit that produce optically detectable signals upon interaction with the PET tracer sample that can be translated into the measurements of the properties relevant to QC. Table 5.3 summarizes the tests developed for FBB and compares traditional QC solution to the approach utilized in Tracer-QC.

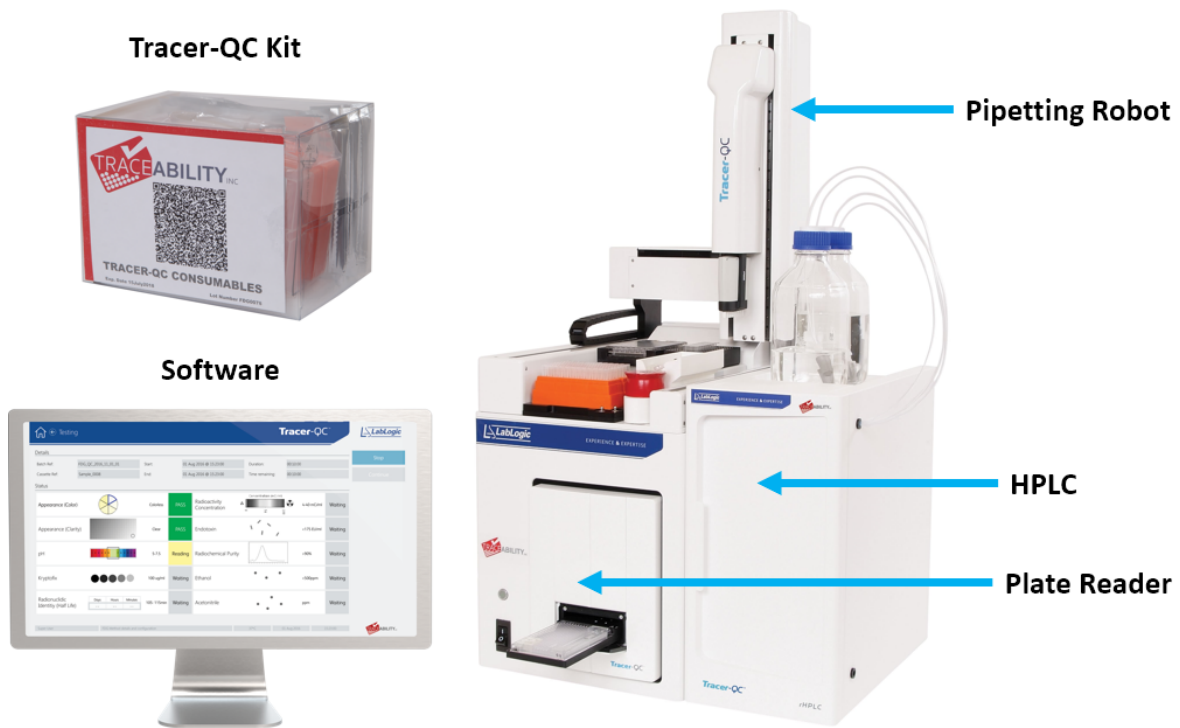


Figure 5.4 Tracer-QC setup

QC Test	Conventional method	Tracer-QC method
Color	visual assessment	absorbance measurement (with disposable indicators)
Clarity	visual assessment	
pH	indicator + visual assessment	
Kryptofix	spot test + visual assessment	
Endotoxin concentration	PTS reader	
Acetonitrile	Gas Chromatograph	emission measurement (with disposable scintillators)
Radionuclidic identity ( $T_{1/2}$ )	Dose calibrator + clock	
Radioactivity concentration	Dose calibrator + syringe	rHPLC integrated in Tracer-QC supported by disposable kit
Radiochemical Identity/Purity	Stand-alone HPLC	
Chemical Identity/purity		
Specific Activity		

**Table 5.3 Automation of [ $^{18}\text{F}$ ]FBB Quality Control Testing**

The principle of operation of Tracer-QC consists of the following aspects.

(1) Generation of optical signals. For color and clarity the signal is the spectrophotometric measurement of absorbance of light passed through the sample in the plate reader. For pH, kryptofix, endotoxin and acetonitrile the sample's interaction with an indicator designated for each of the tests (and mixed with sample by the robot) leads to unique changes in the absorbance spectrum. For radionuclidic identity and radioactivity concentration, the signal is a luminescence measurement detecting the emission of light from scintillating materials that interact with the radioactive sample in the kit. For the HPLC group of tests the signals are the UV and radio-chromatograms generated by traditional HPLC detectors.

(2) Interpretations of signals. Tracer-QC software processes the obtained signals in context of pre-set parameters and measurements from reference standards to determine the values of all QC parameters listed in Table 5.3. Each test has automated suitability checks which confirm whether the produced measurement is valid. After values have been calculated

and verified for all QC tests, the software produces a comprehensive report with these values along with acceptance criteria and pass/fail determination.

These principles allow the entire QC process to be automated and objective while supporting completely traceable and tamper-free data flow from raw measurements to the report. Robustness of the methods is assured by elimination of human factor and nearly complete elimination of multi-use surfaces (except HPLC) enabled by the disposable kit. The user interaction with Tracer-QC is minimal. The user installs the kit, initiates the program, delivers the sample, triggers the analysis and collects the report. After the process is complete and used kit is removed, the system is ready for the next analysis without any further preparation.

The tests listed in Table 5.3 have been developed and validated individually and then merged into an integrated protocol for automated execution. They have been subsequently verified or re-validated as suitable for Quality Control Testing of [ $^{18}\text{F}$ ]FBB produced on the miniaturized platform. The effects of unique composition of [ $^{18}\text{F}$ ]FBB resulting from such synthesis were studied and reflected in method development and validation.

Measurement	STT reactor (open) (n=4)	Teflon-silicon reactor (closed) (n=3)	Teflon-glass reactor (closed) (n=3)
Estimated volatile radioactivity loss during [ <sup>18</sup> F]fluoride drying (%)	15	15	0
Product collection efficiency (%)	40±2	58±1	41±6
Residual radioactivity on reactor chip (%)	2±0	2±0	16±1
Residual radioactivity on cover plate (%)	N/A	13±1	14±3
Total volatile radioactivity loss (%)	59±2	26±2	28±4
Radiochemical conversion (%)	72±6	49±1	66±7
Crude RCY (%)	29±4	28±1	27±4
Can be automated? (Y/N)	Yes	No	No

**Table 5.4 Performance of droplet-based [<sup>18</sup>F]FET low activity synthesis on several platforms.**

## 5.3 Results

### 5.3.1 [<sup>18</sup>F]FET production and testing

In initial synthesis runs with <20 MBq starting activity, the automated droplet synthesis exhibited very good  $70 \pm 9\%$  (n=9) crude RCY. Notably, this was higher than the previously reported manual droplet-based synthesis ( $59 \pm 7\%$ , n=4) (50) or automated results using the passive-transport droplet-based synthesizer ( $54 \pm 6\%$ , n=5) (50). Additionally, the system had an improved synthesis time of 18 min compared to 24 min or 19 min for manual or passive transport automated system respectively. Detailed comparison of various parameters is shown in Table 5.4. Previous work with [<sup>18</sup>F]fallypride showed similar improvements when transitioning from the passive-transport (PT) chip to the STT chip (108).

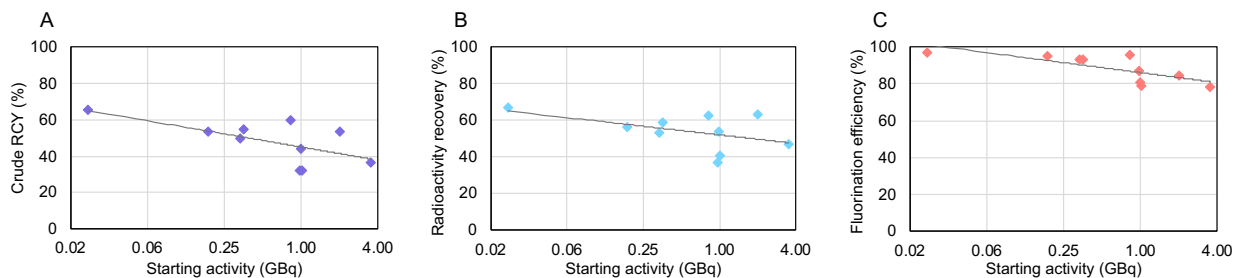


**Figure 5.5 Performance of crude  $[^{18}\text{F}]$ FET droplet-based radiosynthesis as a function of starting activity**

(A) Crude RCY. (B) Radioactivity recovery. (C) Fluorination efficiency. Note that the x-axis is plotted on a logarithmic scale, and a logarithmic trendline is generated for all graphs.

The impact of increased starting activity on the performance of the crude synthesis was also explored (Figure 5.5). A modest decrease in crude RCY was observed, dropping from ~65% to ~40% as activity was increased in the range 0.2 to 3.5 GBq. The crude RCY is a product of radioactivity recovery and fluorination efficiency and both these parameters show a slight decrease with increased starting activity. A similar result was previously observed with  $[^{18}\text{F}]$ fallypride synthesis (107).

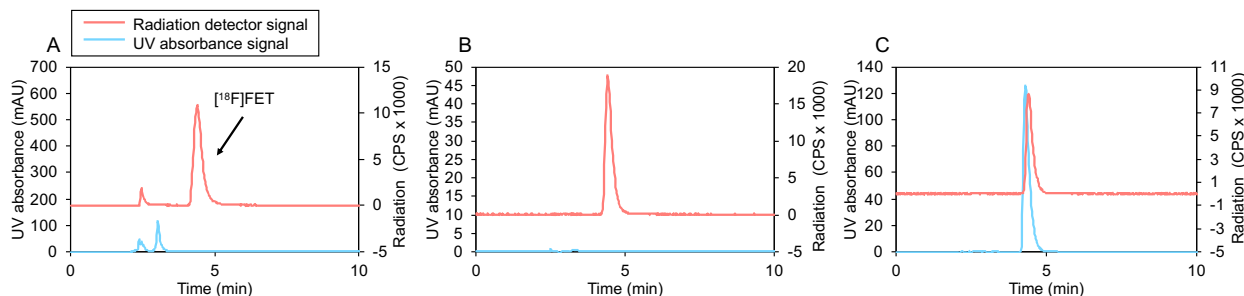


**Figure 5.6 Example HPLC chromatograms for  $[^{18}\text{F}]$ FET**

(A) Crude product. (B) Formulated product. (C) Formulated product co-injected with reference standard.

Three batches of purified and formulated  $[^{18}\text{F}]$ FET were prepared for QC testing. The overall synthesis time, including purification and formulation, was 60 min. For these batches, the

synthesis exhibited  $20 \pm 3\%$  (n=3) overall activity yield, >99% radiochemical purity, and high molar activity ( $570 \pm 140$  GBq/ $\mu$ mol, n=3; EOS). The batches all passed QC tests (Table 5.5). Example chromatograms during [ $^{18}$ F]FET purification and assessment of radiochemical purity and identity are shown in Figure 5.6.



Test	Testing Criteria	Batch 1	Batch 2	Batch 3
<b>Appearance</b>	Clear, colorless, particle free	Pass	Pass	Pass
<b>Radioactivity concentration</b>	7.4-74 MBq/mL [0.2-2 mCi/mL]	47 MBq/mL [1.3 mCi/mL]	56 MBq/mL [1.5 mCi/mL]	46 MBq/mL [1.3 mCi/mL]
<b>Molar Activity</b>	> 37 GBq/μmol [1 Ci/μmol]	420 GBq/μmol [11.4 Ci/μmol]	697 GBq/μmol [18.8 Ci/μmol]	595 GBq/μmol [16.1 Ci/μmol]
<b>Radiochemical identity</b>	Retention time ratio of radio peak vs cold standard (0.9-1.1)	1.0	1.0	1.0
<b>Chemical purity</b>				
a) TBAHCO <sub>3</sub>	< 2.6 mg/V* (<520 mg/L**)	< 45 mg/L	< 45 mg/L	< 45 mg/L
	MeCN < 410 PPM	N.D.**	N.D.	N.D.
b) Residual solvents	MeOH < 3000 PPM	N.D.	N.D.	N.D.
	TA < 5000 PPM	N.D.	N.D.	N.D.
	EtOH < 10%	N.D.	N.D.	N.D.
<b>Radiochemical purity</b>	> 95%	> 99%	> 99%	> 99%
<b>Radionuclide identity</b>	104-115 min	109	108	110
<b>pH</b>	4.0-7.0	5.0	5.5	5.5
<b>Filter integrity</b>	> 50 PSI	> 50 PSI	> 50 PSI	> 50 PSI
<b>Stability on shelf</b>				
a) Appearance	Pass after 240 min	Pass	Pass	Pass
b) pH	Pass after 240 min	Pass	Pass	Pass
c) Radiochemical purity	Pass after 240 min	Pass	Pass	Pass
<b>Gamma ray emission energy</b>	496-526 keV photons	Pass	Pass	Pass
<b>Radionuclide purity</b>	No less than 99.5%	Pass	Pass	Pass
<b>Bacterial endotoxin</b>	< 175 EU/total batch	Pass	Pass	Pass
<b>Sterility</b>	No colony growth observed for 14 days	Pass	Pass	Pass

**Table 5.5 Conventional (manual) quality control testing results for 3 consecutive batches of [<sup>18</sup>F]FET**

\*V is a total maximum injection volume. \*\*The limit is converted to a concentration for the 5 mL formulated volume for comparison with the analytical results. . N.D. = not detected.

### 5.3.2 [<sup>18</sup>F]FBB production and testing

The initial runs using low (<20 MBq) starting activities were performed for syntheses with 2 different precursor volumes (10 μL and 15 μL). The crude RCY was similar in both cases (54 ± 9%, n=5 for 15 μL and 58 ± 7%, n=6 for 10 μL) as were other parameters (Table 5.6). Using a larger precursor volume helped to increase tolerance to any dispensing errors that may occur due to the high viscosity of the precursor solution.

Precursor volume (μL)	15	10	10
Automated or manual	Automated	Automated	Manual
Number of replicates (n)	5	6	4
Radioactivity recovery (%)	63 ± 6	69 ± 9	66 ± 6
[ <sup>18</sup> F]FBB conversion (%)	86 ± 9	86 ± 9	96 ± 1
Crude RCY (%)	54 ± 9	58 ± 7	63 ± 6
Residual activity on chip (%)	7 ± 6	8 ± 4	1 ± 1

**Table 5.6 A comparison of low activity droplet-based [<sup>18</sup>F]FBB synthesis performance**

Comparison shown for a manually versus automatically operated platform), and at 2 different precursor solution volumes.

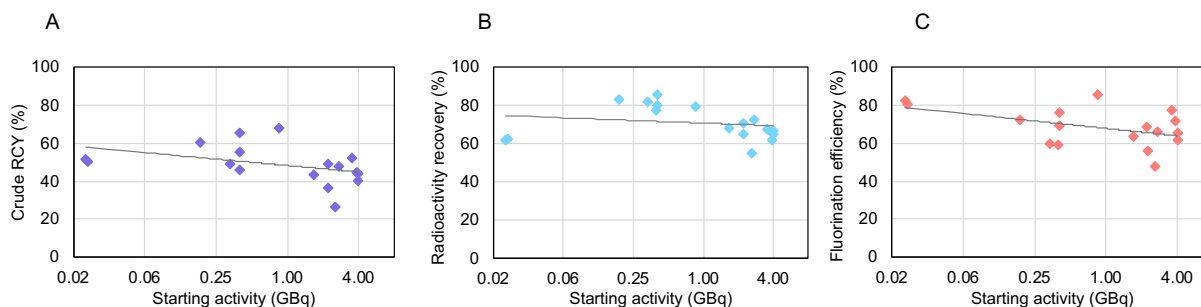


**Figure 5.7 Performance of crude [<sup>18</sup>F]FBB droplet-based radiosynthesis as a function of starting activity**

(A) Crude RCY. (B) Radioactivity recovery. (C) Fluorination efficiency. Note that the x-axis is plotted on a logarithmic scale, and a logarithmic trendline is generated for all graphs.

The impact of starting activity on the synthesis performance was also investigated (Figure 5.7). Across the range of 0.02 to 4.0 GBq, the crude RCY exhibited a slight decrease,

though the impact was negligible up to ~1 GBq of starting activity. Both the component measurements radioactivity recovery and fluorination efficiency exhibited a similar trend.

Complete tracer production – microdroplet synthesis followed by analytical HPLC purification and automated SPE formulation – took ~60 min and resulted in a radiochemically pure (>95%) product. Three consecutive batches exhibited  $15 \pm 4\%$  (n=3) overall activity yield, and high molar activity  $480 \pm 190$  GBq/ $\mu$ mol (n=3; EOS). All batches passed necessary QC tests for pH, residual solvents and purity (Table 5.7). Example chromatograms during [ $^{18}$ F]FBB purification and assessment of radiochemical purity and identity are shown in Figure 5.8.

### 5.3.3 [ $^{18}$ F]FBB Quality Control with Tracer-QC

Another three consecutive batches were prepared for QC analysis with the Tracer-QC system. This set of runs exhibited overall activity yield of  $16 \pm 4\%$  (n=3) and molar activities of  $490 \pm 130$  GBq/ $\mu$ mol (n=2; EOS). Each automated QC analysis produced a summary page along with a detailed 26-page report. All samples passed all acceptance criteria for release of the doses. The acceptance criteria for [ $^{18}$ F]FBB QC are presented in Table 5.8 along with the measurements performed by Tracer-QC. The demonstration with 3 consecutive samples confirms consistency of both synthesis and QC.

Test	Testing Criteria	Batch 1	Batch 2	Batch 3
<b>Appearance</b>	Clear, colorless, particle free	Pass	Pass	Pass
<b>Radioactivity concentration</b>	45-5000 MBq/mL [1.4-135 mCi/mL]	83 MBq/mL [2.2 mCi/mL]	97 MBq/mL [2.6 mCi/mL]	151 MBq/mL [4.1 mCi/mL]
<b>Molar Activity</b>	> 37 GBq/μmol [1 Ci/ μmol]	593 GBq/μmol [16.0 Ci/μmol]	262 GBq/μmol [7.1 Ci/μmol]	583 GBq/μmol [15.7 Ci/μmol]
<b>Radiochemical identity</b>	Retention time ratio of radio peak vs cold standard (0.9-1.1)	1.0	1.0	1.0
<b>Chemical purity</b>				
a) K <sub>222</sub>	< 50 mg/L	< 13 mg/L	< 13 mg/L	< 13 mg/L
	MeCN < 410 PPM	< 10 PPM	< 10 PPM	< 10 PPM
b) Residual solvents	DMSO < 5000 PPM	529 PPM	218 PPM	229 PPM
	Ethanol < 15%	8%	7%	7%
<b>Radiochemical purity</b>	> 95%	97%	98%	98%
<b>Radionuclide identity</b>	105-115 min	113	112	113
<b>pH</b>	4.0 - 8.0	5.5	5.5	5.5
<b>Filter integrity</b>	> 50 PSI	> 50 PSI	> 50 PSI	> 50 PSI
<b>Stability on shelf</b>				
a) Appearance	Pass after 240 min	Pass	Pass	Pass
b) pH	Pass after 240 min	Pass	Pass	Pass
c) Radiochemical purity	Pass after 240 min	Pass	Pass	Pass
<b>Gamma ray emission energy</b>	496-526 keV photons	Pass	Pass	Pass
<b>Radionuclide purity</b>	No less than 99.5%	Pass	Pass	Pass
<b>Bacterial endotoxin</b>	< 175 EU/total batch	Pass	Pass	Pass
<b>Sterility</b>	No colony growth observed for 14 days	Pass	Pass	Pass

**Table 5.7 Conventional (manual) quality control testing results for 3 consecutive batches of [<sup>18</sup>F]FBB.**

Test Parameter	Specification	QC Results		
		Batch #1	Batch #2	Batch #3
Color (mAU)	< 500	98.2	43.7	91.8
Clarity (NTU)	< 10	8.0	7.3	9.9
pH	4.5 – 7.5	5.2	5.3	5.3
Endotoxin (EU/mL)	< 7.5	< 1	< 1	< 1
Acetonitrile (µg/mL)	< 410	< 100	< 100	< 100
Kryptofix (µg/mL)	< 50	< 50	< 50	< 50
Concentration (MBq/mL)	45 – 5000	270 @ 12:46 PM	240 @ 1:09 PM	400 @ 12:16 PM
Half-Life (min)	105 – 115	110.7	113.2	114.6
Chemical Identity (%RRT)	90 – 110	100.0	100.0	100.0
trans-FBB Content (µg/mL)	≤ 3.0	0.53	0.62	0.78
Stilbene-OMs Content (µg/mL)	≤ 3.0	0.00	0.00	0.08
BOC-Stilbene-TEG Content (µg/mL)	≤ 1.5	0.06	0.11	0.00
Unspecified Impurity Content (µg/mL)	≤ 5.0	0.00	0.00	0.00
trans-FBB Radiochemical Identity (%RRT)	90 – 110	100.0	100.0	100.0
cis-FBB Radiochemical Identity (RRT)	1.12 – 1.16	Not Detected	Not Detected	Not Detected
cis/trans-FBB Radiochemical Purity (%)	≥ 93	96.6	95.4	96.4
cis-FBB Radiochemical Content (%)	≤ 6%	0.0	0.0	0.0
Unspecified Radiochemical Impurity (%)	≤ 7%	3.4	4.6	3.6
Specific Activity (GBq/µmol)	≥ 3	196.0 @ 12:46 PM	142.9 @ 1:09 PM	185.3 @ 12:16 PM

**Table 5.8 Tracer-QC quality control results for additional batches of [<sup>18</sup>F]FBB.**

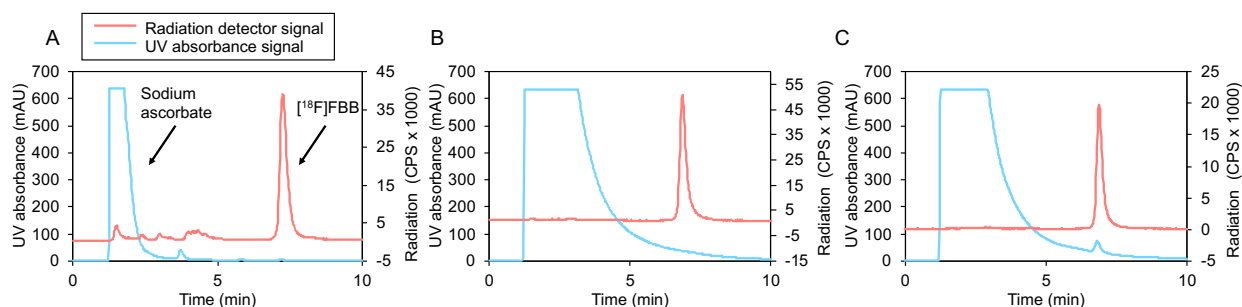


**Figure 5.8 Example HPLC chromatograms for [<sup>18</sup>F]FBB**

(A) Crude product. (B) Formulated product. (C) Formulated product co-injected with reference standard.

## 5.4 Discussion

### 5.4.1 Comparison to conventional synthesis

Compared to conventional synthesis methods, we previously showed (using starting activities <0.4 GBq) that microvolume syntheses overall result in shorter synthesis time (40 min for [<sup>18</sup>F]FET, 55 min for [<sup>18</sup>F]FBB), good radiochemical yields while consuming 100-150x less precursor. In this work we further demonstrate that the synthesis activity scale can be increased up to 4 GBq with minimal modifications to the synthesis method. With higher starting activities the synthesis time is slightly longer, due to the need to dry a larger volume of the radioisotope solution, but still remains <60 min. The yields are comparable to the range reported for conventional methods. Here, [<sup>18</sup>F]FET was produced with  $36 \pm 7\%$  (n=3) overall yield and generally, for conventional syntheses the reported yields vary between 20-40% (187,189,190). Microdroplet [<sup>18</sup>F]FBB synthesis resulted in  $23 \pm 3\%$  (n=6) overall yield comparable to 10-30% yield range of most reported methods (201,206,215,220(p94),221).

### 5.4.2 Activity scaling in droplet micro-radiosynthesizer

In previous work by our group, droplet-based synthesis of [<sup>18</sup>F]fallypride was demonstrated with starting activities ranging up to 41 GBq (107), highlighting the scalability of the droplet radiosynthesis techniques. Up to 7.2 GBq of injectable [<sup>18</sup>F]fallypride was produced,

which would be sufficient for multiple clinical doses. This work further demonstrates that product amounts of other clinically-relevant radiotracers ( $[^{18}\text{F}]\text{FET}$  and  $[^{18}\text{F}]\text{FBB}$ ) can be scaled up to amounts sufficient for clinical PET scans.

One of the major challenges when scaling starting activity of a microvolume synthesis is the relatively high volume of source aqueous  $[^{18}\text{F}]\text{fluoride}$  needed. Depending on the activity concentration, loading a high amount of radioactivity requires volumes of  $[^{18}\text{F}]\text{fluoride}$  larger than the capacity of a droplet micro-radiosynthesizer chip. With a radioactivity concentration of  $\sim 40$  GBq/mL from our cyclotron, 100s of  $\mu\text{L}$  of volume is needed to load 10s of GBq into the reaction chip. One approach for doing so is to use cartridge-based concentration methods. Iwata *et al.* show trapping of  $[^{18}\text{F}]\text{fluoride}$  (up to 6 GBq starting activities) on a conventional anion-exchange cartridge, and elution with MeOH containing Kryptofix 2.2.2 (K222) and  $\text{KHCO}_3$ . The eluate was passed through a cation-exchange cartridge (to remove most of the K222 /  $\text{KHCO}_3$ ) and collected into a V-vial containing a small amount of K222 /  $\text{KHCO}_3$ , followed by evaporation of MeOH, and then the microvolume ( $<20$   $\mu\text{L}$ ) of precursor solution was added to perform the syntheses of  $[^{18}\text{F}]\text{FET}$  and  $[^{18}\text{F}]\text{fallypride}$  (97, 184). In previous work by our group, up to 40 GBq of activity were concentrated using a custom micro-cartridge-based radioisotope concentrator that could concentrate activity from several mL volume to a volume  $<30$   $\mu\text{L}$  (113), which was integrated upstream of a droplet reactor to produce  $[^{18}\text{F}]\text{fallypride}$  (107). Though effective at concentrating the activity, the process took significant time, and efficient elution of  $[^{18}\text{F}]\text{fluoride}$  from the micro-cartridge required a significant amount of base, about 340 nmol (107). A similar amount of base was used by Iwata *et al.* where the amount of K222 /  $\text{KHCO}_3$  was estimated to be 200-520 nmol (97). In our previous work with  $[^{18}\text{F}]\text{fallypride}$ , the base amount from the micro-cartridge was higher than the value obtained during optimization (via direct addition of the base), requiring re-optimization of conditions due to the sensitivity to the base/precursor ratio (107). Since previous optimization of  $[^{18}\text{F}]\text{FET}$  synthesis in droplet format used 113 nmol of  $\text{TBAHCO}_3$  (50), a similar re-optimization would be necessary to integrate with

the micro-cartridge concentrator. In fact, based on previous optimization data (50), the precursor quantity would need to be tripled to achieve adequate yields otherwise the fluorination efficiency and consequently crude RCY would be very low.

To avoid this issue, in this work, we instead demonstrated that activity (up to 4 GBq) can be scaled by directly loading and drying multiple 30  $\mu\text{L}$  droplets of the [ $^{18}\text{F}$ ]fluoride solution (without using a cartridge), resulting in a significantly simpler procedure and more compact synthesis system. This concentration method can be used with any amount of base (in contrast to cartridge concentration method), allowing matching of the amount used in the optimized droplet synthesis protocol, and eliminating the need for re-optimization. While it is possible to load even higher activities with this method, drying a large volume (e.g. 1 mL) would require many (33) droplets to be sequentially loaded and dried. With each evaporation cycle run for 1.5 min, drying of 1 mL would take approximately 50 min. We expect  $\sim 300\text{-}600\ \mu\text{L}$  to be an upper practical limit, which could be concentrated in 15-30 min, though for many applications, smaller volumes and activity levels would be sufficient. For example, the concentration of 100  $\mu\text{L}$  could be completed in  $< 6$  min, which can contain 4 GBq or more of activity, depending on target volume and bombardment parameters. In this work it was shown for syntheses of [ $^{18}\text{F}$ ]FBB that using  $\sim 100\ \mu\text{L}$  of [ $^{18}\text{F}$ ]fluoride ( $\sim 4$  GBq) afforded up to  $\sim 0.7$  GBq of injectable tracer, which is sufficient for a typical clinical PET scan ( $\sim 0.37$  GBq per injection). If needed, additional tracers could subsequently be synthesized from additional aliquots of [ $^{18}\text{F}$ ]fluoride.

#### **5.4.3 Impact of starting activity on synthesis performance**

Increasing starting radioactivity in radiopharmaceutical syntheses (without changing other conditions) can directly affect stoichiometry and amplify radiolysis effects. A slight decrease in synthesis performance was observed for both [ $^{18}\text{F}$ ]FET and [ $^{18}\text{F}$ ]FBB as the starting activity was increased. Both the fluorination efficiency and radioactivity recovery exhibited



declines, resulting in moderately lower crude RCY (and isolated RCY). Performance was relatively unaffected up to ~1 GBq starting activity, and then started to show some reduction. In previous work with [<sup>18</sup>F]fallypride, the decrease in crude RCY only became significant around 20 GBq (107), suggesting this effect is tracer dependent. Though the data in Figure 5.5 and Figure 5.7 represents crude RCY (before purification and formulation) to eliminate confounding factors such as variations in purification or formulation efficiencies, the isolated RCY is expected to follow a similar trend.

Interestingly, an efficient synthesis of [<sup>18</sup>F]FET in microliter (10 µL) volumes was recently demonstrated by Iwata *et al.* using small reaction vials (97). Based on the reported results, the reaction yield was constant when starting activity was varied between 0.1 and 6 GBq. Notably, a higher amount of precursor was used, i.e., 180 nmol compared to 60 nmol in the current work. It was also shown that introduction of additional fluorine-19 carrier does reduce the radiochemical yields significantly (97). These results suggest that the precursor may become a limiting reagent at some point, depending on activity scale and molar activity of the [<sup>18</sup>F]fluoride source. We are continuing to explore the exact mechanism(s) by which the increasing activity level affects the yield and how the effect(s) can be mitigated.

#### **5.4.4 Quality control testing**

After synthesis, purification, and formulation, quality control (QC) testing of the radiopharmaceuticals is a crucial step necessary to ensure safety prior to use in patients (75,248–252). We performed QC testing by conventional methods for both [<sup>18</sup>F]FET and [<sup>18</sup>F]FBB on three consecutive batches each and showed suitability for use in patients. However, these tests require an array of expensive analytical instrumentation, all of which require space, maintenance, training, calibration, and documentation, making conventional QC testing a time-consuming, expensive procedure (77,78). Furthermore, some of the tests require manual handling of the radioactive batches resulting in high radiation exposure to the operator

(79) and higher margin for human error or subjective interpretation. In our case, QC testing had to be carried out in 3 different locations due to limited instrument availability in the research setting. Pairing a compact microfluidic reactor system with a large analytical laboratory facility undermines the economic advantages offered by microfluidic technology. In contrast, usage of a novel compact automated QC testing platform, Tracer-QC (TraceAbility Inc., Van Nuys, CA) has a potential to significantly reduce the overall footprint of tracer production instrumentation. Such an automated approach reduces instrument cost and space requirements and the effort and expertise needed to perform testing (77). We prepared additional three consecutive batches of [ $^{18}\text{F}$ ]FBB and shipped them out for QC testing with this instrument. Notably, only one QC unit (with HPLC) was needed to perform all necessary QC tests which were completed in 30 min each, generating a detailed report with “pass/fail” result for all samples.

There is a number of aspects in which QC automation makes a difference. The top three of them are:

(1) Ease and safety of use. Traditional QC requires highly skilled staff experienced with a variety of analytical instruments. It also relies on high attention to detail and subjective assessments that again require substantial experience. Finally, there is unavoidable handling of unshielded radioactive samples. The automation offered by Tracer-QC eliminates the need for any chemistry training or background. There are no subjective assessments and never a direct line of sight between the user and unshielded sample. The instrument is also very easy to maintain because of its simplicity, absence of cleaning and a large number of automated internal diagnostics.

(2) Efficiency. It is the reason for synthesis miniaturization and the progress reported herein makes a dramatic advance towards it. However, if efficient synthesis is followed by traditional QC, that may negate its benefits. Therefore, for miniaturized synthesis to deliver its maximum benefit to [ $^{18}\text{F}$ ]FBB and a multi-tracer portfolio, it needs to be coupled with compact and efficient QC. Tracer-QC achieves this objective by freeing up the personnel (while it runs

completely unattended), minimizing the footprint needed for addition of new tracers to a facility, and simplifying maintenance and consumables inventory. Facilities utilizing QC automation should be in position to increase their throughput and the number of PET tracers they support.

(3) Compliance. Tracer-QC takes the person out of the equation. It leaves no room for missing a process, record or signature. It is completely objective and has uncompromised, tamper-free and auditable data flow from raw measurements to reports. Finally, it eliminates most contamination risks by using disposable kits.

#### **5.4.5 Prospects for clinical use**

Currently, producing radiopharmaceuticals for clinical use requires investment in a radiochemistry laboratory set up for GMP production, typically with one hot cell and synthesis module per tracer, and a suite of analytical equipment for performing QC tests. Alternatively, such radiopharmaceuticals can sometimes be obtained under expensive contract arrangements with radiopharmacy companies.

The microdroplet synthesis approach coupled with a benchtop automatic QC testing system has the potential to establish a convenient dose-on-demand protocol for PET radiopharmaceutical production suitable for clinical use that requires much smaller investment and lab space, and would require very little of the traditional radiochemistry lab infrastructure and equipment. Including this work, microdroplet synthesis methods have been shown to be compatible with [ $^{18}\text{F}$ ]fallypride (107), [ $^{18}\text{F}$ ]FET, and [ $^{18}\text{F}$ ]FBB syntheses at clinically-relevant quantities, and [ $^{18}\text{F}$ ]FDG (104,106,244,253), [ $^{18}\text{F}$ ]FLT (115,244,254), [ $^{18}\text{F}$ ]SFB (213,244), [ $^{18}\text{F}$ ]FDOPA (106) at lower quantities.

The compact size of the microvolume radiosynthesis system opens up the possibility for a benchtop, self-shielded system, that would require very little laboratory space, and enable the production of tracers without the need for hot cells. To realize this new microscale paradigm for radiopharmaceutical production, the microdroplet synthesis system has to be seamlessly

automated from radioisotope dispensing to complete formulation within a compact system, and would need to be enclosed within shielded and would require a mechanism to capture any volatile radioactivity (86).

On the other hand, the Tracer-QC system is already used at multiple sites for testing of clinical batches produced using conventional synthesis modules and could immediately be integrated with a droplet synthesizer. Trace-Ability is expanding the application of Tracer-QC to more PET tracers. With each new tracer, the incremental effort becomes smaller and smaller since it relies on tests already developed for previous tracers and requires only concerted re-validation effort. There are currently over 20 different QC tests enabled on Tracer-QC platform, which are the most common ones applicable to a broad range of PET tracers.

One of the benefits of microfluidics is that it provides an intrinsic advantage in patient safety of the final product due to the significantly reduced mass of reagents and thus of impurities in the final product. In this work, the tracers synthesized using droplet radiosynthesizer exhibited low amounts of impurities (residual solvents, TBA or  $K_{222}$ ) in most cases below the detection limit. Notably, the starting amounts of toxic compounds is already low and these quantities can potentially be even further reduced to be below acceptable threshold potentially simplifying QC testing requirements. For example, in [ $^{18}\text{F}$ ]FET synthesis the starting amount of  $\text{TBAHCO}_3$  per reaction is 34  $\mu\text{g}$  in total while up to 2.6 mg per injection are allowed. In [ $^{18}\text{F}$ ]FBB synthesis 10  $\mu\text{L}$  of DMSO are consumed per synthesis, and with the formulation volume of  $\sim 2$  mL it would guarantee that the limit of 5000 ppm will not be exceeded even if purification failed to remove any of the DMSO.

At the same time, we are attempting to increase the activity scale of the synthesis, improvements in scanner technology are requiring less activity for clinical PET scans. In particular, recent developments with whole-body PET allowed to obtain good [ $^{18}\text{F}$ ]FDG human scans with only 25 MBq of administered activity (255), about  $\sim 10\times$  lower than what is typically injected. Such advancements mean that the modest sized batches produced here may each be

suitable for many patients, or batches for one or a few patients could be produced at lower activity levels, where the yields are slightly higher.

## 5.5 Conclusion

In this work we demonstrate the use of a compact automated microdroplet synthesizer to rapidly produce batches of formulated [ $^{18}\text{F}$ ]FET and [ $^{18}\text{F}$ ]FBB with high yield and high molar activity. In contrast to previously reported production of [ $^{18}\text{F}$ ]fallypride on a microdroplet chip which was coupled to a separated radionuclide concentrator to increase the synthesis scale (107), the radioisotope was concentrated in this work using a simpler and faster approach still capable of clinically-relevant synthesis scale.

Though a modest reduction in RCY was observed when scaling up, it is nonetheless clear that droplet-based radiochemistry systems have sufficient scaling capacity to produce one or more clinical doses, while offering many additional advantages including compact size, reduced reagent usage, high molar activity (256). Future work will explore more deeply the impact of scaling on reaction performance to determine mitigation strategies.

All batches of prepared radiopharmaceuticals passed clinical quality control requirements using conventional testing protocols. The droplet-base synthesis uses much smaller amounts of reagents than conventional methods, resulting in much lower quantities of impurities, and tests for residual solvents and phase transfer catalyst passed by wide margins (often undetectable amounts). Additionally, for the production of [ $^{18}\text{F}$ ]FBB, an automated benchtop QC testing system (Tracer QC, Trace-Ability, Inc.) was used enabling a faster and more convenient approach. The benchtop quality control coupled with microdroplet synthesis strategies have a potential to establish a robust and economical method for dose-on-demand production of PET radiopharmaceuticals, without requiring large radiochemistry and analytical chemistry facilities.

# Chapter 6: Isotopic exchange labeling of [<sup>18</sup>F]AMBF<sub>3</sub>-TATE in microliter volumes

## 6.1 Introduction

The use of PET (positron emission tomography) has revolutionized applications in cancer diagnosis. To wit, PET provides dynamic, high-resolution spatio-temporal imaging of tumor uptake and clearance of the injected radiotracer. New hybrid imaging machines, which combine PET with CT (X-ray computed tomography) or MRI (magnetic resonance imaging), can enhance tumor images with the superposition of anatomical features including bony structures, soft-tissues, as well as blood flow for proper anatomical registration and assessment of neovascularization (257).

The production of PET radiotracers requires the judicious use of one of several short-lived positron-emitting nuclides, the choice of which is often dictated in part by the tracer's pharmacokinetics. Of the various PET isotopes in use, fluorine-18, however, is the only one that can be produced at large scale (>37 GBq [1 Ci] per run) sufficient for production of many patient doses in a single batch. With a moderate half-life, a track-record in FDA approval of <sup>18</sup>F-labeled radiotracers, low radiotoxicity, and the highest resolution of any PET nuclide due to a low positron energy (258,259), fluorine-18 is the choice isotope for use in PET. Early on, 2-[<sup>18</sup>F]fluoro-2-deoxy-D-glucose ([<sup>18</sup>F]FDG), 3'-[<sup>18</sup>F]fluoro-3'-deoxythymidine ([<sup>18</sup>F]FLT), and 1H-1-(3-[<sup>18</sup>F]fluoro-2-hydroxypropyl)-2-nitroimidazole ([<sup>18</sup>F]FMISO) (260) enabled cancer imaging based on increased metabolism or hypoxia typical of most but not all cancers. Over the past four decades, [<sup>18</sup>F]FDG has become the most extensively used radiotracer. Yet despite its utility, it typically cannot assess tumor subtypes, and it can give both false negatives and positives (261,262).

Over the past two decades, cancer subtypes are increasingly being distinguished by peptides that have emerged from the study of endocrinology and from various combinatorial screens (263–268) that were undertaken to identify target-based diagnostics and therapeutics (269). Radiolabeled peptides have been used in clinical PET imaging to distinguish pathologically distinct cell types via recognition of specific molecular targets – a feat that is impossible with [<sup>18</sup>F]FDG (270–273). Examples of such peptides include octreotate (274–278), bombesin (279), folate (280–285), and RGD (286–288). Drugs based on peptides include Lupron™ for prostate cancer, various octreotate analogs (e.g. Sandostatin™) for neuroendocrine tumor treatment, the folate-vincristine conjugate Vintafolide™ for ovarian cancer (289,290), as well as other potential therapeutic toxin conjugates (291,292). Undeniably, peptides and other relatively large biologic entities provide the needed specificity and affinity for specific recognition of pathognomonic targets, which when properly imaged can enhance personalized diagnosis. In some cases, the same peptide that is used for PET imaging can be engineered for theranostic applications that may include targeted therapy via conjugation/chelation with a radiotoxin, chemotherapeutic, or used fluorescently to guide surgical resections.

Given the molecular complexity of peptides and their general water solubility, peptides have been typically labeled for both diagnostic and radiotherapeutic purposes by radiometal chelation that simply involves heating a peptide-chelator conjugate in the presence of a radiometal (e.g. gallium-68 or copper-64 for imaging or lutetium-177 for therapy). Nevertheless, the use of radiometals for imaging poses several drawbacks, most notably a lack of scalability in their production, the potential for transchelation of the metal *in vivo* (293–295), and generally lower molar activities compared to those labeled with fluorine-18. Yet radiometal chelation remains highly useful for imaging since the production of <sup>18</sup>F-labeled peptides continues to be challenged by the relatively short half-life of fluorine-18 (110 min) and more importantly, by both

solvent and chemical incompatibilities. Anionic [ $^{18}\text{F}$ ]fluoride is unreactive as a nucleophile in water (296) whilst most peptides are insoluble in the dry aprotic solvents that are typically used for  $^{18}\text{F}$ -labeling (297), and electrophilic fluorinating agents (e.g. [ $^{18}\text{F}$ ]F $_2$ ) pose problems including non-selective reaction with cysteine, methionine and tryptophan and generally have lower molar activity compared to anionic [ $^{18}\text{F}$ ]fluoride. Hence, multistep syntheses are usually required such as first synthesizing an  $^{18}\text{F}$ -labeled prosthetic for further conjugation to a peptide via a variety of chemistries including biorthogonal “click” reactions. While feasible, multistep procedures generally suffer from long reaction times and unwanted side-products. Hence any approach that would simplify radiofluorination would be of considerable interest.

Recently, three new methods for one-step/late-stage  $^{18}\text{F}$ -labeling of peptides have appeared: (1) triorganosilyl-fluorides that are labeled by  $^{19}\text{F}$ - $^{18}\text{F}$  isotope exchange (IEX) (160,298), (2) NOTA chelation of aluminum-fluoride (299–301), and (3) organoboronate esters to capture aqueous fluoride as  $^{18}\text{F}$ -labeled organotrifluoroborates (RBF $_3$ s). While all three methods are relatively simple, peptide-BF $_3$  bioconjugates are labeled under fully aqueous conditions and do not require HPLC purification. Nevertheless, to date, only a manual synthesis has been reported for various peptide-BF $_3$  bioconjugates. Moreover, conventional automated radiosynthesizers are not suited to the relatively small reaction volumes needed to achieve high molar activities that can be observed with  $^{18}\text{F}$ -labeled peptide-BF $_3$  conjugates (302). Hence, emerging microfluidic platforms, which offer advantages such as faster synthesis times, reduced reagent consumption, would be expected to afford the requisite low volumes that in turn would increase molar activity values (91,120,178) while also increasing both ease of use and access to peptide-BF $_3$  tracers provided that such a platform could be configured for automated preparation of such conjugates. Our work using electrowetting-on-dielectric (EWOD) microfluidics for the droplet-based radiosynthesis of several  $^{18}\text{F}$ -labeled PET tracers (e.g.



[<sup>18</sup>F]FDG, [<sup>18</sup>F]FLT, [<sup>18</sup>F]fallypride) (104,115,211,244) has provided compelling evidence that it could be readily adapted to these novel peptide tracers.

To interface the unique microfluidic platform of the EWOD system with an aqueous radiofluorination of a peptide-BF<sub>3</sub> conjugate in a one-step automated synthesis with requisite low volumes, we opted to investigate octreotate as there would be considerable interest if it could be labeled with [<sup>18</sup>F]fluoride on a microfluidic platform for eventual translation for imaging neuroendocrine tumors (NETs). The previous report on the preclinical evaluation of the <sup>18</sup>F-labeled BF<sub>3</sub>-conjugate of octreotate, [<sup>18</sup>F]AMBF<sub>3</sub>-TATE, showed excellent pharmacokinetic properties, with high tumor uptake and high contrast ratios, in mice bearing AR42J tumor xenografts (303) underscoring the potential utility of this particular octreotate-derived tracer. Yet this report featured manual labeling within a fully shielded hot-cell using up to 37 GBq [1.0 Ci] of no-carrier-added [<sup>18</sup>F]fluoride consistent with clinical GMP guidelines and since then, there has been no report of an automated synthesis of the same tracer, nor a report on microfluidic synthesis, both of which would be of considerable import in terms of extending the means and methods for producing, distributing, and translating this and other <sup>18</sup>F-labeled peptide tracers. Our choice for [<sup>18</sup>F]AMBF<sub>3</sub>-TATE is based in part on these previous results that now provide an essential set of benchmarks in terms of radiochemical yields, molar activities, reaction times, tumor uptake values and contrast ratios, all of which arguably would need to be recapitulated on an EWOD microfluidic platform in order to consider its use in clinical translation and a means of comparing microfluidic production compared to a manual synthesis.

In turn, an <sup>18</sup>F-labeled octreotate might be expected to compete with [<sup>68</sup>Ga]Ga-DOTATATE, a DOTA-conjugate to the somatostatin analog octreotide that is now used routinely in the United States to determine target expression and stage neuroendocrine tumors (304) for diagnosis or patient stratification for radioligand therapy using [<sup>177</sup>Lu]Lu-DOTATATE, a radiotoxin conjugate based on the same targeting peptide. The great success of SSTR2

imaging using the Tyr<sup>3</sup>-octreotate peptide has paved the way for U.S. FDA approval for Advanced Accelerator Applications (AAA) of NETSPOT, a kit for the preparation of a single patient dose of [<sup>68</sup>Ga]Ga-DOTATATE injection. Notwithstanding the viability of [<sup>68</sup>Ga]Ga-DOTATATE, labeling with Ga-68 can make it difficult to meet the high imaging demand at some facilities, while the development of an <sup>18</sup>F-labeled analog, that could be made in larger multi-patient-dose batches is of considerable practical interest.

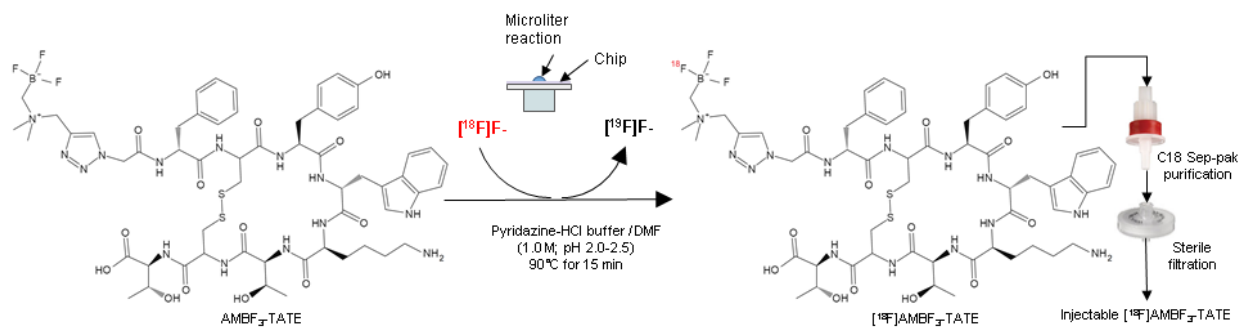


**Figure 6.1 Radiosynthesis of [<sup>18</sup>F]AMBF<sub>3</sub>-TATE via isotopic exchange on a microfluidic chip**

In this paper, we pave the way toward automated production of such tracers by demonstrating the straightforward radiosynthesis of [<sup>18</sup>F]AMBF<sub>3</sub>-TATE (Figure 6.1) in microdroplet format (120). Eventually, the microfluidic chip could form the basis for a compact, inexpensive synthesis kit. Furthermore, herein we report preclinical imaging studies of human SSTR2 transduced and rat SSTR2 wildtype murine xenografts, performed to provide direct comparison of [<sup>68</sup>Ga]Ga-DOTATATE and [<sup>18</sup>F]AMBF<sub>3</sub>-TATE in the same animals. To support clinical translation, a dosimetry analysis of [<sup>18</sup>F]AMBF<sub>3</sub>-TATE is also presented. The microscale synthesis can readily produce clinically-relevant quantities and could be further scaled up using techniques such as concentration of [<sup>18</sup>F]fluoride (305) prior to introduction into the microreactor.

## 6.2 Materials and methods

### 6.2.1 Reagents and materials

No-carrier-added [ $^{18}\text{F}$ ]fluoride was produced by the (p,n) reaction of [ $^{18}\text{O}$ ]H<sub>2</sub>O (84% isotopic purity, Zevacor Pharma, Noblesville, IN, USA) in an RDS-112 cyclotron (Siemens; Knoxville, TN, USA) at 11 MeV using a 1 mL tantalum target with havar foil. [ $^{18}\text{F}$ ]FDG and [ $^{68}\text{Ga}$ ]Ga-DOTATATE were obtained from the UCLA Biomedical Cyclotron Facility.

Acetonitrile (MeCN; anhydrous, 99.8%), methanol (MeOH; anhydrous, 99.8%), ethanol (EtOH; 200 proof), aqueous ammonia solution (28% NH<sub>3</sub> in H<sub>2</sub>O), and N,N-dimethylformamide (DMF; anhydrous, 99.8%) and 0.2  $\mu\text{m}$  inorganic membrane filters (Whatman Anotop, catalog # 6809-3122) were purchased from Sigma-Aldrich (St. Louis, MO, USA). Saline (0.9% sodium chloride injection, USP) was obtained from Hospira Inc. (Lake Forest, IL, USA); pyridazine (>99%) was obtained from Tokyo Chemical Industry Co., Ltd. (Japan), and hydrochloric acid (HCl; 3N) was obtained from HAZCAT (Mariposa, CA, USA). All reagents were used without further processing or purification. Deionized (DI) water was obtained with a purification system (RODI-C-12BL, Aqua solutions, Inc., Georgia, USA). C18 cartridges (Sep-Pak Plus C18) were obtained from Waters (Milford, MA, USA) and were preconditioned before use by flowing 10 mL of MeOH followed by 15 mL of DI water. The AMBF<sub>3</sub>-TATE precursor was prepared as previously described (303).

To prepare a batch of the reaction buffer, 720  $\mu\text{L}$  of pyridazine was added to 5 mL of DMF and 2.5 mL DI water in a 15 mL conical tube. The pH was adjusted to the range 2.0-2.5 with 3M HCl. The final volume was then adjusted with DI water until the final volume reached 10 mL. To prepare a batch of the quench solution (5% NH<sub>3</sub> aq. v/v), 1.8 mL of 28% NH<sub>3</sub> was diluted in 8.2 mL of DI water.

pH test strips (0-14 range, Ricca Chemical Company), and TLC plates (Baker-flex silica gel IB-F sheets 2.5x7.5 cm, J.T. Baker) were purchased from Thermo Fisher Scientific.

### 6.2.2 Chip fabrication

Sulfuric acid (96%, cleanroom MB), hydrogen peroxide (30%, cleanroom LP), acetone (99.5%, cleanroom MB), methanol (99.9%, cleanroom LP) were purchased from XMG Electronic Chemicals Inc. (Houston, TX, USA). Tridecafluoro-1,1,2,2-tetrahydrooctyl trichlorosilane (silane) was purchased from Gelest, Inc. (Morrisville, PA, USA), and Teflon AF 2400 1% solution was purchased from DuPont Fluoroproducts (Wilmington, DE, USA). Tape (TimeMed Label Tape) was obtained from Fisher Scientific.

Glass substrates (25x25x1 mm) were cut from standard microscope slides, and placed in a custom-made teflon rack. The slides were sonicated in acetone for 5 min, then in MeOH for 5 min. Next, the slides were rinsed with DI water and dried using a N<sub>2</sub> gun. The glass slides were submerged in Piranha cleaning solution (3:1 sulfuric acid (96%) and hydrogen peroxide (30 %)) for 15-30 min. After cleaning, the glass pieces were extensively rinsed with DI water and dried with nitrogen. Next, the slides were silanized by placing them in a glass desiccator with few droplets of silane, applying vacuum to the chamber for 5-10 min to reduce pressure, and then sealing the chamber overnight. After silanization, chips were heated at 110°C for 10 min on a hot plate. Teflon AF solution was spin-coated (Headway PWM 32, Headway Research Inc., Garland, TX, USA ) on one side of each chip using the following 3-step program: 500 RPM for 5s (ramp rate 100 RPM/s), 1000 RPM for 30 s (ramp rate 500 RPM/s) and 0 RPM (ramp rate 1000 RPM/s). After coating, the glass chips were heated on a hotplate at 160°C for 10 min, then at 245°C for 10 min. Finally, the chips were baked in a Carbolite oven (HTCR6 28 with 3216P1 programmer option, Carbolite Gero Ltd., UK) at 340°C for 3.5 h.

### 6.2.3 Chip temperature control system

Heating was accomplished via a small rectangular 180 W ceramic heater with a built-in thermocouple (CER-1-01-00098 Ultramic heater, Watlow Electric Manufacturing Co., St. Louis, MO, USA). The thermocouple signal was connected to a data acquisition module (USB-201, Measurement Computing, Norton, MA, USA). A custom program developed with Labview (National Instruments, Austin, TX, USA) performed feedback control of the temperature via an on-off algorithm triggering a solid-state relay to power the heater. The heater was affixed to a thermoelectric (Peltier) device to enable heat insulation during heating steps and accelerated cooling of the chip after these steps. The Peltier was fixed to a heatsink and fan. The chip was placed on top of the ceramic heater with the Teflon-AF side up. A small amount of thermal paste (OmegaTherm 201, Omega Engineering, Inc., Stamford, CT, USA) was used at all thermal junctions.

### 6.2.4 Microdroplet radiosynthesis of [ $^{18}\text{F}$ ]AMBF<sub>3</sub>-TATE

The radiosynthesis was performed in droplets on microfluidic chips composed of Teflon-coated glass substrates. These simple chips serve as surrogates for more sophisticated electrowetting-on-dielectric (EWOD) chips (104,115,211) that could be used to perform fully-automated droplet synthesis. A simple temperature control system was assembled to heat and cool the glass chip (Figure 6.2).

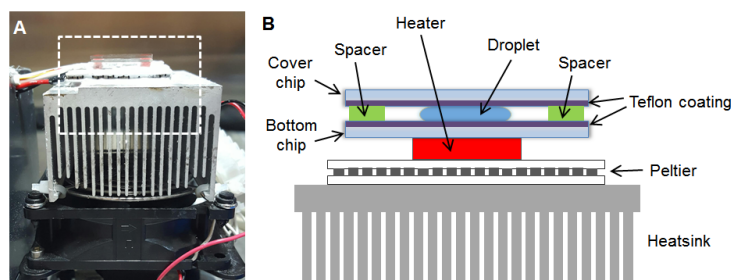


**Figure 6.2 Droplet synthesizer**

(A) Photograph of heating setup and microfluidic reaction chip. (B) Schematic of the chip and heating setup.

$[^{18}\text{F}]\text{AMBF}_3\text{-TATE}$  was synthesized via an isotopic exchange process at a trifluoroborate group, similar to the SiFA methodology first introduced by Schirmacher and Jurkschat in 2006 (160). To maximize the molar activity, the synthesis (303,306) was adapted to the droplet scale (120,183) to minimize the amount of precursor needed (Figure 6.3). Cyclotron-produced aqueous  $[^{18}\text{F}]\text{fluoride}$  (up to 3.7 GBq [100 mCi], 100  $\mu\text{L}$ ) was deposited on the chip surface with addition of equal volume of MeCN (up to 60  $\mu\text{L}$ ) and 10  $\mu\text{L}$  saline; the chip was then heated at 105°C for 2-3 min until only a tiny droplet remained. 5 nmol of TATE- $\text{AMBF}_3$  precursor, dissolved in pyridazine-HCl buffer / DMF (5  $\mu\text{L}$ , 1M, pH 2.0-2.5), was loaded onto the chip and mixed with the dried residue. Next, the droplet was covered with a second chip placed Teflon-side down. This cover chip had narrow strips of tape adhered on the underside of 2 edges to provide a separation between the plates of 150  $\mu\text{m}$  when assembled. The isotopic exchange reaction was carried out for 15 min at 90°C. After removing the top chip, the reaction was quenched by adding a 10 $\mu\text{L}$  droplet of 5% aq.  $\text{NH}_3$  to the reaction droplet. Next, the product was collected from the bottom chip by adding 20  $\mu\text{L}$  of an EtOH/saline mixture (1:1 v/v) to the area where the droplet was in contact with the chip surface, and then transferring the diluted crude product with pipette into a clean vial. The process was then repeated with an additional 20  $\mu\text{L}$ . Residual crude product was collected from the cover chip using a similar process.

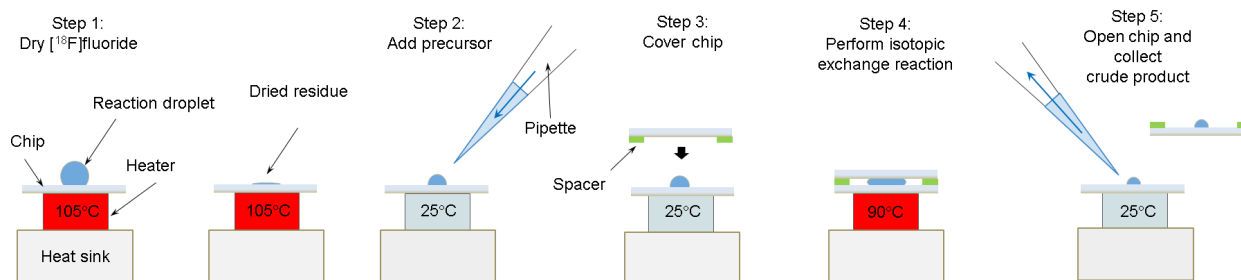


**Figure 6.3 Schematic of the sequence of operations to perform the microdroplet radiosynthesis of  $[^{18}\text{F}]\text{AMBF}_3\text{-TATE}$  on the chip.**

For preclinical imaging purposes the collected product was purified and formulated for injection. It was first diluted with 5% aq.  $\text{NH}_3$  quench solution to a volume of 2 mL and then

slowly passed through the pre-conditioned C18 Sep-pack to trap [<sup>18</sup>F]AMBF<sub>3</sub>-TATE. Next, the cartridge was washed with 4 mL of DI water. Finally, [<sup>18</sup>F]AMBF<sub>3</sub>-TATE was eluted with 0.5 mL EtOH/saline mixture (1:1 v/v), and diluted to ≤10% EtOH with 2.0 mL saline. The resulting product was passed through a sterile 0.2 μm filter into a sterile empty glass vial. If more concentrated product was needed (i.e. to achieve at least 37-74 MBq/mL [1-2 mCi/mL] for imaging), the compound was instead formulated via an evaporation method. The [<sup>18</sup>F]AMBF<sub>3</sub>-TATE was eluted from the cartridge with 2 mL EtOH into a glass vial with Teflon stir bar, and then the solvent was fully evaporated with nitrogen gas flow (7psi) under vacuum for 3-5 mins at 90°C (using an ELIXYS FLEX/CHEM radiosynthesizer, Sofie Biosciences, Inc., Culver City, CA, USA). Next, saline was added to redissolve the residue to the desired concentration and sterile filtration was performed.

#### **6.2.5 Analytical methods for evaluation of synthesis performance**

To understand the performance of each step of the microscale synthesis, radioactivity remaining at intermediate steps was measured, and samples were taken for radio-TLC and/or radio-HPLC analysis.

Measurements of radioactivity were made with a calibrated ion chamber (CRC 25-PET, Capintec, Florham Park, NJ, USA). For radio-TLC analysis, a small sample was transferred with a glass capillary onto a TLC. The plate was developed in MeCN/H<sub>2</sub>O (1:1 v/v), and then scanned with a TLC reader (miniGita star, Raytest, Inc., Wilmington, NC, USA). R<sub>f</sub> for [<sup>18</sup>F]fluoride was 0.0, and for [<sup>18</sup>F]AMBF<sub>3</sub>-TATE was 0.75. Radio-HPLC analysis was performed using a Smartline HPLC system (Knauer, Berlin, Germany) with a pump (Model 1000), degasser (Model 5050), a UV detector (Model 2500) and a radiometric detector (Bioscan B-FC-4000, Bioscan Inc., Washington DC, USA). Samples were separated using a Luna C18 (4.6 x 250mm, 5μm) column (Phenomenex, Torrance, CA, USA) with guard column (SecurityGuard C18, Phenomenex) at a flow rate of 1 mL/min. UV absorbance was measured at 277 nm. A

gradient program was used with the following solvents: 0.1% (v/v) TFA in DI water (solvent A) and MeCN (solvent B). The solvent B concentration changed as follows: 5% from 0-2 min, 5-35% from 2-7 min, 35-65% from 7-15 min, 65-100% from 15-20 min, 100% from 20-25 min, and 100-5% from 25-30 min. The retention time of [ $^{18}\text{F}$ ]fluoride was 2-3 min, and that of [ $^{18}\text{F}$ ]AMBF<sub>3</sub>-TATE was 11-12 min.

Since [ $^{18}\text{F}$ ]fluoride is not accurately quantified via radio-HPLC (307), we used the following 2-step procedure to determine the radiochemical conversion (i.e. incorporation of [ $^{18}\text{F}$ ]fluoride into [ $^{18}\text{F}$ ]AMBF<sub>3</sub>-TATE) of collected crude samples. First, a radio-TLC chromatogram was used to estimate the proportion of non-[ $^{18}\text{F}$ ]fluoride species by computing the area of the second peak and dividing by the sum of the areas of both peaks. Next, the radio-HPLC chromatogram was used to compute the fraction of the desired product by taking the area of the product peak and dividing by the sum of areas of all other peaks, except the [ $^{18}\text{F}$ ]fluoride peak. These two fractions were multiplied to determine the radiochemical conversion. The radiochemical yield (RCY) of the final product was computed as the activity of purified [ $^{18}\text{F}$ ]AMBF<sub>3</sub>-TATE divided by the activity of initial [ $^{18}\text{F}$ ]fluoride, corrected for decay. Since not all samples were purified, we also report the “crude RCY”, which is the activity of collected crude [ $^{18}\text{F}$ ]AMBF<sub>3</sub>-TATE, multiplied by the radiochemical conversion (to determine activity corresponding to [ $^{18}\text{F}$ ]AMBF<sub>3</sub>-TATE), divided by the activity of initial [ $^{18}\text{F}$ ]fluoride.

Molar activity (commonly known as specific activity) was determined by standard procedures. From the UV trace of a radio-HPLC injection, the area under the curve (AUC) corresponding to the product was determined and converted to a molar amount using a calibration curve (Error! Reference source not found.). The injected radioactivity was determined from decay-corrected measurements of the sample vial and syringe before and after HPLC injection. This radioactivity value was multiplied by the radiochemical conversion to determine the radioactivity of [ $^{18}\text{F}$ ]AMBF<sub>3</sub>-TATE injected. The molar activity then was determined by dividing this final radioactivity by the molar amount of AMBF<sub>3</sub>-TATE.



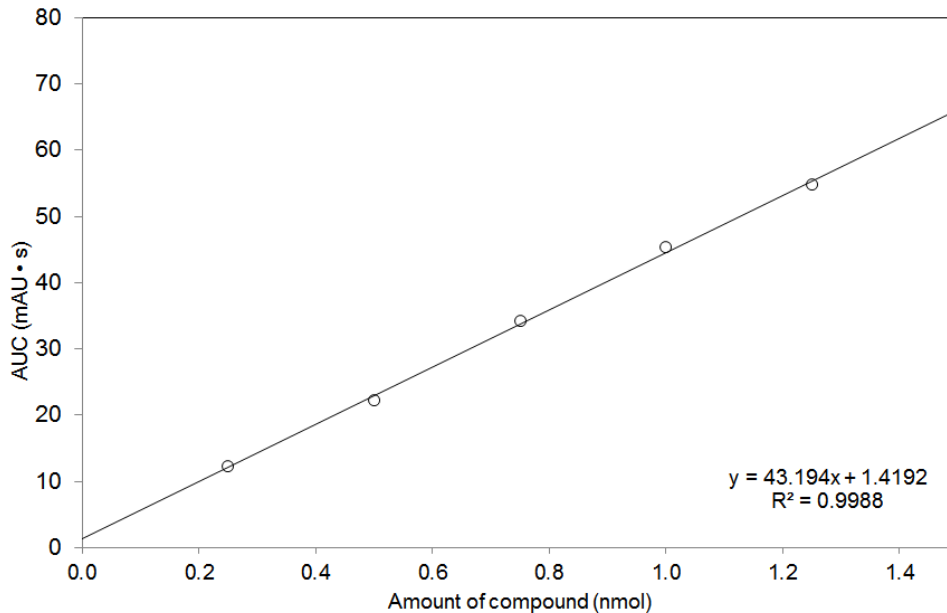


**Figure 6.4 Calibration curve for HPLC determination of molar amount of AMBF<sub>3</sub>-TATE.**

### 6.2.6 Murine tumor models

To evaluate [<sup>18</sup>F]AMBF<sub>3</sub>-TATE *in vivo*, NOD *scid* gamma (NSG) mice (n=4) were first engrafted with 1 x 10<sup>7</sup> AR42J cells (pancreatic NET model cell line naturally expressing SSTR2) in the left shoulder on day -7 and 1 x 10<sup>5</sup> RM1 cells (murine control cells, SSTR2-negative) in the right shoulder on day -3. This tumor inoculation protocol has been optimized to ensure similar tumor sizes of about 50 mm<sup>3</sup> at day 0 for both cell lines. On day 0 [<sup>18</sup>F]FDG PET/CT imaging was performed to assess tumor viability and size. PET/CT imaging with [<sup>18</sup>F]AMBF<sub>3</sub>-TATE and [<sup>68</sup>Ga]Ga-DOTATATE were performed on day 1 and day 2, respectively. Across all imaging days, AR42J tumors were 56 ± 19 mm<sup>3</sup> and RM1 tumors were 111 ± 59 mm<sup>3</sup>. (The RM1 tumors were larger due to their faster growth rate beginning at day 0.) To indicate well-preserved binding capability to the human receptor, RM1 cells stably transduced with human SSTR2 were used (RM1-hSSTR2).

AR42J cells were purchased from American Type Culture Collection (ATCC; Manassas, VA, USA), whereas the RM1 cells were kindly provided by Dr. Michel Sadelain (Memorial Sloan-

Kettering Cancer Center, New York, USA). The cells were grown in Dulbecco's Modified Eagle's Medium (DMEM) with 4.5 g/L glucose, L-glutamine, sodium pyruvate (Cellgro, Corning Life Sciences) and 10% fetal bovine serum (Omega Scientific) at 37°C, 20% O<sub>2</sub> and 5% CO<sub>2</sub>. For tumor injection, the cells were harvested and resuspended in a 1:1 mixture of PBS (Gibco Life Technologies) and Matrigel (Corning Life Sciences).

### 6.2.7 PET/CT imaging and biodistribution

PET/CT images were acquired using the integrated GENISYS 8 microPET/CT (Sofie Biosciences). It has a PET subsection optimized for mouse imaging with an energy window of 150-650 keV and peak sensitivity of approximately 14% at the center of field of view (FOV). The intrinsic detector spatial resolution is 1.5 mm FWHM in the transverse and axial directions. The CT section consists of a gantry and flywheel that uses a 50 kVp, 200 µA x-ray source and flat-panel detector. The CT acquires images in a continuous-rotation mode with 720 projections at 55 msec per projection, and reconstructed using a Feldkamp algorithm.

Tumor-bearing NSG mice underwent static imaging with [<sup>18</sup>F]FDG and [<sup>68</sup>Ga]Ga-DOTATATE, and dynamic and static imaging with [<sup>18</sup>F]AMBF<sub>3</sub>-TATE. For [<sup>18</sup>F]FDG imaging, the mice were fasted 4 hours prior to tracer injection. 0.74 MBq (20 µCi) of [<sup>18</sup>F]FDG were administered via tail vein injection. The mice were kept under 2% isoflurane anesthesia during the tracer uptake of 1 h and 10 min static PET imaging. For [<sup>68</sup>Ga]Ga-DOTATATE imaging, the mice were injected with 1.1 MBq (30 µCi) of the tracer with conscious uptake of 1 h and 10 min static PET. For [<sup>18</sup>F]AMBF<sub>3</sub>-TATE imaging, the mice were injected with 1.1 MBq (30 µCi) [<sup>18</sup>F]AMBF<sub>3</sub>-TATE via a tail vein catheter at the beginning of 1 h dynamic PET scans, followed by 10 min static PET scans at 2 h. All mice received CT scans following each PET imaging. Image analysis was performed using AMIDE version 1.0.5 imaging software (308).

For determining [<sup>18</sup>F]AMBF<sub>3</sub>-TATE dosimetry, male C57BL/6 mice (n=3) were injected with approximately 2.2 MBq (60 µCi) via a tail vein catheter at the beginning of 1 h dynamic PET

scans, followed by static PET scans at 2 h (10 min acquisition), 4 h (15 min acquisition) and 6 h (15 min acquisition). All mice received CT scans following each PET imaging. For improved soft tissue identification, for the last CT scan mice were injected via tail vein catheter with 100  $\mu$ L of Omnipaque 350 immediately before start of the CT scan, followed by an additional injection of 100  $\mu$ L during the first 30 s of scanning. Imaging biodistribution was confirmed by *ex vivo* analysis: each mouse was sacrificed following its last imaging time point and organs (brain, heart, lung, liver, kidneys, spleen, stomach, small intestine, large intestine, muscle, bone, bone marrow and blood) were collected, weighed and counted using a gamma counter (Cobra II Auto-Gamma, Packard Instrument Co., Meriden, USA) with decay correction to time of [ $^{18}$ F]AMBF<sub>3</sub>-TATE injection. Data were normalized to mass of the organs.

### 6.2.8 [ $^{18}$ F]AMBF<sub>3</sub>-TATE dosimetry

From [ $^{18}$ F]AMBF<sub>3</sub>-TATE PET scans of 3 C57BL6 mice, the amount of radioactivity in selected organs was quantified and absorbed doses were calculated based on the respective time-integrated activity coefficients (TIACs; formerly known as residence times, RTs). The dose extrapolation to humans involved scaling the biodistributions and the subsequent calculation of the absorbed doses from the scaled biodistributions. The biodistribution scaling was performed by two alternative methods. Method 1 was based on the assumption that the TIAC for the same organ is the same in mice and humans (309,310). Method 2 considered a relative mass scaling in which the TIAC value in a human organ is set equal to the TIAC value in the same animal organ multiplied by the ratio of whole body and the respective mass of the human and the animal organ(309,310).

TIACs were calculated using the software solution NUKFIT as described by Kletting *et al.*, choosing the optimal fit functions as proposed by the code (311). TIAC values for bladder were calculated based on trapezoidal method. The absorbed dose calculation was performed

for a selected group of organs using OLINDA/EXM v1.1 (312). Details on the methodology used for extrapolating the mouse data to humans are provided below.

### 6.2.9 Calculation of time-integrated activity coefficients (TIACs)

The time integrated activity coefficient (TIAC, and previously called “residence time”) was determined from non-decay-corrected microPET images of mice acquired from time 0 – 6 hr post-injection of tracer. A volume-of-interest (VOI) was drawn for each organ and the total organ radioactivity at time t was determined using *ex vivo* weights (gram) or, if not available, image-derived VOI volume assuming density of tissue was the same as water at 1 g/mL. Organs that used the VOI volume were the gastrointestinal tract (stomach, small and large intestines), kidneys, heart, femur, gallbladder, bladder, and total body.

Generally,

$$\text{total\_radioactivity}_{\text{organ}}(t) = \text{mean\_radioactivity\_concentration}_{\text{organ}}(t) * \text{mass}_{\text{organ}}$$

TIAC of each organ was determined using the NUKFIT software described by Kletting *et al.* with input being total radioactivity of each organ across time, choosing the optimal fit functions as proposed by the code (311).

For scaling to humans, TIAC was calculated using two different methods.

Method 1 is based on the assumption that the TIAC for the same organ is the same in mice and humans (309,310).

$$\text{TIAC}_{\text{organ\_Human}} = \text{TIAC}_{\text{organ\_Mouse}}$$

Method 2 considered a relative mass scaling in which the TIAC value in a human organ is set equal to the TIAC value in the same animal organ multiplied by the ratio of whole body and the respective mass of the human and the animal organ (309).

$$TIAC_{organ\_Human} = TIAC_{organ\_Mouse} * \frac{\left( \frac{\text{organ mass in human}}{\text{total body mass of human}} \right)}{\left( \frac{\text{organ mass in mouse}}{\text{total body mass of mouse}} \right)}$$

For some organs,  $TIAC_{organ\_Mouse}$  was calculated as follows:

#### TIAC of total red marrow

First, the fraction of radioactivity found in red marrow of femur relative to total femur was determined *ex vivo* by flushing red marrow from femur and counting radioactivity in red marrow and femur bone separately. TIAC of femur (bone + red marrow) was determined from microPET VOI analysis. Finally, we scaled up the calculated TIAC for red marrow in femur to red marrow in whole body based on literature values.

$$TIAC_{red\_marrow} = \left( TIAC_{femur} * \frac{\text{radioactivity in red marrow of femur}}{\text{radioactivity in femur}} \right) * \frac{1}{0.11}$$

where 0.11 is a scaling constant representing the estimated fraction of red marrow mass in femur to red marrow mass in whole body of mice based on reported values (313) and calculated as follows:

$$mass_{red\_marrow} = mass_{left\_limb\_marrow} + mass_{right\_limb\_marrow} + mass_{spinal\_cord}$$

$$mass_{red\_marrow} = 0.0166 + 0.0168 + 0.1121 = 0.1455$$

$$scaling\_constant = \frac{mass_{left\_limb\_marrow}}{mass_{red\_marrow}} = \frac{0.0166}{0.1455} = 0.11$$

#### TIAC of total bone

We first calculated the TIAC for total skeleton (bone + red marrow) from microPET images as follows, using AMIDE's 3D isocontour function to create a VOI of the skeleton from the corresponding CT:

$$\text{total radioactivity}_{skeleton}(t) = \text{mean radioactivity\_concentration}_{skeleton\_VOI}(t) * \text{volume}_{skeleton\_VOI}$$

$$TIAC_{bone} = TIAC_{skeleton} - TIAC_{red\_marrow}$$

We assumed total bone is composed of 67% cortical and 33% trabecular bone:

$$TIAC_{cortical\_bone} = TIAC_{bone} * 0.67$$

$$\text{TIAc}_{\text{trabecular\_bone}} = \text{TIAc}_{\text{bone}} * 0.33$$

### TIAc of heart

Since radioactivity was relatively minimal in heart at later time points, we assumed heart content and wall were 90% and 10% of total heart radioactivity, respectively:

$$\text{TIAc}_{\text{heart\_content}} = \text{TIAc}_{\text{total\_heart}} * 0.90$$

$$\text{TIAc}_{\text{heart\_wall}} = \text{TIAc}_{\text{total\_heart}} * 0.10$$

### **6.2.10 Statistical analysis**

Data are presented as mean  $\pm$  standard deviation. All p values were determined with unpaired, two-tailed T tests and values less than 0.05 were considered to be statistically significant. Prism 6 (GraphPad Software) was used to calculate statistics and generate graphs.

## **6.3 Results**

### **6.3.1 Microdroplet radiosynthesis of [<sup>18</sup>F]AMBF<sub>3</sub>-TATE**

We initially performed low-radioactivity fluorination reactions and observed highly-reproducible performance with radiochemical conversion (as determined by a combination of radio-TLC and radio-HPLC analysis of the crude product) of  $50 \pm 6\%$  (n=15), and non-isolated radiochemical yield (crude RCY) of  $17 \pm 3\%$  (n=15). Full production runs were then performed, including cartridge purification and formulation, with up to 3.7 GBq [100 mCi] of activity. The RCY in these experiments was  $16 \pm 1\%$  (n=5). Radiochemical purity was >99%. A representative chromatograms are shown in the Figure 6.6 and Figure 6.7. The molar activity was determined for several syntheses ranging in starting activities from 0.185-1.85 GBq [5-50 mCi]. Molar activity was found to increase with starting activity, ranging from 37 to 185 GBq/ $\mu$ mol [1 to 5 Ci/ $\mu$ mol], all values decay-corrected to EOB (Figure 6.5).

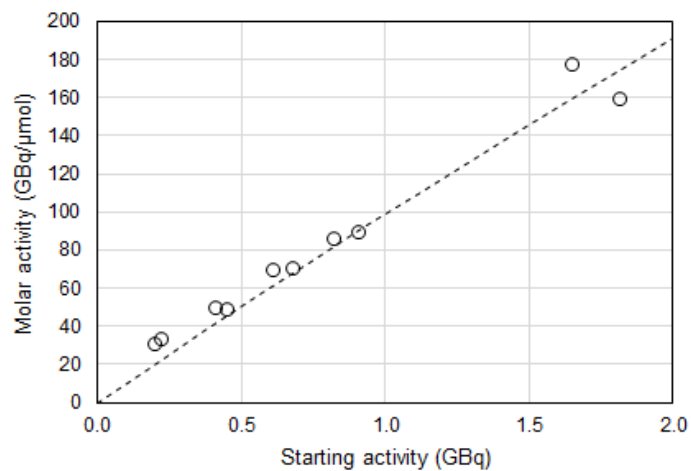


**Figure 6.5 Molar activity of [<sup>18</sup>F] AMBF<sub>3</sub>-TATE as a function of starting activity determined from crude samples.**

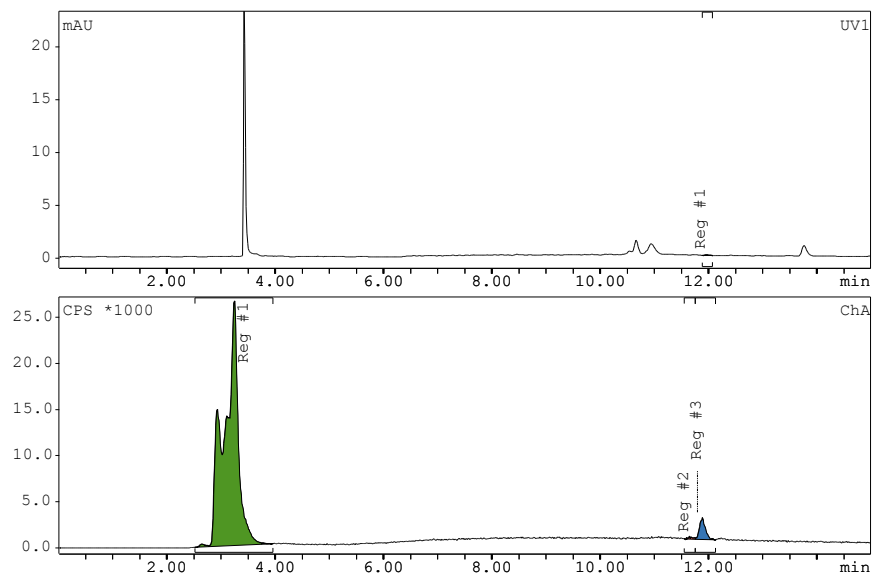


**Figure 6.6 Representative radio-HPLC chromatogram of crude [<sup>18</sup>F]AMBF<sub>3</sub>-TATE**

(Top) UV detector, (bottom) Gamma detector.

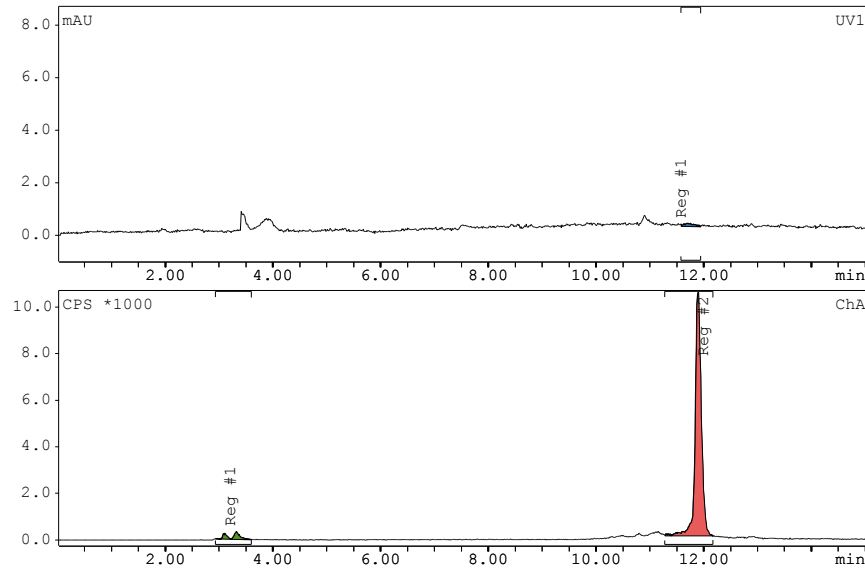


**Figure 6.7 Representative radio-HPLC chromatogram of purified  $[^{18}\text{F}]\text{AMBF}_3\text{-TATE}$**   
(Top) UV detector. (Bottom) Gamma detector.

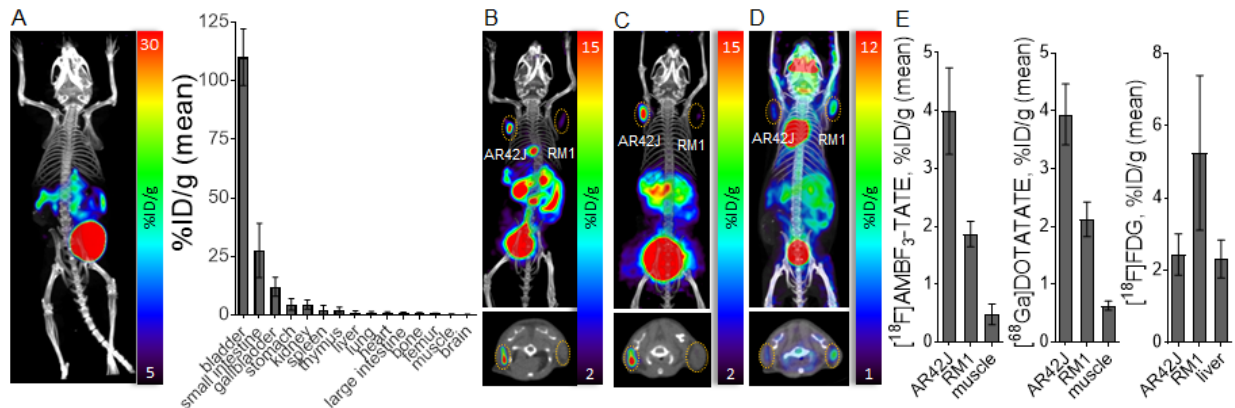


**Figure 6.8 MicroPET/CT imaging**

(A) MIP image and tissue biodistribution of 1.1 MBq injection of  $[^{18}\text{F}]\text{AMBF}_3\text{-TATE}$  in C57BL6 mouse,  $n=3$ . MIP image (top) and transverse slice (bottom) of (B) 1.1 MBq injection of  $[^{18}\text{F}]\text{AMBF}_3\text{-TATE}$ , (C) 1.1 MBq injection of  $[^{68}\text{Ga}]\text{Ga-DOTATATE}$  and (D) 0.74 MBq injection of  $[^{18}\text{F}]\text{FDG}$  of the same NSG mouse engrafted with SSTR2-positive (AR42J; left) and SSTR2-negative (RM1; right) tumor cells. (E) Region-of-interest analysis of PET images,  $n=4$ . Images were acquired for 10 min under 2% isoflurane anesthesia at 1 h post-injection of the PET tracer. Error bars are standard deviations. Tumors are delineated in dashed circles. MIP = maximum intensity projection.



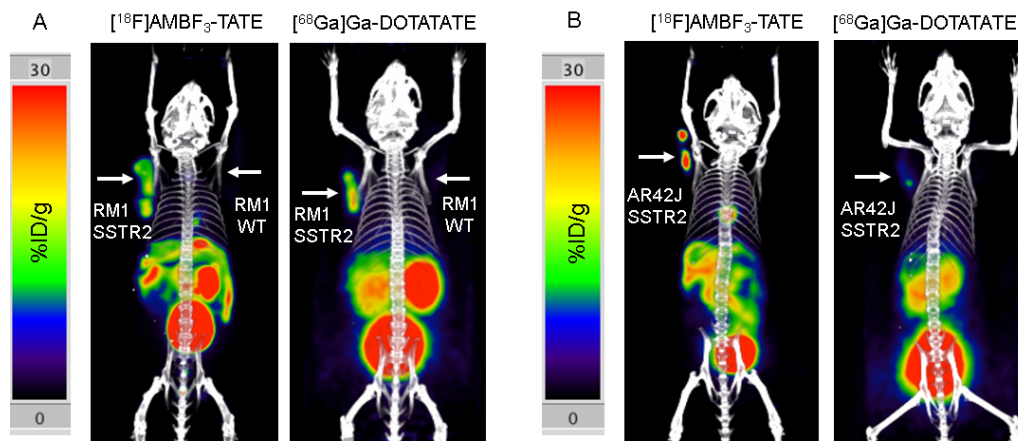


**Figure 6.9 Comparison of  $[^{18}\text{F}]\text{AMBF}_3\text{-TATE}$  and  $[^{68}\text{Ga}]\text{Ga-DOTATATE}$  imaging**  
of (A) human SSTR2-overexpressing RM1 and (B) rat SSTR2-expressing AR42J tumors. Untransduced RM1-WT cells were used as a negative control.

### 6.3.2 Preclinical imaging

The preclinical biodistribution of  $[^{18}\text{F}]\text{AMBF}_3\text{-TATE}$  is summarized in Figure 6.8 and in the Figure 6.9. Highest tracer accumulation was observed in the bladder followed distantly by gastrointestinal tissues (303). Bone retention was within range of background tissues lacking SSTR2, indicating little to no *in vivo* defluorination for  $[^{18}\text{F}]\text{AMBF}_3\text{-TATE}$ .  $[^{18}\text{F}]\text{AMBF}_3\text{-TATE}$  retention was approximately two-fold higher in SSTR2-high AR42J tumors than in SSTR2-low RM1 tumors ( $3.99 \pm 0.75$  %ID/g and  $1.87 \pm 0.22$  %ID/g, respectively;  $p < 1.6\text{e-}3$ ). Time-activity curves derived from PET imaging (Figure 6.10) showed  $[^{18}\text{F}]\text{AMBF}_3\text{-TATE}$  saturation in AR42J tumors by 20 min, but a continuous decline in RM1 tumors after peaking at approximately 10 min.  $[^{68}\text{Ga}]\text{Ga-DOTATATE}$  uptake in the tumors at 1 hr post-injection ( $3.94 \pm 0.53$  %ID/g and  $2.13 \pm 0.30$  %ID/g, respectively;  $p < 9.8 \text{e-}4$ ) was nearly identical to  $[^{18}\text{F}]\text{AMBF}_3\text{-TATE}$ . Results were confirmed with *ex vivo* gamma counter analysis of tissues after the last imaging time point. In contrast,  $[^{18}\text{F}]\text{FDG}$  imaging, a measure of tissue glucose metabolic activity, showed a reverse pattern with lower  $[^{18}\text{F}]\text{FDG}$  metabolism in AR42J tumors than RM1 tumors ( $2.44 \pm 0.57$  %ID/g and  $5.25 \pm 2.14$  %ID/g, respectively;  $p < 4.4\text{e-}2$ ).

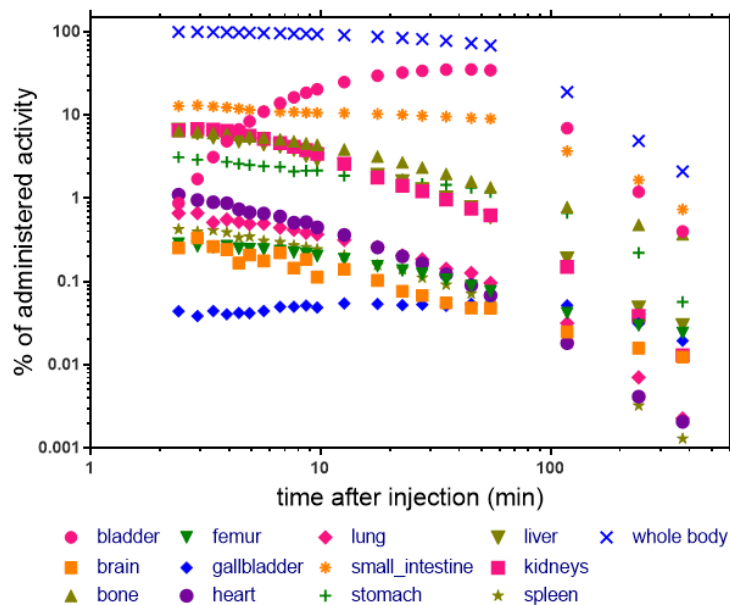


Figure 6.10 Non-decay-corrected [<sup>18</sup>F]AMBF<sub>3</sub>-TATE time activity curves determined from microPET images, averaged over n=3 mice.

Target Organs	Mean TIAC (h)		Standard deviations (h)	
	Method 1	Method 2	Method 1	Method 2
Bladder	5.36E-01	5.36E-01	2.14E-02	2.14E-02
Bone marrow	1.77E-02	2.95E-02	7.99E-03	1.33E-02
Brain	1.73E-03	2.10E-03	4.30E-04	7.10E-04
Gallbladder content	5.34E-03	2.05E-02	4.02E-03	1.58E-02
Heart content	2.74E-03	6.01E-03	1.78E-04	1.08E-03
Heart wall	3.04E-04	6.67E-04	1.97E-05	1.19E-04
Kidneys	4.23E-02	1.27E-02	5.77E-03	2.05E-03
Liver	2.07E-02	1.45E-02	5.56E-03	3.53E-03
Lungs	2.99E-03	6.62E-03	4.89E-04	1.93E-03
Small intestine	2.07E-01	2.37E-01	1.91E-02	1.72E-02
Spleen	1.88E-03	2.95E-03	1.45E-03	1.62E-03
Stomach	3.50E-02	4.94E-03	4.49E-03	3.17E-04
Cortical bone	1.62E-02	1.52E-02	1.23E-02	1.20E-02
Trabecular bone	7.97E-03	7.50E-03	6.06E-03	5.90E-03
Remainder of body	4.70E-01	4.72E-01	9.62E-02	7.50E-02

Table 6.1 Mean time-integrated activity coefficient (TIAC) values for the several organs scaled to humans.

### 6.3.3 Dosimetry analysis

Similarities in somatostatin peptide binding affinity between mouse and human SSTR2 suggest mouse dosimetry provides a good estimation for human dosimetry (314,315). Absorbed doses for [<sup>18</sup>F]AMBF<sub>3</sub>-TATE in humans were extrapolated from mouse PET biodistribution data using two extrapolation methods, Method 1 and Method 2. Organ TIAC values are summarized in Table 6.1 and a full list of the corresponding mean absorbed doses is provided in Table 6.2. The highest TIAC values were observed for the bladder and small intestine based on Method 1 ( $0.536 \pm 0.021$  h and  $0.207 \pm 0.019$  h, respectively). Based on Method 2, the highest TIAC values were observed for the bladder, small intestine and bone marrow ( $0.536 \pm 0.021$  h,  $0.237 \pm 0.017$  h and  $0.030 \pm 0.013$  h, respectively). The highest absorbed dose value using the one-compartment voiding bladder model was  $0.106 \pm 0.003$  mGy/MBq (Method 1) and  $0.107 \pm 0.004$  mGy/MBq (Method 2) for the bladder. All other organs showed significantly lower absorbed dose values. Bladder was the dose-limiting organ and on average the maximum administered human activity limit is estimated as 472 MBq (Method 1) and 469 MBq (Method 2) (FDA Code of Federal Regulations 21CFR361.1). In addition, the effective dose per unit activity has been calculated. However, the quantity “effective dose” can only be applied to the description of stochastic radiation effects and organ absorbed doses of less than 1 Gy. The mean extrapolated effective doses are  $1.26 \times 10^{-2} \pm 3.06 \times 10^{-4}$  mSv/MBq (Method 1) and  $1.16 \times 10^{-2} \pm 1.53 \times 10^{-4}$  mSv/MBq (Method 2). This corresponds to effective doses of 2.6 mSv (Method 1) and 2.4 mSv (Method 2) for an administered activity of 200 MBq, which is lower than that reported for current clinical <sup>18</sup>F- and <sup>68</sup>Ga-labeled PET tracers for imaging SSTR2-expressing tumors (276,316).

Target Organ	Mean absorbed dose coefficients of the organs (mGy/MBq)		Standard deviations (mGy/MBq)	
	Method 1	Method 2	Method 1	Method 2
Adrenals	4.44E-03	3.91E-03	3.96E-04	4.62E-04
Brain	8.40E-04	9.27E-04	1.11E-04	1.58E-04
Breasts	2.20E-03	2.21E-03	3.75E-04	3.12E-04
Gallbladder Wall	1.45E-02	3.80E-02	6.59E-03	2.49E-02
LLI Wall	9.08E-03	9.49E-03	2.20E-04	1.97E-04
Small Intestine	4.54E-02	5.12E-02	3.25E-03	2.85E-03
Stomach Wall	1.71E-02	6.14E-03	1.90E-03	3.38E-04
ULI Wall	1.14E-02	1.24E-02	1.73E-04	2.89E-04
Heart Wall	2.63E-03	3.43E-03	2.12E-04	3.03E-04
Kidneys	2.88E-02	1.09E-02	3.32E-03	1.10E-03
Liver	4.85E-03	4.22E-03	7.34E-04	5.61E-04
Lungs	2.15E-03	2.72E-03	2.48E-04	4.53E-04
Muscle	3.96E-03	3.97E-03	3.67E-04	3.27E-04
Ovaries	1.04E-02	1.11E-02	1.15E-04	1.73E-04
Pancreas	5.51E-03	4.68E-03	5.20E-04	5.75E-04
Red Marrow	5.43E-03	6.26E-03	5.64E-04	9.45E-04
Osteogenic Cells	6.40E-03	6.78E-03	1.96E-04	2.95E-04
Skin	2.45E-03	2.44E-03	3.21E-04	2.66E-04
Spleen	5.35E-03	5.54E-03	1.28E-03	1.52E-03
Testes	4.60E-03	4.63E-03	3.87E-04	2.93E-04
Thymus	2.62E-03	2.71E-03	4.56E-04	3.72E-04
Thyroid	2.53E-03	2.57E-03	4.65E-04	3.75E-04
Urinary Bladder Wall	1.06E-01	1.07E-01	3.00E-03	3.51E-03
Uterus	1.36E-02	1.41E-02	1.53E-04	2.00E-04

**Table 6.2 Mean absorbed dose coefficient values of the organs and the respective standard deviations for both methods using a one-compartment voiding bladder model.**

## 6.4 Discussion

### 6.4.1 Microdroplet radiosynthesis of [<sup>18</sup>F]AMBF<sub>3</sub>-TATE

The total synthesis duration (including purification and formulation) was 35-45 min, making this an attractive platform for on-demand production of [<sup>18</sup>F]AMBF<sub>3</sub>-TATE. It is expected that further developments of the microfluidic system could enable significant reductions of the synthesis time. For example, automation of reagent delivery steps (120), and automation of the purification and formulation process could reduce the time by up to 15 min and increase safety

and simplicity of operation. While the yield was slightly lower than the 20-25% (uncorrected) yield reported by Liu *et al.* for the macroscale synthesis of [<sup>18</sup>F]AMBF<sub>3</sub>-TATE (303), the microscale synthesis used 10x lower precursor (5 nmol vs 50 nmol). Notably, equally high molar activity could be achieved using much lower starting radioactivity (0.93-1.1 GBq [25-30 mCi] instead of 30-37 GBq [800-1000 mCi] to achieve ~110 GBq/μmol [3 Ci/μmol]). This is noteworthy insofar as the chip has significant potential for miniaturized production in a kit-like system (317). Since the quantity and concentration of the tracer were sufficient for imaging, we did not perform significant optimization; however, in the Table 6.3 and Table 6.4 we report a detailed analysis of intermediate measurements during the synthesis and potential optimization strategies. While these yields are still a bit low, yields, purities, and molar activities are suitable to contemplate clinical use for human translation. In addition, the ease of use and the reproducibility in terms of yields and molar activity augur well for eventual clinical use.

By using portions of a large initial batch of [<sup>18</sup>F]fluoride, or by producing small batches of [<sup>18</sup>F]fluoride throughout the day, we anticipate that radiosyntheses on the scale reported herein (i.e. up to ~3.7 GBq [100 mCi]) would be sufficient to supply patient doses throughout the day. Generation of [<sup>18</sup>F]fluoride throughout the day would have the advantage of ensuring similar molar activity for each batch of the tracer, but would require proximity to a cyclotron. In addition, the microdroplet approach may also be compatible with the concept of producing larger multi-dose batches. Though it is often assumed that microfluidic approaches are limited to only low activity levels, we should emphasize that this is not the case: whereas experiments here were limited to <3.7 GBq [100 mCi] for safety reasons, there are approaches to load significantly more activity into microdroplet reactions. One of us previously reported that ~30 GBq [~810 mCi] of [<sup>18</sup>F]fluoride can be concentrated into a volume of 5 μL (305), clearly opening up the possibility to use high levels of activity (sufficient for multiple patient doses) in microdroplet synthesis. Though it remains to be investigated in practice, mathematically, we would predict that the increase in scale from 3.7 – 30 GBq [100-800 mCi] would increase the molar activity 8-

fold, assuming the amount of precursor is fixed at 5 nmol and that the batches of [<sup>18</sup>F]fluoride have similar molar activities. However, due to the increased proportion of [<sup>18</sup>F]fluoride relative to precursor, we would also predict that the RCY could decrease. To counteract this effect, the amount of precursor could be increased (e.g. from 5 to 40 nmol), while still achieving molar activities in the range we report herein. As further evidence that scalable syntheses are well within the realm of possibility, it should also be noted that manual synthesis of [<sup>18</sup>F]AMBF<sub>3</sub>-TATE has been previously performed with 30-37 GBq [0.8 – 1.0 Ci] and 50 nmol precursor, resulting in 20-25% RCY and molar activities >111 GBq/μmol [>3 Ci/μmol] (303).

Parameter	Average ± SD (n=15)
Total radioactivity collected from the chip (%)	37.2 ± 9.0
Residual radioactivity on top chip (%)	20.5 ± 3.0
Residual radioactivity on bottom chip (%)	22.4 ± 4.3
Radioactivity loss during reaction (%)	20.1 ± 6.4
TLC purity ([ <sup>18</sup> F]fluoride incorporation, %)	49.9 ± 6.3
HPLC purity (fraction of product among non-[ <sup>18</sup> F]fluoride peaks, %)	92.7 ± 3.0
Double-corrected purity (%)	46.4 ± 6.7
Crude RCY (%)	16.7 ± 2.6

**Table 6.3 Performance of synthesis of [<sup>18</sup>F]AMBF<sub>3</sub>-TATE as determined from the collected crude product**

All radioactivities are expressed as percentage of starting radioactivity, corrected for decay.

Parameter	Average $\pm$ SD (n=5)
Total radioactivity collected from the chip (%)	34.0 $\pm$ 12.3
Residual radioactivity on top chip (%)	20.6 $\pm$ 2.5
Residual radioactivity on bottom chip (%)	26.2 $\pm$ 7.6
Radioactivity loss during reaction (%)	19.6 $\pm$ 9.1
TLC purity ( $^{18}\text{F}$ fluoride incorporation, %)	56.4 $\pm$ 7.8
HPLC purity (fraction of product among non- $^{18}\text{F}$ fluoride peaks, %)	92.4 $\pm$ 3.3
Double-corrected purity (%)	52.2 $\pm$ 8.0
Crude RCY (%)	16.4 $\pm$ 1.1
Loss on purification (%)	0.6 $\pm$ 0.2
Isolated RCY (%)	15.8 $\pm$ 1.0

**Table 6.4 Performance of full production runs (including purification) for [ $^{18}\text{F}$ ]AMBF<sub>3</sub>-TATE**

All radioactivities are expressed as percentage of starting radioactivity, corrected for decay

Finally, it should be appreciated that the BF<sub>3</sub> moiety can easily be connected to other molecules to create precursors for other radiolabeled peptides and dual-modality tracers (55,318) that can likely be labeled under identical or similar conditions. Microfluidic isotopic exchange labeling could therefore provide a route to a variety of  $^{18}\text{F}$ -labeled compounds with simple production and high molar activity. Despite the low pH and relatively high reaction temperature, these conditions are not unusual in peptide synthesis as much more acidic conditions are typically used for resin cleavage e.g. 80% TFA, conc. HF, and during purification e.g. 1% TFA, pH 0, and are only slightly more acidic than methods commonly used in radiometallation of peptides (i.e., pH 3-4 and similar temperatures). Notably, several peptides and other small molecules have successfully been labeled with this approach (54). While we recognize that not all functional groups (e.g. trityl groups, para-methoxybenzyl acetals) would survive these conditions, for the most part, standard peptides should be compatible. Further development and automation of the microdroplet labeling methods would benefit the development of this whole class of reactions.

### 6.4.2 Preclinical imaging and dosimetry

Preclinical biodistribution and dosimetry calculations for [ $^{18}\text{F}$ ]AMBF<sub>3</sub>-TATE showed significant potential for clinical use and was undertaken to further demonstrate that the radiotracer produced on the EWOD chip would provide clinically useful tracers with dosimetry that could be used to support clinical administration of this tracer as well as the further development of this method for labeling other peptide tracers. In particular, [ $^{18}\text{F}$ ]AMBF<sub>3</sub>-TATE showed very similar biodistribution to [ $^{68}\text{Ga}$ ]Ga-DOTATATE in our experiments, and in comparisons with literature reports (303). [ $^{18}\text{F}$ ]AMBF<sub>3</sub>-TATE tumor imaging corroborated with level of SSTR2 expression, but did not correlate with [ $^{18}\text{F}$ ]FDG, suggesting these two tracers provide different information for therapeutic strategy and response monitoring. Dosimetry calculations showed lower effective dose per unit radioactivity than reported for current clinical  $^{18}\text{F}$ - and  $^{68}\text{Ga}$ -labeled PET tracers for imaging SSTR2-expressing tumors (276,316). Since comparable performance to [ $^{68}\text{Ga}$ ]Ga-DOTATATE (currently the clinical gold standard for imaging SSTR2) was achieved, these data suggest that further study of [ $^{18}\text{F}$ ]AMBF<sub>3</sub>-TATE, including evaluation in humans, is warranted.

## 6.5 Conclusion

We adapted the isotopic exchange based radiosynthesis of [ $^{18}\text{F}$ ]AMBF<sub>3</sub>-TATE to a droplet-based radiochemistry platform and could produce the injection-ready tracer in 16±1% (n=5) overall RCY (decay-corrected) in ~40 min. The small volume synthesis used minimal quantities of precursor (5 nmol), enabling high molar activity to be achieved, even starting from very little radioactivity. The BF<sub>3</sub> chemistry is very convenient, with straightforward purification and formulation performed using solid-phase extraction on a C18 Sep-pak cartridge. Though only demonstrated at scales starting with <3.7 GBq [100 mCi] for safety reasons, it is possible to



leverage technologies to concentrate [ $^{18}\text{F}$ ]fluoride ion for automated microdroplet synthesis to explore the possibility of scale-up to produce [ $^{18}\text{F}$ ]AMBF<sub>3</sub>-TATE for multiple human doses.

Preclinical evaluation with [ $^{18}\text{F}$ ]AMBF<sub>3</sub>-TATE in SSTR2 tumor models showed excellent contrast with surrounding tissues and comparable results to [ $^{68}\text{Ga}$ ]Ga-DOTATATE. Due to the convenient synthetic method, favorable physical properties and scalability of fluorine-18 compared with gallium-68, and encouraging imaging and dosimetry, clinical translation of [ $^{18}\text{F}$ ]AMBF<sub>3</sub>-TATE and further development of the microdroplet synthesis are warranted. We contend that the [ $^{18}\text{F}$ ]AMBF<sub>3</sub>-TATE can be used for diagnosis and [ $^{177}\text{Lu}$ ]Lu-DOTATATE can be used for therapy; eventual demonstration that [ $^{177}\text{Lu}$ ]Lu-DOTATATE can block uptake of [ $^{18}\text{F}$ ]AMBF<sub>3</sub>-TATE would be sufficient to fully qualify this for application as a companion diagnostic. Finally, while we have not addressed the possibility of boron neutron capture therapy (BNCT), the use of  $^{10}\text{B}$ -enriched AMBF<sub>3</sub> might constitute a promising approach that would qualify [ $^{18}\text{F}$ ]AMBF<sub>3</sub>-TATE for diagnosis and [ $^{10}\text{B}$ ]AMBF<sub>3</sub>-TATE for therapy in theranostic applications demanding a single molecule for both diagnosis and therapy.

Notably, we expect that other trifluoroborate conjugates of various other peptides could be labeled with fluorine-18 with high molar activity using the microdroplet approach in the same straightforward, kit-like manner, paving the way to the rapid development of novel  $^{18}\text{F}$ -labeled peptides for potential theranostic applications when paired with appropriate analogs labeled with therapeutic isotopes. Furthermore, the underlying microfluidic technology is anticipated to be compatible with other single-step peptide labeling methods (including organosilane conjugates labeled via isotopic exchange, NOTA conjugates labeled via chelation of [ $^{18}\text{F}$ ]AlF, etc.) or other more complex multi-step processes involving conjugate of modified peptides to  $^{18}\text{F}$ -labeled prosthetic groups. Leveraging the availability of fluorine-18 in high quantities, the microdroplet reactor is capable of producing sufficient quantities of  $^{18}\text{F}$ -labeled peptides for several human doses. Further efforts in automation of the overall droplet radiochemistry process will allow safe investigation of scaling activity levels above 3.7 GBq [100 mCi].

# Chapter 7: Improved method for droplet labeling of trifluoroborates via isotopic exchange

## 7.1 Introduction

Molecular imaging with positron emission tomography (PET) provides high resolution distribution and localization of targets *in vivo* used in clinical diagnostics and preclinical research (5,319). Fluorine-18 is the most commonly used diagnostic radioisotope for PET due to its moderate half-life (110 min), high positron yield (97%), low positron energy and broad availability from medical cyclotrons.

Among various available radiofluorination techniques, F-18/F-19 isotopic exchange (IEX) is a straightforward method for producing fluorine-18 radiopharmaceuticals that can offer simplified purification. In other reactions, it can be difficult to separate the product from the chemically-similar precursor (or derivatives of the reactive precursor), requiring lengthy procedures such as high-performance liquid chromatography (HPLC). Purification in IEX is simpler due to the absence of species chemically similar to the product and solid-phase extraction (SPE) is often sufficient, resulting in a short production time (320). Furthermore, one-step IEX radiolabeling in some cases is performed under aqueous conditions without the need to first thoroughly dry the [<sup>18</sup>F]fluoride via azeotropic distillation, further reducing the production time. There has been particular interest in, and development of, methods based on trifluoroborate (R-BF<sub>3</sub>) IEX labeling. These radiopharmaceuticals are characterized by hydrophilicity, biorthogonality and nontoxicity which leads to enhanced *in vivo* clearance, metabolic stability and safety, respectively (54,321). Another advantage of this class of molecules is that the presence of 3 fluorine atoms in the BF<sub>3</sub> moiety leads to a tripling of the molar activity (a ratio of radioactivity per moles of the compound) compared to precursors with a single fluoride (322,323).

Despite the benefits of IEX syntheses, a longstanding concern about this radiofluorination route has been the lower molar activity of the resulting product. Molar activity represents a measure of radiopharmaceutical quality and needs to remain relatively high ( $> 37$  GBq/ $\mu\text{mol}$ ) to limit pharmacological effects and ensure good visualization of low-abundance targets (59,324). While theoretical maximum for molar activity (a ratio of radioactivity per moles of the compound) is 63.3 TBq/ $\mu\text{mol}$ , practical values for cyclotron-produced [ $^{18}\text{F}$ ]fluoride are typically in the range of 1-10 TBq/ $\mu\text{mol}$  (48,57,322), and 200-300 GBq/ $\mu\text{mol}$  or lower (57,325) for the final fluorine-18-labeled radiopharmaceuticals. The molar activity decreases due to fluorine-19 contamination introduced from the cartridges, tubing, reagents and synthesizer materials used in radiopharmaceutical preparation. Since IEX precursor molecules contain fluorine-19, they introduce a major contaminant source into the reaction. To ensure rapid reactions, a high concentration of the precursor is needed ( $\sim 1$  mM), and its quantity is orders of magnitude higher than the amount of the radioisotope. In typical reaction volumes of 1 mL, the precursor contributes 1  $\mu\text{mol}$ , while, for comparison, a typical conventional synthesis with 37 GBq of starting activity and 1 TBq/ $\mu\text{mol}$  molar activity will contain only 0.04  $\mu\text{mol}$  of fluoride ion. If the starting activity is lower, e.g. 0.037 GBq (only 0.4 nmol of fluoride ion) the difference in precursor and radioisotope quantity is even more substantial ( $\times 2500$ ), meaning that a very large portion of the precursor does not react with the radioisotope. Thus, using high starting activity ( $> 37$  GBq) is particularly necessary in conventional IEX syntheses to maintain acceptable reaction rates and high molar activity.

Using a small reaction volume provides a way to preserve the concentration but reduce the total amount of precursor that is added. Perrin and colleagues developed an improved synthesis technique, using 50 nmol of precursor in  $< 0.1$  mL volume per synthesis of Rhodamine- $^{18}\text{F}$ ArBF<sub>3</sub> (322). With only moderate starting activity (15-18 GBq), high molar activity of 110-260 GBq/ $\mu\text{mol}$  could be achieved. In early work by our group, it was shown that for two trifluoroborate compounds (Rhodamine-AmBF<sub>3</sub> and Rhodamine-ArBF<sub>3</sub>), radiolabeling in

microliter droplets affords extremely high molar activity (up to ~1 TBq/ $\mu$ mol) while using modest starting radioactivity levels (up to 7 GBq). This was achieved by using only 5 nmol of 1mM precursor in a small glass droplet reactor (326). Similarly, with the same setup and precursor quantity our group showed that for production of octreotide analogue [ $^{18}$ F]AmBF<sub>3</sub>-TATE yields very high molar activity (up to 180 GBq/ $\mu$ mol) when starting with up to 2 GBq of [ $^{18}$ F]fluoride (105). Furthermore, we explored application of the same method for IEX radiolabeling of various R-PPh<sub>3</sub>BF<sub>3</sub> prosthetic groups where high molar activities ( up to 129 GBq/ $\mu$ mol) were achieved with only up to 0.9 GBq of starting radioactivity (56). The versatile droplet reaction platform consisted of two 25 mm square Teflon-coated glass substrates, separated by 150  $\mu$ m with the reaction droplet sandwiched in between. In those previous reports, we also confirmed that the molar activity was directly related to the starting activity used in the synthesis, and that the small volume enabled high molar activities of the product (~100 GBq/ $\mu$ mol) even with relatively low starting activities (<4 GBq) (105). This result shows that microfluidic reactions may be an ideal platform for research and development of IEX labeled compounds due to the possibility to achieve high molar activity even in small batch productions (i.e. without requiring high starting activities). This is a critical point because small animal imaging typically requires even higher molar activities than imaging in humans (57,59,324).

Despite the success, the Teflon-coated glass chips were found to have limitations. The disrupted coating could lead to leaking of liquid under the film and loss of positional stability of the droplet, leading to adverse impact on repeatability and yield (86,120). In our lab, we later found that Teflon-coated silicon substrates served as a more robust reaction platform. By incorporating some hydrophilic features (by etching away Teflon in certain regions), droplets could be manipulated and contained precisely, allowing the development of automated synthesizers based on these chips (106,108). Many radiopharmaceuticals have been successfully synthesized on these platforms (50,108–110). The newest droplet reactor uses a surface tension trap (STT) chip comprising an etched hydrophilic circle (4 mm diameter) on a

surface of a hydrophobic Teflon-coated silicon (108). This new chip format is open (without a cover) so that the reaction site is accessible to reagent dispensers and product collection tubing of the automated platform (108).

The aims of the current work were to (i) show further utility of droplet methods for IEX reactions and establish the possibility to perform droplet-based IEX radiofluorination of additional R-BF<sub>3</sub> precursors (to prepare prosthetic groups for <sup>18</sup>F-radiolabeling), and then (ii) use one of these compounds as a model for translating IEX labeling methods to a Teflon-silicon chip format that could be automated, to enable more widespread use by others. The chemistry of IEX radiolabeling with R-BF<sub>3</sub> has continued to be developed, and numerous peptides have been labeled with good molar activity, including Tyr<sub>3</sub>-octreotate (TATE), bradykinin, bombesin and fluorescent RGD (55,321,327).

## 7.2 Materials and methods

### 7.2.1 Reagents

No-carrier-added [<sup>18</sup>F]fluoride was produced by the (p,n) reaction of [<sup>18</sup>O]H<sub>2</sub>O (84% isotopic purity, Zevacor Pharma, Noblesville, IN, USA) in an RDS-112 cyclotron (Siemens; Knoxville, TN, USA) at 11 MeV using a 1 mL tantalum target with havar foil window. Acetonitrile (MeCN; anhydrous, 99.8%), methanol (MeOH; anhydrous, 99.8%), ethanol (EtOH; 200 proof), dimethyl sulfoxide (DMSO, 98%), N,N-dimethylformamide (DMF; anhydrous, 99.8%), hydrochloric acid (HCl; 3N) were purchased from Millipore Sigma (St. Louis, MO, USA). Saline (0.9% sodium chloride injection, USP) was obtained from Hospira Inc. (Lake Forest, IL, USA); pyridazine (N99%) was obtained from Tokyo Chemical Industry Co., Ltd. (Japan). All reagents were used without further processing or purification. Ultrapure 18 MΩ H<sub>2</sub>O was acquired through a Milli-Q Integral 3 purification system (Millipore Sigma, St. Louis, MO, USA). pH test strips (0–14 range, Ricca Chemical Company), and TLC plates (Baker-flex silica gel IB-F sheets 2.5 × 7.5 cm, J.T. Baker) were purchased from Thermo Fisher Scientific.

To prepare a batch of the DMF reaction buffer, 720  $\mu\text{L}$  of pyridazine was added to 5 mL of DMF and 2.5 mL DI water in a 15 mL conical tube. The pH was adjusted to the range 2.0–2.5 with 3M HCl. The final volume was then adjusted with  $\text{H}_2\text{O}$  until the final volume reached 10 mL. DMSO reaction buffer preparation followed the same recipe as the DMF buffer, only different in adding 5 mL of DMSO instead of DMF.

Precursors (2-((2-carboxyethyl)diphenylphosphonio)phenyl)trifluoroborate (DP-II-196-F2932) (**1**), (DP-II-181-F1739), (DP-II-143-F39), (DP-II-195), (DP-II-204-F27) were kindly supplied by Dr. Emmanuel Gras (CNSR, Toulouse, France). From the initial batch, aliquots of precursor were prepared by dissolving the precursor in MeCN at a concentration of 0.5 mM, pipetting 10  $\mu\text{L}$  (5 nmol) portions into individual PCR tubes (AB062, ThermoFisher, Waltham, MA, US), and evaporating solvent with a gentle stream of nitrogen gas. After drying, the 5 nmol aliquots were stored in a freezer for future use.

For each set of up to 4 experiments, a radioisotope stock solution (for up to 4 reactions) was prepared by mixing 10  $\mu\text{L}$  of [ $^{18}\text{F}$ ]fluoride/[ $^{18}\text{O}$ ]H $_2\text{O}$  with 50  $\mu\text{L}$  of saline (to mimic the composition of [ $^{18}\text{F}$ ]fluoride eluted from QMA using sodium chloride used for IEX syntheses (113,306)).

### 7.2.2 Droplet synthesis platform

Radiochemistry to perform the IEX labeling (Figure 7.1A) was carried out using Teflon-coated silicon or glass chips (Figure 7.1B), affixed atop a ceramic heater with thermal paste. The heating platform was based on a design previously described (111) but included 4 independent heaters. Glass chips consisted of 25 mm squares cut from microscope slides with annealed Teflon layer atop, fabricated as reported previously (244). Silicon chips were prepared by coating a 4" silicon wafer with Teflon and cutting it into 25 mm squares. Surface-tension trap (STT) chips were fabricated similarly but a 4mm circular pattern of Teflon was etched away, serving as a hydrophilic reaction site. The fabrication of silicon chips has been previously

reported (106). Experiments were performed with either a closed or open reactor. The closed reactor consisted of 2 Teflon coated glass chips or 2 Teflon coated silicon chips sandwiched together, with the Teflon side facing the reaction droplet in between. The bottom chip was affixed to a heater using thermal paste and initial synthesis steps were performed on this open chip. Before start of radiofluorination, the second (cover) chip, with added stripes of tape on the sides (to provide a separation between the chips of 150  $\mu\text{m}$ ), was carefully placed atop the bottom chip. Open reactor consisted of a silicon STT chip fixed atop the heater and no cover was added. During these initial optimization experiments, reagents were manipulated manually using a micro pipette. The basic process is illustrated in Figure 7.1C and details of each step are provided below.

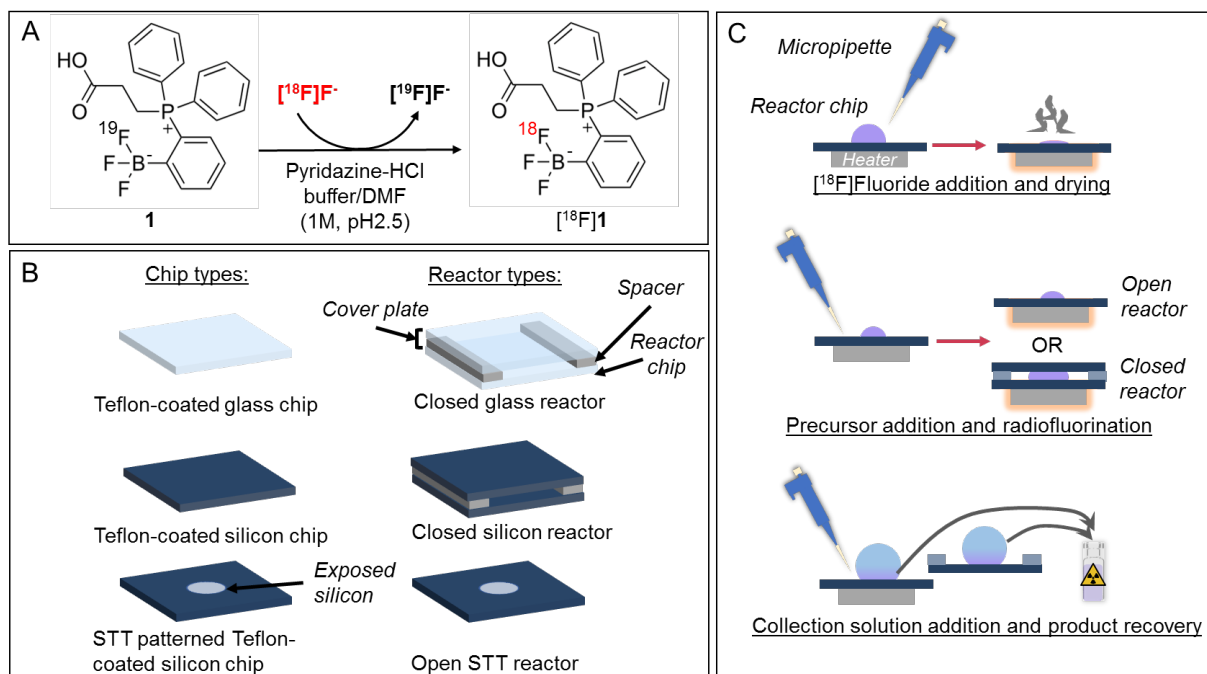


**Figure 7.1: Method illustration for IEX in droplet reactors**

(A) Radiofluorination of precursor **1** via IEX to produce  $[^{18}\text{F}]\mathbf{1}$ . (B) Diagram of different types of chips and reactor configurations used. In the closed configurations, the Teflon-coating of the top chip faces downward. (C) Schematic presentation of droplet synthesis protocol on the open or closed reactor.

### 7.2.3 Radiolabeling procedure on Teflon-glass chips

Radiofluorination of all the precursors was carried out in one step via F-18/F-19 IEX, using previously reported reaction conditions (56,105) (Figure 7.1A). To begin the on-chip synthesis, 12  $\mu\text{L}$  of the radioisotope stock solution was dispensed on the center of the chip and evaporated at 100  $^{\circ}\text{C}$ . Next, a droplet of precursor solution (5 nmol in 5  $\mu\text{L}$  DMF buffer) was added and the reaction carried out at 90 $^{\circ}\text{C}$  for 15 min. After removing the cover chip, the product was collected from the bottom chip by adding 20  $\mu\text{L}$  of a 1:1 (v/v) EtOH/saline mixture to the reaction area and transferring the product into a vial. A similar process was used to collect residual product from the cover plate. The collection step was repeated for both chips with additional 20  $\mu\text{L}$  each of the collection solution. Note that while thorough azeotropic drying of [ $^{18}\text{F}$ ]Fluoride is not necessary due to the aqueous reaction conditions, the evaporation step was performed prior to precursor addition to enable the amount and concentration of precursor to be precisely controlled by addition of well-controlled precursor solution.

### 7.2.4 Optimization of radiolabeling

Optimization of radiofluorination was carried out using precursor **1**. First, the [ $^{18}\text{F}$ ]fluoride/[ $^{18}\text{O}$ ]H $_2\text{O}$  drying step was optimized to minimize the amount of radioactivity loss, measured by comparing the radioactivity remaining on the chip after drying to the initial amount of loaded radioactivity. Experiments were performed on different types of chips to compare the effect of drying temperature, drying time, a presence of DMSO additive.

Next the radiofluorination step was optimized. 5 nmol of precursor **1** in reaction buffer (DMF-based for the closed reactors, DMSO-based for the open reactor) was loaded onto the chip. In closed reaction, the droplet was covered with a second chip placed Teflon-side down. The IEX reaction carried out at 90  $^{\circ}\text{C}$ . After the reaction the product was collected as described above. Optimization experiments explored the impact of type of chip, volume of reaction buffer (i.e. precursor concentration) and reaction time.



### 7.2.5 Synthesis automation

The synthesis is being automated by implementation using the STT-based droplet synthesis platform described previously (108).

### 7.2.6 Analytical methods

A calibrated ion chamber (CRC 25-PET, Capintec, Florham Park, NJ, USA) was used to perform radioactivity measurements. Radio-TLC was used to assess fluorination efficiency, with the aid of a radio-TLC scanner (miniGita star, Raytest, Inc., Wilmington, NC, USA). The TLC plate (Baker-flex silica gel IB-F sheets 2.5 × 7.5 cm, J.T. Baker, Phillipsburg, NJ) was developed in MeCN/H<sub>2</sub>O (1:1 v/v), and R<sub>f</sub> for [<sup>18</sup>F]fluoride was 0.0, and for [<sup>18</sup>F]**1** was 0.75. Radio-HPLC analysis was performed on an analytical-scale Smartline HPLC system (Knauer, Berlin, Germany) with 200 µL injection loop, a pump (Model 1000), degasser (Model 5050), UV detector (Model 2500) and a radiometric detector (Bioscan B-FC-4000, Bioscan Inc., Washington DC, USA). Samples were separated using a C18 column (Luna, 5 µm particles, 100 Å pores, 250 × 4.6 mm, Phenomenex, Torrance, CA, USA) with guard column (SecurityGuard C18, Phenomenex). UV absorbance was measured at 270 nm. Using isocratic conditions with a MeCN:H<sub>2</sub>O 25:75 (v/v) mobile phase delivered at 1 mL/min, the observed retention time of [<sup>18</sup>F]fluoride was between 2 and 3 min, and was 7-8 min for [<sup>18</sup>F]**1**.

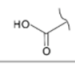
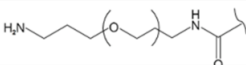
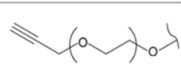
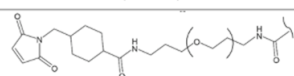
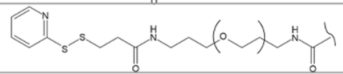
Reaction performance was assessed by calculating the following parameters: product collection efficiency, derived by dividing the collected product radioactivity by starting radioactivity at the beginning of synthesis (correcting for decay); residual radioactivity on the reactor/cover chip, calculated as a fraction of starting radioactivity remaining on the chip after the collection step (correcting for decay); volatile radioactivity loss during drying, computed by subtracting radioactivity on chip from starting radioactivity and dividing the difference by starting radioactivity; volatile radioactivity loss (overall), computed by subtracting residual chip(s) and collected product radioactivities from the starting radioactivity and dividing the difference by

starting radioactivity; radiochemical conversion, the ratio of radiolabeled compound radioactivity to the total sample radioactivity, as determined by radio-TLC; crude radiochemical yield (RCY), calculated by multiplying radiochemical conversion by the product collection efficiency.

## 7.3 Results

### 7.3.1 Generalization of IEX labeling

Previously we showed the IEX labeling of AmBF<sub>3</sub>-TATE to produce [<sup>18</sup>F]AmBF<sub>3</sub>-TATE for PET imaging of SSTR2 receptors (105). The synthesis was performed using Teflon-coated glass chips in the closed configuration, achieving a crude RCY was 17±2 % (n=15). The reaction suffered substantial radioactivity losses (63±8%, n=15), comprising 21±3% (n=15) residual activity on the top chip, 22±4% (n=15) residual activity on the bottom chip, and 20±6% (n=15) volatile activity loss. Applying the same reaction conditions to several R-PPh<sub>3</sub>BF<sub>3</sub> compounds showed similar performance, with ~20% residual activity stuck on each chip, ~20% volatile loss, and ~17% crude RCY (56). The summary of the crude yields for various compounds are shown in Table 7.1.

	R	Crude RCY, d.c.
<u>DP-II-196-F2932</u>		17%, (n=4)
<u>DP-II-181-F1739</u>		25%, (n=6)
<u>DP-II-143-F39</u>		14%, (n=4)
<u>DP-II-195</u>		12%, (n=3)
<u>DP-II-204-F27</u>		17%, (n=4)

**Table 7.1 Summary of radiochemical yields for various R-PPh<sub>3</sub>BF<sub>3</sub> precursors.**

### 7.3.2 Translation to silicon chips

Initial attempts to perform the reaction in a closed Teflon-silicon reactor, crude RCY was <5%, and significant volatile radioactivity losses (70-90%) were observed, and step-by-step

measurements revealed that a significant portion of radioactivity loss (~60%) occurred during the [<sup>18</sup>F]fluoride drying step.

### 7.3.3 Investigation of [<sup>18</sup>F]fluoride drying step

Notably, on the Teflon-coated glass chips, the drying step (starting with 12  $\mu$ L radioisotope stock solution took 120 s until the point where the droplet reached a tiny size (<1  $\mu$ L) and stopped shrinking. The activity loss during drying was negligible.

However, when using Teflon-coated silicon chips, drying took ~60 s and was complete (i.e. forming a solid residue at the end), with a significant radioactivity loss. During detailed investigation of partial drying, it was observed that the loss increases with drying time, going from zero to 55% as heating time was increased from 15 to 75 s (Figure 7.2A). To see if lower temperature could limit the loss, drying was performed at different temperatures until the moment the droplet was dried. A high loss (~60%) was observed for all temperature (60, 70, 80, 90, 100  $^{\circ}$ C).

To slow down evaporation and possibly prevent rapid activity loss, we attempted adding a small amount (1  $\mu$ L) of a high boiling point solvent (DMSO) to the [<sup>18</sup>F]fluoride stock solution (12  $\mu$ L) loaded to the chip. Indeed evaporation at 100  $^{\circ}$ C was slowed down, with the droplet reaching a tiny size at 75 s and ceasing to shrink further. As the drying time increased for up to 120 s the radioactivity loss reached a plateau of ~15% at 75 s and did not increase with additional heating time (Figure 7.2A). Based on these findings, 75 sec drying time was implemented for later experiments. To determine whether this approach may be compatible with scaling to larger amounts of activity (i.e. with greater volume of [<sup>18</sup>F]fluoride solution, but containing the same total amount of saline). After loading a 30  $\mu$ L droplet (containing 1  $\mu$ L of DMSO) and heating at 100 $^{\circ}$ C, the droplet reached the same small size at 150 s and also exhibited low activity loss (Figure 7.2A).

After showing that DMSO addition could significantly reduce losses on the Teflon-coated silicon chips, when then attempted drying on the STT-patterned. On these chips, evaporation occurred at even faster rates, perhaps due to further spreading of the droplet (and increasing its surface area) on the hydrophilic reaction region. For 12  $\mu\text{L}$  droplets of radioisotope stock solution (with no DMSO), complete drying (with visible residue) was observed after 30s, and up to 60% activity loss was observed. When spiked with 1  $\mu\text{L}$  of DMSO, the loss after 30s was reduced to 13%, but the droplet was not fully evaporated ( $>5 \mu\text{L}$ ). Additional drying up to 60s reduced the  $[^{18}\text{F}]$ fluoride volume, but the activity loss increased to 30% (Figure 7.2B), thus 30s was chosen for subsequent experiments.

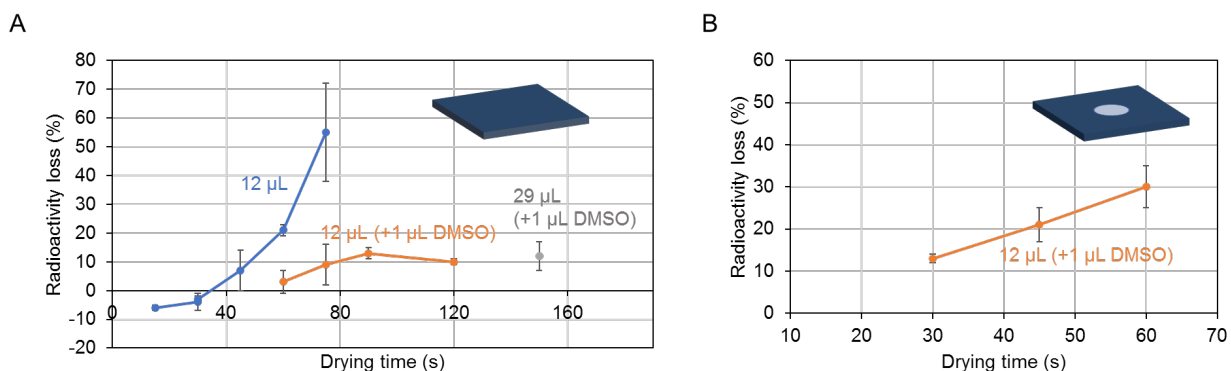


**Figure 7.2: Radioactivity loss during  $[^{18}\text{F}]$ fluoride drying under different drying conditions on a non-patterned silicon chip**

Each data point is the average of  $n=3$  replicates, except for points at 120 s and 150 s, for which  $n=4$ . The labels indicate the volume of radioisotope stock solution added, and the quantity of that volume that is DMSO (if any). (B) Radioactivity loss during  $[^{18}\text{F}]$ fluoride drying under different conditions on a patterned chip. Each data point is the average of  $n=2$  replicates.

### 7.3.4 Investigation of IEX radiolabeling step

Next the performance of the labeling step was optimized. For the closed Teflon-silicon reactor, the reaction performance was measured for different volumes of reaction buffer, each containing 5 nmol of precursor (Figure 7.3A). It was found that 4  $\mu\text{L}$  (5 nmol) gives slightly improved yields compared to the previously used 5  $\mu\text{L}$  (5 nmol) volume, and this was applied to all future syntheses. At this volume, the crude RCY was  $28 \pm 1\%$  ( $n=3$ ), with collection efficiency

of  $58 \pm 1\%$  (n=3) and radiochemical conversion of  $49 \pm 1\%$  (n=1). Residual activities of  $13 \pm 1\%$  (n=3) and  $2 \pm 0\%$  (n=3) was stuck on the cover plate and the reactor chip respectively, and  $26 \pm 2\%$  (n=3) of activity was identified as volatile loss (Table 7.2).

For comparison, the same conditions were applied for the closed Teflon-glass reactor. The resulting crude RCY was  $27 \pm 4\%$  (n=3), with  $41 \pm 6\%$  (n=3) collection efficiency and  $66 \pm 7\%$  (n=3) radiochemical conversion. Significant losses of radioactivity were found on the chips after product collection:  $14 \pm 3\%$  (n=3) and  $16 \pm 1\%$  (n=3) of the starting activity on the cover plate and the reactor chip, respectively. Furthermore, the volatile loss was  $28 \pm 4\%$  (n=3). Details are summarized in Table 7.2.

Measurement	STT reactor (open) (n=4)	Teflon-silicon reactor (closed) (n=3)	Teflon-glass reactor (closed) (n=3)
Estimated volatile radioactivity loss during [ <sup>18</sup> F]fluoride drying (%)	15	15	0
Product collection efficiency (%)	40±2	58±1	41±6
Residual radioactivity on reactor chip (%)	2±0	2±0	16±1
Residual radioactivity on cover plate (%)	N/A	13±1	14±3
Total volatile radioactivity loss (%)	59±2	26±2	28±4
Radiochemical conversion (%)	72±6	49±1	66±7
Crude RCY (%)	29±4	28±1	27±4
Can be automated? (Y/N)	Yes	No	No

**Table 7.2: Summary of performance of droplet-based IEX reactions using various reactor format**

Loss during drying was not measured, but was estimated based on prior experiments. % values are calculated as a ratio in reference to starting activity per experiment.

The conditions were then translated to the open reaction on a Teflon-silicon STT chip (i.e. with optimized drying condition including addition of 1  $\mu$ L of DMSO, and using 4  $\mu$ L precursor solution volume). Note that we observed the reaction mixture completely evaporated after ~5 min, so the reaction was stopped at 5 min. Under these conditions, crude RCY of  $29 \pm 4\%$  (n=4) was achieved, collection efficiency was  $40 \pm 2\%$  (n=4) and radiochemical conversion

was  $72 \pm 6\%$  ( $n=4$ ). Notably, only  $2 \pm 0\%$  ( $n=4$ ) of the radioactivity was leftover on the reactor chip after product recovery, but  $59 \pm 2\%$  ( $n=4$ ) was attributed to volatile radioactivity loss.

Results are tabulated in Table 7.2 for comparison to other reactor formats.

We briefly investigated the influence of reaction time on the synthesis performance (Figure 7.3B). Interestingly, increased heating time (even though the solvent has apparently evaporated) from 5 min to 7 min may enable a slight improvement in performance. However, the data from this reaction time optimization set showed overall lower performance than previous experiments (i.e. crude RCY of  $19 \pm 0\%$  ( $n=2$ ) for 5 min and crude RCY of  $23\%$  ( $n=1$ ) for 7 min), so further study is necessary.

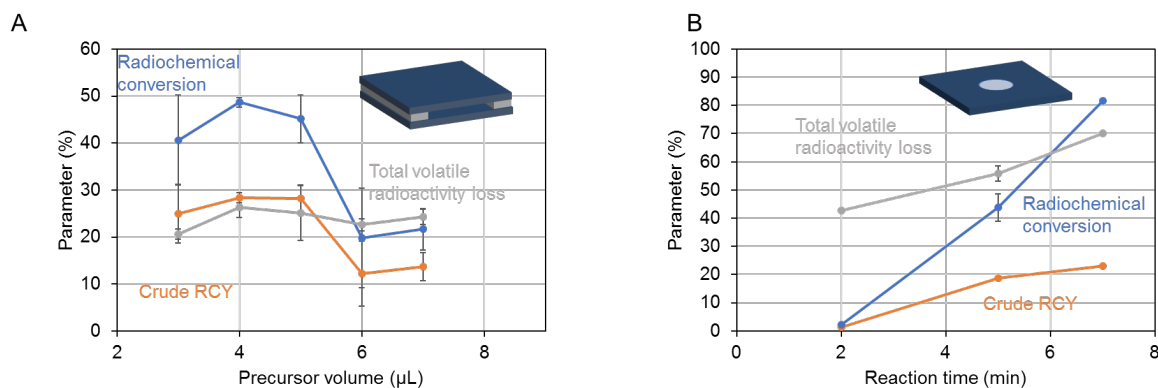


**Figure 7.3: Reaction performance summary**

(A) Impact of varying precursor volume on reaction performance in a closed reactor (silicon substrates). For 3, 4, 5, 6, and 7 μL experiments, the number of replicates are  $n=2$ ,  $n=3$ ,  $n=5$ ,  $n=3$ ,  $n=2$ , respectively. (B) Impact of reaction time on reaction performance on an open reactor (STT chip). For 2, 5, and 7 min experiments, the number of replicates are  $n=1$ ,  $n=2$ , and  $n=1$ , respectively.

The final crude product was also injected onto radio-HPLC to confirm product identity as shown on **Figure 4**.

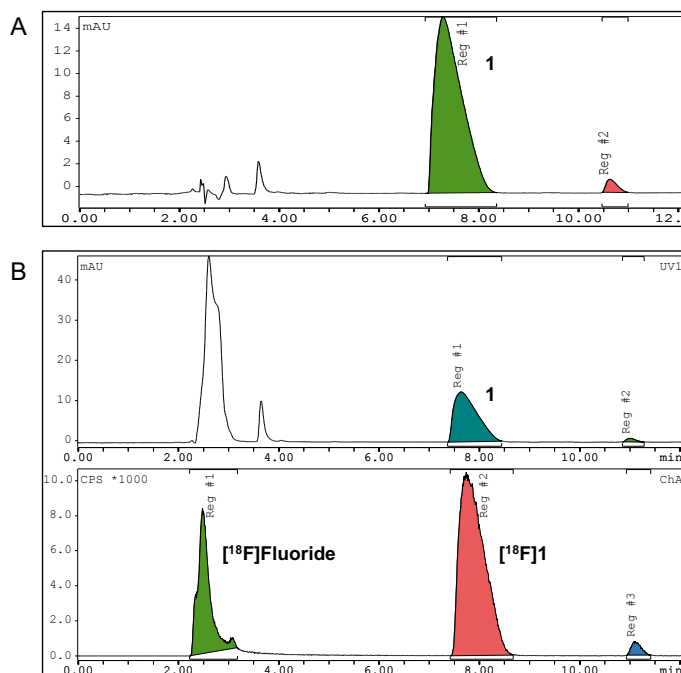


**Figure 7.4: HPLC chromatograms of non-radiolabeled and radiolabeled compound 1**

Note that a few impurities exist in the precursor that lead to labeled and unlabeled impurities in the crude reaction mixture. (A) A UV-chromatogram of injected non-radiolabeled compound 1 (B) Radio-HPLC co-injection of radiofluorinated [ $^{18}\text{F}$ ]1 with non-radioactive standard 1.

### 7.3.5 Automated synthesis

Automation of the synthesis using the STT-patterned Teflon-silicon chips is currently underway.

## 7.4 Discussion

### 7.4.1 Comparison of R-PPh<sub>3</sub>BF<sub>3</sub> to R-BF<sub>3</sub> syntheses

We previously reported synthesis of [ $^{18}\text{F}$ ]AMBF<sub>3</sub>-TATE on closed Teflon-glass chips with a crude RCY of  $17 \pm 3\%$  ( $n=15$ ) (105). Here, using the exact same conditions, the synthesis of several (2-((2-R)diphenylphosphonio)phenyl)trifluoroborate (R-PPh<sub>3</sub>BF<sub>3</sub>) compounds (56) proceeded with similar performance (Table 7.2). The average crude RCY over all replicates for all compounds was  $20 \pm 8\%$  ( $n=20$ ). For compound 1, the crude RCY was  $17 \pm 2\%$  ( $n=4$ ). This result suggests that IEX with the BF<sub>3</sub> moiety has comparable reactivity in the context in which it appears for these two classes of trifluoroborates. Note that apparently some of the precursor

compounds (all except DP-II-196-F2932 and DP-II-195) were not stable under the transport and/or storage conditions and exhibited some impurities, leading to corresponding UV and gamma peaks in the HPLC chromatograms of the crude product. In some cases (compound DP-II-195), new peaks appeared during labeling, suggesting that this compound may not be stable under the labeling conditions, and may be difficult to purify using only downstream SPE.

Interestingly, after optimization, we found the crude RCY on Teflon-glass chips for compound **1** to be  $27\pm 4\%$  ( $n=3$ ). However, since only very minor changes were made, we suspect the improvement may instead be attributed to differences in heating of the chip. In the previous platform, heat was provided by a thermoelectric element (Peltier) with a  $\sim 1$  cm diameter circular heating block affixed to it. In the current system, heat is provided by a 25 mm x 25 mm ceramic heater (Ultramic CER-1-01- 00093, Watlow, St. Louis, MO, USA), which likely can transfer heat more rapidly to the chip.

These new results suggest that with an improved experimental setup from droplet radiosynthesis, significantly higher yield can be achieved for IEX radiofluorination of  $\text{BF}_3$  compounds than previously reported.

#### **7.4.2 Effect of reactor format**

Interestingly, under optimized conditions, all 3 reaction platforms (Teflon-coated glass in closed format, Teflon-coated silicon in closed format, and STT-patterned Teflon-coated silicon in open format) showed similar crude RCY of the IEX labeling process.

Comparing the Teflon-coated silicon reactor (closed) versus the Teflon-coated glass reactor (closed), the former exhibited higher activity loss during [ $^{18}\text{F}$ ]fluoride drying (estimated  $\sim 15\%$  versus  $\sim 0\%$ ), and reduced radiochemical conversion (49% versus 66%), but exhibited reduced residual radioactivity on the reactor chip (2% versus 16%), estimated  $\sim 11\%$  vs 28% volatile activity losses during fluorination, and thus an overall increased collection efficiency (58% versus 41%).



Comparing the STT Teflon-silicon chip (open) to the Teflon-silicon chip (closed), overall volatile radioactivity losses (during both [ $^{18}\text{F}$ ]fluoride drying and fluorination) were higher (59% versus 26%), as expected due to the much larger exposed surface area of the droplet during the radiofluorination. On the other hand, an improved radiochemical conversion was observed (72% versus 49%) and residual radioactivity on the chip was versus low (2% versus 15% on both chips of the closed Teflon-silicon reactor). Subtracting losses during the drying step, volatile losses during the radiofluorination portion are 11% for the Teflon-silicon closed reactor, and 44% for the STT-patterned Teflon-silicon open reactor. It may be possible, that an improved apparent reaction conversion is related to the fact that unreacted [ $^{18}\text{F}$ ]fluoride leaves the open reactor more easily in its volatile [ $^{18}\text{F}$ ]HF form. As it can also be seen in Figure 7.3B, the increase in volatile loss correlates with increasing reaction conversion. More detailed studies are needed to fully understand the dynamics of IEX radiolabeling and volatile loss in these droplet reactors.

### 7.4.3 Volatile activity losses

We previously observed radioactivity loss during IEX fluorination, likely due to the formation of [ $^{18}\text{F}$ ]HF under the highly acidic reaction conditions, which can form a vapor and escape from the droplet. While for the Teflon-coated glass chips, we did not observe radioactivity loss during the initial [ $^{18}\text{F}$ ]fluoride drying with saline, a similar process on Teflon-coated silicon resulted in major radioactivity loss (up to 60%). Because both chips feature a Teflon-coating in contact with the radioisotope solution droplet, the reason for this difference remains unclear. A similar volatile loss was observed during drying on the STT-patterned Teflon-coated silicon chips, suggesting that the difference may not be due to the materials in contact with the droplet but rather some other properties of the overall system, e.g. heating characteristics. In some cases, Cerenkov imaging of the chips (108) were performed after drying and there was no sign of splashing, splattering or other effects, suggesting a purely

volatile loss of activity. In this study we were able to modify the drying procedures by addition of a small amount of DMSO and limit radioactivity loss to ~15%. Current drying procedure may require further time optimization for the open reactor to expand this method for different volumes of [ $^{18}\text{F}$ ]fluoride mixture.

Interestingly, no significant radioactivity losses have been observed when [ $^{18}\text{F}$ ]fluoride is dried in the presence of phase transfer catalysts and bases such as Kryptofix 2.2.2 /  $\text{K}_2\text{CO}_3$  or  $\text{TBAHCO}_3$  during the radiosyntheses of numerous tracers using the STT-patterned silicon chips (50,109). Perhaps additives can be included with the [ $^{18}\text{F}$ ]fluoride/saline mixture, though the impact on the pH and performance of the resulting reaction droplet need to be explored.

#### **7.4.4 Automation**

Despite the lack of improved performance in the STT-patterned Teflon-silicon chip, an enormous advantage of the open chip is the ability to easily automated the synthesis using existing platforms (108) that dispense reagents using dispensers above the chip, and collect product by lowering a collection tube down into the crude reaction droplet. Development of this automated protocol is currently underway.

### **7.5 Conclusion**

In this work it was demonstrated that reaction conditions developed previously for IEX labeling of [ $^{18}\text{F}$ ]AMBF<sub>3</sub>-TATE also gave similar performance when applied to a set of precursors based on a R-PPh<sub>3</sub>-BF<sub>3</sub> moiety, suggesting the advantages of droplet radiosynthesis (minimal reagent consumption, high molar activity) can be applied to a broad class of precursors.

The initial results were obtained using reaction droplets sandwiched within closed Teflon-coated glass reactors, but automation is difficult to apply to such a closed chip setup. In an attempt to translate the Teflon-coated glass conditions to an open reactor, comparisons were made among 3 different reactor types (closed Teflon-coated glass reactor, closed Teflon-coated silicon reactor and open silicon STT reactor). All exhibited comparable overall crude RCY

(~30%), despite the differences in conversion, residual losses on chips, and volatile losses. Successful transition to the open format paves the way for automation on our existing droplet-synthesis platform (108).

We anticipate that this improved technique provides an economic and automated procedure that can be more widely adopted by others to synthesize  $\text{BF}_3$ -based radiotracers and prosthetic groups to use these compounds in research, or to develop new tracers based on this simple labeling route (i.e. under aqueous conditions and avoiding HPLC purification). Though isotopic exchange has often been regarded as a low-molar-activity approach, the availability of automated microscale methods that can achieve high molar activity even in small batches, could possibly reinvigorate interest in the application of IEX syntheses as a basis for the synthesis of diverse tracers with high molar activity.

Ongoing work is aimed at further characterization of the prosthetic groups (Table 7.1) and conjugating these to biomolecules to develop novel PET imaging tracers.

## Chapter 8: Future outlook

As it was discussed in Chapter 1, many challenges surround radiopharmaceutical production for PET diagnostics, making it an expensive and complex process. Miniaturization of various aspects of the PET tracer production can potentially overcome some of the challenges by creating more compact, economic and efficient devices. Due to the reduction of shielding, physical footprint and reagent consumption microfluidics can enable low-cost decentralized production of PET tracers, with the tracers produced on demand in the imaging centers, instead of centralized large-batch production and distribution. While microfluidic analogues of conventional radiosynthesizers exist, their use is not yet widespread, in part due to high cost, dependence on specialized parts and limitations of the macro-to-micro interface. Additional challenges come in when the production practices need to be validated and approved in compliance with various regulations for use in clinic. Among other groups, our lab developed several microfluidic instruments aimed to replace various parts of PET tracer production.

This dissertation focused on microscale radiosynthesis of PET tracers to demonstrate the versatility and advantages of droplet-based synthesis methods. In Chapter 2, the droplet synthesis is applied to a novel compound consuming much less precursor than the conventional approach used side by side. Chapters 3 and 4 show the successful miniaturization and automation of production for clinically relevant tracers to produce quantities suitable for preclinical imaging. Chapter 5 shows that droplet synthesis can be scaled up easily to produce few human doses of tracers, and that the resulting radiopharmaceutical passes all necessary quality control requirements. Chapters 6 and 7 apply droplet synthesis to a special class of isotope exchange (IEX) reactions. The IEX syntheses most greatly benefit from drastic precursor reduction and high molar activity not bound to high starting radioactivity requirements. Miniaturization of the isotope exchange syntheses could make these types of reactions more attractive for the researchers, allowing to develop more tracers that take advantage of the

simplified purification and rapid synthesis time. Notably, the work here highlights collaborative efforts between chemistry and biology researchers, to synthesize radiopharmaceuticals for new probe validation and *in vivo* studies, as well as the industry to aid in device validation. It is important that such collaborative efforts continue and that the researchers can make use of the affordable droplet approaches. Additionally, as a continuation of Chapter 7, we are planning to install a droplet synthesizer to be used in another radiochemistry lab where novel tracers are being developed.

While manual synthesis using droplet technique can be routinely performed for the economic synthesis of various PET tracers and readily applied for pre-clinical studies, there are many challenges to be faced in order to make these devices available for widespread use and eventually in clinic. Since the ultimate goal is to move from centralized large-batch production to a decentralized on-demand production, the synthesizers have to be easy to use, cost-efficient, safe and reliable.

Current automated droplet radiosynthesizers are in the prototype stage and further efforts are needed to create a user-friendly final design, with low operation and system cost. Currently, the automated synthesizer requires a lot of expertise and manual intervention to calibrate, setup and clean the system for each production. In the future, automated calibration and cleaning protocols need to be developed. Hands-free realization of this concept can be achieved with a cassette-based approach where the user has to just replace the cassette containing non-radioactive reagents and cleaning solvents between the syntheses, while the system does the rest. It is important that the disposables (e.g. chips or hypothetical cassettes) are kept to a minimum and are low cost. The parts of the system that are in contact with the radioactivity are to be enclosed and shielded. Since in the foreseeable future purification will be carried out with HPLC, the radiosynthesizer will have to be integrated with HPLC to perform automated product delivery. The prototype for automated HPLC injector already exists in our lab, but further optimization and integration is required.

Apart from the droplet radiosynthesizer itself, other steps of tracer production are yet to be fully miniaturized. The tracer purification step currently still relies on the bulky HPLC systems, though in some cases miniaturization can be achieved using SPE cartridges. Miniaturization of the formulation step has been demonstrated using SPE micro-cartridges and microfluidic tracer concentration system built in our lab. QC still remains a challenge, though we believe the microchip CE has potential to greatly simplify and miniaturize some of the crucial QC tests.

The ideal end goal of PET tracer miniaturization is a fully automated, integrated device requiring minimal user intervention, that handles full production from radioisotope dispensing to quality control. While, the development of such technology would take many years in the future, the versatile droplet techniques presented in this work can encourage and propel further advancements of radiochemistry miniaturization and its application in clinic. The methods published herein are readily suitable for research applications and can provide the scientists with economical batches of diverse PET tracers. We envision that the droplet-based radiopharmaceutical production approaches would be beneficial to the field of radiochemistry, making PET tracer production simpler, cheaper, safer, more accessible and promote the use of powerful PET diagnostics all over the world, including low resource setting.

## References

1. Ter-Pogossian MM, Phelps ME, Hoffman EJ, Mullani NA. A positron-emission transaxial tomograph for nuclear imaging (PETT). *Radiology*. 1975;114:89-98.
2. Phelps ME, Hoffman EJ, Mullani NA, Ter-Pogossian MM. Application of annihilation coincidence detection to transaxial reconstruction tomography. *J Nucl Med*. 1975;16:210-224.
3. Ametamey SM, Honer M, Schubiger PA. Molecular Imaging with PET. *Chem Rev*. 2008;108:1501-1516.
4. Le Bars D. Fluorine-18 and medical imaging: Radiopharmaceuticals for positron emission tomography. *Journal of Fluorine Chemistry*. 2006;127:1488-1493.
5. Phelps ME. Molecular Imaging with Positron Emission Tomography. *Annual Review of Nuclear and Particle Science*. 2002;52:303-338.
6. Velikyan I. <sup>68</sup>Ga-Based Radiopharmaceuticals: Production and Application Relationship. *Molecules*. 2015;20:12913-12943.
7. Berg E, Cherry SR. Innovations in Instrumentation for Positron Emission Tomography. *Seminars in Nuclear Medicine*. 2018;48:311-331.
8. Gu Z, Taschereau R, Vu NT, et al. Performance Evaluation of G8, a High-Sensitivity Benchtop Preclinical PET/CT Tomograph. *Journal of Nuclear Medicine*. 2019;60:142-149.
9. Lasne M-C, Perrio C, Rouden J, et al. Chemistry of  $\beta^+$ -Emitting Compounds Based on Fluorine-18. In: Krause W, ed. Contrast Agents II: Optical, Ultrasound, X-Ray and Radiopharmaceutical Imaging. Topics in Current Chemistry. Berlin, Heidelberg: Springer Berlin Heidelberg; 2002:201-258.
10. Sanchez-Crespo A. Comparison of Gallium-68 and Fluorine-18 imaging characteristics in positron emission tomography. *Applied Radiation and Isotopes*. 2013;76:55-62.
11. Kubota K. From tumor biology to clinical PET: A review of positron emission tomography (PET) in oncology. *Ann Nucl Med*. 2001;15:471-486.
12. Langen K-J, Galldiks N, Hattingen E, Shah NJ. Advances in neuro-oncology imaging. *Nat Rev Neurol*. 2017;13:279-289.
13. Galldiks N, Lohmann P, Albert NL, Tonn JC, Langen K-J. Current status of PET imaging in neuro-oncology. *Neuro-Oncology Advances*. 2019;1.
14. Zhu L, Ploessl K, Kung HF. PET/SPECT imaging agents for neurodegenerative diseases. *Chem Soc Rev*. 2014;43:6683-6691.
15. Pan JA, Salerno M. Clinical Utility and Future Applications of PET/CT and PET/CMR in Cardiology. *Diagnostics*. 2016;6:32.

16. Tarkin JM, Joshi FR, Rudd JHF. PET imaging of inflammation in atherosclerosis. *Nat Rev Cardiol.* 2014;11:443-457.
17. Werner RA, Chen X, Rowe SP, Lapa C, Javadi MS, Higuchi T. Recent paradigm shifts in molecular cardiac imaging—Establishing precision cardiology through novel 18F-labeled PET radiotracers. *Trends in Cardiovascular Medicine.* 2020;30:11-19.
18. Antonios JP, Soto H, Everson RG, et al. Detection of immune responses after immunotherapy in glioblastoma using PET and MRI. *PNAS.* 2017;114:10220-10225.
19. Mayer AT, Natarajan A, Gordon SR, et al. Practical Immuno-PET Radiotracer Design Considerations for Human Immune Checkpoint Imaging. *Journal of Nuclear Medicine.* 2017;58:538-546.
20. Donnelly DJ. Small Molecule PET Tracers in Drug Discovery. *Seminars in Nuclear Medicine.* 2017;47:454-460.
21. Waaijer SJH, Kok IC, Eisses B, et al. Molecular Imaging in Cancer Drug Development. *J Nucl Med.* 2018;59:726-732.
22. Avril S, Muzic RF, Plecha D, Traughber BJ, Vinayak S, Avril N. 18F-FDG PET/CT for Monitoring of Treatment Response in Breast Cancer. *J Nucl Med.* 2016;57:34S-39S.
23. Deroose CM, Stroobants S, Liu Y, Shankar LK, Bourguet P. Using PET for therapy monitoring in oncological clinical trials: challenges ahead. *Eur J Nucl Med Mol Imaging.* 2017;44:32-40.
24. Dunphy MPS, Lewis JS. Radiopharmaceuticals in Preclinical and Clinical Development for Monitoring of Therapy with PET. *J Nucl Med.* 2009;50:106S-121S.
25. Glaudemans AWJM, de Vries EFJ, Galli F, Dierckx RAJO, Slart RHJA, Signore A. The Use of 18F-FDG-PET/CT for Diagnosis and Treatment Monitoring of Inflammatory and Infectious Diseases. *Clinical and Developmental Immunology.* 2013;2013:1-14.
26. Kulkarni HR, Singh A, Langbein T, et al. Theranostics of prostate cancer: from molecular imaging to precision molecular radiotherapy targeting the prostate specific membrane antigen. *Br J Radiol.* 2018;91:20180308.
27. Coenen HH, Elsinga PH, Iwata R, et al. Fluorine-18 radiopharmaceuticals beyond [18F]FDG for use in oncology and neurosciences. *Nuclear Medicine and Biology.* 2010;37:727-740.
28. Phelps ME. Positron emission tomography provides molecular imaging of biological processes. *PNAS.* 2000;97:9226-9233.
29. Chassoux F, Artiges E, Semah F, et al. 18F-FDG-PET patterns of surgical success and failure in mesial temporal lobe epilepsy. *Neurology.* 2017;88:1045-1053.
30. Parida GK, Roy SG, Kumar R. FDG-PET/CT in Skeletal Muscle: Pitfalls and Pathologies. *Seminars in Nuclear Medicine.* 2017;47:362-372.



31. Rice L, Bisdas S. The diagnostic value of FDG and amyloid PET in Alzheimer's disease—A systematic review. *European Journal of Radiology*. 2017;94:16-24.
32. Treglia G. Diagnostic Performance of 18F-FDG PET/CT in Infectious and Inflammatory Diseases according to Published Meta-Analyses. *Contrast Media & Molecular Imaging*. <https://www.hindawi.com/journals/cmimi/2019/3018349/>.
33. Walker Z, Gandolfo F, Orini S, et al. Clinical utility of FDG PET in Parkinson's disease and atypical parkinsonism associated with dementia. *Eur J Nucl Med Mol Imaging*. 2018;45:1534-1545.
34. Saint-Aubert L, Lemoine L, Chiotis K, Leuzy A, Rodriguez-Vieitez E, Nordberg A. Tau PET imaging: present and future directions. *Mol Neurodegeneration*. 2017;12:19.
35. Boccardi M, Altomare D, Ferrari C, et al. Assessment of the Incremental Diagnostic Value of Florbetapir F 18 Imaging in Patients With Cognitive Impairment: The Incremental Diagnostic Value of Amyloid PET With [18F]-Florbetapir (INDIA-FBP) Study. *JAMA Neurology*. 2016;73:1417-1424.
36. Hanseeuw BJ, Betensky RA, Jacobs HIL, et al. Association of Amyloid and Tau With Cognition in Preclinical Alzheimer Disease: A Longitudinal Study. *JAMA Neurology*. 2019;76:915-924.
37. Degenhardt EK, Witte MM, Case MG, et al. Florbetapir F18 PET Amyloid Neuroimaging and Characteristics in Patients With Mild and Moderate Alzheimer Dementia. *Psychosomatics*. 2016;57:208-216.
38. Beaurain M, Salabert A-S, Ribeiro MJ, et al. Innovative Molecular Imaging for Clinical Research, Therapeutic Stratification, and Nosography in Neuroscience. *Front Med*. 2019;6.
39. Croteau E, Renaud JM, Richard MA, Ruddy TD, Bénard F, deKemp RA. PET Metabolic Biomarkers for Cancer. *Biomark Cancer*. 2016;8s2:BIC.S27483.
40. Langen K-J, Stoffels G, Filss C, et al. Imaging of amino acid transport in brain tumours: Positron emission tomography with O-(2-[18F]fluoroethyl)-L-tyrosine (FET). *Methods*. 2017;130:124-134.
41. Lau EWF, Drummond KJ, Ware RE, et al. Comparative PET study using F-18 FET and F-18 FDG for the evaluation of patients with suspected brain tumour. *Journal of Clinical Neuroscience*. 2010;17:43-49.
42. Marcu LG, Moghaddasi L, Bezak E. Imaging of Tumor Characteristics and Molecular Pathways With PET: Developments Over the Last Decade Toward Personalized Cancer Therapy. *International Journal of Radiation Oncology\*Biophysics\*Physics*. 2018;102:1165-1182.
43. Vallabhajosula S, Solnes L, Vallabhajosula B. A Broad Overview of Positron Emission Tomography Radiopharmaceuticals and Clinical Applications: What Is New? *Seminars in Nuclear Medicine*. 2011;41:246-264.

44. Barrio M, Czernin J, Fanti S, et al. The Impact of Somatostatin Receptor-Directed PET/CT on the Management of Patients with Neuroendocrine Tumor: A Systematic Review and Meta-Analysis. *Journal of Nuclear Medicine*. 2017;58:756-761.
45. Waldmann CM, Stuparu AD, van Dam RM, Slavik R. The Search for an Alternative to [68Ga]Ga-DOTA-TATE in Neuroendocrine Tumor Theranostics: Current State of 18F-labeled Somatostatin Analog Development. *Theranostics*. 2019;9:1336-1347.
46. Guillaume M, Luxen A, Nebeling B, Argentini M, Clark JC, Pike VW. Recommendations for fluorine-18 production. *International Journal of Radiation Applications and Instrumentation Part A Applied Radiation and Isotopes*. 1991;42:749-762.
47. Jacobson O, Kiesewetter DO, Chen X. Fluorine-18 Radiochemistry, Labeling Strategies and Synthetic Routes. *Bioconjugate Chem*. 2015;26:1-18.
48. Kilbourn MR, Rodnick ME, Clark M. Production of Short Half-Life PET Radionuclides. In: *Handbook of Radiopharmaceuticals*. John Wiley & Sons, Ltd; 2020:45-69.
49. Brooks AF, Makaravage KJ, Wright J, Sanford MS, Scott PJH. Fluorine-18 Radiochemistry. In: *Handbook of Radiopharmaceuticals*. John Wiley & Sons, Ltd; 2020:251-289.
50. Lisova K, Chen BY, Wang J, Fong KM-M, Clark PM, van Dam RM. Rapid, efficient, and economical synthesis of PET tracers in a droplet microreactor: application to O-(2-[18F]fluoroethyl)-L-tyrosine ([18F]FET). *EJNMMI radiopharm chem*. 2019;5:1.
51. Vallabhajosula S. 18F-Labeled Positron Emission Tomographic Radiopharmaceuticals in Oncology: An Overview of Radiochemistry and Mechanisms of Tumor Localization. *Seminars in Nuclear Medicine*. 2007;37:400-419.
52. Zlatopolskiy BD, Zischler J, Krapf P, et al. Copper-Mediated Aromatic Radiofluorination Revisited: Efficient Production of PET Tracers on a Preparative Scale. *Chemistry – A European Journal*. 2015;21:5972-5979.
53. Krishnan HS, Ma L, Vasdev N, Liang SH. 18F-Labeling of Sensitive Biomolecules for Positron Emission Tomography. *Chem Eur J*. 2017;23:15553-15577.
54. Bernard-Gauthier V, Bailey JJ, Liu Z, et al. From Unorthodox to Established: The Current Status of 18F-Trifluoroborate- and 18F-SiFA-Based Radiopharmaceuticals in PET Nuclear Imaging. *Bioconjugate Chem*. 2016;27:267-279.
55. Liu Z, Pourghiasian M, Radtke MA, et al. An Organotrifluoroborate for Broadly Applicable One-Step 18F-Labeling. *Angew Chem Int Ed*. 2014;53:11876-11880.
56. Lisova K, Pla D, Sergeev, Gras G, van Dam RM, van Dam, R.Michael. Leveraging microvolume radiochemistry and trifluoroborate chemistry to synthesize 18F-labeled prosthetic groups via isotopic exchange with high specific activity. In: *The 22nd International Symposium on Radiopharmaceutical Sciences*. Vol 60. Dresden, Germany: *Journal of Labelled Compounds and Radiopharmaceuticals*; 2017:S37.

57. Sergeev M, Lazari M, Morgia F, et al. Performing radiosynthesis in microvolumes to maximize molar activity of tracers for positron emission tomography. *Communications Chemistry*. 2018;1:10.
58. Hutchins GD, Miller MA, Soon VC, Receveur T. Small Animal PET Imaging. *ILAR J*. 2008;49:54-65.
59. Jagoda EM, Vaquero JJ, Seidel J, Green MV, Eckelman WC. Experiment assessment of mass effects in the rat: implications for small animal PET imaging. *Nuclear Medicine and Biology*. 2004;31:771-779.
60. GE Healthcare. FASTlab 2 Multi-Tracer Platform. [http://www3.gehealthcare.com/en/products/categories/molecular\\_imaging/pet-radiopharmacy/tracer\\_center\\_equipment/fastlab](http://www3.gehealthcare.com/en/products/categories/molecular_imaging/pet-radiopharmacy/tracer_center_equipment/fastlab).
61. Siemens Healthcare. Explora GN - Overview. <http://usa.healthcare.siemens.com/molecular-imaging/cyclotron-chemistry-solution/explora-gn>.
62. IBA. Synthra: Small dimensions. Huge potential.
63. GE Healthcare. TRACERlab. [http://www.gehealthcare.com/euen/fun\\_img/products/radiopharmacy/products/tracerlabfx.c.html](http://www.gehealthcare.com/euen/fun_img/products/radiopharmacy/products/tracerlabfx.c.html).
64. Synthra GmbH Home Page. <http://synthra.com/>.
65. Eckert & Ziegler Eurotope GmbH. Modular-Lab PharmTracer. <http://www.ezag.com/home/products/radiopharma/radiosynthesis-technology/modular-lab-pharmtracer.html>.
66. Lazari M, Quinn KM, Claggett SB, et al. ELIXYS - a fully automated, three-reactor high-pressure radiosynthesizer for development and routine production of diverse PET tracers. *EJNMMI Res*. 2013;3:52.
67. SOFIE. ELIXYS FLEX/CHEM. <http://sofiebio.com/products/chemistry/elixys/>.
68. SOFIE. ELIXYS PURE/FORM. Sofie Biosciences. <http://sofiebio.com/products/chemistry/elixys-pureform/>.
69. Bruton L, Scott PJH. Automated Synthesis Modules for PET Radiochemistry. In: *Handbook of Radiopharmaceuticals*. John Wiley & Sons, Ltd; 2020:437-456.
70. Phillips TM, Corradini D. *Handbook of HPLC, Second Edition*. CRC PressINC; 2010.
71. Elizarov AM. Microreactors for radiopharmaceutical synthesis. *Lab Chip*. 2009;9:1326-1333.
72. Chao PH, Collins J, Argus JP, Tseng W-Y, Lee JT, Dam RM van. Automatic concentration and reformulation of PET tracers via microfluidic membrane distillation. *Lab Chip*. 2017;17:1802-1816.

73. Lemaire C, Plenevaux A, Aerts J, et al. Solid phase extraction - an alternative to the use of rotary evaporators for solvent removal in the rapid formulation of PET radiopharmaceuticals. *Journal of Labelled Compounds and Radiopharmaceuticals*. 1999;42:63-75.
74. USP 35 - NF 50. Chapter 823: Positron Emission Tomography Drugs for Compounding, Investigational, and Research Uses. In: ; 2012:398-406.
75. CFR - Code of Federal Regulations Title 21. <http://www.accessdata.fda.gov/scripts/cdrh/cfdocs/cfcfr/CFRSearch.cfm>.
76. European Pharmacopeia (EP). Technical guide for the elaboration of monographs on radiopharmaceutical preparations. In: Strasbourg, France: European directorate for the quality of medicines & healthcare; 2010.
77. Elizarov AM. Automation of PET Radiopharmaceutical Quality Control. In: Handbook of Radiopharmaceuticals. John Wiley & Sons, Ltd; 2020:457-489.
78. Ha NS, Sadeghi S, van Dam RM. Recent Progress toward Microfluidic Quality Control Testing of Radiopharmaceuticals. *Micromachines*. 2017;8:337.
79. Ferguson D, McGrath S, O'Hara G, Marshall C. Investigation of staff finger doses during quality control of FDG production. *Health Physics*. 2011;100:523–529.
80. QC1. Automatic quality control for PET and MI tracers. <http://www.qc1.com>. <http://www.qc1.com/>.
81. Trace-ability, Inc. - SBIR Source. SBIRSource.com. <http://sbirsource.com/sbir/firms/26162-trace-ability-inc>.
82. Anzellotti AI, McFarland AR, Ferguson D, Olson KF. Towards the Full Automation of QC Release Tests for [18F]fluoride-labeled Radiotracers. *Current Organic Chemistry*. 2013;17:2153-2158.
83. Zhu S, Mosessian S, Kroeger K, et al. Transforming an Academic Radiochemistry Facility for Positron Emission Tomography Drug cGMP Compliance. *Mol Imaging Biol*. 2020;22:256-264.
84. Knapp K-A, Nickels ML, Manning HC. The Current Role of Microfluidics in Radiofluorination Chemistry. *Mol Imaging Biol*. 2020;22:463-475.
85. Pascali G, Salvadori PA. Opportunities and challenges in the utilization of microfluidic technologies to the production of radiopharmaceuticals. *Chimica Oggi - Chemistry Today*. 2016;34:28-32.
86. Wang J, van Dam RM. High-Efficiency Production of Radiopharmaceuticals via Droplet Radiochemistry: A Review of Recent Progress. *Mol Imaging*. 2021;19:1-21.
87. Arima V, Watts P, Pascali G. Microfluidics in Planar Microchannels: Synthesis of Chemical Compounds On-Chip. In: Castillo-León J, Svendsen WE, eds. Lab-on-a-Chip

- Devices and Micro-Total Analysis Systems. Springer International Publishing; 2015:197-239.
88. Razzaq T, Kappe CO. Continuous Flow Organic Synthesis under High-Temperature/Pressure Conditions. *Chemistry – An Asian Journal*. 2010;5:1274-1289.
  89. Wiles C, Watts P. Continuous Flow Reactors, a Tool for the Modern Synthetic Chemist. *Eur J Org Chem*. 2008;2008:1655-1671.
  90. Liu Z, Schaap KS, Ballemans L, et al. Measurement of reaction kinetics of [177Lu]Lu-DOTA-TATE using a microfluidic system. *Dalton Trans*. 2017;46:14669-14676.
  91. Pascali G, Watts P, Salvadori PA. Microfluidics in radiopharmaceutical chemistry. *Nuclear Medicine and Biology*. 2013;40:776-787.
  92. Pfaff S, Philippe C, Pichler V, Hacker M, Mitterhauser M, Wadsak W. Microfluidic 68 Ga-labeling: a proof of principle study. *Dalton Transactions*. 2018;47:5997-6004.
  93. Wright BD, Whittenberg J, Desai A, et al. Microfluidic Preparation of a 89Zr-Labeled Trastuzumab Single-Patient Dose. *J Nucl Med*. 2016;57:747-752.
  94. Zeng D, Desai AV, Ranganathan D, Wheeler TD, Kenis PJA, Reichert DE. Microfluidic radiolabeling of biomolecules with PET radiometals. *Nuclear Medicine and Biology*. 2013;40:42-51.
  95. Saiki H, Iwata R, Nakanishi H, et al. Electrochemical concentration of no-carrier-added [18F]fluoride from [18O]water in a disposable microfluidic cell for radiosynthesis of 18F-labeled radiopharmaceuticals. *Applied Radiation and Isotopes*. 2010;68:1703-1708.
  96. Wong R, Iwata R, Saiki H, Furumoto S, Ishikawa Y, Ozeki E. Reactivity of electrochemically concentrated anhydrous [18F]fluoride for microfluidic radiosynthesis of 18F-labeled compounds. *Applied Radiation and Isotopes*. 2012;70:193-199.
  97. Iwata R, Terasaki K, Ishikawa Y, et al. A concentration-based microscale method for 18F-nucleophilic substitutions and its testing on the one-pot radiosynthesis of [18F]FET and [18F]fallypride. *Applied Radiation and Isotopes*. August 2020:109361.
  98. Lebedev A, Miraghaie R, Kotta K, et al. Batch-reactor microfluidic device: first human use of a microfluidically produced PET radiotracer. *Lab Chip*. 2012;13:136-145.
  99. Zhang X, Liu F, Knapp K-A, Nickels ML, Manning HC, Bellan LM. A simple microfluidic platform for rapid and efficient production of the radiotracer [18F]fallypride. *Lab Chip*. 2018;18:1369-1377.
  100. Chen S, Ding H, Shah GJ, van Dam RM, Kim C-J. EWOD Microdevices for Synthesis of 18F-Labeled Tracers for Positron Emission Tomography (PET). In: Technical Digest of the Solid-State Sensor, Actuator and Microsystems Workshop. Hilton Head Island, SC; 2010:37-40.

101. Kim C-J, van Dam RM, Chen S, Ding H. Radiosynthesis of Positron Emission Tomography (PET) Imaging Probes on Electrowetting-on-Dielectric (EWOD) Chip. June 2010.
102. Nelson WC, Kim C-J 'CJ.' Droplet Actuation by Electrowetting-on-Dielectric (EWOD): A Review. *Journal of Adhesion Science and Technology*. 2012;26:1747-1771.
103. Keng PY, Ding H, Chen S, et al. Digital microfluidics: Toward a bench-top platform for on-demand radiosynthesis of diverse PET tracers. August 2010.
104. Keng PY, Chen S, Ding H, et al. Micro-chemical synthesis of molecular probes on an electronic microfluidic device. *PNAS*. 2012;109:690-695.
105. Lisova K, Sergeev M, Evans-Axelsson S, et al. Microscale radiosynthesis, preclinical imaging and dosimetry study of [18F]AMBF3-TATE: A potential PET tracer for clinical imaging of somatostatin receptors. *Nuclear Medicine and Biology*. 2018;61:36-44.
106. Wang J, Chao PH, Hanet S, Dam RM van. Performing multi-step chemical reactions in microliter-sized droplets by leveraging a simple passive transport mechanism. *Lab Chip*. 2017;17:4342-4355.
107. Wang J, Chao PH, Slavik R, Dam RM van. Multi-GBq production of the radiotracer [18F]fallypride in a droplet microreactor. *RSC Adv*. 2020;10:7828-7838.
108. Wang J, Chao PH, Dam RM van. Ultra-compact, automated microdroplet radiosynthesizer. *Lab Chip*. 2019:2415-2424.
109. Lisova K, Wang J, Chao PH, van Dam RM. A simple and efficient automated microvolume radiosynthesis of [18F]Florbetaben. *EJNMMI Radiopharmacy and Chemistry*. 2020;5:30.
110. Wang J, Holloway T, Lisova K, Dam RM van. Green and efficient synthesis of the radiopharmaceutical [18F]FDOPA using a microdroplet reactor. *React Chem Eng*. 2020;5:320-329.
111. Rios A, Wang J, Chao PH, Dam RM van. A novel multi-reaction microdroplet platform for rapid radiochemistry optimization. *RSC Adv*. 2019;9:20370-20374.
112. Jones J, Rios A, Chao P, Wang J, van Dam RM. High-throughput microdroplet radiochemistry platform to accelerate radiotracer development. In: *Journal of Labelled Compounds & Radiopharmaceuticals*. Vol 62. ; 2019:S350-S351.
113. Chao PH, Lazari M, Hanet S, Narayanam MK, Murphy JM, van Dam RM. Automated concentration of [18F]fluoride into microliter volumes. *Applied Radiation and Isotopes*. 2018;141:138-148.
114. Tarn MD, Pascali G, De Leonardis F, Watts P, Salvadori PA, Pamme N. Purification of 2-[18F]fluoro-2-deoxy-d-glucose by on-chip solid-phase extraction. *J Chromatogr A*. 2013;1280:117-121.

115. Javed MR, Chen S, Kim H-K, et al. Efficient Radiosynthesis of 3'-Deoxy-3'-18F-Fluorothymidine Using Electrowetting-on-Dielectric Digital Microfluidic Chip. *J Nucl Med.* 2014;55:321-328.
116. Chen S, Lei J, van Dam RM, Keng P-Y, Kim C-J "CJ." Planar alumina purification of 18F-labeled radiotracer synthesis on EWOD chip for positron emission tomography (PET). In: Proceedings of the 16th International Conference on Miniaturized Systems for Chemistry and Life Sciences. Okinawa, Japan; 2012:1771-1773.
117. Ha NS, Ly J, Jones J, Cheung S, van Dam RM. Novel volumetric method for highly repeatable injection in microchip electrophoresis. *Analytica Chimica Acta.* 2017;985:129-140.
118. Jones J, Ha NS, Barajas AG, Chatziioannou AF, van Dam RM. Integration of High-Resolution Radiation Detector for Hybrid Microchip Electrophoresis. *Anal Chem.* 2020;92:3483-3491.
119. Ming-Wei Wang, Wei-Yu Lin, Kan Liu, Masterman-Smith M, Kwang-Fu Shen C. Microfluidics for Positron Emission Tomography Probe Development. *Molecular Imaging.* 2010;9:175-191.
120. Keng PY, van Dam RM. Digital Microfluidics: A New Paradigm for Radiochemistry. *Mol Imag.* 2015;14:579-594.
121. Gu Z, Taschereau R, Prout DL, Vu N, Chatziioannou A. Performance evaluation of HiPET, a High Sensitivity and High Spatial Resolution DOI PET Tomograph. In: Atlanta, Georgia, USA: IEEE NPSS; 2017.
122. Toschi L, Finocchiaro G, Bartolini S, Gioia V, Cappuzzo F. Role of gemcitabine in cancer therapy. *Future Oncology.* 2005;1:7-17.
123. Heinemann V, Hertel LW, Grindey GB, Plunkett W. Comparison of the Cellular Pharmacokinetics and Toxicity of 2',2'-Difluorodeoxycytidine and 1- $\beta$ -d-Arabinofuranosylcytosine. *Cancer Res.* 1988;48:4024-4031.
124. Mackey JR, Mani RS, Selner M, et al. Functional Nucleoside Transporters Are Required for Gemcitabine Influx and Manifestation of Toxicity in Cancer Cell Lines. *Cancer Res.* 1998;58:4349-4357.
125. Huang P, Chubb S, Hertel LW, Grindey GB, Plunkett W. Action of 2',2'-Difluorodeoxycytidine on DNA Synthesis. *Cancer Res.* 1991;51:6110-6117.
126. Hodge LS, Taub ME, Tracy TS. The Deaminated Metabolite of Gemcitabine, 2',2'-Difluorodeoxyuridine, Modulates the Rate of Gemcitabine Transport and Intracellular Phosphorylation via Deoxycytidine Kinase. *Drug Metab Dispos.* 2011;39:2013-2016.
127. Shipley LA, Brown TJ, Cornpropst JD, Hamilton M, Daniels WD, Culp HW. Metabolism and disposition of gemcitabine, and oncolytic deoxycytidine analog, in mice, rats, and dogs. *Drug Metab Dispos.* 1992;20:849-855.

128. Veltkamp SA, Pluim D, Eijndhoven MAJ van, et al. New insights into the pharmacology and cytotoxicity of gemcitabine and 2',2'-difluorodeoxyuridine. *Mol Cancer Ther.* 2008;7:2415-2425.
129. Bender DM, Bao J, Dantzig AH, et al. Synthesis, Crystallization, and Biological Evaluation of an Orally Active Prodrug of Gemcitabine. *J Med Chem.* 2009;52:6958-6961.
130. Bergman AM, Adema AD, Balzarini J, et al. Antiproliferative activity, mechanism of action and oral antitumor activity of CP-4126, a fatty acid derivative of gemcitabine, in in vitro and in vivo tumor models. *Invest New Drugs.* 2011;29:456-466.
131. Couvreur P, Stella B, Reddy LH, et al. Squalenoyl Nanomedicines as Potential Therapeutics. *Nano Lett.* 2006;6:2544-2548.
132. Moysan E, Bastiat G, Benoit J-P. Gemcitabine versus Modified Gemcitabine: A Review of Several Promising Chemical Modifications. *Mol Pharmaceutics.* 2013;10:430-444.
133. Tsume Y, Drelich AJ, Smith DE, Amidon GL. Potential Development of Tumor-Targeted Oral Anti-Cancer Prodrugs: Amino Acid and Dipeptide Monoester Prodrugs of Gemcitabine. *Molecules.* 2017;22:1322.
134. Vale N, Ferreira A, Fernandes I, et al. Gemcitabine anti-proliferative activity significantly enhanced upon conjugation with cell-penetrating peptides. *Bioorganic & Medicinal Chemistry Letters.* 2017;27:2898-2901.
135. Vandana M, Sahoo SK. Long circulation and cytotoxicity of PEGylated gemcitabine and its potential for the treatment of pancreatic cancer. *Biomaterials.* 2010;31:9340-9356.
136. Ferraboschi P, Ciceri S, Grisenti P. Synthesis of Antitumor Fluorinated Pyrimidine Nucleosides. *Organic Preparations and Procedures International.* 2017;49:69-154.
137. Dasari M, Acharya AP, Kim D, et al. H-Gemcitabine: A New Gemcitabine Prodrug for Treating Cancer. *Bioconjugate Chem.* 2013;24:4-8.
138. Liu L-H, Qiu W-X, Li B, et al. A Red Light Activatable Multifunctional Prodrug for Image-Guided Photodynamic Therapy and Cascaded Chemotherapy. *Advanced Functional Materials.* 2016;26:6257-6269.
139. Maiti S, Park N, Han JH, et al. Gemcitabine–Coumarin–Biotin Conjugates: A Target Specific Theranostic Anticancer Prodrug. *J Am Chem Soc.* 2013;135:4567-4572.
140. Yang Z, Lee JH, Jeon HM, et al. Folate-Based Near-Infrared Fluorescent Theranostic Gemcitabine Delivery. *J Am Chem Soc.* 2013;135:11657-11662.
141. "Design and Synthesis of 4-N-Alkanoyl and 4-N-Alkyl Gemcitabine Analogu" by Jesse E. Pulido. <https://digitalcommons.fiu.edu/etd/1232/>.
142. Pulido J, Sobczak AJ, Balzarini J, Whuk SF. Synthesis and Cytostatic Evaluation of 4-N-Alkanoyl and 4-N-Alkyl Gemcitabine Analogues. *J Med Chem.* 2014;57:191-203.



143. Alauddin MM. Positron emission tomography (PET) imaging with  $^{18}\text{F}$ -based radiotracers. *Am J Nucl Med Mol Imaging*. 2011;2:55-76.
144. Campbell MG, Mercier J, Genicot C, Gouverneur V, Hooker JM, Ritter T. Bridging the gaps in  $^{18}\text{F}$  PET tracer development. *Nature Chemistry*. 2017;9:1-3.
145. Hoover AJ, Lazari M, Ren H, et al. A Transmetalation Reaction Enables the Synthesis of [ $^{18}\text{F}$ ]5-Fluorouracil from [ $^{18}\text{F}$ ]Fluoride for Human PET Imaging. *Organometallics*. 2016;35:1008-1014.
146. Neumann CN, Hooker JM, Ritter T. Concerted nucleophilic aromatic substitution with  $^{19}\text{F}^-$  and  $^{18}\text{F}^-$ . *Nature*. 2016;534:369-373.
147. Taylor NJ, Emer E, Preshlock S, et al. Derisking the Cu-Mediated  $^{18}\text{F}$ -Fluorination of Heterocyclic Positron Emission Tomography Radioligands. *J Am Chem Soc*. 2017;139:8267-8276.
148. Brown K, Dixey M, Weymouth-Wilson A, Linclau B. The synthesis of gemcitabine. *Carbohydrate Research*. 2014;387:59-73.
149. Hertel LW, Kroin JS, Misner JW, Tustin JM. Synthesis of 2-deoxy-2,2-difluoro-D-ribose and 2-deoxy-2,2'-difluoro-D-ribofuranosyl nucleosides. *The Journal of Organic Chemistry*. 1988;53:2406-2409.
150. Meyer J-P. Synthetic routes to  $^{18}\text{F}$ -labelled gemcitabine and related 2'-fluoronucleosides. 2015.
151. Laing RE, Walter MA, Campbell DO, et al. Noninvasive prediction of tumor responses to gemcitabine using positron emission tomography. *Proceedings of the National Academy of Sciences*. 2009;106:2847-2852.
152. Lee JT, Campbell DO, Satyamurthy N, Czernin J, Radu CG. Stratification of nucleoside analog chemotherapy using 1-(2'-deoxy-2'- $^{18}\text{F}$ -fluoro- $\beta$ -D-arabinofuranosyl)cytosine and 1-(2'-deoxy-2'- $^{18}\text{F}$ -fluoro- $\beta$ -L-arabinofuranosyl)-5-methylcytosine PET. *J Nucl Med*. 2012;53:275-280.
153. Radu CG, Shu CJ, Nair-Gill E, et al. Molecular imaging of lymphoid organs and immune activation using positron emission tomography with a new  $^{18}\text{F}$ -labeled 2'-deoxycytidine analog. *Nat Med*. 2008;14:783-788.
154. Artin E, Wang J, Lohman GJS, et al. Insight into the Mechanism of Inactivation of Ribonucleotide Reductase by Gemcitabine 5'-Diphosphate in the Presence or Absence of Reductant. *Biochemistry*. 2009;48:11622-11629.
155. Gens TA, Wethington JA, Brosi AR. The Exchange of  $\text{F}^{18}$  between Metallic Fluorides and Silicon Tetrafluoride. *The Journal of Physical Chemistry*. 1958;62:1593-1593.
156. Winfield JM. Preparation and use of  $^{18}\text{F}$ -fluorine labelled inorganic compounds. *Journal of Fluorine Chemistry*. 1980;16:1-17.

157. Rosenthal MS, Bosch AL, Nickles RJ, Gatley SJ. Synthesis and some characteristics of no-carrier added [<sup>18</sup>F]fluorotrimethylsilane. *The International Journal of Applied Radiation and Isotopes*. 1985;36:318-319.
158. Dialer LO, Selivanova SV, Müller CJ, et al. Studies toward the Development of New Silicon-Containing Building Blocks for the Direct <sup>18</sup>F-Labeling of Peptides. *J Med Chem*. 2013;56:7552-7563.
159. Mu L, Höhne A, Schubiger PA, et al. Silicon-Based Building Blocks for One-Step <sup>18</sup>F-Radiolabeling of Peptides for PET Imaging. *Angewandte Chemie International Edition*. 2008;47:4922-4925.
160. Schirmacher R, Bradtmöller G, Schirmacher E, et al. <sup>18</sup>F-Labeling of Peptides by means of an Organosilicon-Based Fluoride Acceptor. *Angewandte Chemie International Edition*. 2006;45:6047-6050.
161. Schulz J, Vimont D, Bordenave T, et al. Silicon-Based Chemistry: An Original and Efficient One-Step Approach to [<sup>18</sup>F]-Nucleosides and [<sup>18</sup>F]-Oligonucleotides for PET Imaging. *Chem Eur J*. 2011;17:3096-3100.
162. Jordheim LP, Cros E, Gouy M-H, et al. Characterization of a Gemcitabine-Resistant Murine Leukemic Cell Line. *Clinical Cancer Research*. 2004;10:5614-5621.
163. Cividini F, Filoni DN, Pesi R, Allegrini S, Camici M, Tozzi MG. IMP–GMP specific cytosolic 5'-nucleotidase regulates nucleotide pool and prodrug metabolism. *Biochimica et Biophysica Acta (BBA) - General Subjects*. 2015;1850:1354-1361.
164. Sigmond J, Honeywell RJ, Postma TJ, et al. Gemcitabine uptake in glioblastoma multiforme: potential as a radiosensitizer. *Annals of Oncology*. 2009;20:182-187.
165. Mahfouz RZ, Jankowska A, Ebrahim Q, et al. Increased CDA Expression/Activity in Males Contributes to Decreased Cytidine Analog Half-Life and Likely Contributes to Worse Outcomes with 5-Azacytidine or Decitabine Therapy. *Clin Cancer Res*. 2013;19:938-948.
166. Zauri M, Berridge G, Thézénas M-L, et al. CDA directs metabolism of epigenetic nucleosides revealing a therapeutic window in cancer. *Nature*. 2015;524:114-118.
167. Ebrahim Q, Mahfouz R, Ng KP, Sauntharajah Y. High cytidine deaminase expression in the liver provides sanctuary for cancer cells from decitabine treatment effects. *Oncotarget*. 2012;3:1137-1145.
168. Weizman N, Krelin Y, Shabtay-Orbach A, et al. Macrophages mediate gemcitabine resistance of pancreatic adenocarcinoma by upregulating cytidine deaminase. *Oncogene*. 2014;33:3812-3819.
169. Krajewska E, Shugar D. Alkylated cytosine nucleosides: substrate and inhibitor properties in enzymatic deamination. *Acta Biochim Pol*. 1975;22:185-194.

170. Ménard-Moyon C, Ali-Boucetta H, Fabbro C, Chaloin O, Kostarelos K, Bianco A. Controlled Chemical Derivatisation of Carbon Nanotubes with Imaging, Targeting, and Therapeutic Capabilities. *Chemistry – A European Journal*. 2015;21:14886-14892.
171. Aboagye EO, Price PM, Jones T. In vivo pharmacokinetics and pharmacodynamics in drug development using positron-emission tomography. *Drug Discovery Today*. 2001;6:293-302.
172. Ambrosini V, Quarta C, Nanni C, et al. Small Animal PET in Oncology: The Road from Bench to Bedside. *Cancer Biotherapy & Radiopharmaceuticals*. 2009;24:277-285.
173. Ciernik F, Dizendorf E, Baumert B, et al. Radiation Treatment Planning with an Integrated Positron Emission and Computer Tomography (PET/CT): A Feasibility Study. *International Journal of Radiation Oncology Biology Physics*. 2003;57:853-863.
174. Kitson S, Cuccurullo V, Ciarmiello A, Salvo D, Mansi L. Clinical Applications of Positron Emission Tomography (PET) Imaging in Medicine: Oncology, Brain Diseases and Cardiology. *Current Radiopharmaceuticals*. 2009;2:224-253.
175. Phelps ME. PET: The Merging of Biology and Imaging into Molecular Imaging. *J Nucl Med*. 2000;41:661-681.
176. Sergeev M, Lazari M, Morgia F, et al. Performing radiosynthesis in microvolumes to maximize molar activity of tracers for positron emission tomography. *Communications Chemistry*. 2018;1:10.
177. Chao PH, Wang J, Van Dam RM. A fully automated radiosynthesis platform for scalable production and purification of PET tracers. In: Proceedings of the 22nd International Conference on Miniaturized Systems for Chemistry and Life Sciences. Kaohsiung, Taiwan: Royal Society of Chemistry; 2018:1155-1158.
178. Rensch C, Jackson A, Lindner S, et al. Microfluidics: A Groundbreaking Technology for PET Tracer Production? *Molecules*. 2013;18:7930-7956.
179. Miller PW, deMello AJ, Gee AD. Application of Microfluidics to the Ultra-Rapid Preparation of Fluorine-18 Labelled Compounds. *Current Radiopharmaceuticals*. 2010;3:254-262.
180. Pascali G, Matesic L. How Far Are We from Dose On Demand of Short-Lived Radiopharmaceuticals? In: Kuge Y, Shiga T, Tamaki N, eds. Perspectives on Nuclear Medicine for Molecular Diagnosis and Integrated Therapy. Springer Japan; 2016:79-92.
181. Dooraghi AA, Keng PY, Chen S, et al. Optimization of microfluidic PET tracer synthesis with Cerenkov imaging. *Analyst*. 2013;138:5654-5664.
182. Elizarov AM, van Dam RM, Shin YS, et al. Design and Optimization of Coin-Shaped Microreactor Chips for PET Radiopharmaceutical Synthesis. *J Nucl Med*. 2010;51:282-287.

183. Keng PY, Sergeev M, van Dam RM. Advantages of Radiochemistry in Microliter Volumes. In: Kuge Y, Shiga T, Tamaki N, eds. *Perspectives on Nuclear Medicine for Molecular Diagnosis and Integrated Therapy*. Springer Japan; 2016:93-111.
184. Iwata R, Pascali C, Terasaki K, Ishikawa Y, Furumoto S, Yanai K. Practical microscale one-pot radiosynthesis of <sup>18</sup>F-labeled probes. *Journal of Labelled Compounds and Radiopharmaceuticals*. 2018;61:540-549.
185. Wester HJ, Herz M, Weber W, et al. Synthesis and Radiopharmacology of O-(2-[<sup>18</sup>F]fluoroethyl)-L-Tyrosine for Tumor Imaging. *J Nucl Med*. 1999;40:205-212.
186. Yanai A, Harada R, Iwata R, et al. Site-Specific Labeling of F-18 Proteins Using a Supplemented Cell-Free Protein Synthesis System and O-2-[<sup>18</sup>F]Fluoroethyl-L-Tyrosine: [<sup>18</sup>F]FET-HER2 Affibody Molecule. *Mol Imaging Biol*. 2019;21:529-537.
187. Bourdier T, Greguric I, Roselt P, Jackson T, Faragalla J, Katsifis A. Fully automated one-pot radiosynthesis of O-(2-[<sup>18</sup>F]fluoroethyl)-L-tyrosine on the TracerLab FXFN module. *Nuclear Medicine and Biology*. 2011;38:645-651.
188. Bouvet V, Wuest M, Tam P-H, Wang M, Wuest F. Microfluidic technology: an economical and versatile approach for the synthesis of O-(2-[<sup>18</sup>F]fluoroethyl)-L-tyrosine ([<sup>18</sup>F]FET). *Bioorg Med Chem Lett*. 2012;22:2291-2295.
189. Lakshminarayanan N, Kumar A, Roy S, Pawar Y, Chaudhari PR, Rajan MGR. Fully automated synthesis of O-(2'-[<sup>18</sup>F]fluoroethyl)-L-tyrosine ([<sup>18</sup>F]FET) using solid phase extraction (SPE) purification with neutral alumina. *J Radioanal Nucl Chem*. June 2016:1-9.
190. Hamacher K, Coenen HH. Efficient routine production of the <sup>18</sup>F-labelled amino acid O-(2-[<sup>18</sup>F]fluoroethyl)-L-tyrosine. *Applied Radiation and Isotopes*. 2002;57:853-856.
191. Ly J, Ha NS, Cheung S, van Dam RM. Toward miniaturized analysis of chemical identity and purity of radiopharmaceuticals via microchip electrophoresis. *Anal Bioanal Chem*. 2018;410:2423-2436.
192. Taschereau R, Vu NT, Chatziioannou AF. Calibration and data standardization of a prototype bench-top preclinical CT. In: 2014 IEEE Nuclear Science Symposium and Medical Imaging Conference (NSS/MIC). ; 2014:1-2.
193. Kuik W-J, Kema IP, Brouwers AH, et al. In Vivo Biodistribution of No-Carrier-Added 6-<sup>18</sup>F-Fluoro-3,4-Dihydroxy-L-Phenylalanine (<sup>18</sup>F-DOPA), Produced by a New Nucleophilic Substitution Approach, Compared with Carrier-Added <sup>18</sup>F-DOPA, Prepared by Conventional Electrophilic Substitution. *J Nucl Med*. 2015;56:106-112.
194. Langen K-J, Hamacher K, Weckesser M, et al. O-(2-[<sup>18</sup>F]fluoroethyl)-L-tyrosine: uptake mechanisms and clinical applications. *Nuclear Medicine and Biology*. 2006;33:287-294.
195. Heiss P, Mayer S, Herz M, Wester H-J, Schwaiger M, Senekowitsch-Schmidtke R. Investigation of Transport Mechanism and Uptake Kinetics of O-(2-[<sup>18</sup>F]Fluoroethyl)-L-Tyrosine In Vitro and In Vivo. *J Nucl Med*. 1999;40:1367-1373.

196. Langen K-J, Jarosch M, Mühlensiepen H, et al. Comparison of fluorotyrosines and methionine uptake in F98 rat gliomas. *Nuclear Medicine and Biology*. 2003;30:501-508.
197. Hardy J, Selkoe DJ. The amyloid hypothesis of Alzheimer's disease: progress and problems on the road to therapeutics. *Science*. 2002;297:353-356.
198. Ossenkoppele R, Jansen WJ, Rabinovici GD, et al. Prevalence of Amyloid PET Positivity in Dementia Syndromes: A Meta-analysis. *JAMA*. 2015;313:1939-1950.
199. Klunk WE, Engler H, Nordberg A, et al. Imaging brain amyloid in Alzheimer's disease with Pittsburgh Compound-B. *Annals of Neurology*. 2004;55:306-319.
200. Yeo JM, Waddell B, Khan Z, Pal S. A systematic review and meta-analysis of 18F-labeled amyloid imaging in Alzheimer's disease. *Alzheimers Dement (Amst)*. 2015;1:5-13.
201. Zhang W, Oya S, Kung M-P, Hou C, Maier DL, Kung HF. F-18 Polyethyleneglycol stilbenes as PET imaging agents targeting A $\beta$  aggregates in the brain. *Nuclear Medicine and Biology*. 2005;32:799-809.
202. Brendel M, Probst F, Jaworska A, et al. Glial Activation and Glucose Metabolism in a Transgenic Amyloid Mouse Model: A Triple-Tracer PET Study. *J Nucl Med*. 2016;57:954-960.
203. Brendel M, Jaworska A, Overhoff F, et al. Efficacy of chronic BACE1 inhibition in PS2APP mice depends on the regional A $\beta$  deposition rate and plaque burden at treatment initiation. *Theranostics*. 2018;8:4957-4968.
204. Sabri O, Seibyl J, Rowe C, Barthel H. Beta-amyloid imaging with florbetaben. *Clin Transl Imaging*. 2015;3:13-26.
205. Blume T, Focke C, Peters F, et al. Microglial response to increasing amyloid load saturates with aging: a longitudinal dual tracer in vivo  $\mu$ PET-study. *J Neuroinflammation*. 2018;15:307.
206. Rominger A, Brendel M, Burgold S, et al. Longitudinal Assessment of Cerebral  $\beta$ -Amyloid Deposition in Mice Overexpressing Swedish Mutant  $\beta$ -Amyloid Precursor Protein Using 18F-Florbetaben PET. *J Nucl Med*. 2013;54:1127-1134.
207. Sacher C, Blume T, Beyer L, et al. Longitudinal PET Monitoring of Amyloidosis and Microglial Activation in a Second-Generation Amyloid- $\beta$  Mouse Model. *J Nucl Med*. 2019;60:1787-1793.
208. Kung M-P, Kung HF. Mass effect of injected dose in small rodent imaging by SPECT and PET. *Nuclear Medicine and Biology*. 2005;32:673-678.
209. Snellman A, Rokka J, López-Picón FR, et al. In vivo PET imaging of beta-amyloid deposition in mouse models of Alzheimer's disease with a high specific activity PET imaging agent [18F]flutemetamol. *EJNMMI Res*. 2014;4:37.

210. Maeda J, Ji B, Irie T, et al. Longitudinal, Quantitative Assessment of Amyloid, Neuroinflammation, and Anti-Amyloid Treatment in a Living Mouse Model of Alzheimer's Disease Enabled by Positron Emission Tomography. *J Neurosci.* 2007;27:10957-10968.
211. Javed MR, Chen S, Lei J, et al. High yield and high specific activity synthesis of [<sup>18</sup>F]fallypride in a batch microfluidic reactor for micro-PET imaging. *Chem Commun.* 2014;50:1192-1194.
212. Wang J, Holloway T, Lisova K, Dam RM van. Green and efficient synthesis of the radiopharmaceutical [<sup>18</sup>F]FDOPA using a microdroplet reactor. *React Chem Eng.* December 2019.
213. Kim H-K, Rashed Javed M, Chen S, et al. On-demand radiosynthesis of N -succinimidyl-4-[<sup>18</sup>F]fluorobenzoate ([<sup>18</sup>F]SFB) on an electrowetting-on-dielectric microfluidic chip for 18 F-labeling of protein. *RSC Adv.* 2019;9:32175-32183.
214. Fiel SA, Yang H, Schaffer P, et al. Magnetic Droplet Microfluidics as a Platform for the Concentration of [<sup>18</sup>F]Fluoride and Radiosynthesis of Sulfonyl [<sup>18</sup>F]Fluoride. *ACS Appl Mater Interfaces.* 2015;7:12923-12929.
215. Patt M, Schildan A, Barthel H, et al. Metabolite analysis of [<sup>18</sup>F]Florbetaben (BAY 94-9172) in human subjects: a substudy within a proof of mechanism clinical trial. *J Radioanal Nucl Chem.* 2010;284:557-562.
216. Wang H, Guo X, Jiang S, Tang G. Automated synthesis of [<sup>18</sup>F]Florbetaben as Alzheimer's disease imaging agent based on a synthesis module system. *Applied Radiation and Isotopes.* 2013;71:41-46.
217. Rowe CC, Ackerman U, Browne W, et al. Imaging of amyloid  $\beta$  in Alzheimer's disease with 18F-BAY94-9172, a novel PET tracer: proof of mechanism. *The Lancet Neurology.* 2008;7:129-135.
218. Wang J, Rios A, Lisova K, Slavik R, Chatziioannou AF, van Dam RM. High-throughput radio-TLC analysis. *Nuclear Medicine and Biology.* 2020;82-83:41-48.
219. Collins J, Waldmann CM, Drake C, et al. Production of diverse PET probes with limited resources: 24 <sup>18</sup>F-labeled compounds prepared with a single radiosynthesizer. *PNAS.* 2017;114:11309–11314.
220. Wang H, Shi H, Yu H, Jiang S, Tang G. Facile and rapid one-step radiosynthesis of [<sup>18</sup>F]BAY94-9172 with a new precursor. *Nuclear Medicine and Biology.* 2011;38:121-127.
221. Brendel M, Jaworska A, Grießinger E, et al. Cross-Sectional Comparison of Small Animal [<sup>18</sup>F]-Florbetaben Amyloid-PET between Transgenic AD Mouse Models. *PLOS ONE.* 2015;10:e0116678.
222. Scott PJH, Hockley BG, Kung HF, Manchanda R, Zhang W, Kilbourn MR. Studies into Radiolytic Decomposition of Fluorine-18 Labeled Radiopharmaceuticals for Positron Emission Tomography. *Appl Radiat Isot.* 2009;67:88-94.

223. Dunet V, Pomoni A, Hottinger A, Nicod-Lalonde M, Prior JO. Performance of 18F-FET versus 18F-FDG-PET for the diagnosis and grading of brain tumors: systematic review and meta-analysis. *Neuro-oncology*. 2016;18:426-434.
224. Raccagni I, Belloli S, Valtorta S, et al. [18F]FDG and [18F]FLT PET for the evaluation of response to neo-adjuvant chemotherapy in a model of triple negative breast cancer. *PLOS ONE*. 2018;13:e0197754.
225. Cerami C, Iaccarino L, Perani D. Molecular Imaging of Neuroinflammation in Neurodegenerative Dementias: The Role of In Vivo PET Imaging. *International Journal of Molecular Sciences*. 2017;18:993.
226. Chiaravalloti A, Danieli R, Lacanfora A, Palumbo B, Caltagirone C, Schillaci O. Usefulness of 18F Flortbetaben in Diagnosis of Alzheimer's Disease and Other Types of Dementia. <https://www.ingentaconnect.com/contentone/ben/car/2017/00000014/00000002/art00005>.
227. Juneau Daniel, Golfam Mohammad, Hazra Samir, et al. Positron Emission Tomography and Single-Photon Emission Computed Tomography Imaging in the Diagnosis of Cardiac Implantable Electronic Device Infection. *Circulation: Cardiovascular Imaging*. 2017;10:e005772.
228. Granados U, Fuster D, Pericas JM, et al. Diagnostic Accuracy of 18F-FDG PET/CT in Infective Endocarditis and Implantable Cardiac Electronic Device Infection: A Cross-Sectional Study. *J Nucl Med*. 2016;57:1726-1732.
229. Colombo I, Overchuk M, Chen J, Reilly RM, Zheng G, Lheureux S. Molecular imaging in drug development: Update and challenges for radiolabeled antibodies and nanotechnology. *Methods*. 2017;130:23-35.
230. Naganawa M, Gallezot J-D, Rossano S, Carson RE. Quantitative PET Imaging in Drug Development: Estimation of Target Occupancy. *Bull Math Biol*. 2019;81:3508-3541.
231. Yaghoubi SS, Campbell DO, Radu CG, Czernin J. Positron Emission Tomography Reporter Genes and Reporter Probes: Gene and Cell Therapy Applications. *Theranostics*. 2012;2:374-391.
232. Challapalli A, Aboagye EO. Positron Emission Tomography Imaging of Tumor Cell Metabolism and Application to Therapy Response Monitoring. *Front Oncol*. 2016;6:44.
233. Martinez O, Sosabowski J, Maher J, Papa S. New Developments in Imaging Cell-Based Therapy. *J Nucl Med*. 2019;60:730-735.
234. Molecular Imaging and Contrast Agent Database (MICAD). Bethesda (MD): National Center for Biotechnology Information (US); 2004.
235. Radiosynthesis Database of PET Probes (RaDaP). <http://www.nirs.qst.go.jp/research/division/mic/db2/>.

236. Frank C, Winter G, Rensei F, et al. Development and implementation of ISAR, a new synthesis platform for radiopharmaceutical production. *EJNMMI radiopharm chem.* 2019;4:24.
237. Zhang X, Liu F, Payne AC, Nickels ML, Bellan LM, Manning HC. High-Yielding Radiosynthesis of [68Ga]Ga-PSMA-11 Using a Low-Cost Microfluidic Device. *Mol Imaging Biol.* July 2020.
238. Frank C, Winter G, Rensei F, et al. Enhancing radiotracer development: Channel routing on ISAR without single fluid bus constraint. *J Nucl Med.* 2018;59:671-671.
239. Awasthi V, Watson J, Gali H, et al. A “dose on demand” Biomarker Generator for automated production of [18F]F- and [18F]FDG. *Applied Radiation and Isotopes.* 2014;89:167-175.
240. Liang SH, Yokell DL, Normandin MD, et al. First Human Use of a Radiopharmaceutical Prepared by Continuous-Flow Microfluidic Radiofluorination: Proof of Concept with the Tau Imaging Agent [18F]T807. *Mol Imaging.* 2014;13:1-5.
241. Liang SH, Yokell DL, Jackson RN, et al. Microfluidic continuous-flow radiosynthesis of [18F]FPEB suitable for human PET imaging. *Med Chem Commun.* 2014;5:432-435.
242. Akula MR, Collier TL, Blevins DW, Kabalka GW, Osborne D. Sequential Preparation of [18F]FLT and [18F]FMISO Employing Advion NanoTek® Microfluidic Synthesis System. *Advances in Molecular Imaging.* 2019;9:53-59.
243. Zheng M-Q, Collier L, Bois F, et al. Synthesis of [18F]FMISO in a flow-through microfluidic reactor: Development and clinical application. *Nuclear Medicine and Biology.* 2015;42:578-584.
244. Chen S, Javed MR, Kim H-K, et al. Radiolabelling diverse positron emission tomography (PET) tracers using a single digital microfluidic reactor chip. *Lab Chip.* 2014;14:902-910.
245. Lisova K, Wang J, Rios A, van Dam RM. Adaptation and optimization of [F-18] Florbetaben ([F-18] FBB) radiosynthesis to a microdroplet reactor. In: *Journal of Labelled Compounds & Radiopharmaceuticals.* Vol 62. WILEY 111 RIVER ST, HOBOKEN 07030-5774, NJ USA; 2019:S353-S354.
246. Kuntzsch M, Lamparter D, Bruggener N, Muller M, Kienzle GJ, Reischl G. Development and Successful Validation of Simple and Fast TLC Spot Tests for Determination of Kryptofix® 2.2.2 and Tetrabutylammonium in 18F-Labeled Radiopharmaceuticals. *Pharmaceuticals (Basel).* 2014;7:621-633.
247. Halvorsen NE, Kvernenes OH. A Fast and Simple Method for the Determination of TBA in 18F-Labeled Radiopharmaceuticals. *Pharmaceuticals.* 2020;13:27.
248. Fermi E. Quality Control of PET Radiopharmaceuticals. In: *Molecular Imaging: Radiopharmaceuticals for PET and SPECT.* Springer Berlin Heidelberg; 2009:197-204.
249. Scott PJH, Hockley BG. *Radiochemical Syntheses, Radiopharmaceuticals for Positron Emission Tomography.* Hoboken, NJ, USA: John Wiley & Sons; 2011.



250. U.S. Pharmacopeia (USP). General Chapter <823>: Positron Emission Tomography Drugs for Compounding, Investigation, and Research Uses. November 2011.
251. European directorate for the quality of medicines & healthcare. "Unfair" regulatory stance on radiotracers poses threat to PET's future. AuntMinnie.com. <http://www.auntminnie.com/index.aspx?sec=ser&sub=def&pag=dis&itemid=102799>.
252. Lodi F, Boschi S. Quality Control of PET Radiopharmaceuticals. In: Basic Science of PET Imaging. Springer, Cham; 2017:105-126.
253. Koag MC, Kim H-K, Kim AS. Efficient microscale synthesis of [18F]-2-fluoro-2-deoxy-d-glucose. *Chemical Engineering Journal*. 2014;258:62-68.
254. Koag MC, Kim H-K, Kim AS. Fast and efficient microscale radiosynthesis of 3'-deoxy-3'-[18F]fluorothymidine. *Journal of Fluorine Chemistry*. 2014;166:104-109.
255. Badawi RD, Shi H, Hu P, et al. First Human Imaging Studies with the Explorer Total-Body Pet Scanner. *J Nucl Med*. February 2019;jnumed.119.226498.
256. Wang J, van Dam RM. High-Efficiency Production of Radiopharmaceuticals via Droplet Radiochemistry: A Review of Recent Progress. *Mol Imaging*. 2020;19:1536012120973099.
257. Bockisch A, Freudenberg LS, Schmidt D, Kuwert T. Hybrid Imaging by SPECT/CT and PET/CT: Proven Outcomes in Cancer Imaging. *Seminars in Nuclear Medicine*. 2009;39:276-289.
258. Laforest R, Liu X. Image quality with non-standard nuclides in PET. *Q J Nucl Med Mol Imaging*. 2008;52:151-158.
259. Kemerink GJ, Visser MGW, Franssen R, et al. Effect of the positron range of <sup>18</sup>F, <sup>68</sup>Ga and <sup>124</sup>I on PET/CT in lung-equivalent materials. *Eur J Nucl Med Mol Imaging*. 2011;38:940-948.
260. Rischin D, Hicks RJ, Fisher R, et al. Prognostic Significance of [18F]-Misonidazole Positron Emission Tomography–Detected Tumor Hypoxia in Patients With Advanced Head and Neck Cancer Randomly Assigned to Chemoradiation With or Without Tirapazamine: A Substudy of Trans-Tasman Radiation Oncology Group Study 98.02. *JCO*. 2006;24:2098-2104.
261. Chang JM, Lee HJ, Goo JM, et al. False Positive and False Negative FDG-PET Scans in Various Thoracic Diseases. *Korean Journal of Radiology*. 2006;7:57-69.
262. Strauss LG. Fluorine-18 deoxyglucose and false-positive results: a major problem in the diagnostics of oncological patients. *Eur J Nucl Med*. 1996;23:1409-1415.
263. Newton-Northup JR, Figueroa SD, Deutscher SL. Streamlined in vivo selection and screening of human prostate carcinoma avid phage particles for development of peptide based in vivo tumor imaging agents. *Comb Chem High Throughput Screen*. 2011;14:9-21.

264. Xiao W, Wang Y, Lau EY, et al. The Use of One-Bead One-Compound Combinatorial Library Technology to Discover High-Affinity  $\alpha v \beta 3$  Integrin and Cancer Targeting Arginine-Glycine-Aspartic Acid Ligands with a Built-in Handle. *Mol Cancer Ther.* 2010;9:2714-2723.
265. Lee S, Xie J, Chen X. Peptide-Based Probes for Targeted Molecular Imaging. *Biochemistry.* 2010;49:1364-1376.
266. Hong H, Goel S, Zhang Y, Cai W. Molecular Imaging with Nucleic Acid Aptamers. *Curr Med Chem.* 2011;18:4195-4205.
267. Gong P, Shi B, Zheng M, et al. PEI protected aptamer molecular probes for contrast-enhanced in vivo cancer imaging. *Biomaterials.* 2012;33:7810-7817.
268. Gagnon MKJ, Hausner SH, Marik J, Abbey CK, Marshall JF, Sutcliffe JL. High-throughput in vivo screening of targeted molecular imaging agents. *Proc Natl Acad Sci U S A.* 2009;106:17904-17909.
269. Mansi L, Virgolini I. Diagnosis and therapy are walking together on radiopeptides' avenue. *Eur J Nucl Med Mol Imaging.* 2011;38:605-612.
270. Banerjee SR, Pomper MG. Clinical applications of Gallium-68. *Applied Radiation and Isotopes.* 2013;76:2-13.
271. Avril N, Menzel M, Dose J, et al. Glucose Metabolism of Breast Cancer Assessed by  $^{18}\text{F}$ -FDG PET: Histologic and Immunohistochemical Tissue Analysis. *J Nucl Med.* 2001;42:9-16.
272. Alberini J-L, Edeline V, Giraudet AL, et al. Single photon emission tomography/computed tomography (SPET/CT) and positron emission tomography/computed tomography (PET/CT) to image cancer. *J Surg Oncol.* 2011;103:602-606.
273. Pecking AP, Bellet D, Alberini JL. Immuno-SPET/CT and immuno-PET/CT: a step ahead to translational imaging. *Clin Exp Metastasis.* 2012;29:847-852.
274. Öberg K. Diagnostic work-up of gastroenteropancreatic neuroendocrine tumors. *Clinics (Sao Paulo).* 2012;67:109-112.
275. Kwekkeboom DJ, Kam BL, Essen M van, et al. Somatostatin receptor-based imaging and therapy of gastroenteropancreatic neuroendocrine tumors. *Endocr Relat Cancer.* 2010;17:R53-R73.
276. Walker RC, Smith GT, Liu E, Moore B, Clanton J, Stabin M. Measured Human Dosimetry of  $^{68}\text{Ga}$ -DOTATATE. *J Nucl Med.* 2013;54:855-860.
277. Vliet EI van, Teunissen JJM, Kam BLR, Jong M de, Krenning EP, Kwekkeboom DJ. Treatment of Gastroenteropancreatic Neuroendocrine Tumors with Peptide Receptor Radionuclide Therapy. *NEN.* 2013;97:74-85.

278. Singla S, Gupta S, Reddy RM, Durgapal P, Bal CS.  $^{68}\text{Ga}$ -DOTA-NOC PET and Peptide Receptor Radionuclide Therapy in Management of Bilateral Ovarian Metastases from Gastrointestinal Carcinoid. *Jpn J Clin Oncol*. 2012;42:1202-1206.
279. Yu Z, Ananias HJK, Carlucci G, et al. An update of radiolabeled bombesin analogs for gastrin-releasing peptide receptor targeting. *Curr Pharm Des*. 2013;19:3329-3341.
280. Müller C. Folate-Based Radiotracers for PET Imaging—Update and Perspectives. *Molecules*. 2013;18:5005-5031.
281. Betzel T, Müller C, Groehn V, et al. Radiosynthesis and Preclinical Evaluation of 3'-Aza-2'-[ $^{18}\text{F}$ ]fluorofolic Acid: A Novel PET Radiotracer for Folate Receptor Targeting. *Bioconjugate Chem*. 2013;24:205-214.
282. Fischer CR, Müller C, Reber J, et al. [ $^{18}\text{F}$ ]Fluoro-Deoxy-Glucose Folate: A Novel PET Radiotracer with Improved in Vivo Properties for Folate Receptor Targeting. *Bioconjugate Chem*. 2012;23:805-813.
283. Muller C. Folate based radiopharmaceuticals for imaging and therapy of cancer and inflammation. *Curr Pharm Des*. 2012;18:1058-1083.
284. Sega EI, Low PS. Tumor detection using folate receptor-targeted imaging agents. *Cancer Metastasis Rev*. 2008;27:655.
285. Low PS, Henne WA, Doorneweerd DD. Discovery and Development of Folic-Acid-Based Receptor Targeting for Imaging and Therapy of Cancer and Inflammatory Diseases. *Acc Chem Res*. 2008;41:120-129.
286. Wan W, Guo N, Pan D, et al. First Experience of  $^{18}\text{F}$ -Alfatide in Lung Cancer Patients Using a New Lyophilized Kit for Rapid Radiofluorination. *J Nucl Med*. 2013;54:691-698.
287. Choi H, Phi JH, Paeng JC, et al. Imaging of Integrin  $\alpha\text{v}\beta\text{3}$  Expression Using  $^{68}\text{Ga}$ -RGD Positron Emission Tomography in Pediatric Cerebral Infarct. *Mol Imaging*. 2013;12:7290.2012.00036.
288. Beer AJ, Haubner R, Sarbia M, et al. Positron Emission Tomography Using [ $^{18}\text{F}$ ]Galacto-RGD Identifies the Level of Integrin  $\alpha\text{v}\beta\text{3}$  Expression in Man. *Clin Cancer Res*. 2006;12:3942-3949.
289. Vlahov IR, Leamon CP. Engineering Folate–Drug Conjugates to Target Cancer: From Chemistry to Clinic. *Bioconjugate Chem*. 2012;23:1357-1369.
290. Teng L, Xie J, Teng L, Lee RJ. Clinical translation of folate receptor-targeted therapeutics. *Expert Opin Drug Deliv*. 2012;9:901-908.
291. Pozsgai E, Schally AV, Halmos G, Rick F, Bellyei S. The Inhibitory Effect of a Novel Cytotoxic Somatostatin Analogue AN-162 on Experimental Glioblastoma. *Horm Metab Res*. 2010;42:781-786.

292. Hohla F, Buchholz S, Schally AV, et al. Targeted cytotoxic somatostatin analog AN-162 inhibits growth of human colon carcinomas and increases sensitivity of doxorubicin resistant murine leukemia cells. *Cancer Letters*. 2010;294:35-42.
293. Hanaoka H, Tominaga H, Yamada K, et al. Evaluation of <sup>64</sup>Cu-labeled DOTA-D-Phe(1)-Tyr(3)-octreotide (<sup>64</sup>Cu-DOTA-TOC) for imaging somatostatin receptor-expressing tumors. *Ann Nucl Med*. 2009;23:559-567.
294. Boswell CA, Sun X, Niu W, et al. Comparative in Vivo Stability of Copper-64-Labeled Cross-Bridged and Conventional Tetraazamacrocyclic Complexes. *J Med Chem*. 2004;47:1465-1474.
295. Bass LA, Wang M, Welch MJ, Anderson CJ. In Vivo Transchelation of Copper-64 from TETA-Octreotide to Superoxide Dismutase in Rat Liver. *Bioconjugate Chem*. 2000;11:527-532.
296. Zhan C-G, Dixon DA. Hydration of the Fluoride Anion: Structures and Absolute Hydration Free Energy from First-Principles Electronic Structure Calculations. *J Phys Chem A*. 2004;108:2020-2029.
297. Cai L, Lu S, Pike VW. Chemistry with [<sup>18</sup>F]Fluoride Ion. *European Journal of Organic Chemistry*. 2008;2008:2853-2873.
298. Niedermoser S, Chin J, Wängler C, et al. In Vivo Evaluation of <sup>18</sup>F-SiFAlin-Modified TATE: A Potential Challenge for <sup>68</sup>Ga-DOTATATE, the Clinical Gold Standard for Somatostatin Receptor Imaging with PET. *J Nucl Med*. 2015;56:1100-1105.
299. McBride WJ, Sharkey RM, Karacay H, et al. A Novel Method of <sup>18</sup>F Radiolabeling for PET. *J Nucl Med*. 2009;50:991-998.
300. Laverman P, D'Souza CA, Eek A, et al. Optimized labeling of NOTA-conjugated octreotide with F-18. *Tumor Biol*. 2012;33:427-434.
301. McBride WJ, Sharkey RM, Goldenberg DM. Radiofluorination using aluminum-fluoride (Al<sup>18</sup>F). *EJNMMI Research*. 2013;3:36.
302. Liu Z, Li Y, Lozada J, et al. Stoichiometric Leverage: Rapid <sup>18</sup>F-Aryltrifluoroborate Radiosynthesis at High Specific Activity for Click Conjugation. *Angewandte Chemie International Edition*. 2013;52:2303-2307.
303. Liu Z, Pourghiasian M, Bénard F, Pan J, Lin K-S, Perrin DM. Preclinical Evaluation of a High-Affinity <sup>18</sup>F-Trifluoroborate Octreotate Derivative for Somatostatin Receptor Imaging. *J Nucl Med*. 2014;55:1499-1505.
304. Herrmann K, Czernin J, Wolin EM, et al. Impact of <sup>68</sup>Ga-DOTATATE PET/CT on the Management of Neuroendocrine Tumors: The Referring Physician's Perspective. *J Nucl Med*. 2015;56:70-75.
305. Elizarov AM, van Dam RM, Shin YS, et al. Design and Optimization of Coin-Shaped Microreactor Chips for PET Radiopharmaceutical Synthesis. *J Nucl Med*. 2010;51:282-287.

306. Liu Z, Lin K-S, Bénard F, et al. One-step <sup>18</sup>F labeling of biomolecules using organotrifluoroborates. *Nat Protocols*. 2015;10:1423-1432.
307. Ory D, Van den Brande J, de Groot T, et al. Retention of [<sup>18</sup>F]fluoride on reversed phase HPLC columns. *Journal of Pharmaceutical and Biomedical Analysis*. 2015;111:209-214.
308. Loening AM, Gambhir SS. AMIDE: a free software tool for multimodality medical image analysis. *Mol Imaging*. 2003;2:131-137.
309. Repetto-Llamazares AHV, Larsen RH, Mollatt C, Lassmann M, Dahle J. Biodistribution and Dosimetry of <sup>177</sup>Lu-tetumomab, a New Radioimmunoconjugate for Treatment of Non-Hodgkin Lymphoma. *Curr Radiopharm*. 2013;6:20-27.
310. Sparks RB, Aydogan B. Comparison of the Effectiveness of Some Common Animal Data Scaling Techniques in Estimating Human Radiation Dose. In: Proceedings of the Sixth International Radiopharmaceutical Dosimetry Symposium. Gatlinburg, TN: Oak Ridge Associated Universities, TN (United States); 1996:705-716.
311. Kletting P, Schimmel S, Kestler HA, et al. Molecular radiotherapy: The NUKFIT software for calculating the time-integrated activity coefficient. *Med Phys*. 2013;40:102504.
312. Stabin MG, Sparks RB, Crowe E. OLINDA/EXM: The Second-Generation Personal Computer Software for Internal Dose Assessment in Nuclear Medicine. *J Nucl Med*. 2005;46:1023-1027.
313. A. Bitar, A. Lisbona, M. Bardiès. S-factor calculations for mouse models using Monte-Carlo simulations. *Quart J Nucl Med Mol Imag*. 2007;51:343-351.
314. Bruns C, Raulf F, Hoyer D, Schloos J, Lübbert H, Weckbecker G. Binding properties of somatostatin receptor subtypes. *Metabolism*. 1996;45:17-20.
315. Yamada Y, Post SR, Wang K, Tager HS, Bell GI, Seino S. Cloning and functional characterization of a family of human and mouse somatostatin receptors expressed in brain, gastrointestinal tract, and kidney. *PNAS*. 1992;89:251-255.
316. Dubash SR, Keat N, Mapelli P, et al. Clinical Translation of a Click-Labeled <sup>18</sup>F-Octreotate Radioligand for Imaging Neuroendocrine Tumors. *J Nucl Med*. 2016;57:1207-1213.
317. Keng PY, Esterby M, van Dam RM. Emerging Technologies for Decentralized Production of PET Tracers. In: Hsieh C-H, ed. Positron Emission Tomography - Current Clinical and Research Aspects. Rijeka, Croatia: InTech; 2012:153-182.
318. Pourghiasian M, Liu Z, Pan J, et al. <sup>18</sup>F-AmBF3-MJ9: A novel radiofluorinated bombesin derivative for prostate cancer imaging. *Bioorganic & Medicinal Chemistry*. 2015;23:1500-1506.
319. Clark PM, Ebiana VA, Gosa L, Cloughesy TF, Nathanson DA. Harnessing Preclinical Molecular Imaging to Inform Advances in Personalized Cancer Medicine. *J Nucl Med*. 2017;58:689-696.

320. Perrin DM. [18F]-Organotrifluoroborates as Radioprosthetic Groups for PET Imaging: From Design Principles to Preclinical Applications. *Acc Chem Res.* 2016;49:1333-1343.
321. Bernard-Gauthier V, Lepage ML, Waengler B, et al. Recent Advances in 18F Radiochemistry: A Focus on B-18F, Si-18F, Al-18F, and C-18F Radiofluorination via Spirocyclic Iodonium Ylides. *J Nucl Med.* 2018;59:568-572.
322. Liu Z, Li Y, Lozada J, et al. Rapid, one-step, high yielding 18F-labeling of an aryltrifluoroborate bioconjugate by isotope exchange at very high specific activity. *Journal of Labelled Compounds and Radiopharmaceuticals.* 2012;55:491-496.
323. Ting R, Adam MJ, Ruth TJ, Perrin DM. Arylfluoroborates and Alkylfluorosilicates as Potential PET Imaging Agents: High-Yielding Aqueous Biomolecular 18F-Labeling. *J Am Chem Soc.* 2005;127:13094-13095.
324. Hume SP, Gunn RN, Jones T. Pharmacological constraints associated with positron emission tomographic scanning of small laboratory animals. *European Journal of Nuclear Medicine and Molecular Imaging.* 1998;25:173-176.
325. Briard E, Zoghbi SS, Siméon FG, et al. Single-Step High-Yield Radiosynthesis and Evaluation of a Sensitive 18F-Labeled Ligand for Imaging Brain Peripheral Benzodiazepine Receptors with PET. *Journal of Medicinal Chemistry.* 2009;52:688-699.
326. Sergeev M, Lazari M, Liu Z, Perrin D, van Dam RM. Increasing the specific activity of isotopic exchange radiofluorination using microfluidics. December 2016.
327. Lau J, Pan J, Rousseau E, et al. Pharmacokinetics, radiation dosimetry, acute toxicity and automated synthesis of [18F]AmBF3-TATE. *EJNMMI Research.* 2020;10:25.